The University Of Sheffield.

EFFICIENCY OPTIMISED CONTROL OF INTERIOR MOUNTED PERMANENT MAGNET MACHINES FOR ELECTRIC VEHICLE TRACTION

By:

MIKAIL KOC

A thesis submitted in partial fulfilment of the requirements for the degree of Doctor of Philosophy

The University of Sheffield
Faculty of Engineering
Department of Electronic and Electrical Engineering

DEC, 2016

To my late mother;

MELEK

May her soul rest in peace!

ACKNOWLEDGMENTS

The completion of this thesis owes much to many people and I would like to take this opportunity to acknowledge them for the contributions they all made.

First and foremost, I would like to express my deep sense of gratitude and indebtedness to my supervisor Prof. Jiabin Wang for his invaluable guidance, ceaseless encouragement and inspiration in the journey to the completion of this thesis. I am truly grateful for all the effort he has put into my supervision as a conscientious and more than qualified supervisor.

I would also like to express my special thanks to my wife Fatma. I owe an indescribable debt for your love, continuous support, endless patience, cooking, unflagging faith in me and playing such a large part in seeing this work finally completed. I love you and no doubt our little princess Melek - my late mother's namesake.

This thesis has also been a story of Dr. Tianfu Sun who is not only my colleague in electrical machines and drives research group but one of my close friends in the UK. I am immensely thankful to Dr. Sun for his unreserved stimulating ideas, valuable discussions and contributions throughout. I am thankful to my other colleagues in the group including, Dr. Xiao Chen for his high fidelity machine models, Mr. Sreeju S. Nair, Dr. Bhaskar Sen and Mr. Chaohui Liu for the insightful discussions we had together.

Much is owed to my father Mehmet Ali who has raised three motherless children. I, therefore, must express my heartfelt thanks to my father as well as my brother and sister Alper and Emel for their unconditional love and support both in life and in education.

Mikail Koç

ABSTRACT

Electric vehicles (EV) are playing a momentous role to the wide society as they facilitate the use of clean energy technologies. Interior mounted permanent magnet (IPM) synchronous machines are commonly employed in EVs owing to their superior characteristics such as high efficiency and power density and a wide field weakening operating range. High efficiency motor operation extends EVs drive range with the same amount of energy. Advanced control techniques to achieve high efficiency operation and smooth output torque production are, therefore, highly important areas to be researched. This thesis deals with the state-of-art motor drives and further develops advanced control strategies for minimum loss operation with good torque control quality.

Modern AC drives can be classified in two groups, *viz.*, field oriented control (FOC) and direct torque control (DTC). Whilst the former controls the phase currents for torque realization, the latter controls the torque directly. This thesis researches both and the novel advanced techniques are underpinned by extensive simulations and supported by experimental validations on a prototype motor designed for a specific class of EVs.

The biggest challenge associated with the FOC drives is to improve the efficiency due to highly nonlinear characteristics of IPM machines. It has been discovered that even if the machine parameters are accurately modelled and stored in controllers to achieve optimal efficiency operation in a great number of FOC based IPM drives, there is still much deviation from the ideal operating points. A novel approach for online efficiency optimisation is proposed and comprehensively analysed in this thesis.

The challenges pertinent to the DTC based IPM drives are to improve the observer quality and to reduce the strong coupling and the nonlinearity in the control loops. Novel observer structures, and the decoupled and linearized control techniques are among the novel contributions for DTC drives in this thesis. In addition, a comprehensive analysis of the relationship between stator flux vector and the torque has not been performed in the literature. The detailed analysis is made in this thesis and the maximum torque per voltage (MTPV) control theory for DTC drives is introduced.

It is noteworthy that this thesis is based on comparative studies between the state-of-art and the proposed techniques throughout, and hence offers an insightful understanding for modern IPM drives.

TABLE OF CONTENTS

LIST OF FIGURES

LIST OF TABLES

LIST OF PUBLICATIONS

Journal papers:

[J1] T. Sun, J. Wang, M. Koc, and X. Chen, "Self-Learning MTPA Control of Interior Permanent Magnet Synchronous Machine Drives Based on Virtual Signal Injection," *IEEE Transactions on Industry Applications*, vol. 52, p. 3062-3070, Jul. 2016.

[J2] T. Sun, J. Wang, and M. Koc, "Virtual Signal Injection Based Direct Flux Vector Control of IPMSM Drives," *IEEE Transactions on Industrial Electronics*, vol. 63, p. 4773-4782, Aug. 2016.

[J3] M. Koc, T. Sun, and J. Wang, "Performance improvement of direct torque controlled interior mounted permanent magnet drives by employing a linear combination of current and voltage based flux observers," *Power Electronics, IET*, vol. 9, p. 2052-2059, Aug. 2016.

[J4] M. Koc, J. Wang, and T. Sun, "An Inverter Nonlinearity Independent Flux Observer for Direct Torque Controlled High Performance Interior Permanent Magnet Brushless AC Drives," *IEEE Transactions on Power Electronics*, vol. 32, p. 490-502, Jan. 2017.

[J5] T. Sun, J. Wang, and M. Koc, "Self-learning Direct Flux Vector Control of Interior Permanent Magnet Machine Drives," *IEEE Transactions on Power Electronics*, in press, 2016.

[J6] T. Sun, J. Wang, and M. Koc, "On Accuracy of Virtual Signal Injection based MTPA Operation of Interior Permanent Magnet Synchronous Machine Drives," *IEEE Transactions on Power Electronics*, accepted, Nov. 2016.

Journal papers under preparation:

[J7] M. Koc, J. Wang, and T. Sun, "MTPV control theory in direct torque controlled IPM drives" *IEEE Transactions on Power Electronics*, planned to be submitted.

[J8] M. Koc, T. Sun, and J. Wang, "Improved Virtual Signal Injection Based MTPA Tracking for IPM Drives" *IEEE Transactions on Industrial Electronics*, planned to be submitted.

[J9] T. Sun, J. Wang, and M. Koc, "Hybrid Control of Interior Permanent Magnet Synchronous Machine Drives," *IEEE Transactions on Power Electronics*, planned to be submitted.

Conference papers:

[C1] T. Sun, J. Wang, M. Koc, and X. Chen, "Self-learning MTPA control of interior permanent magnet synchronous machine drives based on virtual signal injection," in *Electric Machines & Drives Conference (IEMDC), 2015 IEEE International*, p. 1056-1062, 10-13 May 2015.

[C2] M. Koc, J. Wang, and T. Sun, "Stator flux oriented control for high performance interior permanent magnet synchronous machine drives," in *Power Electronics, Machines and Drives (PEMD 2016), 8th IET International Conference on*, p. 1-6, 19-21 April 2016.

[C3] M. Koc, T. Sun, and J. Wang, "A linear combination of current and voltage based flux observers for direct torque controlled IPM drives," in *Power Electronics, Machines and Drives (PEMD 2016), 8th IET International Conference on*, p. 1-6, 19-21 April 2016.

LIST OF ACRONYMS

2D	Two dimensional
3D	Three dimensional
AW	Anti-windup
BLAC	Brushless AC machine
BPF	Band-pass filter
CB	Current based (estimations based on phase currents)
CLTF	Closed-loop transfer function
DTC	Direct torque control
EV	Electric vehicle
FB	Feedback
FF	Feed-forward
FOC	Field oriented control
FW	Field weakening
GHG	Greenhouse gases
HEV	Hybrid electric vehicle
ICE	Internal combustion engine
IPM	Interior mounted permanent magnet
IPMSM	Interior mounted permanent magnet synchronous machine
IM	Induction machine
LPF	Low-pass filter
LUT	Look-up table
MTPA	Maximum torque per ampere
MTPV	Maximum torque per voltage
OM	Over modulation
PC	Personal computer
PI	Proportional integral
PM	Permanent magnet
PWM	Pulse width modulation
P-MOB	Personal mobility
SFVC	Stator flux vector control
SPM	Surface mounted permanent magnet
SVPWM	Space vector pulse width modulation
THD	Total harmonic distortion
VB	Voltage based (estimations based on phase voltages)
VSI	Voltage source inverter

LIST OF SYMBOLS

A	Amplitude of the high frequency signal
$\alpha\beta$	2-axis stationary reference frame
dq	2-axis rotating rotor reference frame
$f\tau$	2-axis rotating stator flux reference frame
B	Viscous friction coefficient
℃	Celsius degree
δ	Angle between PM and stator flux linkages (torque angle)
δ_{max}	Maximum torque angle
Δ	Error of the state variables
e	Error terms
E	Induced voltage of a machine (back EMF)
f_{inv}	Inverter switching frequency
F	Any voltage, current or flux linkage vector
$I_{\alpha\beta}$	$\alpha\beta$- axis currents
I_{cr}	Critical current
I_{dq}	dq- axis currents
I_{dq}^{h}	High frequency signal injected dq- axis currents
$I_{f\tau}$	$f\tau$- axis currents
I_{max}	Maximum current
I_s	Stator current
J	Inertia of a machine
K	Gain of a filter
K_i	Integral gain
K_p	Proportional gain
L_{dq}	dq- axis inductances
M	Modelling error matrix
M^{-1}	Inverse of the matrix M
n_{min}	Minimum number of samples per period
p	Number of pole-pairs
P_{in}	Input power
P_{Fe}	Iron loss of a machine
P_J	Copper loss of a machine
P_{loss}	Electrical power loss of a machine
P_{out}	Output power
θ_e	Rotor position angle
θ_f	Stator flux phase angle ($\theta_f = \theta_e + \delta$)
R	Phase resistance of a machine
R_n	Nominal value of the phase resistance of a machine
R_{ON}^{D}	On-state resistance of freewheeling diode
R_{ON}^{S}	On-state resistance of active switch
T^h	High frequency signal injected torque component
T_d	Dead-time
T_e	Electromagnetic torque
T_s	Sampling time
V	Magnitude of the operating voltage

$V_{\alpha\beta}$	$\alpha\beta$- axis voltages
V_{dc}	DC-link voltage
V_{dq}	dq- axis voltages
$V_{f\tau}$	$f\tau$- axis voltages
V_{max}	Maximum available voltage
V_s	Stator voltage
V_{Th}^{D}	Threshold voltage of freewheeling diode
V_{Th}^{S}	Threshold voltage of active switch
β	Current angle between the stator current vector and the q- axis
$\emptyset$	Power factor angle
ρ	Saliency ratio of a BLAC machine
ω	Electrical angular speed
ω_m	Mechanical speed
ω_n	Natural frequency
ξ	Damping ratio
$\Psi_{\alpha\beta}$	$\alpha\beta$- axis flux linkages
Ψ_{dq}	dq- axis flux linkages
Ψ_m	Permanent magnet flux linkage
Ψ_{ratio}	Ratio of the stator flux magnitude to the PM flux linkage
Ψ_s	Stator flux linkage

CHAPTER 1 – GENERAL INTRODUCTION

1.1. RESEARCH MOTIVATION

The majority of today's transportation vehicles are powered by fossil fuels through internal combustion engines (ICE). However, the fossil fuel resources are limited and non-renewable. In addition, the use of conventional resources has a significant contribution to air pollution and climate change due to inevitable emissions of greenhouse gases (GHG), and harmful pollutants. Accordingly, industrialized countries have agreed to reduce the GHG emissions in their countries at a certain rate under Kyoto Protocol in 1997 in order to protect ecology [1, 2]. Electric vehicles (EV) and hybrid electric vehicles (HEV) are, therefore, becoming an important alternative for personal mobility and for public transportation as they facilitate the use of renewable and sustainable energy technologies with reduced GHG emissions. Thus, both the academic world and the transportation industry are undertaking significant research on development of EVs.

Interior mounted permanent magnet (IPM) synchronous machines are commonly employed in electric vehicles owing to their superior characteristics such as:

- High efficiency,
- Low acoustic noise,
- Low rotor losses,
- Robustness since the magnets are buried,
- Wide constant power operating range,
- Highest torque to power ratio of all machines as a result of high saliency and reluctance torque.

However, IPM machines exhibit highly non-linear characteristics due to magnetic saturations, and the load and temperature dependent machine parameters such as inductances, armature resistance and permanent magnet flux linkage. In addition, inverters which are employed as power converters in machine drive systems exhibit nonlinearity depending on threshold voltages of electronic devices and duration of dead-time to prevent shoot-through phenomenon. Consequently, voltage distortion occurs at the output of the inverter. Furthermore, there is a variation on the available DC link voltage in a practical implementation. These operation and temperature dependent nonlinear characteristics of the inverter and the motor as well as the variation on the DC link voltage pose a great challenge for control of IPM machines to achieve fast dynamic response, energy efficient operation and smooth output torque.

The key objective of this thesis is, therefore, to achieve high efficiency motor operation with good torque control quality over an entire speed range by adopting advanced control techniques and parameter adaptation laws. Because transportation is one of the main sectors which dominate energy consumption and hence the GHG emissions, the research in this field plays an important role to the wide society for the development of eco-friendly EVs.

1.2. GENERAL INTRODUCTION TO MODERN IPM-BLAC DRIVES

Brush-less AC (BLAC) machines can be classified as salient or non-salient types based on the orientation of magnets in the rotor. Whilst surface mounted permanent magnet (SPM) types have no saliency, inset and interior mounted BLAC machines are classified as salient machines [3]. Saliency is an attractive feature for BLAC machines in particular for traction applications because high saliency is conducive to the high torque density due to reluctance torque, and hence more extended speed range. However, the utilization of the reluctance torque renders IPM-BLAC drives to be controlled in a more complicated way than their SPM-BLAC counterparts.

Control of the machines can be classified into two categories based on how to obtain rotor position and machine speed. Typical is sensor-based control where a position sensor (an encoder or a resolver) is employed to obtain the rotor position and the machine speed. The other is sensor-less control where the position angle and the speed is estimated from phase voltages, currents and parameters by employing a computational technique or an observer. One of the well-known control techniques for the sensor-less drives is high-frequency low-magnitude carrier signal injection method. However, none of the sensor-less control techniques is perfect since parameters may significantly vary at various operating conditions and there may be serious problems at low speeds especially at zero speed where the electrical frequency of the machine is zero. This thesis deals with sensor-based control in which accurate rotor position information is readily available and sensor-less control is out of the scope.

Modern AC drives can be classified into two categories based on how to control the torque. These are direct torque controlled (DTC) drives and field oriented controlled (FOC) drives where the torque is controlled indirectly via *d*- and *q*- axis currents in the rotor reference frame. Whilst the FOC drives are usually realized in the rotor (*dq*) reference frame, DTC drives may be realized in a synchronous or stationary reference

frame depending on the control system configuration. A typical DTC implementation is formulated in the stator flux reference frame ($f\tau$) which rotates at the synchronous speed with the rotor in steady-states.

Control of the IPM machines can be classified into three categories based on the operating region, *viz.*, maximum torque per ampere (MTPA), field/flux weakening (FW) and maximum torque per voltage (MTPV) regions. Drives formulated in rotor and in stator flux reference frames, and the operating regions in these frames will be discussed in great details later in this thesis.

Machine drives can be classified as position, speed or torque controlled drives based on the input of the system. As can be seen from Fig. 1.1, neither position, nor speed controlled drives can be implemented unless stable torque control is achieved. Therefore, the torque control is of the main concern in this thesis.

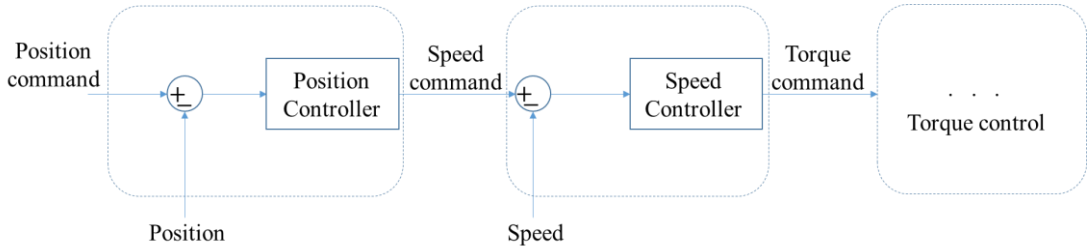

Fig. 1.1 Block diagram of a typical drive system

Fig. 1.2 illustrates the block diagram of a typical closed-loop drive system. For traction applications, the input of the system is generally torque command, the source is DC-link voltage source and hence the power converter is the voltage source inverter (VSI). The feedback of the closed-loop drive system may be rotor position angle, speed, measured DC-link voltage, motor/ambient/inverter temperature, or measured phase currents or voltages depending on the designed control system configuration.

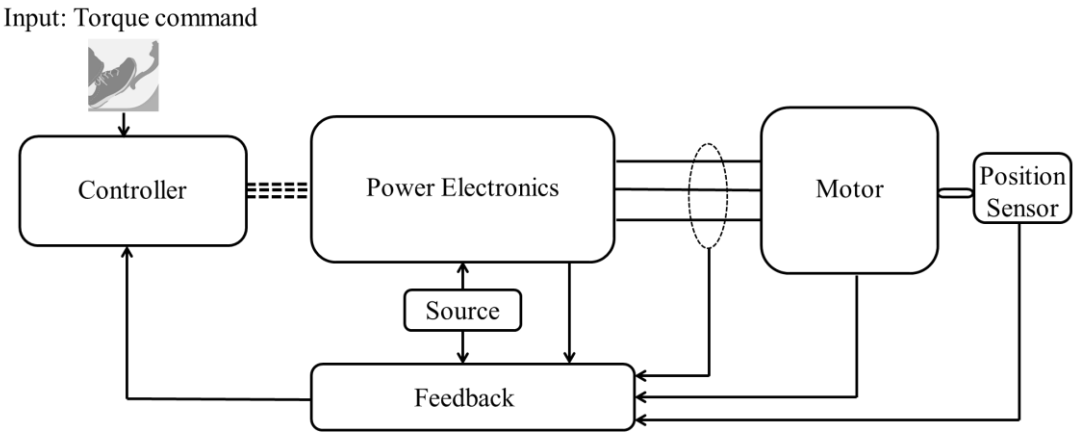

Fig. 1.2 Block diagram of a typical closed-loop drive system

1.2.1. DRIVE SYSTEM SETUP

Because the experiments throughout the thesis have been carried out with one test rig, the drive system will be briefly introduced in this section. Fig. 1.3 illustrates the view of the experimental hardware setup of a 10 kW IPM drive system. The mechanical setup, i.e., the IPM machine, torque transducer and dynamometer are shown in Fig. 1.3-(a), the power electronics converter setup, i.e., the controller, inverter, DC-link voltage source connection, communication channel and current transducers are shown in Fig. 1.3-(b) and the power analyser is shown in Fig. 1.3-(c). The prototype IPM machine (P-MOB Motor) has been designed for electric vehicle traction applications for a wide speed range of operation and its specifications are listed in Table 1.1.

Proposed control techniques are implemented in real-time in a microprocessor based controller which generates switching signals for the inverter to drive the motor. The inverter is specifically designed for prototype IPM machine. The inverter device data was obtained from manufacturer's datasheet and the nominal specifications are listed in Table 1.2. The drive torque is measured in experiments by a high precision in-line torque transducer as shown in Fig. 1.3-(a). The rotor position is measured by a magnetic encoder and hence the position angle and the speed are readily available in the controller. The current/voltage waveforms are captured by the power analyser as shown in Fig. 1.3-(c).

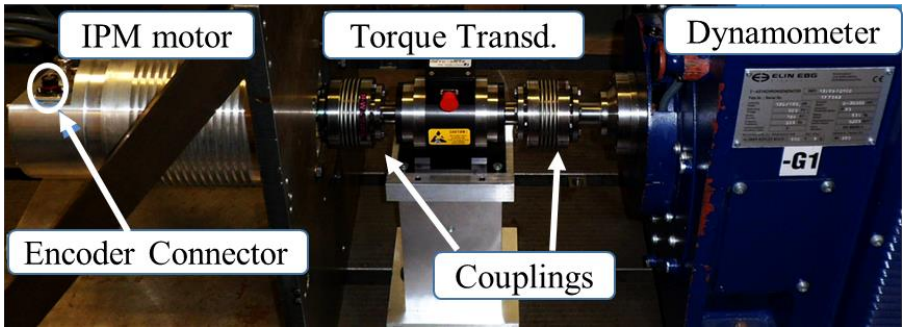

(a) Mechanical setup

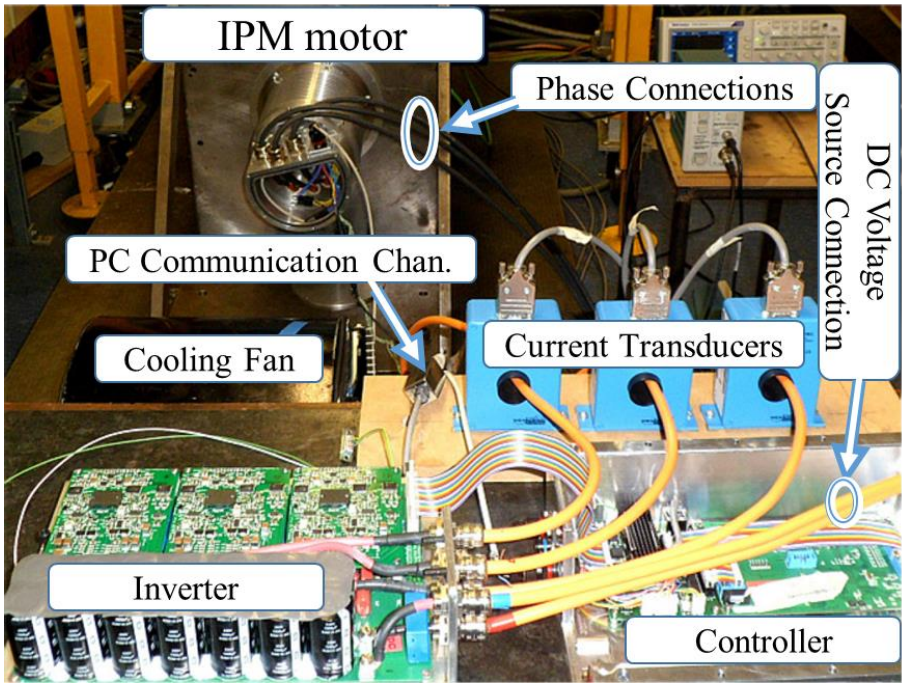

(b) Power electronics converter setup

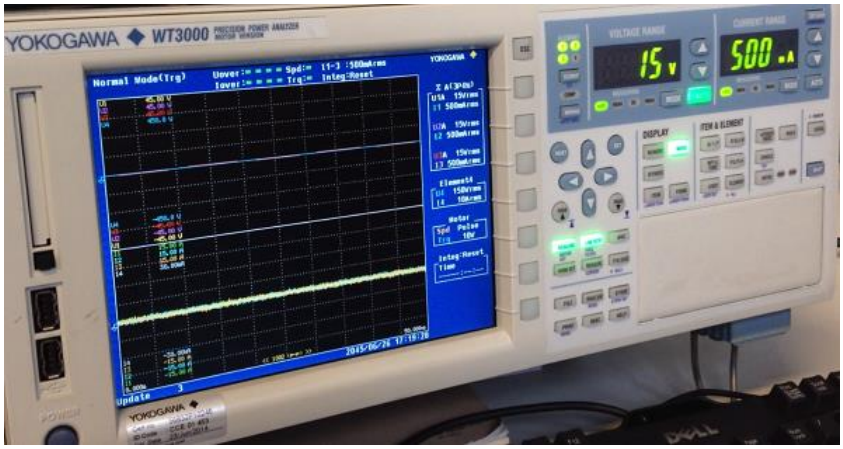

(c) Power analyser

Fig. 1.3 Experimental hardware setup

Drive tests can be performed either by operating the test drive under speed control mode and the dynamometer in torque control mode, or the test drive under torque control

mode and the dynamometer under speed control mode. Since the drive under test is developed for EV traction and operates mainly in torque control, the tests were performed with the latter in this thesis.

Table 1.1 Specifications of the prototype IPM machine (P-MOB)

Number of pole-pairs/Nominal phase resistance	3 / 0.0512 Ω
Continuous current/maximum current	58.5 A / 118 A
DC link voltage	120 V
Base speed / maximum speed	1350/4500 r/min
Continuous torque / peak torque	35.5/70 Nm
Nominal *dq*- axis inductances (L_{dq})	0.545/1.571 mH
Nominal permanent magnet flux linkage (Ψ_m)	0.11 Wb
Inertia (J)	0.0073 kg.m^2
Viscous friction coefficient (B)	1/300 Nm.s/rad
Peak power below base speed	10 kW
Peak power at maximum speed	7 kW

Table 1.2 Inverter specifications

T_s - Sampling period	125μs (8kHz)
T_d - Dead-time to prevent shoot-through	3μs
V_{Th}^S - Threshold voltage of active switch	0.85 V
V_{Th}^D - Threshold voltage of freewheeling diode	0.8 V
R_{ON}^S - On-state resistance of active switch	5 mΩ
R_{ON}^D - On-state resistance of freewheeling diode	4.5 mΩ
Manufacturer	Siemens

1.2.2. POWER CONVERSION

Power conversion technique is crucial for a good torque control quality. The conversion from a DC source to an AC load can be achieved by either variable (irregular) or constant switching frequency based control techniques. These have been reported widely in the literature and their superior and inferior features for IPM drives are briefly discussed in this section. The variable switching frequency based control is usually referred as hysteresis or bang-bang technique and the constant switching frequency based control can be achieved by different carrier based pulse-width-modulation (PWM)

techniques. Table 1.3 presents different PWM techniques and their maximum DC-link voltage utilization ratios [4].

Table 1.3 Maximum DC-link voltage utilization of modulation techniques

Six-step PWM	Space Vector PWM (SVPWM)	Third harmonic injection PWM	Sinusoidal PWM
63.67% $\left(=\frac{2}{\pi}\right)$	57.74% $\left(=\frac{1}{\sqrt{3}}\right)$	57.74% $\left(=\frac{1}{\sqrt{3}}\right)$	50% $\left(=\frac{1}{2}\right)$

As can be seen from the table, battery utilization of sinusoidal PWM is less and hence it is not preferred in EV applications.

One of the over-modulation strategies discussed in [5-7] can be adopted to maximize the DC-link utilization with six-step operation. However, non-sinusoidal (square-wave) voltage when the hexagon is fully utilized increases the harmonics significantly [8] and this results in current distortion and the increased torque ripple [6, 9, 10]. Therefore, the extended speed range and the torque control quality might be compromised.

Space vector PWM has a minimum number of switching in one sampling period as only one switch changes state at once and hence switching losses and harmonic distortion is lower. Accordingly, it is the most commonly employed modulation technique in modern drives [11-23].

Hysteresis technique with irregular switching, on the other hand, is one of the early switching techniques. It chooses one of the six active vectors based on the information coming from hysteresis bands [24] and may use the zero vectors depending on the controller design [25]. To date, hysteresis based control techniques have been adopted to IPM-BLAC machine drives extensively [24-32].

A comprehensive comparative study between constant and variable switching based IPM-BLAC drives has been undertaken by [24]. It has been shown that the total harmonic distortion (THD) with the SVPWM based drive is significantly lower than the hysteresis based drive where the switching is only updated at the sampling instant. Accordingly, the current waveforms of the variable switching based drive has higher current distortion and hence the ripples on torque and flux is significantly higher in both

MTPA and FW operations. Therefore, the modulation technique employed throughout is based on SVPWM strategy in this thesis.

In the following sections (1.3 & 1.4), the fundamental theory for control of IPM machines, high efficiency control techniques for modern drives, superior and inferior features of the different techniques reported in the literature, and the challenges associated with high efficiency operation are briefly discussed. However, it is noteworthy that the comprehensive literature review with particular attention to certain problems of state-of-art drives will also be discussed at the beginning of each main chapter.

1.3. FIELD ORIENTED CONTROL (FOC) BASED IPM-BLAC DRIVES

Stator current vector controlled brushless-AC drives are commonly referred to as field oriented control (FOC) in the literature. The phase currents are transformed to rotor reference frame and the control is realized in this frame (*dq*). The advantage of the control in rotor frame is that the machine currents can be controlled and limited directly, whereas the limitation cannot be directly posed in direct torque controlled (DTC) drives. The phase currents can easily be measured for feedback control and hence eliminates the need for a flux observer which is a must for DTC based IPM drives. The IPM-BLAC machine modelling in rotor reference frame can be described as follows:

1.3.1. MACHINE MODELLING IN ROTOR FRAME

Clark and Park transformations of three-axis stationary ABC frame equations give two-axis rotating reference frame equations of AC machines. It is noteworthy that Clark transformation can be defined in different conventions in the literature such as x3/2 peak, peak or root-mean-square (rms) conventions. The modelling throughout the thesis is based on the most common peak convention modelling for BLAC machines since this convention is magnitude invariant and universal.

Rotor *(dq)* frame modelling of brushless-AC machines is obtained when the rotor angle (θ_e - Fig. 1.4) is employed in the Park transformation.

The well-known peak convention modelling of IPM machines in the rotor reference frame are given as follows [29].

$$\begin{bmatrix} V_d \\ V_q \end{bmatrix} = R \begin{bmatrix} I_d \\ I_q \end{bmatrix} + \frac{d}{dt} \begin{bmatrix} \Psi_d \\ \Psi_q \end{bmatrix} + \omega \begin{bmatrix} -\Psi_q \\ \Psi_d \end{bmatrix} \tag{1.1}$$

$$\begin{bmatrix} \Psi_d \\ \Psi_q \end{bmatrix} = \begin{bmatrix} L_d & 0 \\ 0 & L_q \end{bmatrix} \begin{bmatrix} I_d \\ I_q \end{bmatrix} + \begin{bmatrix} \Psi_m \\ 0 \end{bmatrix} \tag{1.2}$$

$$T_e = \frac{3p}{2} \left[\Psi_d I_q - \Psi_q I_d \right] \tag{1.3}$$

where $I_{dq}, V_{dq}, \Psi_{dq}$ are the rotor frame currents, voltages and flux linkages, respectively. Ψ_m is the permanent magnet (PM) flux linkage, p is pole-pair number, R is the phase resistance, ω is electrical angular speed, T_e is the electromagnetic torque and L_{dq} are the *dq*- axis inductances, respectively. The flux linkages are non-linear functions of the currents due to magnetic saturation, and vary with rotor position and temperature. The position-dependent flux linkage characteristics result from slotting and space harmonics in a practical IPM.

Fig. 1.4 illustrates the two axis stationary and rotating rotor reference frames where I_s, V_s and Ψ_s are the stator current, voltage and flux linkage vectors, respectively. β is defined as the current angle or advance angle in the literature and it is the angle between stator current vector (I_s) and the q- axis. θ_e is the rotor position angle and hence the *dq*- frame is defined as the rotor reference frame.

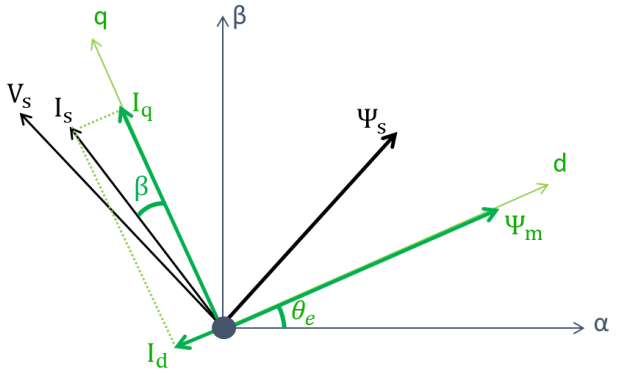

Fig. 1.4 Stationary ($\alpha\beta$) and rotating rotor (*dq)* reference frames

High efficiency operation, of course, requires minimum loss at any operating region. The electrical power loss of a machine is expressed by:

$$P_{loss} = P_{Fe} + P_J \tag{1.4}$$

where P_{Fe} is the iron loss (or core loss = eddy current loss + hysteresis losses), P_J is the copper loss (I^2R losses). Equivalent circuit of BLAC machines representing the power losses in (1.4) is demonstrated in Fig. 1.5 in the rotor reference frame.

Based on the machine modelling and the current and voltage constraints in a drive system, high efficiency operation can be classified in three categories, *viz.* MTPA, FW and MTPV operations. It should be noted that BLAC machines are classified in two groups based on the location of the critical current point in which the *d*- axis flux linkage is zero. Operation trajectories (MTPA, FW, MTPV) of these two types are shown in Fig. 1.6 (a) and (b), respectively. As will be seen, the machines whose critical current point I_{cr} is inside the current boundary require MTPV control for high efficiency operation whereas the others do not. Further discussions on the critical current point and the MTPV control will be made in section 1.3.4. Also, the theoretical analysis on the operating trajectories shown in Fig. 1.6 will be given in details in sections 4.2.1 and 4.3.1 later in the thesis.

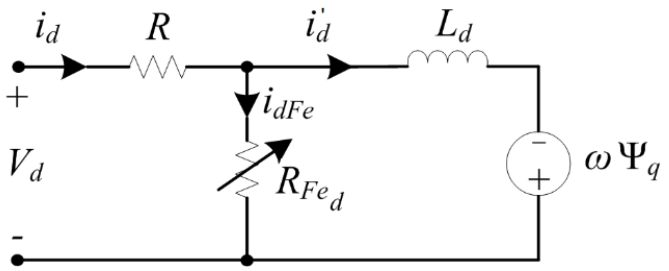

(a) Equivalent *d*- axis

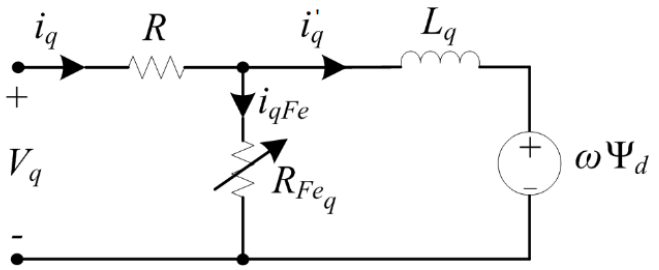

(b) Equivalent *q*- axis

Fig. 1.5 Equivalent circuit of BLAC machines in rotor reference frame *(dq)* including iron loss

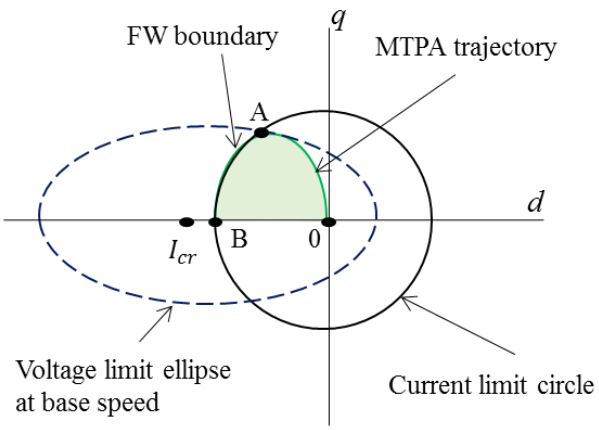

(a) Type I

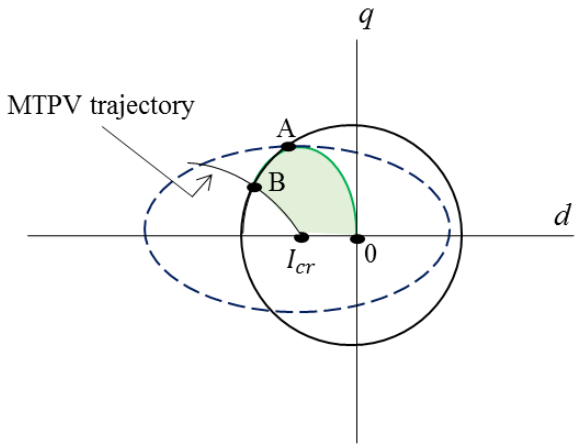

(b) Type II

Fig. 1.6 Operation trajectories of IPM-BLAC machines

The high efficiency operation techniques for wide speed range operation are discussed separately as follows.

1.3.2. MTPA CONTROL (CONSTANT TORQUE REGION)

MTPA is a control strategy in the constant torque region. It minimizes the copper losses when machine operates below the base speed. The maximum DC-link voltage utilization is obtained at the base speed. MTPA trajectory follows the curve from 0 to A in Fig. 1.6 as torque increases. As can be seen, the MTPA trajectory and the voltage limit ellipse at the base speed intersect with each other at point A. Maximum torque is obtained at this point which can be demanded from the machines to accelerate the speed in a constant torque region (MTPA).

R_{Fe} in Fig. 1.5 represents the equivalent resistance value of iron loss. Due to the difficulty of its accurate modelling and its negligible influence on the optimal current

trajectory for loss minimisation [33], the iron loss is commonly neglected in the constant torque region in the literature [18]. Therefore, the electromagnetic torque is maximized per stator current magnitude in order to minimize the copper losses, *i.e.* maximum torque per ampere (MTPA) control.

The MTPA is achieved by posing *d*- axis current to zero in non-salient (SPM, $L_d = L_q$) machine drives. However, as for salient (IPM) machine drives there is a reluctance torque which needs to be utilized to achieve high efficiency operation. Hence, accurate utilization of the reluctance torque requires more sophisticated control techniques for IPM types than their SPM counterparts.

MTPA control for IPM-BLAC machine drives is parameter dependent and obtaining accurate *d*- axis current is a great challenge as machine parameters of IPM types are highly nonlinear [18].

The theoretical analysis of the MTPA control and the further discussions with state-of-art MTPA realization techniques will be made in Chapter 5 in great details where a novel approach is also introduced.

1.3.3. FW CONTROL (CONSTANT POWER REGION)

The field weakening control is the control above the base speed. At steady states, one obtains the voltage magnitude from (1.1).

$$V^2 = R^2 {I_s}^2 + \omega^2 \left({\Psi_d}^2 + {\Psi_q}^2 \right) = R^2 {I_s}^2 + \omega^2 {\Psi_s}^2 \tag{1.5}$$

where V is the magnitude of the operating voltage and Ψ_s is the magnitude of the stator flux linkage. The induced voltage of a machine is obtained from (1.5) and it is given in (1.6).

$$E = \sqrt{V^2 - R^2 {I_s}^2} = \omega \, \Psi_s \tag{1.6}$$

As can be deduced from (1.6), when the maximum induced voltage is reached which coincides to the full utilization of DC-link voltage, the stator flux magnitude needs to be weakened as the speed increases. This phenomenon is called as field/flux weakening (FW).

In Fig. 1.6, current limit circle and voltage limit ellipse intersect with each other at point A. This intersection point is the point where the transition from MTPA to field-

weakening or vice-versa needs to be triggered. Whilst the machines should operate only on the curve from 0 to A to achieve MTPA operation below the base speed, the operation is in the highlighted area in a FW region above the base speed. As speed increases further than base speed, voltage ellipse shrinks and torque capability of a machine reduces along with the trajectory from A to B due to weakened stator flux magnitude.

In FOC drives, the realization of a FW operation can be classified in three categories based on how to generate the reference *dq*- axis currents or, in other words, how to weaken the stator flux magnitude. These are feed-forward FW (FF-FW) control, feedback FW (FB-FW) control and hybrid (FF-FB FW) control.

1.3.3.1. OPEN-LOOP (FEED-FORWARD) FW CONTROL

In feed-forward FW control schemes the *dq*- axis reference currents (I_{dq}^{*}) for both MTPA and FW regions are generated in the feed-forward path based on the torque demand, the maximum current limit, operating speed, DC-link voltage and the machine parameters [34-42]. It is an open-loop FW control system where the saturation of voltage is not utilized as a feedback to generate or compensate the reference *dq*- axis currents. On the contrary, the maximum available voltage is considered in the feed-forward path. The shortcoming of a feed-forward FW control scheme is that the drive system is dependent on machine parameters not only in an MTPA region but in a FW region, too, since the stator flux magnitude which is weakened in a FW region is calculated from machine parameters and DC-link voltage in the feed-forward path.

1.3.3.2. CLOSED-LOOP (FEEDBACK) FW CONTROL

In feedback FW control schemes the *dq*- axis reference currents for MTPA operation are generated based on the torque demand, the maximum current limit and the machine parameters [43-48]. As for FW region, the voltage saturations of the current regulators are utilized as a feedback to the control system to adjust the *d*- axis current reference. Since the reference currents are generated based on the utilization of the voltage saturation in a FW region, there is no requirement for accurate knowledge of machine parameters in this region. Therefore, the model dependent inaccuracies in the FW operating region is compensated by the feedback loop. However, the *d*- and *q*- axis current controllers are coupled, and control performance deteriorates.

1.3.3.3. HYBRID FW CONTROL

In hybrid FW control schemes, the reference currents for both MTPA and FW regions are generated in the feed-forward path such as in a FF-FW control scheme and are compensated in a FW region by utilization of the voltage saturations of the current regulators in order to compensate for the machine parameter variations such as in FB-FW control scheme [49]. The hybrid FW control is often implemented by employing two dimensional look-up tables (2D-LUTs) whose inputs are reference torque and stator flux magnitude while the outputs are *dq*- axis reference currents [50-53]. The use of feed-forward improves response time in the field weakening region, but the coupling problem between the two current control loops remains.

1.3.4. MTPV CONTROL

Maximum torque per voltage (MTPV) operation occurs in the FW region when the voltage constraint will limit the machine current below its maximum. In this region, it is no longer convenient to exploit the maximum current to achieve the maximum electromagnetic torque [54]. Thus, the current limitation should be imposed online to realize the MTPV control for those machines which require MTPV operation.

The MTPV control may be required depending on the machine design. As can be seen in Fig. 1.6-(a), whilst type I machines, whose critical current point I_{cr} is outside the current limit circle, do not require MTPV operation, the current trajectory of type II machines (Fig. 1.6-b) need to be imposed from B to I_{cr} in order to maximize the torque to the EMF voltage and hence to achieve maximum torque per stator flux magnitude.

I_{cr} is the point where the stator flux magnitude becomes zero (theoretical deepest field weakening). As can be seen in Fig. 1.6, *q*- axis current and hence *q*- axis flux linkage are zero at point I_{cr}. By imposing *d*- axis flux linkage to zero, (1.7) is obtained.

$$I_{cr} = -\frac{\Psi_m}{L_d} \tag{1.7}$$

Clearly, I_{cr} is unique for a given machine and known as critical current. MTPV control has been discussed in detail in [37] and it has been shown that the optimum constant power operation is obtained when $I_{cr} \approx -I_{max}$, *i.e* , $I_{cr} \approx B$ in Fig. 1.6-(a).

The location of the critical current point of the prototype machine whose ratings are listed in Table 1.1 is outside the current limit circle (type I, Fig. 1.6-a). Hence, the prototype machine does not require MTPV control.

1.3.5. PROBLEMS OF IPM DRIVES UNDER FOC

It is a great challenge for FOC drives to cope with the machine parameter variations and resultant efficiency degradation of an IPM drive system. In a practical application, magnetic saturation, temperature, cross-coupling, manufacture tolerance and material property variations might contribute to parameter deviations greatly from those employed in a model based control system design. Although the parameter variations can be addressed by utilization of the current regulator saturations in a FW region as introduced by [45], a large number of FOC drives still suffer from model dependency in an MTPA region [6, 33, 36, 49]. It will be shown in Chapter 5 that numerous drives reported in the literature suffer from inefficient operation even if the machine parameters employed in the controller are accurate.

In addition, the field weakening operation in *dq*- axis current controlled drives is realized in a coupled manner. In other words, the stator flux magnitude is weakened by regulating both the *d*- and *q*- axis currents. The coupling between the two control loops may result in oscillatory responses and hence increase in the torque ripple in a FW operation.

Further, because FW operation cannot be realized directly in FOC drives, how to generate the reference *dq*- axis currents based on the weakened stator flux magnitude is not straightforward and indirect.

In order to address the above challenges associated with FOC drives, *i.e.* model dependent operation, coupled flux weakening control and indirect realization of a FW operation, direct torque control has become an important alternative for IPM-BLAC machines.

1.4. DIRECT TORQUE CONTROL (DTC) BASED IPM-BLAC DRIVES

Because the electromagnetic torque can directly be regulated as a state variable in machine drives, direct torque control (DTC) has become an attractive alternative to FOC

drives in the literature. Initially, DTC has been applied to induction machines (IM) and then it has become popular since late 90s for IPM-BLAC machines [29]. However, classical DTC schemes have been implemented via hysteresis controllers extensively [24-32]. DTC drives based on SVPWM technique are becoming more common in recent years [12-14, 55-58] due to its superior features to irregular switching [24] as has been discussed in section 1.2.2.

Despite the fact that torque seems to be controlled directly, it will be shown in this thesis (Chapter 4) that the DTC is, indeed, direct control of the stator flux vector and indirect control of torque in IPM-BLAC drives. Therefore, the DTC drives should be referred to as stator flux vector controlled drives as it is more insightful definition than DTC. DTC is formulated in the stator flux reference frame and hence the basic equations will be given in the following section which will be referred throughout the thesis.

1.4.1. MACHINE MODELLING IN STATOR FLUX FRAME

It has been discussed in section 1.3.1 that the rotor frame modelling is obtained when the rotor angle (θ_e) is employed in the Park transformation. Similarly, instead of the rotor angle, when the stator flux phase angle ($\theta_f = \theta_e + \delta$, Fig. 1.7) is employed in the Park transformation, the stator flux oriented brushless-AC machine modelling can be obtained. The new reference system is called *fτ* frame in which the *f*- axis is aligned with the stator flux vector and the *τ*- axis leads the *f*- axis by 90 degrees. Alternatively, transformation from the rotor reference frame to the stator flux reference frame can be obtained from Fig. 1.7 as follows:

$$\begin{bmatrix} F_f \\ F_\tau \end{bmatrix} = \begin{bmatrix} cos\delta & sin\delta \\ -sin\delta & cos\delta \end{bmatrix} \begin{bmatrix} F_d \\ F_q \end{bmatrix} \tag{1.8}$$

where F can be any voltage, current or flux linkage vector. δ is the torque (load) angle. The torque angle is constant in steady-states. As can be seen in Fig. 1.7, the torque angle is the angular displacement between the PM flux linkage and the stator flux linkage and it is given in (1.9).

$$\delta = \tan^{-1}\left(\frac{\Psi_q}{\Psi_d}\right) \tag{1.9}$$

Hence, the *dq*- axis model can be transformed to the *fτ* frame by (1.8) and (1.9) to obtain the machine model in the stator flux frame. The well-known mathematical expressions of the brushless AC machines in the *fτ* frame are given as follows [59].

$$\begin{bmatrix} V_f \\ V_\tau \end{bmatrix} = R \begin{bmatrix} I_f \\ I_\tau \end{bmatrix} + \frac{d}{dt} \begin{bmatrix} \Psi_s \\ 0 \end{bmatrix} + \Psi_s \begin{bmatrix} 0 \\ \omega + \frac{d\delta}{dt} \end{bmatrix} \tag{1.10}$$

$$T_e = \frac{3p}{2} \left(\frac{\Psi_s \Psi_m \sin \delta}{L_d} + \frac{(L_d - L_q) {\Psi_s}^2 \sin 2\delta}{2 L_d L_q} \right) \tag{1.11}$$

where $[V_f \quad V_\tau]^T$ and $[I_f \quad I_\tau]^T$ denotes the *fτ* frame voltage and current vectors, respectively, and Ψ_s is the magnitude of stator flux linkage vector. Substituting (1.8) and (1.9) for the current vector into (1.3) gives an expression for the electromagnetic torque.

$$T_e = \frac{3p}{2} \Psi_s I_\tau \tag{1.12}$$

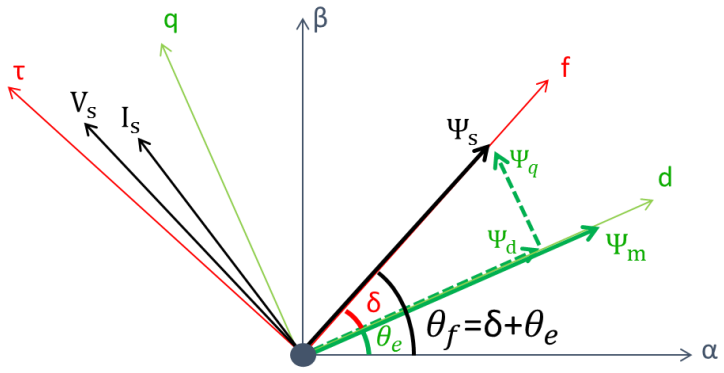

Fig. 1.7 Stationary ($\alpha\beta$), rotating rotor (*dq)* and rotating stator flux (*fτ*) reference frames

1.4.2. OBSERVERS FOR FEEDBACK CONTROL

Observer quality is of paramount importance in the stator flux vector controlled motor drives as the stator flux is not directly measurable and hence the drives rely on estimated state variables for feedback control. The quality of the flux observer is particularly crucial since the coordinate transformation in (1.8) and torque estimation (1.11) all rely on the accuracy of the observed flux vector.

As yet, a large number of flux observers have been reported and employed in drives [19, 57-64]. These observers can be classified in three categories, viz., current based, voltage based and hybrid closed loop flux observers.

The observers which have been employed in state-of-the-art drives will be investigated in great details in Chapters 2 and 3 where novel observer structures are proposed.

1.4.3. MTPA CONTROL (CONSTANT TORQUE REGION)

In stator flux vector controlled drives, the MTPA control is achieved by optimal stator flux magnitude as opposed to optimal *d*- axis current in current vector controlled drives. This is generally achieved by a look-up table whose input is the reference electromagnetic torque and output is the reference stator flux magnitude [12, 14, 26, 57]. The look-up table can either be calculated offline or by experiments easily as the torque is the product of flux and the current (1.12).

1.4.4. FW CONTROL (CONSTANT POWER REGION)

Field weakening realization of the stator flux vector controlled IPM drives is easier than of rotor oriented current vector controlled IPM drives as the stator flux magnitude can be weakened directly. Considering steady state, one can obtain the stator flux limitation from (1.10) and it is given in (1.13).

$$\Psi_s \leq \frac{\sqrt{{V_{max}}^2 - \left(RI_f\right)^2} - RI_\tau}{\omega} \tag{1.13}$$

where V_{max} is the maximum available voltage which is limited by the DC-link voltage and the modulation technique.

As can be seen, the stator flux magnitude limitation in (1.13) can directly be imposed to stator flux vector controlled IPM-BLAC drives. By doing so, the FW implementation can be realized in an easy and decoupled manner compared to FOC drives. Thus, the ease and decoupled realization of the FW control are the attractive features of the stator flux vector controlled IPM-BLAC drives [12, 14].

1.4.5. MTPV CONTROL

Maximum torque per voltage operation of stator flux vector controlled IPM-BLAC drives has been introduced and discussed by Gianmario Pellegrino, et al., [54, 59, 65]. It has been pointed out that the MTPV control coincides with a specific value of the torque angle δ shown in Fig. 1.7. However, neither the theory of the MTPV control has been analysed nor has accurate MTPV control been achieved in [54, 59, 65, 66] due to inaccurate limitation of the torque angle δ. The MTPV control is considered in Chapter 4. It will be shown that there is an optimum maximum torque angle per stator flux magnitude which coincides with the MTPV trajectory. This implies that the torque angle constraint should be imposed online as a function of stator flux magnitude. However, the above drive schemes reported recently limit the torque angle by a constant value. In addition, because the torque angle is not a regulated state variable in these schemes, an additional PI regulator is employed to realize the MTPV control. It will be shown in Chapter 4 that the torque angle limitation can be imposed directly to the proposed stator flux vector controlled IPM-BLAC drives online without the need for an additional PI regulator.

1.4.6. PROBLEMS OF IPM DRIVES UNDER DTC

DTC drives have become an important alternative to FOC based IPM-BLAC drives in late 90s due to their widely accepted attractive and superior features. However, there are some alleged features about DTC which are often cited in the literature and may be misleading.

- Fast torque response [27-29, 67, 68],
- Machine parameter independent control except for the stator resistance [24, 27-29, 67, 68],
- Inherently sensor-less control technique [27-29, 67, 68].

These may be true for DTC based induction machine (IM) drives with hysteresis flux and torque controllers and irregular switching. It is generally recognised that such control would lead to unacceptable torque ripple and poor performance in IPM drives. Thus, most DTCs for IPM drives are implemented through carrier based approaches. Torque realization in DTC based IPM drives is in fact indirect through direct control of the stator flux vector with observed flux and torque as feedback. Thus, the well-known

feature of having faster torque response with these drives is not always accurate as the response time is also limited by the observer response time, in particular for those drives which employ filters in the observer. On the contrary, a FOC drive with a reasonably fast current control might have much faster torque response time.

In addition, machine parameter independent control definition for DTC drives is not accurate as the reference stator flux magnitude for MTPA operation is generated by employing machine parameters, *i.e.*, *dq*- axis inductances and the permanent magnet flux linkage [12, 14, 28, 57, 58, 69-71]. Further to model dependent stator flux reference generator, the stator flux estimation at low speeds is commonly obtained by current model based estimation techniques as the voltage based flux observers deteriorate when the machine speed approaches to zero [12, 14, 20, 21, 54, 59, 65]. Therefore, a typical DTC drive is model dependent similar to FOC drives unless parameter variations are addressed.

Moreover, because the voltage based observers have poor performance at low speeds and the current model based estimation techniques are commonly employed to avoid this problem [12, 14, 19-21, 72-74], inherently sensor-less control definition is also in question as the current model based flux estimation is obtained in the rotor reference frame (*dq*), which requires rotor position angle.

Although the forgoing alleged features may not be true, the stator flux vector controlled IPM drives have still superior features to FOC drives such as ease of flux weakening realization in a decoupled manner which results in reduced torque ripple in a constant power operation. Also, the field weakening operation can be realized directly unlike FOC drives where the flux is weakened indirectly by altering both d- and q- axis currents.

The challenges associated with the stator flux vector controlled IPM-BLAC drives are to improve the flux observer quality, reduce the model dependency and address the high nonlinearity in the torque control loop. These challenges will be discussed in details in the thesis with novel advanced techniques to alleviate these problems.

1.5. THESIS OUTLINE

This thesis consists of six chapters in total. Whilst the two are associated with general introduction and the conclusions as well as further research, four chapters are

more intense with technical contents and the research contributions. The literature review and the state-of-art machine drives are described mainly in the first chapter and at the beginning of each chapter where a specific problem is addressed. The thesis is structured as follows:

Chapter 1 discusses general introduction to modern IPM-BLAC machine drives. The test rig in which the experiments have been carried out throughout the thesis and the power conversion techniques to drive BLAC machines are briefly discussed in this chapter. In addition, efficient control techniques for wide speed range of operations are described by referring the literature. Each of MTPA, FW and MTPV control techniques are outlined for both FOC and DTC drives. The fundamental equations for these control techniques and for the IPM machine modelling in the rotor and in the stator flux synchronous reference frames are also presented. More importantly, the challenges associated with FOC and DTC based IPM drives are summarised with reference to state-of-the-art drives.

Chapter 2 highlights a significant problem associated with a large number of DTC based machine drives in which the well-known Gopinath style closed-loop flux observers are employed. The aim of this observer is to take advantage of the current and the voltage based estimations at low and at high speeds, respectively. However, the cross-interference of the extremely poor voltage based estimation at low speeds may deteriorate the drive performance significantly, leading to a poor torque control quality. The problems associated with this observer structure as well as its improved version reported in the literature are analysed theoretically and verified by simulations and experiments. An alternative flux observer structure, therefore, is proposed in Chapter 2 with a straightforward implementation compared to the conventional Gopinath style observers. The implementation of the proposed drive are presented and discussed in details. The superiority and the efficacy of the proposed drive are verified by experimental results in this chapter.

Chapter 3 proposes a novel flux observer with high fidelity machine models for DTC drives accounting for magnetic saturations in the stator and the rotor cores and the cross-coupling effects of the *dq*- axis flux linkages. The proposed observer is also robust against the variation of the armature resistance due to temperature, inverter voltage drop and the distortion effect of dead-time (blanking time) to prevent shoot-through in the power electronics. The influence of the modelling errors associated with the proposed

observer is analysed theoretically and compensated in FW operation utilizing the voltage error. Since the dominating factor of the modelling errors is the machine temperature variation, the simulation studies are carried out to investigate how temperature variation degrades the drive performance. In addition, comparative studies are performed to verify the superiority of the proposed observer over various types of conventional observer structures. A thorough comparison between conventional observers and the proposed observer through simulations and experiments reveals the superiority of the proposed observer.

Chapter 4 performs an in-depth analysis of the stator flux vector controlled (SFVC; known as DTC) BLAC drives. The influence of the nonlinearity between torque and the torque angle δ (Fig. 1.7) is evaluated and the linearization strategy is described considering the machine operating trajectories. In addition, the MTPV control theory for SFVC based BLAC drives is investigated and the implementation technique is introduced. The stator flux phase angle can be realized by controlling torque, the τ- axis current or the torque angle δ in SFVC based drives. Hence, the chapter also analyses each of them and discusses the issues pertinent to the conventional torque or τ- axis current controlled drives such as the coupled control issues. In view of that, a novel direct, decoupled and linearized stator flux vector controlled IPM-BLAC drive is proposed in this chapter. The reference torque angle generation for the proposed drive is discussed in details. In addition, the control tuning for the proposed drive with desired bandwidth owing to linearization in the feed-forward path is studied. Afterwards, the effectiveness and the efficacy of the proposed drive are verified by experimental results.

Chapter 5 investigates the online efficiency optimization techniques for FOC based IPM-BLAC drives and proposes a novel virtual signal injection based efficiency optimized control technique. First, the relationship between the efficiency and the current angle β (Fig. 1.4) is analysed and a comprehensive literature review is reported in order to show how the state-of-art drives obtain the current angle for high efficiency operation in order to deal with the machine parameter variations during operation. Then, the problems of the conventional current angle optimization techniques are elaborated. To address these problems, the proposed virtual signal injection based online current angle optimization is introduced and discussed in details. Comparisons between the recently reported virtual signal injection based drives and the proposed one are made by theoretical analysis. The error analysis of the existing and the proposed approaches are also analysed

theoretically. Furthermore, two high fidelity machine models designed for EV traction applications are employed to show how close the operation of these drives to ideal MTPA trajectory. The implementation strategy and the design of signal processing unit to improve the response time of the existing approach are also described. Lastly, the influence of the machine parameter variations are discussed by comparative studies between the reported and the proposed drives.

Chapter 6 summarizes the contributions of this thesis to new knowledge and points out the scope for potential further research.

1.6. RESEARCH CONTRIBUTIONS

The major contributions of the thesis can be classified in five groups as follows:

First, an alternative current and voltage based flux observer structure is proposed in which the two significant problems associated with the state-of-art structures are addressed. The problems are the cross-interference of the observer modes of operation and the considerable nonlinearity during the transition between the observer modes. Accordingly, the accuracy of the estimated variables reduces, which results in poor torque control quality, in particular at low speeds. The proposed combination is much simpler to implement and greatly improves the torque control quality at low speeds.

Second, a novel high fidelity model based flux observer is proposed. Conventionally, current and voltage based flux estimations are dominant at low and high operating speeds, respectively, whereas the case is different in the proposed approach. The measured phase currents are utilized as feedback in the new observer structure to compensate for inverter nonlinearities, dead-time and integrator drift at any speed. Improved accuracy over a wide operating range is verified by realistic simulations and experiments.

Third, the MTPV control theory for DTC based IPM-BLAC drives is introduced and analysed. Although the MTPV control has already been discussed for FOC based IPM-BLAC drives in which the *dq*- axis currents are regulated, there is a gap in the literature for DTC drives. Hence, the strategy to maximize the torque per stator flux magnitude is a new contribution to knowledge. It will be shown that the MTPV control is achieved by online limitation of the torque angle in DTC drives.

Fourth, a novel direct, decoupled and linearized stator flux vector controlled IPM-BLAC drive is proposed. Two control variables in a large number of DTC drives in the literature are coupled. Theoretical analysis reveals that these DTC drives have problems such as high nonlinearity in the control loop and control coupling problem in any of MTPA, FW and MTPV regions. The proposed drive addresses these problems and facilitates simple control tuning based on desired control bandwidth.

Fifth, online MTPA tracking for high efficiency operation in field oriented controlled IPM-BLAC drives is proposed by employing virtual signal injection based control technique. Conventionally, accurate MTPA tracking cannot be achieved even though the nonlinear machine parameters employed in the controller are modelled accurately. The deviation from the MTPA trajectory becomes more significant with loading. In addition, the virtual signal injection based drives reported recently suffer from considerably slow converging time and hence slow response time. The proposed drive achieves fast response.

CHAPTER 2 – PERFORMANCE IMPROVEMENT OF DTC DRIVES BY EMPLOYING A LINEAR COMBINATION OF CURRENT AND VOLTAGE BASED FLUX OBSERVERS

2.1. INTRODUCTION AND LITERATURE REVIEW

The DTC drives rely on observer quality for feedback control unlike FOC drives in which the measured currents are employed as a feedback to the drive system without the need for an observer (the rotor position information is readily available). Hence the observer accuracy and its response time is of paramount importance in the DTC based drive systems.

It is well known in the literature that the current based flux and torque estimations are advantageous at low speeds whereas the voltage based estimation perform better at high speeds. In those drives which employ only the voltage based estimations [57, 58], the machine operation is investigated either above certain speeds or the estimation is manually switched from current based to voltage based modes of operation as the voltage based estimations deteriorate when speed approaches to zero. Hence, for a wide speed range of operation, closed-loop flux observers, known as Gopinath style, which combine current and voltage based estimations have been developed in [61] and employed extensively in recent work on IPM machine drives [12, 19-22, 54, 59, 60, 62, 65, 72-75], surface mounted permanent magnet machine drives [54, 76], synchronous reluctance machine drives [54] and induction machine drives [54, 61, 63]. Thus, the conventional closed-loop observer is quite common and widely employed in state-of-the-art drives.

Whilst the aim of these closed-loop observers is to take merits of the current and the voltage based estimations at low and high speeds, respectively, it has been discovered through detailed studies that the interference between the two modes exists in the closed-loop combination of the two estimation techniques. This may result in significant degradation of the drive performance at low speeds where the inverter nonlinearity and the voltage drop across stator resistance become dominant. Accordingly, although the current based estimation is expected to be dominant, the residual error of the extremely poor voltage based estimation may cause significant distortions on the current waveforms leading to a poor torque control quality.

A second issue of the conventional Gopinath style closed-loop observer is that the estimated flux follows a significantly nonlinear flux transition trajectory from current based to voltage based modes of operation and vice-versa. This results in poor performance during transitions since the observer accuracy reduces due to the high

nonlinearity on the trajectory. Fig. 2.1-(a) illustrates the estimated flux vector transition trajectory in complex domain from current to voltage based modes of operation. $\hat{\vec{\Psi}}_{s\_CB}$ and $\hat{\vec{\Psi}}_{s\_VB}$ are the current and the voltage based estimated flux vectors, respectively. Despite the fact that linearization of the trajectory has been studied in [63] as shown in Fig. 2.1-(b), none of the above drives have employed the linearization technique due to its implementation complexity. Hence, a large number of state-of-the-art drives still suffer from the nonlinear transitions.

To overcome the issues associated with deteriorated drive performance at low speeds due to the cross-interference and nonlinear flux transition trajectory between the two modes, an alternative combination is proposed. In the proposed approach, current based and voltage based estimations are not combined in a closed-loop manner, on the contrary, the two estimators are combined in such a way that the transition from one to other follows a linear trajectory. By doing so, the two major problems; cross-interferences and the poor transitions between the two modes are avoided together with a much simpler combination. It is noteworthy that despite the closed-loop observers sound to perform better, in fact, the drive system itself is in closed-loop in either cases whether the observer is closed or open-loop.

The main content of this chapter has been published by the author in [J3] and [C3] detailed in List of Publications.

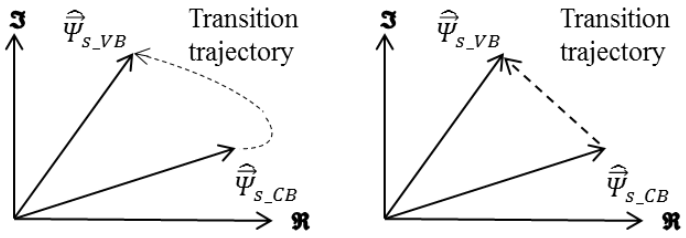

(a) conventional (b) proposed in [63]

Fig. 2.1 Trajectory of the conventionally estimated stator flux vector in complex domain

2.2. CONTROL SYSTEM CONFIGURATION

Fig. 2.2 illustrate the schematic of the DTC based drive system where '*' and '^' denote reference and estimated values, respectively. '**' represents the voltage

commands which are confined by the voltage constraint. The reference and estimated state variables are illustrated in 'red' and 'blue' colours, respectively, in Fig. 2.2.

Since the voltage magnitude is usually below the constraint in the constant torque region, the unsaturated command voltages with '*' and '**' are the same in this region unless the controller tracking error is very large, which is possible in transient condition. Once the voltage saturates, the differences between the saturated command voltage and the confined voltage is utilized to stop the integrator action of the PI controller. This is due to the need to prevent the controller from winding up the integrators. By doing so, the anti-windup (AW) phenomenon is achieved by the classical "*integrator clamp*" technique [77, 78].

The coupling term $(\omega_e \Psi_s)$ in (1.10) is compensated in the feed-forward path as shown in Fig. 2.2. The reference stator flux magnitude is employed in the decoupling as it is independent from observer error and the noise on the observed flux.

The space vector modulation (SVPWM) technique is employed to control the switches of the inverter due to its superior features which has been discussed widely in section 1.2.2. The reference voltages are, therefore, transformed to the stationary frame before being fed to the SVPWM block. The maximum DC-link voltage utilization of the SVPWM technique in the linear modulation region is given in Table 1.3. Thus, the maximum voltage is given by (2.1) where V_{dc} is the measured DC-link voltage. By doing so, the voltage variation of a practical implementation is taken into account and addressed online.

$$V_{max} = \frac{V_{dc}}{\sqrt{3}} \tag{2.1}$$

In a practical implementation of an electric vehicle traction application, the battery or the DC-link voltage might vary around $\mp 15\%$ depending on the remaining level of the energy stored in the battery. If the variation of the DC-link voltage is not considered and the DC-link voltage information in the controller deviates from the actual voltage, this will ultimately cause either early or late field weakening operation.

In early FW operation, the DC-link voltage is not fully utilized, thus the current magnitude in a FW operation becomes higher than expected which leads to an increase

in winding copper loss and in the undesired torque ripples. Thus, efficiency degrades as the available voltage is not fully utilized. Because of the lower available current for torque production, the acceleration performance also degrades as the torque capability will reduce.

Late FW, on the other hand, exhibits different resultant effects depending on the control system configuration. In the experimental test rig shown in Fig. 1.3, the drive might operate either in speed or in torque controlled modes. If the speed is not held by the dynamometer and the motor is controlled in the speed control mode (cruise control), then the late FW causes inability to achieve operation in the extended speed region. In other words, it will result in a gap between command speed and the actual speed. However, if the speed is set by the dynamometer and the motor is controlled in torque control mode, then the late FW triggering causes controller saturation which may lead to a stability problem, and hence poor torque control. At high speeds, incorrect voltage vector due to the controller saturation may give rise to unexpected generating mode of operation and an increase in the DC-link. Because the power source is able to operate in two ways (bi-directional) in the test rig, the generated energy may be safely absorbed by the source. However, when the induced voltage reaches to maximum voltage ratings of the capacitors on the inverter, the capacitors may blow up and the inverter might damage. Hence, late FW not only results in poor torque control, but may also risk unstable operation.

As a result, online measurement of the DC-link voltage is highly important in traction applications in particular for constant power operation where the maximum voltage is reached.

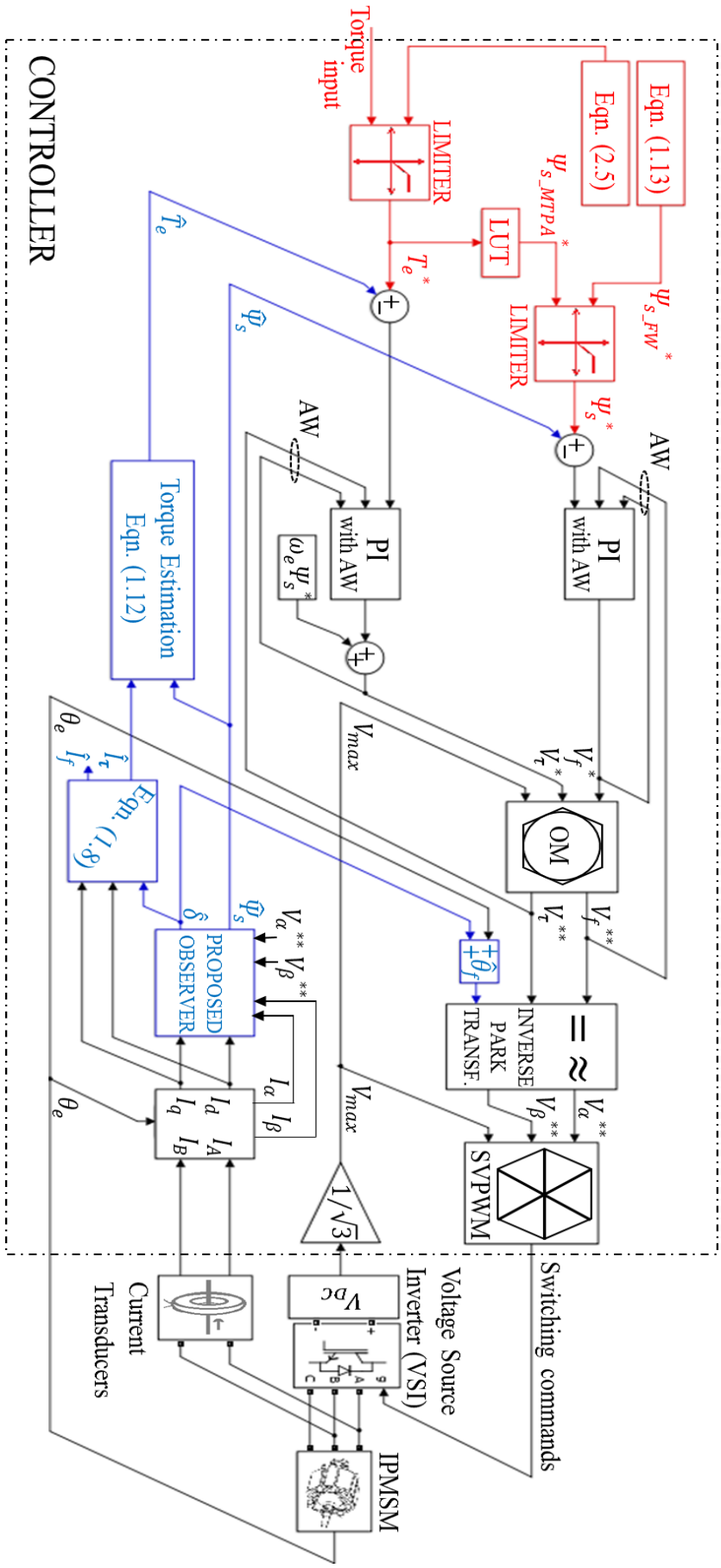

Fig. 2.2 Schematic of the drive system

Unlike classical FOC drives, a current limit cannot be imposed directly in DTC drives since the currents are not the directly controlled state variables. Instead, a torque limit may be imposed for indirect limitation of the currents. Equations (2.2) and (2.3) give voltage and current constraints of the IPM-BLAC drive, respectively, in the $f\tau$ reference frame.

$$|V| = \sqrt{V_f^2 + V_\tau^2} \leq V_{max} \tag{2.2}$$

$$|I| = \sqrt{I_f^2 + I_\tau^2} \leq I_{max} \tag{2.3}$$

Rearranging (2.3), one can obtain the τ- axis current constraint as given in (2.4). Substituting (2.4) into (1.12) yields the limit for electromagnetic torque as given in (2.5).

$$I_\tau \leq \sqrt{{I_{max}}^2 - {I_f}^2} \tag{2.4}$$

$$T_e \leq \frac{3}{2}\, p\, \Psi_s \sqrt{{I_{max}}^2 - {I_f}^2} \tag{2.5}$$

Therefore, the voltage and current limits are imposed by (2.2) and (2.5), respectively.

As has been discussed previously in section 1.4.4, the field weakening operation may be triggered by (1.13) automatically in DTC based control schemes. The stator flux magnitude reference which is generated from a LUT for MTPA operation is, therefore, limited simply by (1.13) to achieve FW operation as illustrated in Fig. 2.2.

The estimated torque accuracy is only dependent on the flux observer accuracy and this can be explained as follows. The accurate rotor position information is readily available via a magnetic encoder, thus the *dq*- axis currents can be considered as measured currents as the coordinate transformation from the stationary frame to the synchronous rotor frame will be accurate. The transformation from measured *dq*- axis currents to the $f\tau$ frame is obtained by (1.8) where the accuracy is only dependent on the estimated torque angle and hence dependent on the flux observer. The estimated torque is obtained by (1.12). As can be deduced from (1.12), the accuracy of the estimated torque is dependent on the estimated stator flux magnitude and on the τ- axis current. As has been discussed,

because the estimated τ- axis current is only dependent on the torque angle accuracy, the torque estimation is eventually dependent on only the accuracy of the estimated stator flux vector, *i.e.*, magnitude of the stator flux linkage and its phase angle (Ψ_s, δ). As a result, the quality of the flux observer is of paramount importance in DTC based AC drives.

2.3. ANALYSIS OF CONVENTIONAL STATE-OF-THE-ART OBSERVERS

As mentioned previously, the voltage based flux estimation has shortcomings at low operating frequencies whereas it is more accurate than the current based estimation at high operating frequencies. This has led researchers to seek for a combination of the two estimation strategies in such a way that the current based estimation is dominant at low speeds whereas the voltage based estimation becomes dominant at high speeds.

A Gopinath style closed loop flux observer, therefore, has been introduced in [61] for induction machines where the current and voltage based estimations become dominant at low and high operating frequencies, respectively. However, the observer suffers from high flux transition trajectory which is addressed in [63]. The two observers and their detailed analysis which has not been discussed in the literature will be presented in sections 2.3.1 and 2.3.2 separately as follows.

2.3.1. CLOSED-LOOP FLUX OBSERVERS WITH NONLINEAR TRAJECTORY

The simplified block scheme of the conventional Gopinath style closed loop flux observer is illustrated in Fig. 2.3. It should be noted that "closed-loop" merely means that the combination of the two estimations is made through a feedback mechanism. The transition of the observer mode of operation from current to voltage based estimation and vice-versa can be adjusted by the PI controller whose details can be found in [60].

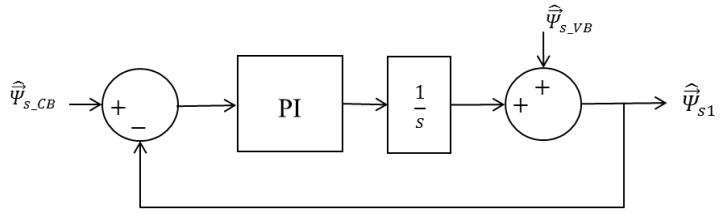

Fig. 2.3 Simplified schematic representation of the conventional observer with nonlinear flux trajectory

The output of the observer is given by:

$$\hat{\vec{\Psi}}_{s1} = \big(1 - F(s)\big)\hat{\vec{\Psi}}_{s\_CB} + F(s)\hat{\vec{\Psi}}_{s\_VB} \tag{2.6}$$

where, $F(s)$ is the observer characteristic equation whose frequency response is tuned by the PI control parameters for input selection. The observer characteristic equation is given by:

$$F(s) = \frac{s^2}{s^2 + K_p s + K_i} \tag{2.7}$$

Fig. 2.4 (a) and (b) illustrate the Bode magnitude plots of $F(j\omega)$ and $[1 - F(j\omega)]$, respectively, for conventional observer with a cut-off frequency of 25 Hz (=500 r/min speed in the experimental test rig). Therefore, as can be seen on the magnitude (abs) plot of Fig. 2.4, below the cut-off frequencies $F(j\omega)$ approaches to zero and above the cut-off frequencies $[1 - F(j\omega)]$ approaches to zero so that current and voltage based estimations become dominant at low and high frequencies, respectively.

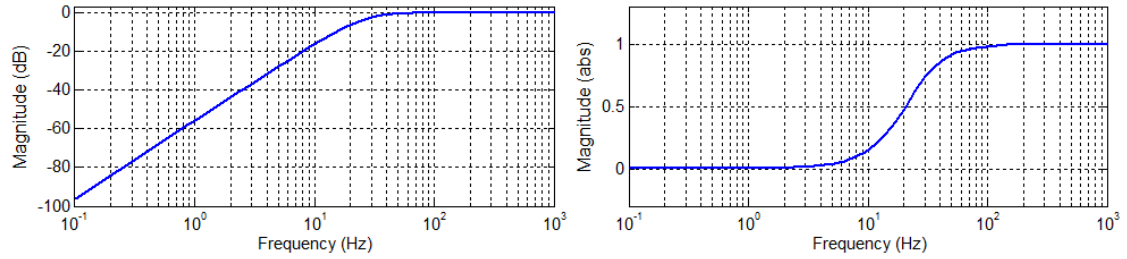

(a) Bode magnitude plot of $F(j\omega)$

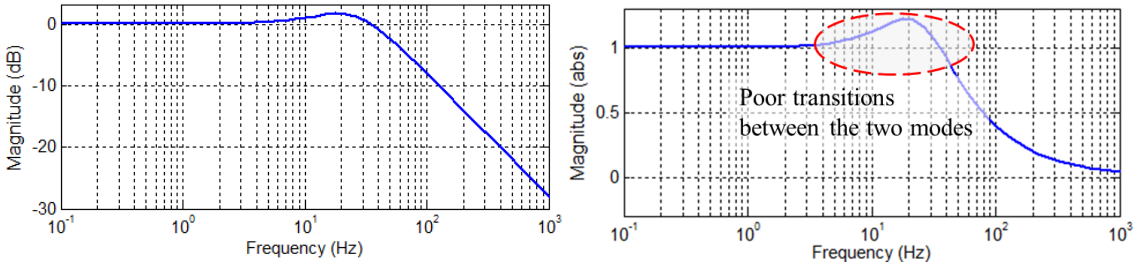

(b) Bode magnitude plot of $[1 - F(j\omega)]$

Fig. 2.4 Bode magnitude plots of conventional observer with nonlinear flux trajectory

It is seen on Fig. 2.4-(b) that the transition between the two modes is very poor and nonlinear, and hence reduces the accuracy of the observer during transitions. It is evident

in Fig. 2.1-(a) and Fig. 2.4-(b) that the estimated flux vector $\left(\hat{\vec{\Psi}}_{s1}\right)$ diverge from both the voltage and the current based estimated flux vectors at certain frequencies. However, it is expected to converge one of them while diverging from another. It is seen on Fig. 2.4-(b) that the diversion due to the nonlinearity occurs between ~2 Hz and ~35 Hz. The two operating frequencies refer to 40 r/min and 700 r/min, respectively, with the IPM motor whose specifications have been listed in Table 1.1. This means that the observed flux vector employed in the controller diverges from both the current and the voltage based estimated flux vectors between 40 and 700 r/min operating speeds. Hence, the accuracy of the observed flux vector reduces at a wide speed range (from 40 to 700 r/min) and hence the effect of the nonlinear flux transition trajectory is quite significant.

2.3.2. CLOSED-LOOP FLUX OBSERVERS WITH LINEAR TRAJECTORY

Because of the aforementioned momentous nonlinearity in the observed flux vector, the linearization study has been presented in [63]. The simplified block scheme of the Gopinath style closed loop flux observer with the linearized flux transition trajectory is illustrated in Fig. 2.5.

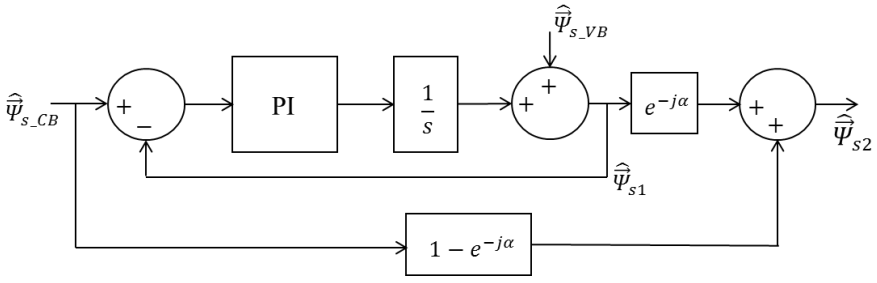

Fig. 2.5 Simplified schematic representation of the conventional observer with linear flux trajectory

The output of the improved observer is given by:

$$\hat{\vec{\Psi}}_{s2} = \big(1 - G(s)\big)\hat{\vec{\Psi}}_{s\_CB} + G(s)\hat{\vec{\Psi}}_{s\_VB} \tag{2.8}$$

where, $G(s)$ is the observer characteristic equation whose frequency response is tuned by the PI control parameters for input selection. The observer characteristic equation is given by:

$$G(s) = \frac{s^2}{s^2 + K_p s + K_i} e^{-j\alpha} \tag{2.9}$$

where α is the angle of the characteristic equation and it is given by (2.10).

$$\alpha = \left(\pi - \tan^{-1}\left(\frac{K_p \omega_e}{K_i - {\omega_e}^2}\right)\right) \tag{2.10}$$

where w_e is the electrical angular speed of the machine.

Fig. 2.6 (a) and (b) illustrate the Bode magnitude plots of $G(j\omega)$ and $[1 - G(j\omega)]$, respectively, for the observer with linearized flux transition trajectory where the cut-off frequency has been adjusted to the same (25 Hz).

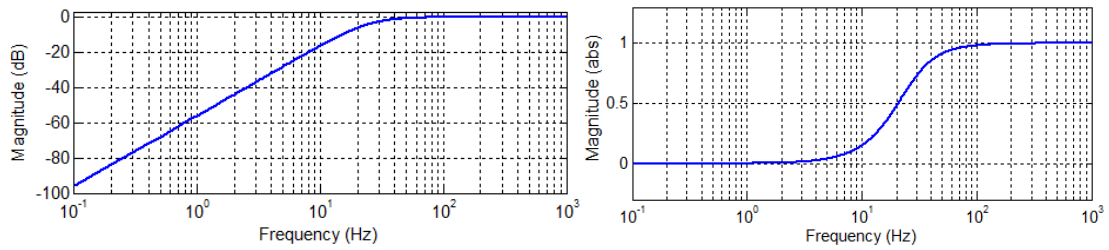

(a) Bode magnitude plot of $G(j\omega)$

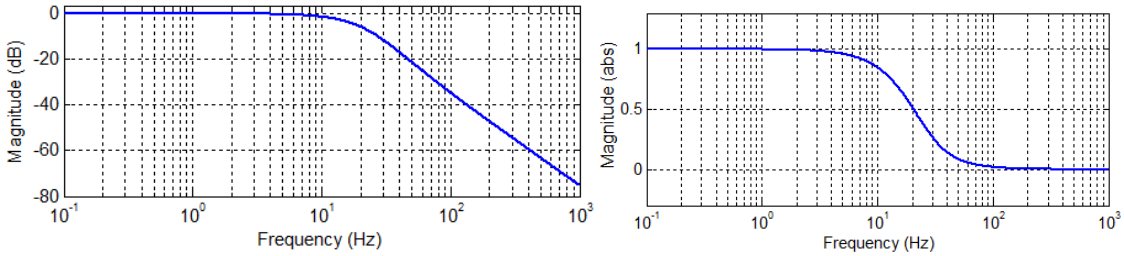

(b) Bode magnitude plot of $[1 - G(j\omega)]$

Fig. 2.6 Bode magnitude plots of conventional observer with linearized flux trajectoryy

Although the nonlinearity of the conventional observer has been addressed as can be seen on Fig. 2.6-(b), a large number of recent papers on DTC drives including [12] and [55] still suffer from the poor transitions because of the implementation complexity of the linearization. Despite the fact that the schematic representation shown in Fig. 2.5 seems to be simple, in fact, the conventional observer, its PI controller gain tuning, and the linearization with the exponential function shown in (2.9) and (2.10) are difficult to implement and hence the linearization has not been addressed in a great number of drives.

Additionally, both of the conventional observers depicted in Fig. 2.3 and Fig. 2.5 suffer from cross-interferences of the two modes. As can be seen on the magnitude (abs) plots of Fig. 2.4 and Fig. 2.6 at low speeds when frequency is low, $F(j\omega) \approx 0$ and

$G(j\omega) \approx 0$, and at high speeds, $[1 - F(j\omega)] \approx 0$ and $[1 - G(j\omega)] \approx 0$. However, it is evident on the magnitude (dB) plots of the figures that the attenuations of the two modes are finite. Consequently, the cross-interferences of the two modes are only avoided at standstill and infinite speed in theory. It is worth noting that the interference of the voltage based mode is much more significant than the current since the poor performance of the voltage based mode at low speeds may result in significant current distortions and hence reduced torque control quality in machine drives.

2.3.3. PROBLEMS PERTINENT TO CLOSED-LOOP OBSERVERS

As has been discussed, a great number of DTC drives suffer from nonlinear transition at a wide speed range. In addition, cross-interferences of the two estimation techniques may seriously deteriorate the drive performance in particular at low speeds.

The cross interference issue has been further investigated by simulation studies in order to validate how seriously it may deteriorate DTC drive performance employing conventional Gopinath style closed-loop flux observers. The motor and the inverter specifications are listed in Table 1.1 and Table 1.2, respectively. A high fidelity machine model [79, 80] which accounts for magnetic saturation and the effects of slotting of a real IPM machine has been employed and the inverter nonlinearities have been represented in the simulations, and hence the results are very close to a real world drive. The high-fidelity machine model is given in the appendix. The drive system shown in Fig. 2.2 has been implemented with the conventional observer (Fig. 2.3) and simulated at 25 r/min speed and 40 Nm torque.

It is seen from Fig. 2.7-a that although the estimated flux ($\widehat{\vec{\Psi}}_{s1}$ in (2.6)) appears to follow the reference flux reasonably well, the actual flux, which cannot be measured in a practical drive, is heavily distorted and exhibits peak distortion 6-times in the fundamental period as shown in Fig. 2.7-(b). This is indeed caused by the 6-step voltage distortion which results from inverter nonlinearity. Despite the low magnitude of $F(j\omega) \approx 0.01$ in (2.6) associated with the voltage based mode, the extremely poor voltage based estimation shown in Fig. 2.7-(c) results in poor performance of the drive. The flux distortion gives rise to significant current waveform distortions, Fig. 2.7-(d), which matches well with the experimental results given in section 2.5. Because of the distorted current waveforms, the estimated flux by the current based mode is also distorted as shown in Fig. 2.7-(e). As a result, the actual torque is significantly distorted

as shown in Fig. 2.7-(f). It is noteworthy that the estimated fluxes shown in Fig. 2.7-(b) and (e) are very similar to each other as expected. This is due to $[1 - F(j\omega)] \approx 0.99$ and hence the observer output is very similar to the current based estimation.

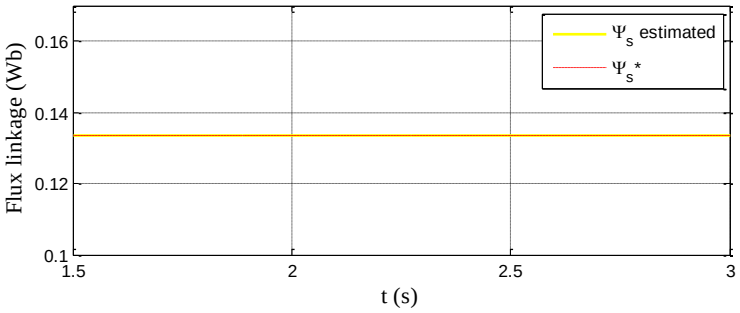

(a) Estimated flux, $\left|\widehat{\Psi}_{s1}\right|$ in (2.6)

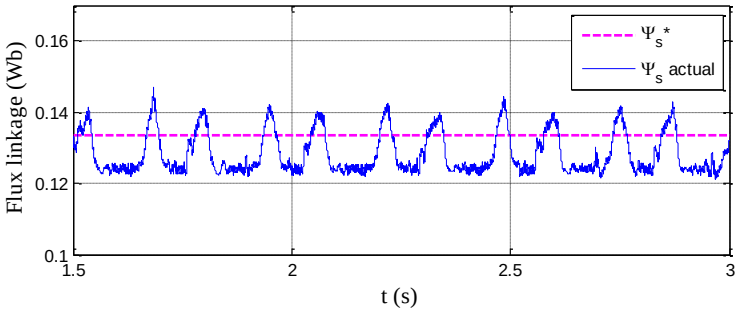

(b) Actual flux

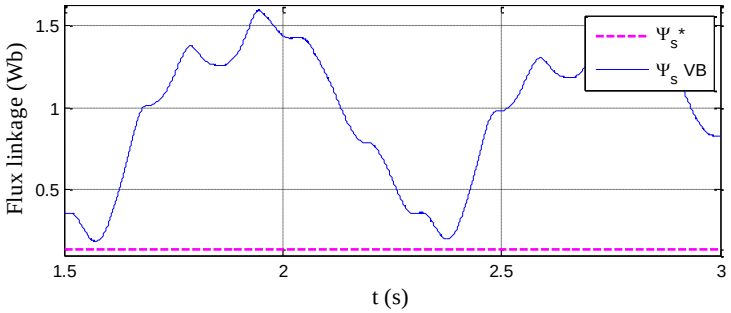

(c) Estimated flux, $\left|\widehat{\Psi}_{s\_VB}\right|$ in (2.6)

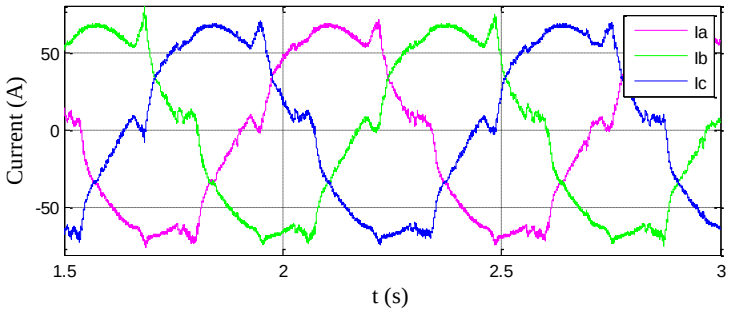

(d) Current waveforms

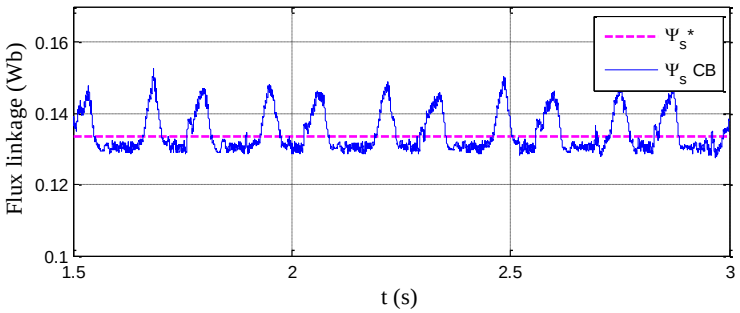

(e) Estimated flux, $\left|\widehat{\Psi}_{s\_CB}\right|$ in (2.6)

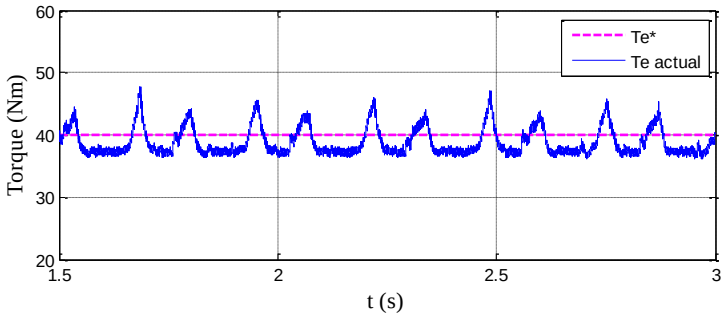

(f) Actual torque

Fig. 2.7 Simulation results of the conventional drive at 25 r/min and 40 Nm

It is noteworthy that the low speed performance of the conventional observer shown in Fig. 2.3 has been simulated previously by [60]. However, since the inverter nonlinearities have not been represented in the simulations (perfect inverter), the results were not distorted as demonstrated by Fig. 2.7.

To address the issue, the inaccurate estimation of the voltage based mode must be completely attenuated at low speeds so that the system performance deterioration due to cross-interference can be avoided. Hence, a much simpler combination of the voltage and the current based flux estimation strategies with linear flux transition avoiding cross-interferences is proposed as follows.

2.4. PROPOSED FLUX OBSERVER WITH LINEAR TRAJECTORY

In the proposed approach, the current and the voltage based estimated stator flux vectors are combined in such a way that the transition from one to other follows a linear trajectory. The transition speed range is adjusted by the designer and the cross-interference issues of the observer modes of operation are avoided by complete

attenuation with the proposed strategy. The current and the voltage based estimated flux vectors are combined in (2.11) to form the output of the proposed technique.

$$\hat{\vec{\Psi}}_{s3} = \begin{cases} \hat{\vec{\Psi}}_{s\_CB} & \omega \le \omega_{CB} \\ \hat{\vec{\Psi}}_{s\_CB}\dfrac{\omega_{VB}-\omega}{\omega_{range}} + \hat{\vec{\Psi}}_{s\_VB}\dfrac{\omega-\omega_{CB}}{\omega_{range}} & \omega_{CB} < \omega < \omega_{VB} \\ \hat{\vec{\Psi}}_{s\_VB} & \omega \ge \omega_{VB} \end{cases} \tag{2.11}$$

where ω_{CB} and ω_{VB} are the predefined speeds where the current and the voltage based modes are enabled or suspended. ω is the operating speed and it can be either electrical speed or mechanical speed in rad/s or in r/min as long as all speeds in (2.11) are in the same unit. ω_{range} is the range of the transition speed between ω_{CB} and ω_{VB} to avoid sudden change of the estimated variables. A bigger range makes the transition smoother but increases the effect of the poor performing mode when the speed is between ω_{CB} and ω_{VB}. Hence, the trade-off can be optimized for a certain drive. It is noteworthy that the transition range, ω_{range}, cannot be defined by the designer in conventional closed-loop observers, hence the trade-off cannot be optimized. Theoretically, the transition speed could be chosen based on the speed where the voltage based estimation is more accurate than the current based.

As can be seen in (1.2), the current based flux linkage estimation is dependent on machine parameters, *i.e.,* the inductances and the magnetic flux linkage. To circumvent the problems associated with the parameter nonlinearities, these machine parameters are modelled as functions of *d*- and *q*- axis currents based on the experimentally calibrated FE data of the machine under study and they are stored as look-up tables. Highly nonlinear parameter maps of the IPM machine given in Table 1.1 are illustrated in Fig. 2.8. The stator flux vector, *i.e.* the magnitude and the phase angle (δ – Fig. 1.7) is obtained by substituting (1.2) into (1.8) and into (1.9), respectively.

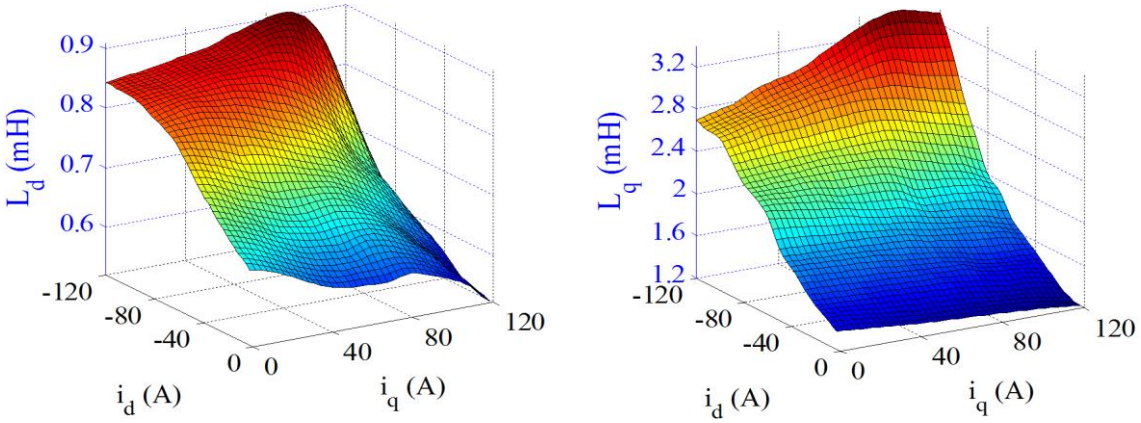

(a) *d*- axis inductance as a function of *dq*- axis currents (b) *q*- axis inductance as a function of *dq*- axis currents

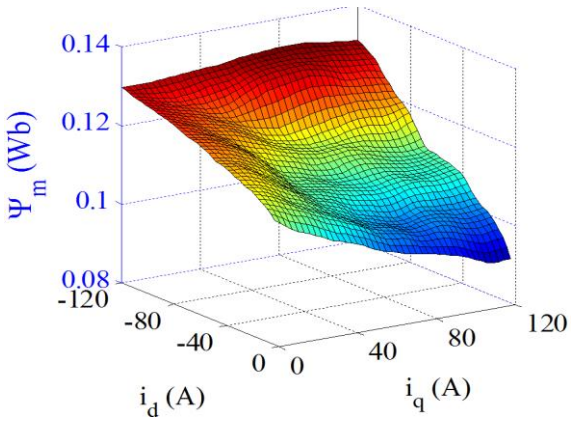

(c) Permanent magnet flux linkage as as a function of *dq*- axis currents

Fig. 2.8 Nonlinear IPM machine parameters

The voltage based stator flux estimation is commonly obtained in the stationary frame as the coordinate transformation and hence the rotor position information is not needed. The well-known estimation technique by the stationary frame voltages and the currents is expressed by (2.12).

$$\widehat{\Psi}_\alpha = \int (V_\alpha - RI_\alpha)dt \quad \& \quad \widehat{\Psi}_\beta = \int (V_\beta - RI_\beta)dt \tag{2.12}$$

In general, the inverter reference voltages are employed for estimations as shown in Fig. 2.2 since the measurement of the discrete phase voltages is costly due to the additional hardware requirement. Accordingly, the estimation is very poor at low speeds where the inverter nonlinearity becomes prominent. Because pure integration in (2.12) does not work due to well-known integrator drift problem, the integrators are commonly replaced by low-pass filters [81] together with phase and magnitude compensations as

depicted in Fig. 2.9 where ω_c and ω_e are cut-off frequency of the filters and the electrical speed in rad/s, respectively.

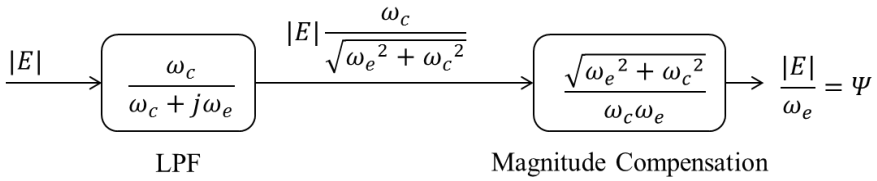

(a) Magnitude compensation

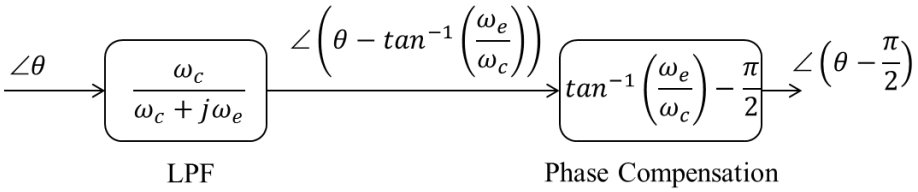

(b) Phase compensation

Fig. 2.9 Magnitude and phase compensations associated with voltage based estimation

Because the magnitude and the phase compensations are disregarded in [57, 58, 71], the drive efficiency would reduce as the estimated stator flux magnitude and its phase angle are inherently altered by the filters.

It is worth mentioning that the compensation outputs should be appropriate to that of the integration output as shown in Fig. 2.9 since the aim is to integrate the induced voltages to obtain the flux.

It should also be noted that high cut-off frequency of the filters may give rise to torque and flux oscillations whilst low cut-off frequency results in slow response. Hence, there is a trade-off between the response time and the response quality.

Cartesian to polar coordinate transformation of the estimated flux linkages gives the stator flux vector, *i.e.* the amplitude and the phase angle ($\theta_f = \theta_e + \delta$ – Fig. 1.7).

The flow-chart of the proposed combination is illustrated in Fig. 2.10 and the flux transition trajectory with the proposed combination is illustrated in complex domain in Fig. 2.11.

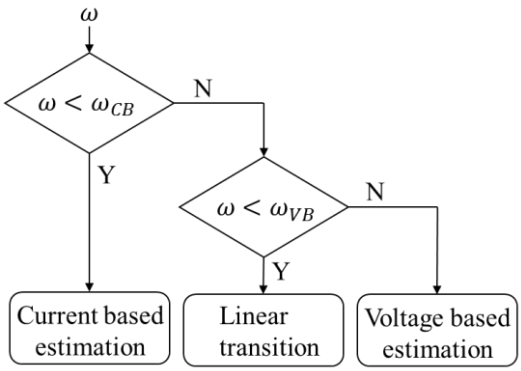

Fig. 2.10 Flow-chart of the proposed approach

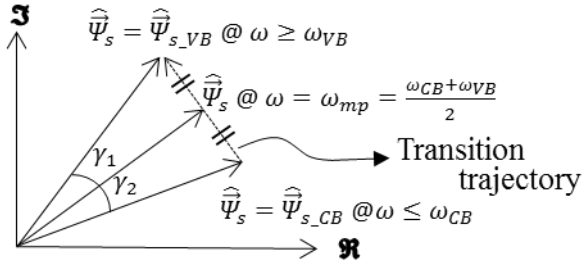

Fig. 2.11 Transition trajectory of the estimated stator flux vector in complex domain

It is seen in Fig. 2.11 that when speed is in the midpoint (ω_{mp}), the estimated output vector with the proposed approach follows the shortest path between the two vectors *i.e.* $\gamma_1 = \gamma_2$. Hence, the linear transition is achieved with a much simple combination.

2.5. EXPERIMENTAL VALIDATION OF PROPOSED OBSERVER

In order to validate the superiority and the performance improvement of the direct torque controlled drive with the proposed observer, experiments have been carried out by comparing the drive to the conventional schemes. The test rig with a 10 kW IPM-BLAC machine has been described in section 1.2.1 and depicted in Fig. 1.3. The schematic of the DTC based drive system is illustrated in Fig. 2.2.

2.5.1. LOW SPEED PERFORMANCE COMPARISON

The test drive was performed with the three observer options which are the two conventional observers discussed in sections 2.3.1 and 2.3.2 and the proposed observer. The machine was operated at various torque and speed operating points.

The transition speed from current to voltage based modes of operation is adjusted to 500 r/min *(=25 Hz electrical frequency same as in Fig. 2.4 and Fig. 2.6)* so that the current

and the voltage based modes are expected to be dominant below and above 500 r/min, respectively.

The current waveforms with the three drives at these operating points are illustrated in Fig. 2.12 – Fig. 2.15. It is seen from the experimental results that the drives with the conventional observers are significantly vulnerable to the residual error coming from poor performing voltage based estimation at low speeds. Although the PI gains of the two conventional observers were tuned to be the same in the two conventional observers, the drive with the linearized flux trajectory is more affected by the cross-interference issue. In contrast, the issue has been avoided in the proposed approach and the current waveforms being much improved with a linear combination.

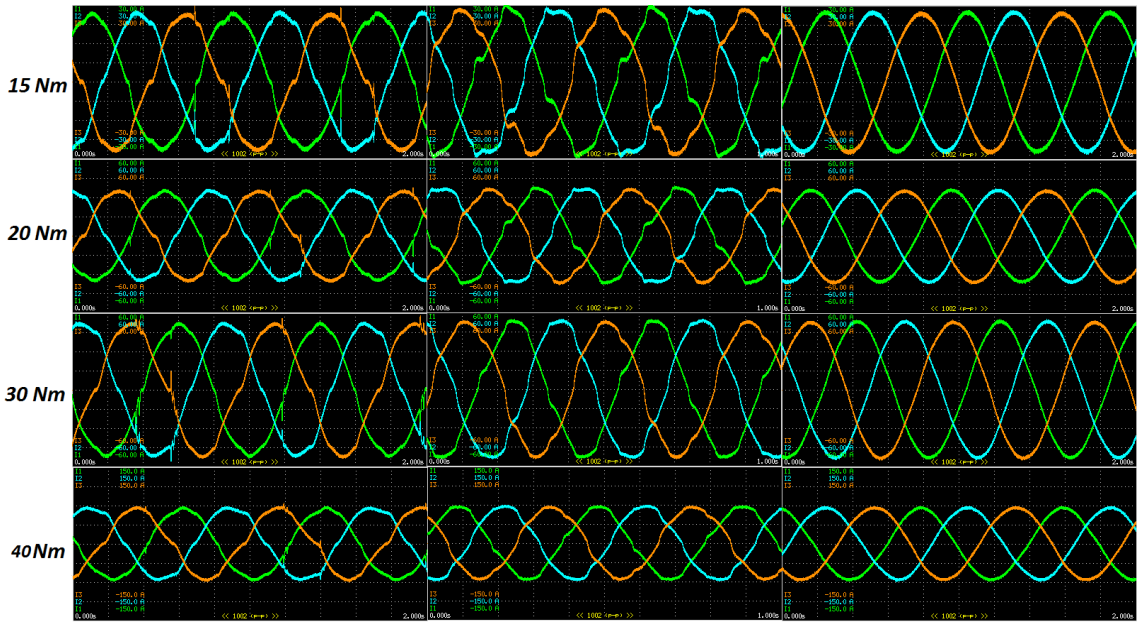

(a) Conventional observer: Fig. 2.3 (b) Conventional observer: Fig. 2.5 (c) Proposed Observer

Fig. 2.12 Experimental results at 25 r/min

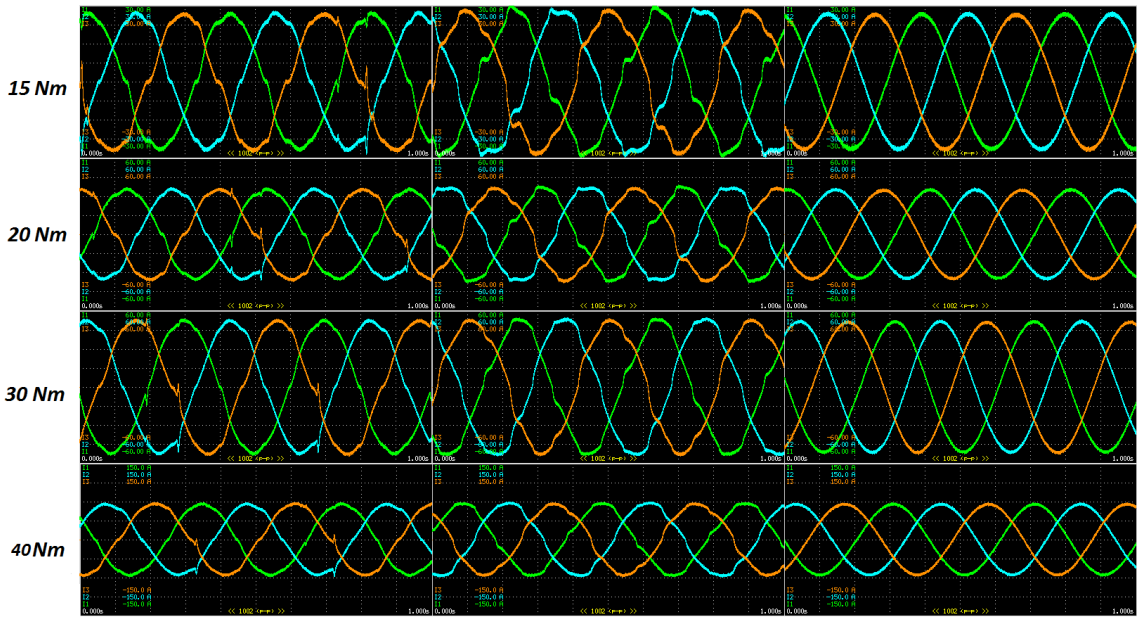

(a) Conventional observer: Fig. 2.3 (b) Conventional observer: Fig. 2.5 (c) Proposed Observer

Fig. 2.13 Experimental results at 50 r/min

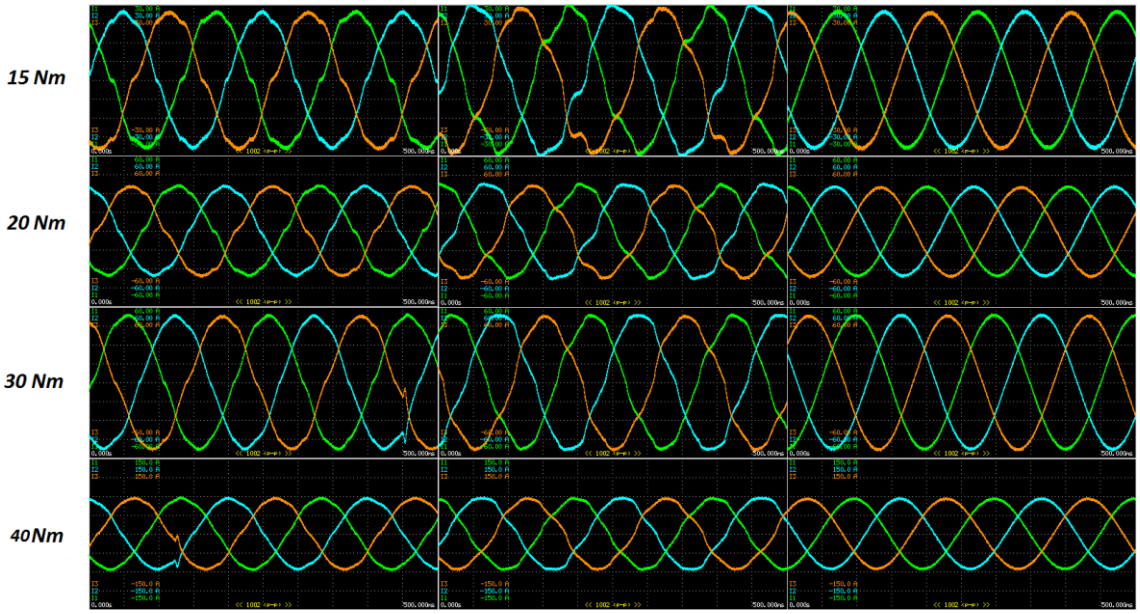

(a) Conventional observer: Fig. 2.3 (b) Conventional observer: Fig. 2.5 (c) Proposed Observer

Fig. 2.14 Experimental results at 100 r/min

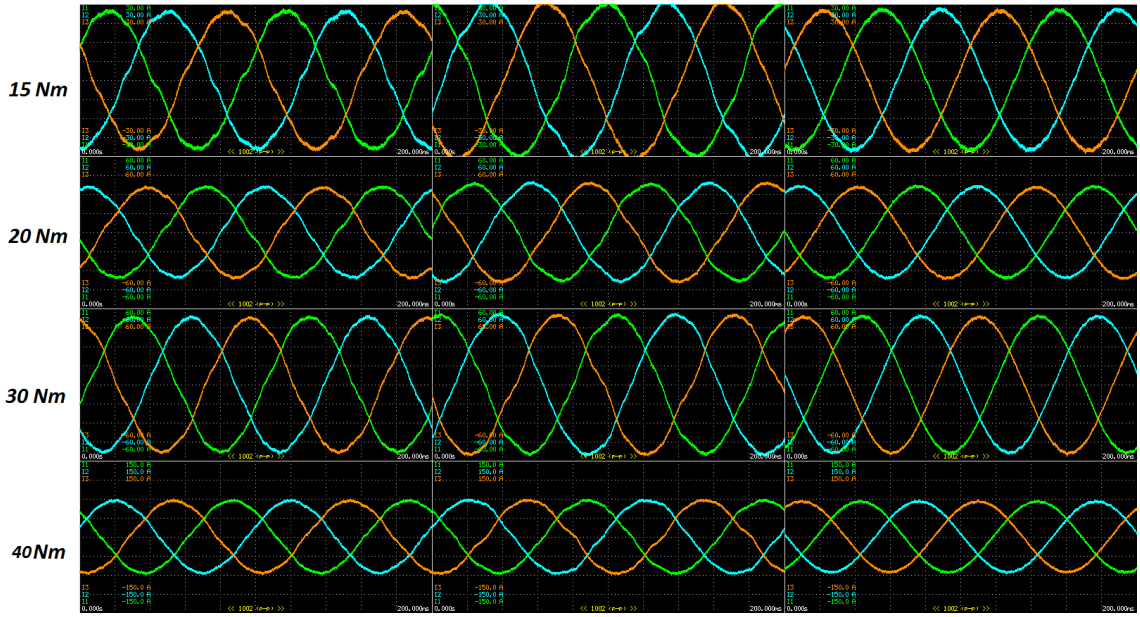

(a) Conventional observer: Fig. 2.3 (b) Conventional observer: Fig. 2.5 (c) Proposed Observer

Fig. 2.15 Experimental results at 200 r/min

2.5.2. TRANSITION PERFORMANCE VALIDATION

The robustness of the drive in two observer modes of operation is validated in this section. From the current to the voltage based modes of operation and vice-versa and the drive performance between the two modes will be experimentally presented.

The controlled state variables; the electromagnetic torque and the stator flux linkage responses of the drives from current to voltage based mode and vice-versa are illustrated in Fig. 2.16 – (a) and (b), respectively. It is seen from the results that the proposed drive is robust to change of the observer mode of operation as the transition is linear and smooth. It should be noted that the ripple on the estimated flux linkage increases when the current based mode becomes dominant. This is as expected because of the current measurement noise. The noise is filtered at high speeds by LPFs shown in Fig. 2.9 with a cut-off frequency of 10Hz. One can deduce from Fig. 2.16 that the electromagnetic torque is affected by the current measurement noise at any speed as can be deduced from (1.12), hence the high frequency ripple on the estimated torque remains similar in both modes of operation.

Because the transition occurs between the two predefined speeds, *i.e.* ω_{CB}=450 r/min and ω_{VB}=550 r/min, performance tests have been carried out when γ_1 in Fig. 2.11 is equal to γ_2. Drive robustness to change of the torque when the estimated flux is equally far from current and voltage based modes of operations has been validated in Fig. 2.17 (a – c). The phase currents when the torque is 50 Nm is illustrated in Fig. 2.17 – (d). It is seen that the current waveforms are not deteriorated during flux transition.

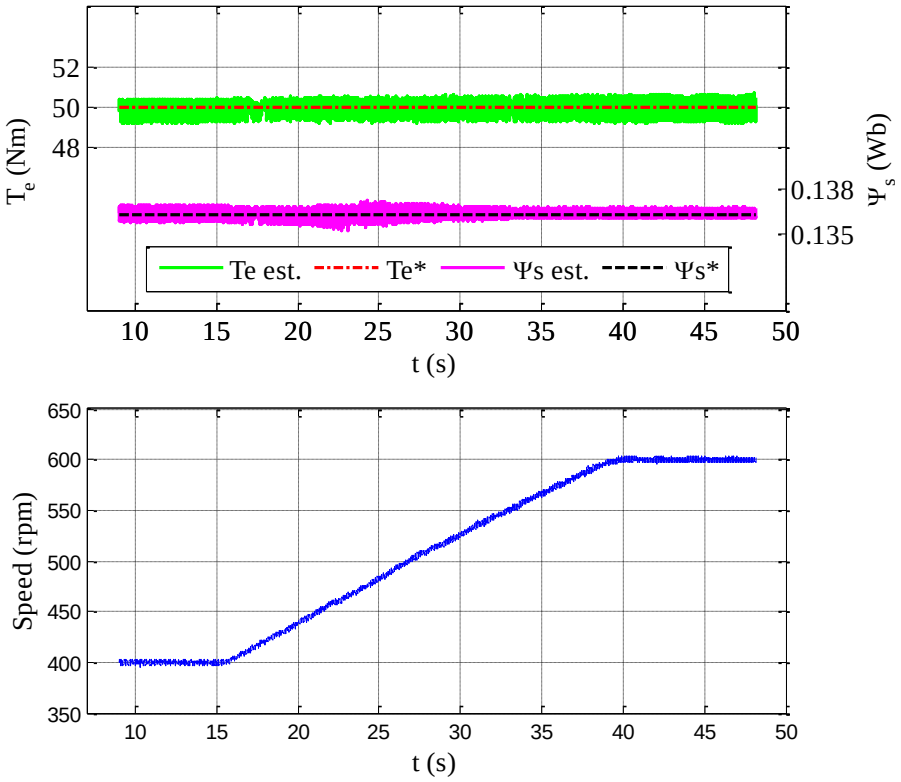

(a) Regulated torque and flux linkage responses from $\gamma_2 = 0$ to $\gamma_1 = 0$

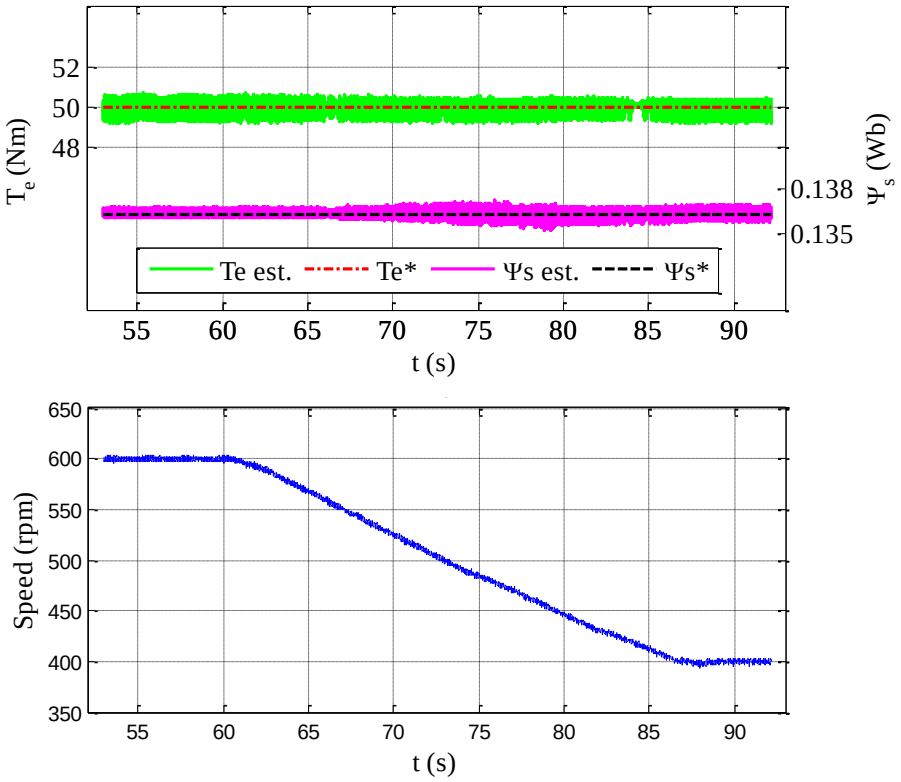

(b) Regulated torque and flux linkage responses from $\gamma_1 = 0$ to $\gamma_2 = 0$

Fig. 2.16 Drive performance from current to voltage based mode and vice-versa

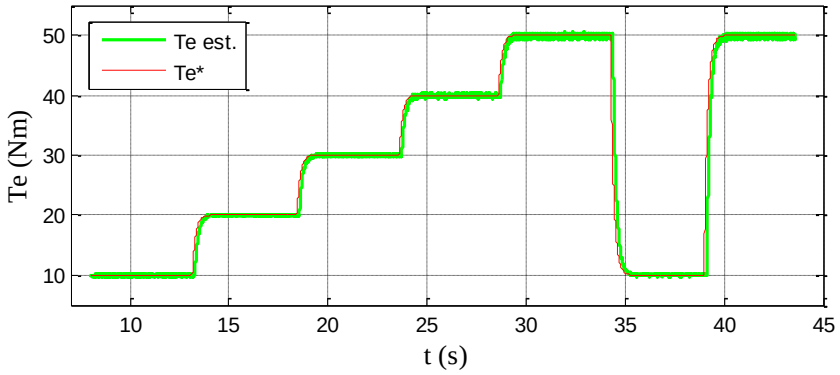

(a) Regulated electromagnetic torque responses

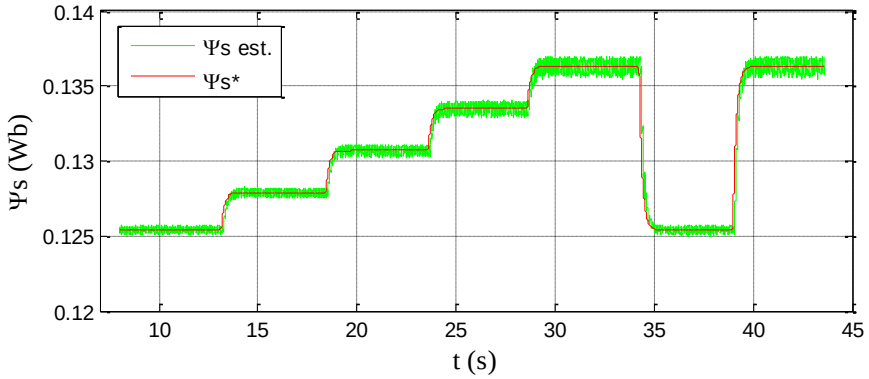

(b) Regulated stator flux magnitude responses

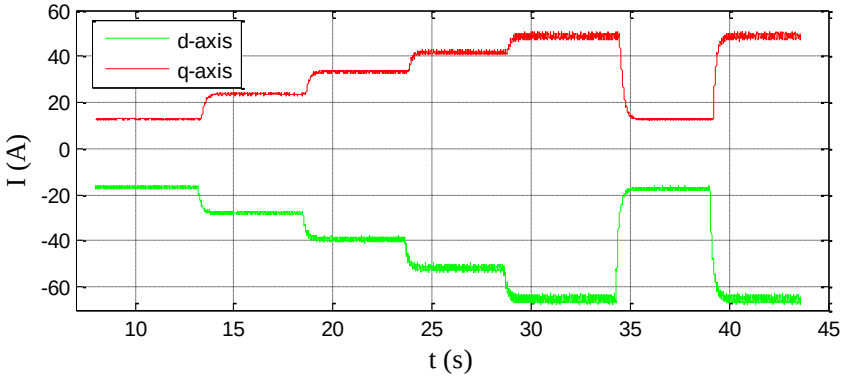

(c) Measured *dq*-axis currents

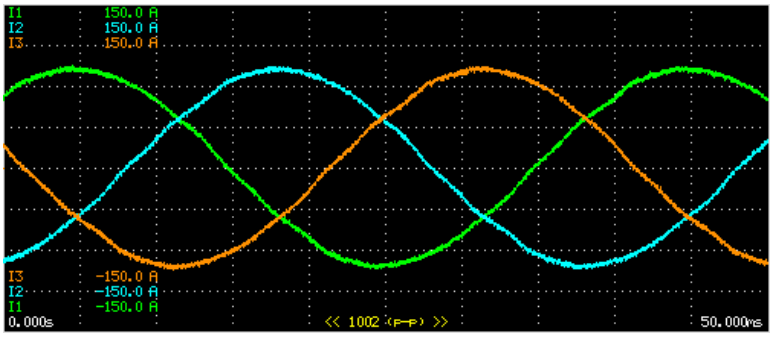

(d) Current waveform at 50Nm torque

Fig. 2.17 Drive performance at $\gamma_1 = \gamma_2$

2.5.3. FIELD WEAKENING VALIDATION

The voltage based estimations have already been validated and widely employed at high speeds in the literature [26, 57, 58]. Transient performance in FW region and the smooth transitions from MTPA to FW regions and vice-versa are illustrated in Fig. 2.18 when the drive operates in the voltage based mode at a load torque of 20 Nm. The FW is automatically triggered at the speed of 1709 r/min by (1.13). It is seen that the estimated flux in the constant torque region has lower ripple than that in the FW region as the current magnitude and the noise increases when (1.13) is imposed to weaken the flux (magnetic field).

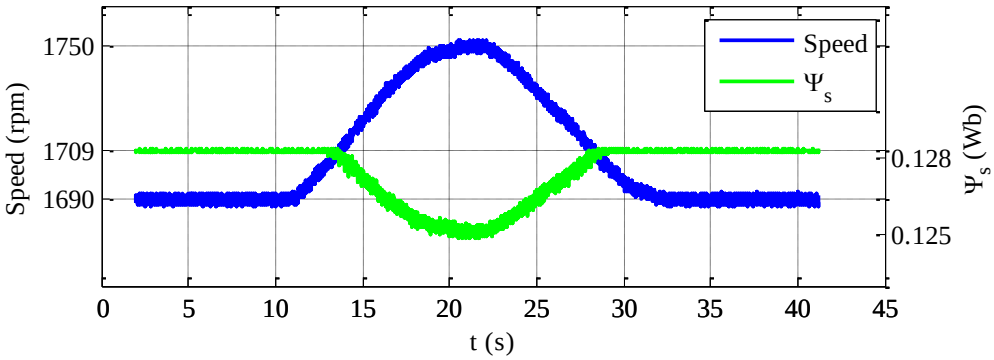

Fig. 2.18 Smooth FW to MTPA and MTPA to FW transition validation

2.6. SUMMARY

It has been validated that the extremely poor voltage based flux estimation significantly deteriorates the drive performance at low speeds despite the current based mode is expected to be dominant. The residual error coming from poorly estimated flux vector by the voltage based mode must be completely eliminated from the drive system in order to address the problem effectively.

In addition, it has been shown that the drives with the conventional Gopinath style closed loop flux observers suffer from poor performance during flux transitions due to the significant nonlinearity on the transition trajectory. This results in reduced accuracy over a wide speed range as the observer output diverges from both the current and the voltage based estimated fluxes.

To address the problems associated with the conventional observers which are commonly employed in the literature, an alternative combination of the current and the voltage based estimations have been proposed and discussed in details in this chapter.

Since the working principle of the conventional closed-loop observers is often cloudy in the literature, the combined observer characteristics can be better understood by the proposed scheme. The superiority of the proposed approach can be listed as follows:

- Much simpler and straightforward implementation,
- Linear trajectory and hence improved observer accuracy over a wide speed range,
- Facilitates to define the transition range between the observer modes,
- Significantly improves the current, flux and torque waveforms and hence the drive performance.

CHAPTER 3 – A FLUX OBSERVER WITH HIGH FIDELITY MACHINE MODELS FOR DTC DRIVES

3.1. INTRODUCTION AND LITERATURE REVIEW

It has been discussed previously that the flux observer quality is crucial in DTC drives. Thus far, numerous flux observers have been reported and employed in AC drives [19, 57-64]. These observers can be categorised into three groups which are the current based, voltage based and the closed loop flux observers which combine the first two. A novel combination technique of the two estimators has been introduced in the previous chapter [56]. The problems associated with the conventional observers can be summarized as follows.

A voltage based estimation is robust to machine parameter variations except the armature resistance variation, however the accuracy significantly deteriorates at low speeds. The deterioration is more serious if the inverter reference voltages are employed for the estimation. The reference voltages are commonly preferred in drives as the measurement of the discrete phase voltages is costly due to additional hardware requirements. Accordingly, the flux estimation at low speeds, where the voltage magnitude and the operating frequency are very low, is greatly influenced by the inverter voltage distortion and as a result, the estimation is not accurate. Consequently, the drive is likely to fail as the estimated flux in the controller may significantly differ from the actual flux. In reality, drives cannot start properly if the estimation is done with the voltage based estimator [24, 57, 58, 71, 82]. In this case, the operation of the machines has been investigated either at high speeds or the estimation method has been switched manually from the current mode to the voltage based mode of operation. However, the voltage based estimation is not perfect even at high speeds and may still be remarkably effected by the dead-time, nonlinear characteristics of the inverter and the variation of resistance even at high speeds unless their compensation is done properly. Moreover, since the voltage based estimation suffers from the drifting due to well-known integrator drift phenomenon, commonly, low-pass filters are employed to address the problem [54, 57, 60, 68, 83] but this ultimately reduces the response time. The low-pass filter inherently alters the magnitude and the phase. Therefore, the altered magnitude and phase of the estimated variables needs to be compensated. Even with appropriate compensations, the flux and torque responses might be significantly oscillatory due to the presence of the filters [14].

A current based estimation, on the other hand, is robust to dead-time, nonlinear inverter characteristics and variation of the stator resistance but the current based technique suffers when motor parameters vary. In a practical application, IPM-BLAC machine parameters may change significantly depending on a number of factors such as motor magnet temperature, manufacture tolerance, magnetic saturation, cross - coupling, and the material property variations [18]. These might significantly contribute to the parameter deviations from those employed in the current based estimation resulting in problems such as increased inaccuracies in the feedback of the closed-loop drive system and hence reduced drive system efficiency. It is noteworthy that, although the current based estimation is sensitive to the rotor position angle inaccuracies in sensor-less drives, the accurate position angle is readily available in the drives of concern, and a sensor-less drive is out of the scope in this study.

Considering the merits of the current and the voltage based estimations at low and high speeds, respectively, the closed-loop observers which combine the two techniques have become universal and employed greatly in AC drives [12, 19-23, 54, 59-63, 65, 66, 72-76, 84-88]. Thus, a great number of state-of-art direct torque controlled drives employ the current and the voltage based estimations at low speeds and at high speeds, respectively. However, significant problems associated with the closed-loop observers have been discussed widely in the previous chapter. To address the problems such as cross-interferences of the two modes and the reduced accuracy at a wide speed range due to the nonlinear flux trajectory have been addressed with a new combination strategy of the two observers [56].

Despite the fact that conventional closed-loop observers have been significantly improved by the novel strategy described in the previous chapter, there are still inherent problems as the drive system relies on two different estimators at low and high speeds. Accordingly, any of these combined observers inherits the inaccuracies pertinent to the current and the voltage based estimations at low and high speeds, respectively.

At low speeds, in which the combined structure is employed, inaccuracies in the estimated variables might be high depending on the magnetic saturation. To overcome this, [60] proposed modified approach for FOC based IPM drives in order to improve the performance of the current controllers owing to more accurate decoupling in the feed-forward path. Although, the new structure is robust against parameter variations, the performance get worse when speed approaches to standstill due to the speed division in

the structure. Moreover, it is not easy to balance the tradeoff between the observer and the controller bandwidth to optimize the performance. The work published recently [19] proposes a disturbance-input-decoupling observer for DTC drives which is similar to the work reported in [60]. The new technique achieves robust observation even at stand-still. However, the use of high-pass and low-pass filters increase the complexity of the proposed structure, causes response delay and may result in oscillations in the state variables [14]. Although the machine parameters, modelled as *dq*- axis currents shown in Fig. 2.8 may be employed to improve the low speed accuracy, the modelling does not consider the cross-coupling effects of the *dq*- axis flux linkages. Also, the drive still suffers from the issues pertinent to hybrid observers such as the variation of the actual torque when the motor changes observer mode of operation. This issue will be discussed further with experimental results.

Eventually, inaccurate estimation will deteriorate the quality of the torque control as well as the system efficiency. A new observer structure is proposed in order to address the above-mentioned problems. The new structure takes the followings into account:

- magnetic saturations in rotor/stator cores,
- cross – coupling of *dq*- axis flux linkages,
- spatial harmonics in the magneto – motive force,

The proposed approach is also robust against the followings:

- variation of the stator resistance with machine temperature,
- inverter voltage drop,
- dead-time.

Furthermore, the new structure is also robust against flux and torque oscillations and deteriorated performance which is a significant problem in conventional combined structures when observer changes mode of operation. Consequently, the proposed drive has high performance over a wide speed range.

The main content of this chapter has been published by the author in [J4] detailed in List of Publications.

3.2. CONTROL SYSTEM CONFIGURATION

Fig. 3.1 illustrate the schematic of the proposed DTC based drive system where '*' and '^' denote reference and estimated values, respectively. '**' represents the voltage commands which are confined by the voltage constraint. The reference and the estimated state variables are illustrated in 'red' and 'blue' colours, respectively, the feedback loop to compensate FW errors of the proposed observer is illustrated in 'purple', the anti-windup implementation is illustrated in 'yellow' and the modulation technique for the power conversion is illustrated in 'green'. SVPWM is employed as a modulation technique whose superior features have been discussed in previous sections 1.2.2 and 2.2.

The coupling term $(\omega_e \Psi_s)$ in (1.10) is decoupled as shown in Fig. 3.1. The reference stator flux magnitude is employed in the decoupling as it is clearer than the observed flux. The anti-windup (AW) protection is achieved by the classical "*integrator clamp*" technique [77, 78]. Because the DC-link voltage might vary significantly ($\mp 15\%$) in a practical implementation of an electric vehicle applications, it is of advantageous to employ the measured DC-link voltage in the controller as shown in the drive schematic.

The FB loop is employed to compensate observer inaccuracies in FW region. The voltage saturation in a FW operation is commonly utilized via FB loop in recent years by employing different approaches [33, 49, 50, 89]. The FB loop employed in the proposed drive will be further discussed in this chapter (section 3.3.2).

The torque and the flux limits are imposed by (2.5) and (1.13), respectively, to operate under current and voltage constraints.

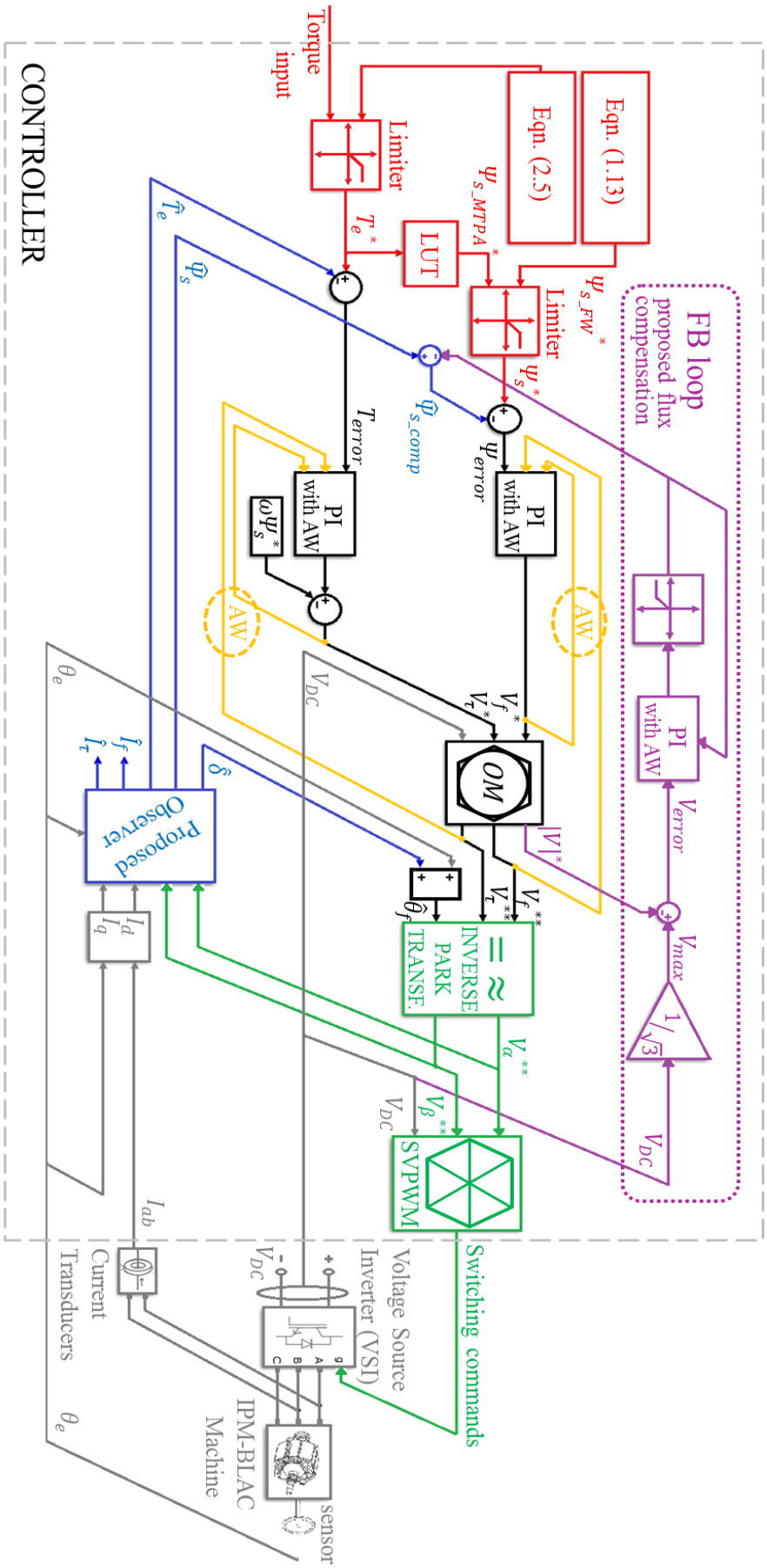

Fig. 3.1 Schematic of the proposed drive system

3.3. PROPOSED HIGH FIDELITY FLUX OBSERVER

The voltage equations in the rotor reference frame are obtained from (1.1) and they can be expressed in the s-domain as follows:

$$\begin{bmatrix} V_d^{**}(s) \\ V_q^{**}(s) \end{bmatrix} = R_n \begin{bmatrix} I_d(s) \\ I_q(s) \end{bmatrix} + \begin{bmatrix} s & -\omega \\ \omega & s \end{bmatrix} \begin{bmatrix} \widehat{\Psi}_d(s) \\ \widehat{\Psi}_q(s) \end{bmatrix} \tag{3.1}$$

where ** and ^ denote the command voltages and the estimated *dq*- axis flux linkages, respectively, and R_n is the nominal stator resistance. The flux linkages are functions of the rotor position and the *dq*- axis currents. They can be obtained by experiments or from the machine finite element analysis.

$$\Psi_d = f(I_d, I_q, \theta_e) \quad \& \quad \Psi_q = g(I_d, I_q, \theta_e) \tag{3.2}$$

From (3.2), one can determine the *dq*- axis currents from inverse functions of f and g as follows:

$$I_d = f^{-1}(\Psi_d, \Psi_d, \theta_e) \quad \& \quad I_q = g^{-1}(\Psi_d, \Psi_d, \theta_e) \tag{3.3}$$

Computationally efficient high-fidelity mapping of the *dq*- axis flux linkages and their inverses (*dq*- axis current maps) have been elaborated in great detail recently [79, 80]. Thus, the estimated (model predicted) *dq*- axis currents can be expressed as:

$$\hat{I}_d = f^{-1}(\widehat{\Psi}_d, \widehat{\Psi}_q, \theta_e) \quad \& \quad \hat{I}_q = g^{-1}(\widehat{\Psi}_d, \widehat{\Psi}_q, \theta_e) \tag{3.4}$$

As can be seen, the spatial harmonics are considered in (3.4). $\hat{I}_{dq}$ currents can be converted into two dimensional maps by taking the mean of the *dq*- axis flux linkages over one electric cycle. Thus, f^{-1} and g^{-1} functions in (3.4) can be expressed as given by (3.5). By doing so, the maps require a smaller amount of memory in the controller.

Fig. 3.2 illustrates the flux linkages of the test machine in Table 1.1 as functions of currents at 70℃ magnet temperature and Fig. 3.3 illustrate the currents as functions of flux linkages by performing the inverse solutions of *f* and *g* functions.

$$\hat{I}_d = f_1(\hat{\Psi}_d, \hat{\Psi}_q) \quad \& \quad \hat{I}_q = g_1(\hat{\Psi}_d, \hat{\Psi}_q). \tag{3.5}$$

It is noteworthy that the machine parameters L_d, L_q and Ψ_m can also be modelled as functions of *dq*- axis currents and the model predicted (or estimated) currents can be obtained from the nonlinear machine parameter maps from (1.2).

$$\hat{I}_d = \frac{\hat{\Psi}_d - \Psi_m(I_d, I_q)}{L_d(I_d, I_q)} \quad \& \quad \hat{I}_q = \frac{\hat{\Psi}_q}{L_q(I_d, I_q)} \tag{3.6}$$

The $\hat{I}_{dq}$ currents in (3.4) or (3.5), or the nonlinear motor parameters are stored in the controller as lookup tables. Then, the errors between the measured and the model predicted currents in any forms of (3.4), (3.5) or (3.6) (based on the observer design) are utilized to adjust the inverter reference voltages via two PI compensators as follows:

$$\begin{bmatrix} V_d^{**}(s) \\ V_q^{**}(s) \end{bmatrix} = R_n \begin{bmatrix} I_d(s) \\ I_q(s) \end{bmatrix} + \begin{bmatrix} s & -\omega \\ \omega & s \end{bmatrix} \begin{bmatrix} \hat{\Psi}_d(s) \\ \hat{\Psi}_q(s) \end{bmatrix} - \begin{bmatrix} K_p + \frac{K_i}{s} & 0 \\ 0 & K_p + \frac{K_i}{s} \end{bmatrix} \begin{bmatrix} I_d(s) - \hat{I}_d(s) \\ I_q(s) - \hat{I}_q(s) \end{bmatrix} \tag{3.7}$$

where K_p is the proportional and K_i is the integral compensators, respectively, in the proposed approach.

Fig. 3.4 shows the schematic of the proposed unified observer structure. As will be seen, the current errors are driven to zero via two independent PI compensators at steady-states. By doing so, the errors in the observed flux resulting from nonlinear inverter behavior, dead-time and resistance variation are all compensated and hence the accuracy of the resultant $\hat{\Psi}_{dq}$ will much increase.

It is worth mentioning that although any of (3.4), (3.5) or (3.6) can be employed in the proposed approach, (3.4) and (3.5) are more accurate than the (3.6) since the cross-coupling effects of the flux linkages are also accounted in high fidelity machine modelling. It is also worth mentioning that (3.1) in its simple form cannot be employed

as an estimator for the flux linkage due to the well-known integrator drift problem which does not exist in the proposed technique owing to the PI compensators.

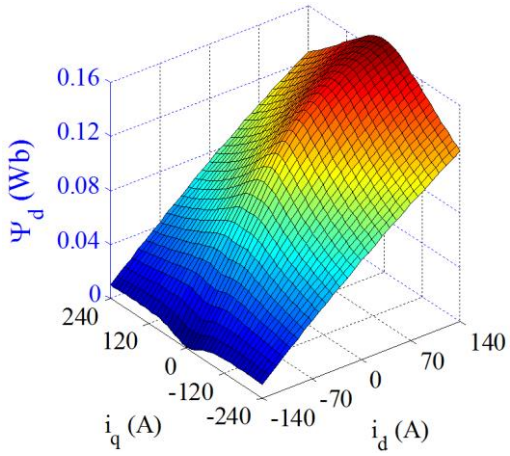

(a) *d*- axis flux map

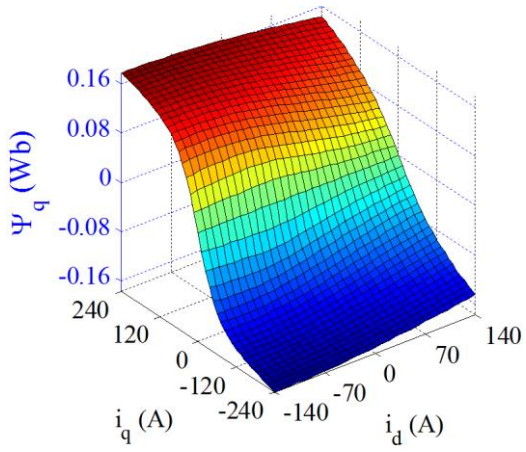

(b) *q*- axis flux map

Fig. 3.2 Flux linkage maps as functions of currents at 70℃ rotor temp.

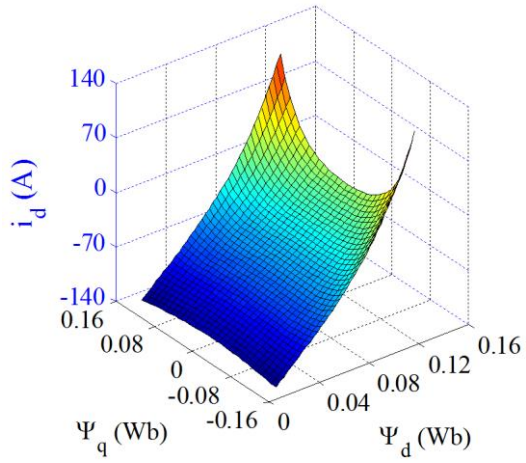

(a) *d*- axis current

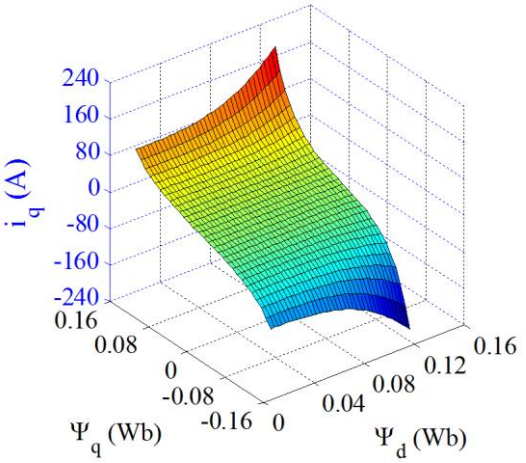

(b) *q*- axis current

Fig. 3.3 Current maps as functions of flux linkages at 70℃ rotor temp.

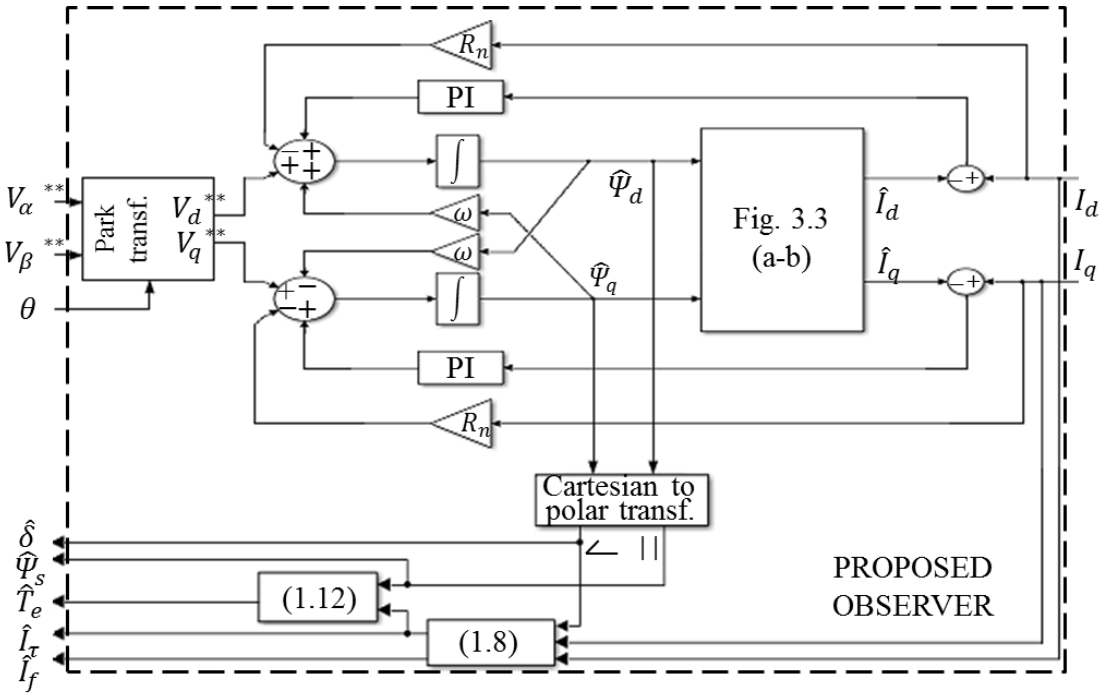

Fig. 3.4 Schematic of the proposed observer

3.3.1. MODELLING ERROR ANALYSIS

The *dq*- axis currents are expressed by any form of the (3.4), (3.5) or (3.6). However, finite element analysis based or experimentally derived models are not ideal due to deviation of the real-world machine parameters. The deviations of the parameters due to variations of the material properties and manufacturing tolerance such as assembly gaps between the rotor core and the permanent magnets can be addressed by calibrations based on back electromotive force measurements [79, 80]. However, the parameters may still deviate depending on operating temperature of the machine. Subtracting (1.1) from (3.7) yields;

$$\begin{bmatrix}\Delta V_d(s)\\ \Delta V_q(s)\end{bmatrix} = \Delta R\begin{bmatrix}I_d(s)\\ I_q(s)\end{bmatrix} + \begin{bmatrix}s & -\omega\\ \omega & s\end{bmatrix}\begin{bmatrix}\Delta \Psi_d(s)\\ \Delta \Psi_q(s)\end{bmatrix} + \begin{bmatrix}K_p + \dfrac{K_i}{s} & 0\\ 0 & K_p + \dfrac{K_i}{s}\end{bmatrix}\begin{bmatrix}\Delta I_d(s)\\ \Delta I_q(s)\end{bmatrix} \tag{3.8}$$

where $\Delta I, \Delta V, \Delta \Psi$ and ΔR represent the current errors between the measured and the estimated, the voltage errors between the machine voltages and the inverter reference, the flux error between the estimated and actual machine flux and the resistance error between

the actual and the nominal value, respectively. One can obtain the model predicted currents from (3.5):

$$\begin{bmatrix}\hat{I}_d\\ \hat{I}_q\end{bmatrix}=\begin{bmatrix}f_1(\hat{\Psi}_d,\hat{\Psi}_q)\\ g_1(\hat{\Psi}_d,\hat{\Psi}_q)\end{bmatrix}+\begin{bmatrix}\Delta f_1\\ \Delta g_1\end{bmatrix}=\begin{bmatrix}f_1(\Psi_d-\Delta\Psi_d,\Psi_q-\Delta\Psi_q)\\ g_1(\Psi_d-\Delta\Psi_d,\Psi_q-\Delta\Psi_q)\end{bmatrix}+\begin{bmatrix}\Delta f_1\\ \Delta g_1\end{bmatrix} \tag{3.9}$$

where $[\Delta f_1 \quad \Delta g_1]^T$ are defined as the modelling errors. From Taylor's series expansion, the above can also be expressed as:

$$\begin{bmatrix}\hat{I}_d\\ \hat{I}_q\end{bmatrix}=\begin{bmatrix}f_1(\Psi_d,\Psi_q)+\dfrac{\partial f_1}{\partial \Psi_d}(-\Delta\Psi_d)+\dfrac{\partial f_1}{\partial \Psi_q}(-\Delta\Psi_q)\\ g_1(\Psi_d,\Psi_q)+\dfrac{\partial g_1}{\partial \Psi_d}(-\Delta\Psi_d)+\dfrac{\partial g_1}{\partial \Psi_q}(-\Delta\Psi_q)\end{bmatrix}+\begin{bmatrix}\Delta f_1\\ \Delta g_1\end{bmatrix} \tag{3.10}$$

where $f_1(\Psi_d,\Psi_q)=I_d$ and $g_1(\Psi_d,\Psi_q)=I_q$. Hence,

$$\begin{bmatrix}\hat{I}_d\\ \hat{I}_q\end{bmatrix}=\begin{bmatrix}I_d\\ I_q\end{bmatrix}-\begin{bmatrix}J_{11} & J_{12}\\ J_{21} & J_{22}\end{bmatrix}\begin{bmatrix}\Delta\Psi_d\\ \Delta\Psi_q\end{bmatrix}+\begin{bmatrix}\Delta f_1\\ \Delta g_1\end{bmatrix} \tag{3.11}$$

where $J_{11}=\frac{\partial f_1}{\partial \Psi_d}, J_{12}=\frac{\partial f_1}{\partial \Psi_q}, J_{21}=\frac{\partial g_1}{\partial \Psi_d}, J_{22}=\frac{\partial g_1}{\partial \Psi_q}$. Therefore, the *dq*- axis current errors in (3.8) are given by:

$$\begin{bmatrix}\Delta I_d\\ \Delta I_q\end{bmatrix}=\begin{bmatrix}I_d-\hat{I}_d\\ I_q-\hat{I}_q\end{bmatrix}=\begin{bmatrix}J_{11} & J_{12}\\ J_{21} & J_{22}\end{bmatrix}\begin{bmatrix}\Delta\Psi_d\\ \Delta\Psi_q\end{bmatrix}-\begin{bmatrix}\Delta f_1\\ \Delta g_1\end{bmatrix} \tag{3.12}$$

Substituting (3.12) into (3.8) gives;

$$\begin{bmatrix}\Delta V_d(s)\\ \Delta V_q(s)\end{bmatrix}=\begin{bmatrix}\Delta RI_d(s)\\ \Delta RI_q(s)\end{bmatrix}-\begin{bmatrix}\Delta f_1\left(K_p+\dfrac{K_i}{s}\right)\\ \Delta g_1\left(K_p+\dfrac{K_i}{s}\right)\end{bmatrix}+M\begin{bmatrix}\Delta\Psi_d(s)\\ \Delta\Psi_q(s)\end{bmatrix} \tag{3.13}$$

where $M = \begin{bmatrix} \left(K_p + \frac{K_i}{s}\right) J_{11} + s & \left(K_p + \frac{K_i}{s}\right) J_{12} - \omega \\ \left(K_p + \frac{K_i}{s}\right) J_{21} + \omega & \left(K_p + \frac{K_i}{s}\right) J_{22} + s \end{bmatrix}$

The resultant *dq*- axis flux errors in the proposed observer structure are obtained from (3.13) as follows:

$$\begin{bmatrix} \Delta\Psi_d(s) \\ \Delta\Psi_q(s) \end{bmatrix} = \Delta\Psi_I(s) - \Delta\Psi_R(s) + \Delta\Psi_M(s) \tag{3.14}$$

where $\Delta\Psi_I, \Delta\Psi_R$ and $\Delta\Psi_M$ are the errors in the observed flux due to inverter voltage drop, resistance variation and modelling errors, respectively, and given by (3.15).

$$\begin{aligned} \Delta\Psi_I(s) &= M^{-1} \begin{bmatrix} \Delta V_d(s) \\ \Delta V_q(s) \end{bmatrix} \\ \Delta\Psi_R(s) &= M^{-1} \begin{bmatrix} \Delta RI_d(s) \\ \Delta RI_q(s) \end{bmatrix} \\ \Delta\Psi_M(s) &= M^{-1} \begin{bmatrix} \Delta f_1 \left(K_p + \frac{K_i}{s}\right) \\ \Delta g_1 \left(K_p + \frac{K_i}{s}\right) \end{bmatrix} \end{aligned} \tag{3.15}$$

The steady-state flux linkage errors are obtained by (3.16).

$$\begin{aligned} \lim_{s\to 0} \begin{bmatrix} \Delta\Psi_d(s) \\ \Delta\Psi_q(s) \end{bmatrix} &= \lim_{s\to 0} \Delta\Psi_I(s) - \lim_{s\to 0} \Delta\Psi_R(s) + \lim_{s\to 0} \Delta\Psi_M(s) \\ &= \begin{bmatrix} 0 \\ 0 \end{bmatrix} - \begin{bmatrix} 0 \\ 0 \end{bmatrix} + \begin{bmatrix} c_1 \\ c_2 \end{bmatrix} \end{aligned} \tag{3.16}$$

M^{-1}, c_1, c_2 and further theoretical analysis can be found in the appendix. c_1 and c_2 are the constants to represent the steady-state flux errors associated with the modelling errors in the proposed structure. Therefore, it is theoretically verified that the proposed scheme is robust against inverter voltage drop and resistance variation which are important problems in the conventional observers. These inaccuracies are driven to zero at steady-states via the feedback mechanism of the proposed method. However, it is

evident that the errors associated with the modelling errors still exist. In this case, the feedback mechanism has a filtering effect to reduce the measurement noise. The voltage feedback loop in Fig. 3.1 is proposed for compensation of the modelling errors in the constant power operating region.

3.3.2. FEEDBACK OBSERVER MODELLING ERROR COMPENSATION

Deviations from the calibrated model is dominated by the motor temperature variation. A temperature sensor might be employed for compensation of such errors. However, the additional sensor will inevitably increase the cost. Also, measured winding temperature may differ from the temperature of the permanent magnets and hence the temperature variation may not be compensated accurately.

The influence of the temperature variation on the stator flux vector is investigated with the test motor in Table 1.1. Table 3.1 presents the behaviour of the stator flux vector at different machine temperatures when the drive is operated with 20Nm torque.

Table 3.1 Stator flux vector versus motor magnet temperature at 20 Nm

	Motor magnet temp. (℃)	$\lvert\Psi_s\rvert$ (Wb)	δ (°)
(a)	30	0.1354	30
	60	0.1342	30.8
	100	0.1328	31.8
(b)	30	0.0837	33.9
	60	0.0832	35
	100	0.0821	36.7

(a) $MTPA$ $(\omega_m = 1000\, r/min)$ (b) FW $(\omega_m = 2500\, r/min)$

As will be seen temperature rise results in reduced stator flux magnitude and increased torque angle δ. This can be explained simply as follows. When temperature increases, the magnet is forced to operate with reduced remanent flux density and hence the permanent magnet flux linkage (Ψ_m) reduces. The consequence of the reduced magnetic flux linkage is illustrated in Fig. 3.5 where superscript " $'$ " denotes the variables at a higher temperature. As can be seen, the *d*- axis flux linkage reduces. Thus, the torque

angle and the stator flux magnitude increases and reduces, respectively, when the operating temperature increases.

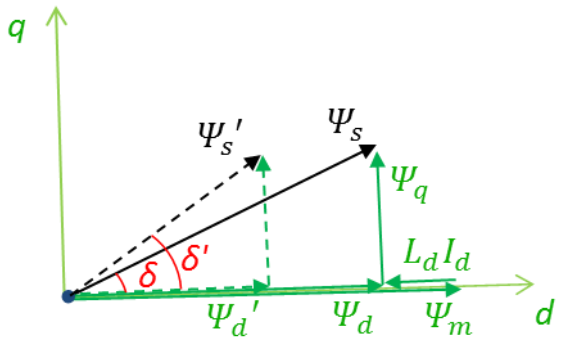

Fig. 3.5 Influence of the temperature on the stator flux vector

The stator flux magnitude is overestimated when the permanent magnet temperature is higher than reference temperature employed in the observer (e.g. 70℃ in Fig. 3.3). On the contrary, the torque angle (δ) is underestimated. Because torque is a function of the stator flux vector (*section 2.2 – last paragraph*), the opposite trend of the change in the magnitude and the angle δ due to temperature variation results in less influence on the estimated torque error.

The stator flux magnitude underestimation will result the drive reaching voltage saturation before the FW is triggered. This is because of the fact that the actual flux magnitude is higher than the value employed in the controller. In this case, the magnitude of the control voltage vector will be greater than V_{max}. Thus, the voltage feedback loop as illustrated in Fig. 3.1 can compensate for the flux underestimation errors once the voltage reaches V_{max}, *i.e.*, in FW operation. The error is used by the feedback PI controller for compensation. Consequently, late FW due to underestimated flux can be avoided in the proposed drive.

3.4. COMPARATIVE SIMULATION STUDIES BETWEEN THE CONVENTIONAL AND THE PROPOSED OBSERVERS

The drives with conventional and the proposed observer structures are compared and the effectiveness and superiority of the proposed scheme is evidenced by simulation studies in this section. The ratings of the simulated IPM machine and the power converter are listed in Table 1.1 and Table 1.2, respectively.

A high-fidelity, computationally efficient and electro-thermally coupled machine model [80] has been employed in the simulations in order to represent the real electromagnetic behaviour of the IPM machine considering the temperature and resistance variations and the magnetic saturations in the stator and rotor cores. Though the motor magnet and winding temperatures might be different from each other in practice, they are assumed to be the same in the simulations for simplicity.

Table 3.2 presents simulated accuracy tests of the drive system shown in Fig. 3.1 with the conventional observer over a wide speed and torque operating range (maximum speed: 4500 r/min, peak torque: 70 Nm). The observer employed in the drive is the most common Gopinath style closed-loop observer. The conventional observer has been discussed in the previous chapter in detail and its schematic is illustrated in Fig. 2.3. The transition speed, where the observer mode of operation changes from current to voltage based estimations or vice-versa, has been adjusted to 500 r/min so that the voltage based estimation is dominant at the given speed range in Table 3.2. The table illustrates the steady-state errors of the estimated stator flux magnitude and the torque which are the two regulated state variables. The accuracies are shown as percentages of their actual values defined by (3.17).

$$Error = (Estimated\ value - Actual\ value)/Actual\ value \times 100\ \% \tag{3.17}$$

Similarly, Table 3.3 presents the same accuracy tests with the proposed observer. Current – flux maps shown in Fig. 3.3 at the70℃ reference temperature are employed in the observer. The proportional and integral compensators have been set to 6 and 30, respectively.

As can be deduced from the comparisons of Table 3.2 and Table 3.3, the proposed technique with its feedback modelling error compensation presents very low error over a wide operating range. Whilst the torque error is within 2% in the proposed drive, it may increase up to 13% in case of the conventional observer is employed. Similarly, the stator flux magnitude error is within 3% in the proposed drive but may increase up to 11.2% when the conventional one is employed. Negative signs in Table 3.3 indicate that the actual value is greater than the estimated *i.e.*, underestimation. As has been discussed, the underestimation of the stator flux magnitude results in late triggering of field weakening operation whereas the overestimation causes early triggering. As can be seen, there is no

negative flux error when the conventional observer is employed (overestimation). This is because the voltage magnitude used in the observer is always greater than that applied to the motor due to inverter voltage drop. Hence, it is evident that the feedback loop cannot compensate the steady state errors of the estimated flux in conventional drives as the voltage does not saturate because of earlier triggering of field weakening operation. However, as seen in Table 3.3, the feedback loop of the proposed drive compensates the flux errors in field weakening operation when the motor magnet temperature is lower than the reference and this is indicated as FB.

It is worth mentioning that temperature rise reduces the accuracies of voltage based observer and hence the conventional combined observer since the stator resistance increases with temperature. Table 3.2 shows that its effect on the conventional observer may be more severe than the modelling errors associated with the proposed structure. By way of example, when the machine operates at 1000 r/min and 40 Nm, the temperature variation from 30℃ to 100℃ increases the stator flux magnitude error from 2.7% to 4.4% if the conventional observer is employed whereas the error varies from -0.4% to 0.3% with the proposed observer.

The average stator flux errors in Table 3.2 and Table 3.3 are illustrated in Fig. 3.6. Likewise, the average torque errors are illustrated in Fig. 3.7. Overall is the average of the all test points in Table 3.2 and Table 3.3. The simulated drives, which are very close to real world drive, validate significant improvement on the estimation accuracy in steady states when the proposed observer is employed.

Table 3.2 Accuracy tests of the conventional observer

Torque (Nm)	Motor Temperature °C	Speed (r/min) 500 a	500 b	1000 a	1000 b	1500 a	1500 b	2500 a	2500 b	3500 a	3500 b	4500 a	4500 b
		a: Stator flux error (%) b: Torque error (%)											
20	30	1.9	2.5	2.4	2.6	2.1	2.1	1	2.2	0.7	1.8	1.2	1.2
	60	2.8	3.5	2.9	3.1	2.4	2.5	1.4	2.8	1.5	2.7	2.3	2.6
	100	3.8	5	3.5	3.7	2.8	3	2	3.5	2.6	4.2	3.4	4.1
40	30	5	4.8	2.7	3	1.3	1.1	1.7	1.7	Outside the operating region			
	60	6	6.4	3.4	4	1.9	1.9	2.7	2.8				
	100	7.4	8.5	4.4	5.1	2.7	2.8	4	4.2				
60	30	8.5	8.6	3.2	3.6	1.5	1.1						
	60	9.6	10.3	4.2	5	2.4	2.1						
	100	11.2	13	5.5	7	3.7	3.3						
		MTPA				FW							

Table 3.3 Accuracy tests of the proposed observer

Torque (Nm)	Motor Temperature °C	Speed (r/min) 500 a	500 b	1000 a	1000 b	1500 a	1500 b	2500 a	2500 b	3500 a	3500 b	4500 a	4500 b
		a: Stator flux error (%) b: Torque error (%)											
20	30	-1.1	-2	-1.1	-2	-1.1	-2	**FB**	-0.5	**FB**	-0.7	**FB**	-1
	60	-0.3	-0.6	-0.3	-0.5	-0.3	-0.6	**FB**	-0.2	**FB**	-0.4	**FB**	-0.5
	100	0.8	1.3	0.8	1.3	0.8	1.3	2.3	0.2	2.9	-0.2	3	-0.2
40	30	-0.4	-1.5	-0.4	-1.5	**FB**	-1.5	**FB**	-0.4	Outside the operating region			
	60	-0.1	-0.3	-0.1	-0.3	**FB**	-0.5	**FB**	-0.1				
	100	0.3	1.4	0.3	1.4	0.4	0.7	1.1	0.3				
60	30	-0.1	-2	-0.1	-2	**FB**	-1.1						
	60	0	-0.8	0	-0.8	**FB**	-0.5						
	100	-0.1	0.8	0	0.8	0.9	0.3						
		MTPA				FW							

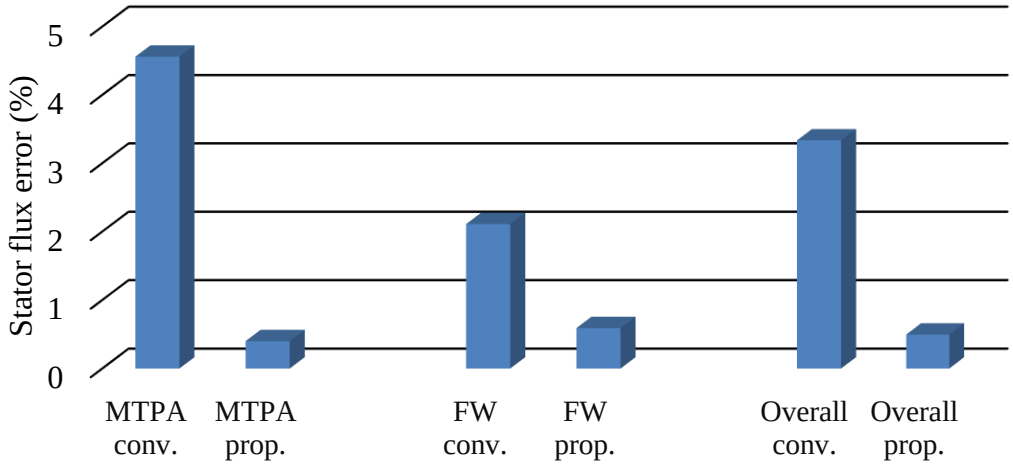

Fig. 3.6 Comparison of average stator flux errors based on data given in Table 3.2 and Table 3.3

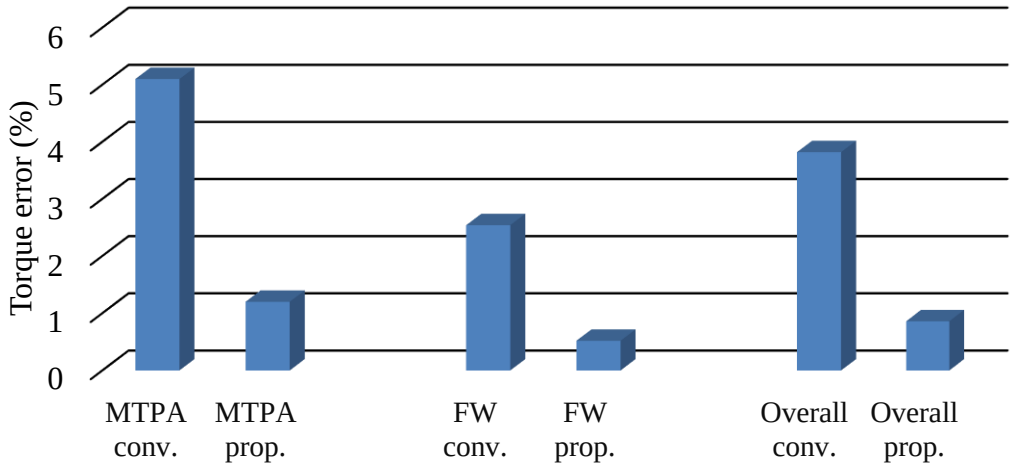

Fig. 3.7 Comparison of average torque errors based on data given in Table 3.2 and Table 3.3

Fig. 3.8 (a) and (b) show the simulated torque and the stator flux magnitude responses at 1000 r/min when the voltage based and the proposed observer is employed, respectively. An ideal inverter is employed until t=0.5s and then a nonlinear inverter model (Table 1.2) with 3μs dead-time is employed in the simulated drive. As can be seen when the voltage based observer or the combined hybrid observers (either closed or open loop combinations) are employed, both of the torque and the flux reduces with inverter voltage drop. It is noteworthy that when the voltage based estimations are employed oscillations exist in the response. This is because of the low-pass filters. These problems are not present in Fig. 3.8-(b) with the proposed observer. It is noteworthy that the influence of the inverter voltage drop on the voltage based estimation is relatively large as the 120V of DC link voltage is very low.

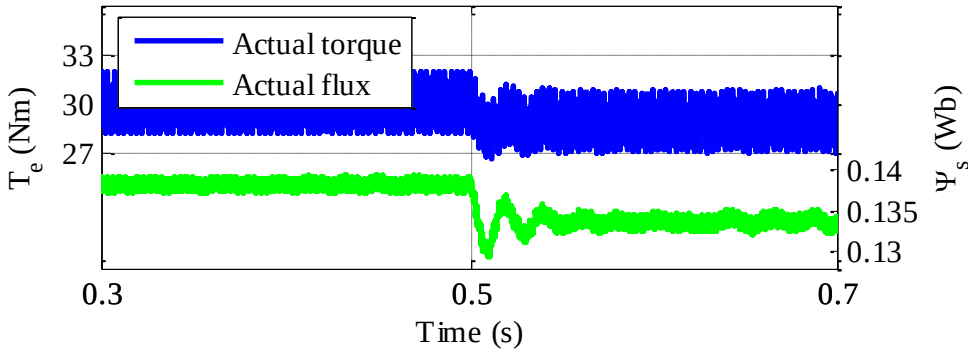

(a) Voltage based observer

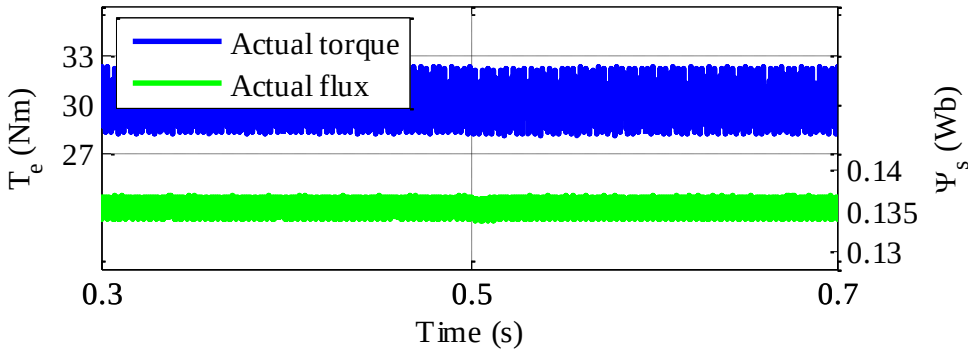

(b) Proposed observer

Fig. 3.8 Inverter nonlinearity effect when the voltage based observer is employed

3.5. COMPARATIVE EXPERIMENTAL RESULTS BETWEEN CONVENTIONAL AND THE PROPOSED OBSERVER

Experiments have been carried out to validate the superiority of the proposed drive in Fig. 3.1 both in constant torque and constant power operating regions. The details of the test rig, the motor and the inverter specifications have been discussed and listed in section 1.2.1. For comparisons, both the proposed and the conventional (3.5) structures are implemented and experimentally tested.

Fig. 3.9 compares the torque responses which result with the conventional and proposed observer when the motor speed varies between 300 r/min and 800 r/min with torque reference of 20Nm. The poor torque response of the conventional observer (Fig. 2.3) illustrates the inherent problem of the hybrid observers which has been employed in recent publications [12, 15, 19-21, 55, 56, 90]. Because the current based estimation with nominal machine parameters and the voltage based estimation are dominant below and above, respectively, 500 r/min transition speed, the non-linear flux transition from the current to the voltage based estimations or vice-versa results in 10% (2 Nm out of 20 Nm) torque variation. On the contrary, the resultant torque in the proposed drive is robust against speed variations. This is because the proposed observer estimates the flux and the

torque with a unified structure which compensate the inverter nonlinearity and the dead-time, and voltage drop in phase resistance at any speed.

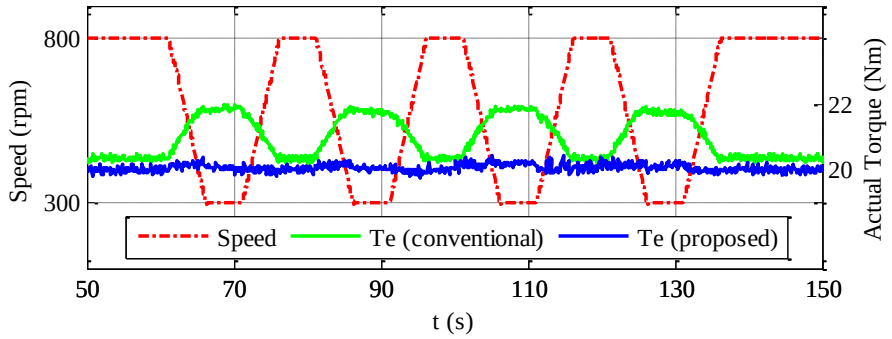

Fig. 3.9 Transition issue of conventional observers

Fig. 3.10 compares current waveforms which are obtained with the conventional and the proposed observers when the drives operate at 100 r/min and 15 Nm. It has already been discussed in great detail that the conventional closed loop observers suffer from the residual error caused by the voltage based estimation at low speeds so the performance and the current waveforms deteriorate significantly. Although this problem has been addressed by a novel combination strategy, the experiments have been carried out to validate that the proposed closed-loop observer does not suffer from the cross-interference issues. The nonlinear machine parameters shown in Fig. 2.8 have been employed in the conventional observers to improve the low speed accuracy. As can be seen, the current waveforms are much improved thanks to PI compensators of the proposed observer since the effect of the inverter nonlinearities are driven to zero in steady-states (3.16).

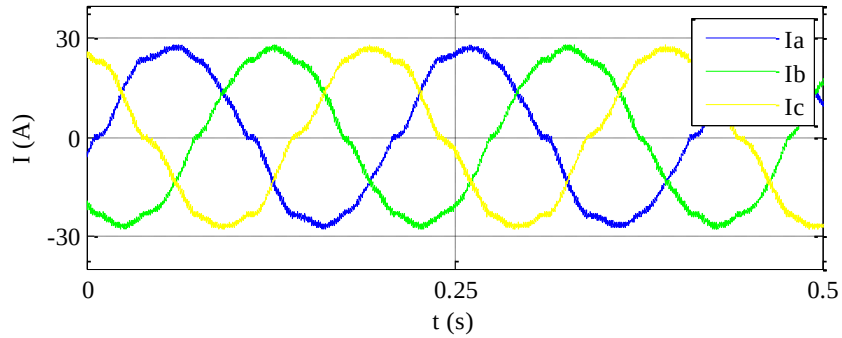

(a) Conventional observer Fig. 2.3

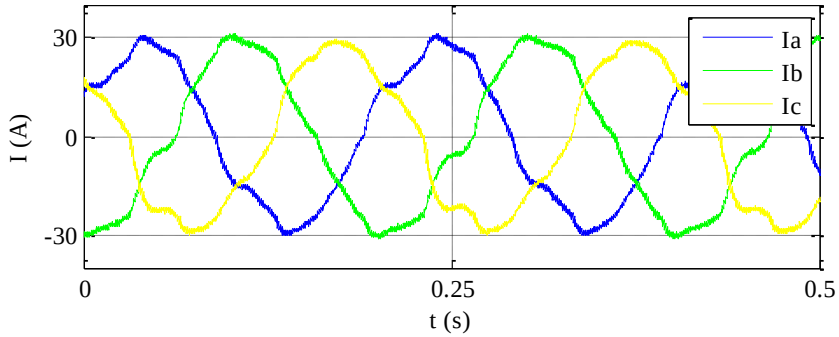

(b) Conventional observer Fig. 2.5

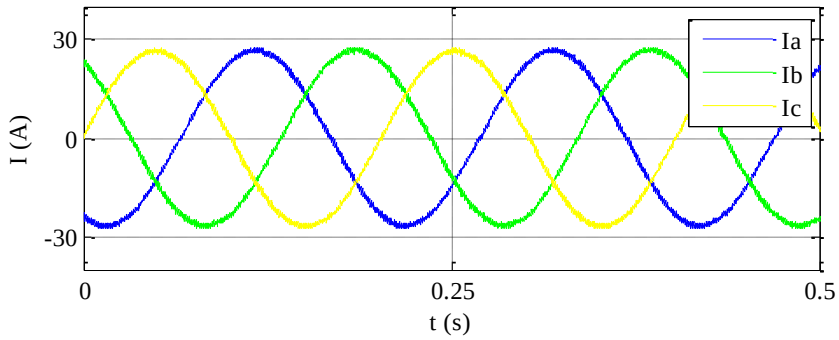

(c) Proposed observer

Fig. 3.10 Comparison of current waveforms comparisons at 100 r/min and 15Nm

Fig. 3.11 and Fig. 3.12 illustrate the current waveforms at speeds of 50 and 700 r/min, respectively, when the torque demand is zero. Since the no load operation is demanded, the phase currents are expected to be very small. In fact, this is the case in the proposed drive. However, inaccurate estimations with the conventional observer structures result in a large current flow even though the demand torque is zero. This will of course result in reduced drive efficiency. This problem is caused by torque estimation error. The observed torque tracking the zero demand does not imply that the actual torque is also zero. Thus, this operation is not a “no load” operation in strict sense. The current deviation from zero is dependent on the inaccuracy of the estimation. The voltage based estimation employs low-pass filters with 10 Hz cut-off frequency to prevent integrator drift and the phase and magnitude compensations are implemented as shown in Fig. 2.9. As can be seen, the influence of the inverter nonlinearity and the voltage drop is more pronounced with the voltage based estimator even though the speed is 700 r/min. As has been discussed, this is due to the fact that the low DC link voltage of the drive under tests. The results validate significant accuracy improvement with the proposed observer.

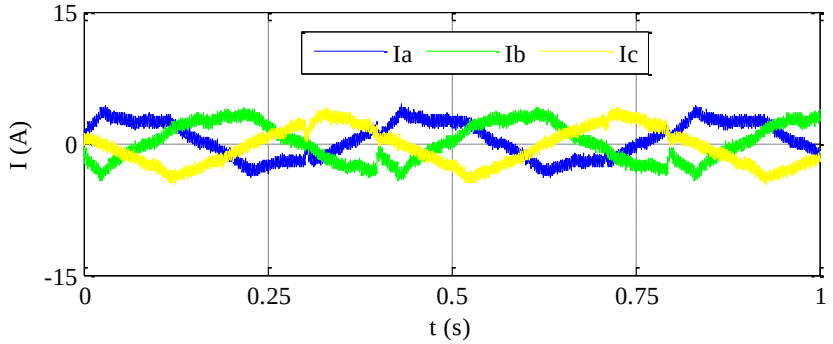

(a) Conventional observer Fig. 2.3

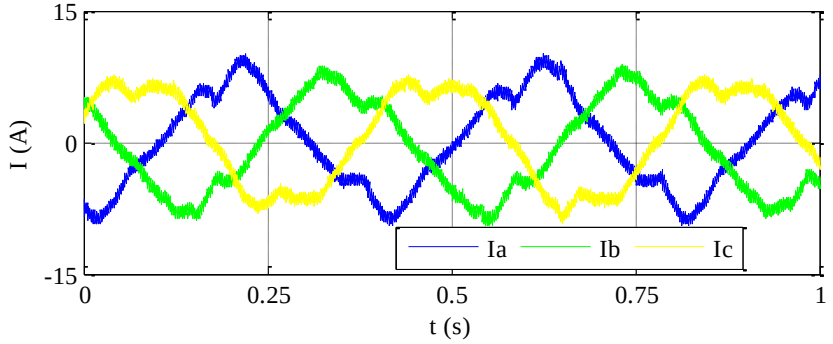

(b) Conventional observer Fig. 2.5

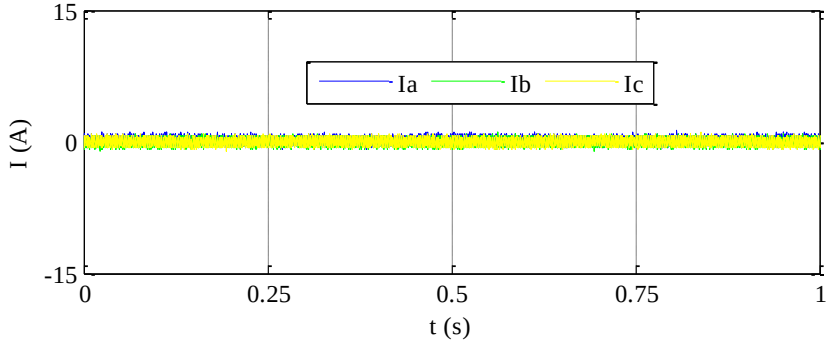

(c) Proposed observer

Fig. 3.11 Measured current waveforms with zero torque demand at 50 r/min

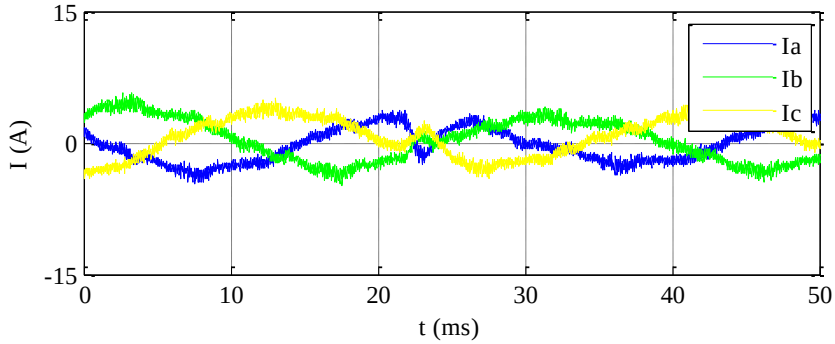

(a) Conventional observer Fig. 2.3

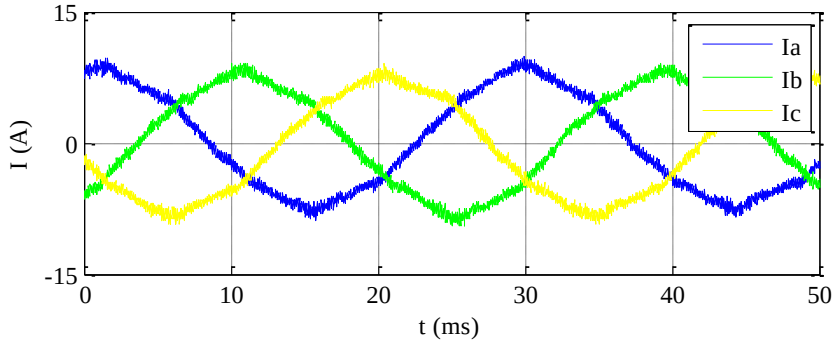

(b) Voltage based estimation

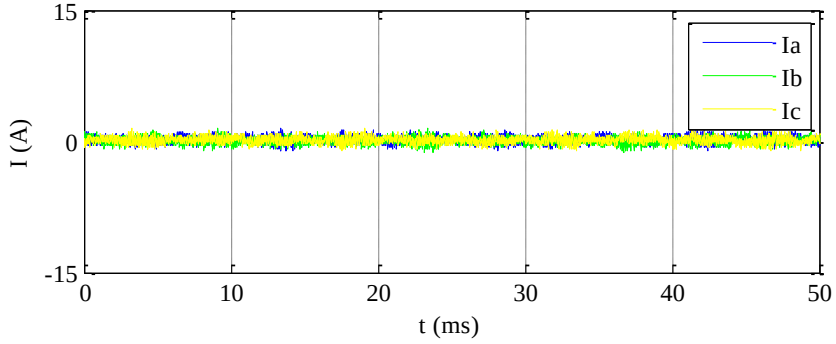

(c) Proposed observer

Fig. 3.12 Measured current waveforms with zero torque demand at 700 r/min

A test in deep field weakening operation is carried out with the proposed structure in order to validate its performance in high speed operation and its independence from nonlinear inverter characteristics, dead-time and variation of the stator resistance. The test is done at the peak power of 7.85kW (3000 rpm and 25 Nm) and results are shown in Fig. 3.13. Disturbances to V_{dq}^{**} and R_n are injected deliberately into the observer structure shown in Fig. 3.4 at t=42s and t=48s, respectively. V_{dq}^{**} and R_n are multiplied by 80% and 200%, respectively. Despite the extremely inaccurate phase voltages and stator resistance in the observer structure, the proposed drive is still quite robust. As can be seen, the disturbances injected deliberately are compensated by the measured currents via the observer feedback correction mechanism. As will be seen from Fig. 3.13-(d) that extremely inaccurate phase voltage information in the observer did not deteriorate the current waveforms unlike the conventional closed-loop observer structures. It can be deduced from comparisons of Fig. 3.8 and Fig. 3.13-(c) that the proposed drive is robust against the inverter nonlinearities.

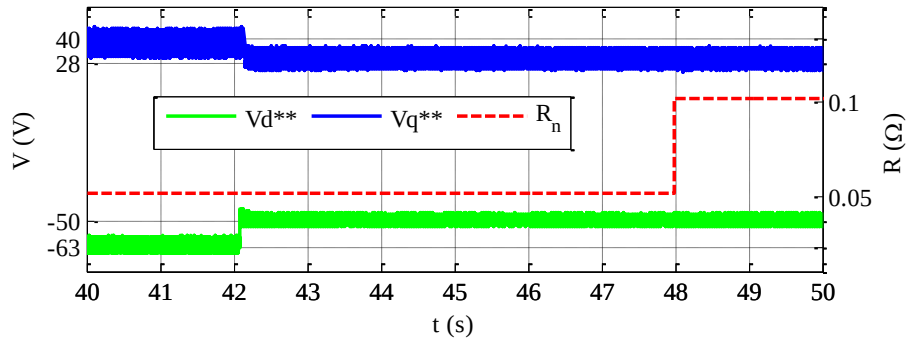

(a) Voltage and resistance disturbances

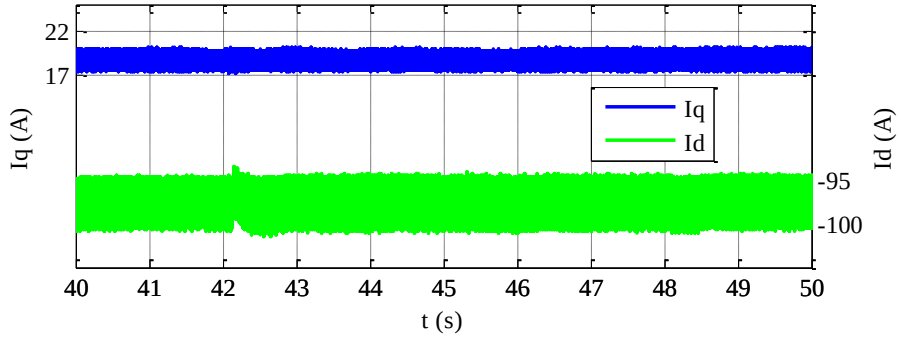

(b) *dq*-axis currents

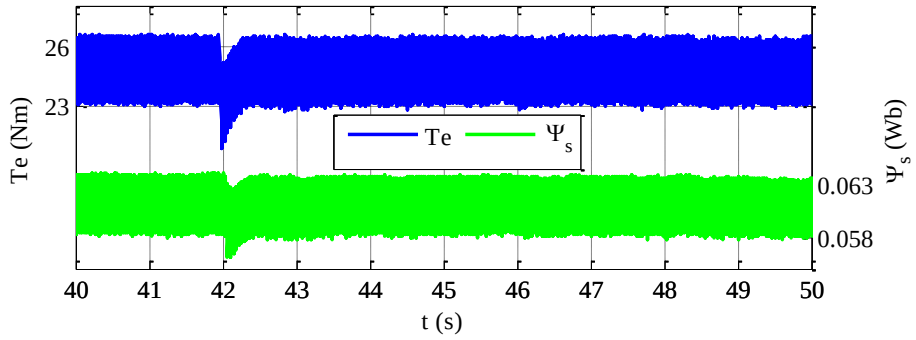

(c) Torque and stator flux responses to disturbances

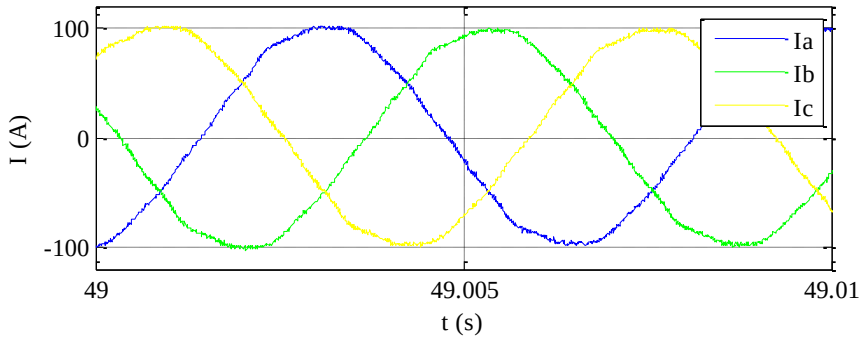

(d) Phase currents after disturbances

Fig. 3.13 Deep field weakening test at 3000 r/min and 25Nm

As has been discussed, the proposed observer can be formed by any (3.4), (3.5) or (3.6). The rest of the experiments have been carried out by employing (3.6).

Smooth transitions from constant torque to constant power operating region under no-load and 15Nm load torque conditions are shown in Fig. 3.14 (a) and (b), respectively. As has been discussed, the FW operation is automatically triggered in DTC based IPM drives by employing (1.13).

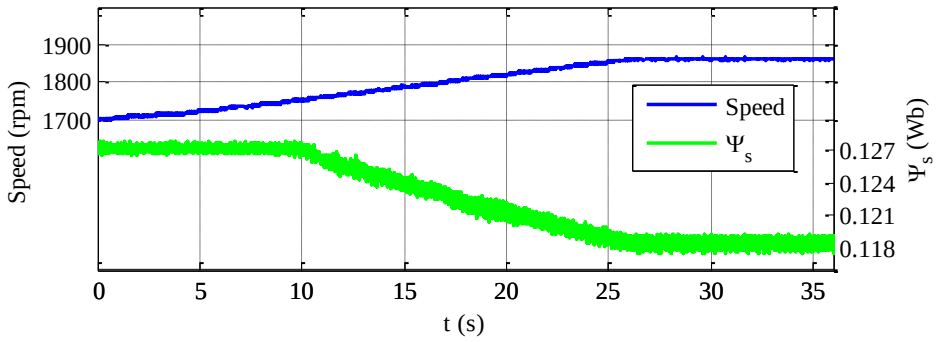

(a) No-load transition

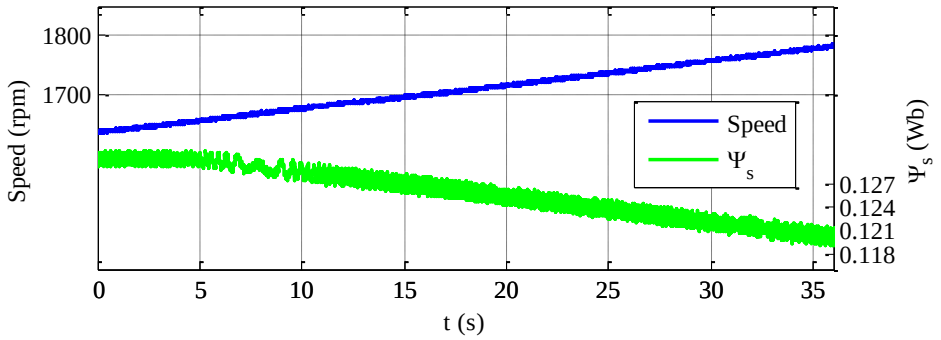

(b) 15 Nm loaded transition

Fig. 3.14 FW transitions of the proposed drive

Fig. 3.15 shows the estimated torque in the experimental drive system at steady state when speed is 2700 rpm and torque is 15Nm. Conventional and the proposed observer structures are used in the drives. The conventional one is the current based estimation with nonlinear machine parameters $L_d(I_d,I_q)$, $L_q(I_d,I_q)$ and $\Psi_m(I_d,I_q)$ given in Fig. 2.8. As can be seen the proposed observer results in much lower ripple as the PI compensators have a filtering effect. It is noteworthy that the proposed closed-loop observer does not suffer from integrator drift associated with pure integration whose details can be found in section 2.4 as the PI compensators avoid drifting. Thus, the LPFs (which need to be employed in the observer introduced in the previous chapter) are not necessarily required in the proposed observer.

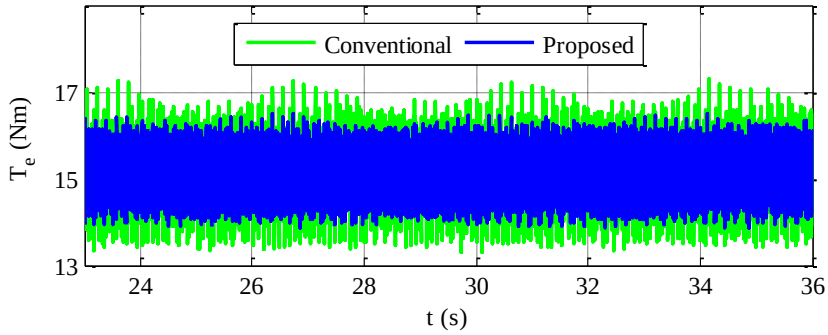

Fig. 3.15 Comparison of torque ripples at twice the base speed: 2700 rpm

Fig. 3.16 (a) and (b) illustrate the torque responses of the proposed drive system when torque command increases in steps of 5 Nm at 1000 rpm (constant torque region) and 2000 r/min (constant power region), respectively. As can be seen from the figures, the actual torque follows the commands closely and this verifies the good accuracy of the proposed observer. It is noteworthy that a rate limiter is imposed on the command torque in the drive system in order to avoid uncomfortable jerks of the electric vehicle traction system, hence the torque response is slightly slower.

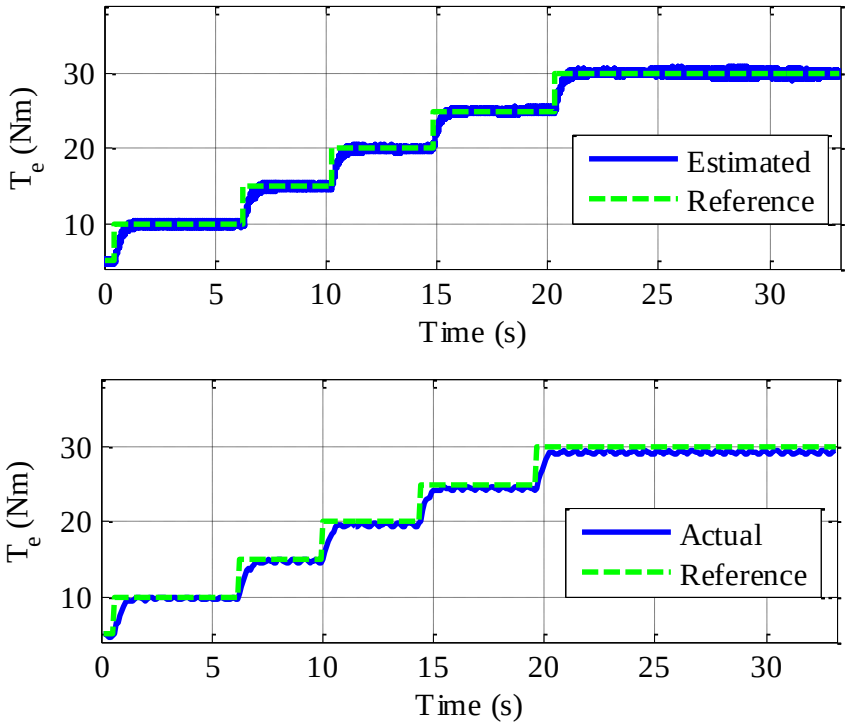

(a) 1000 rpm, MTPA

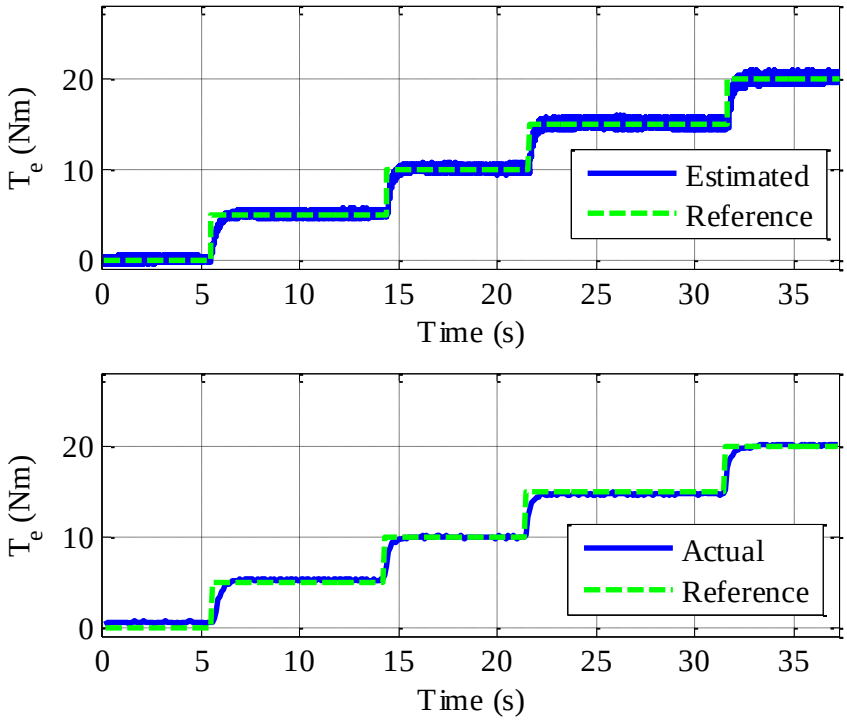

(b) 2000 rpm, FW

Fig. 3.16 Torque step responses in the proposed drive system

Fig. 3.17 (a) shows the flux and torque responses to a step change in command torque when the proposed drive is performed at 2700 rpm, twice the base speed. Similarly, torque and *d*- axis current responses to step changes in command torque are illustrated in Fig. 3.17 b.

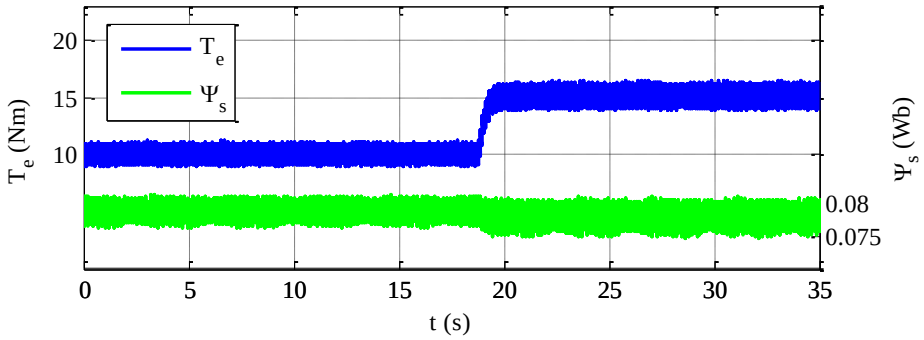

(a) Torque and stator flux responses

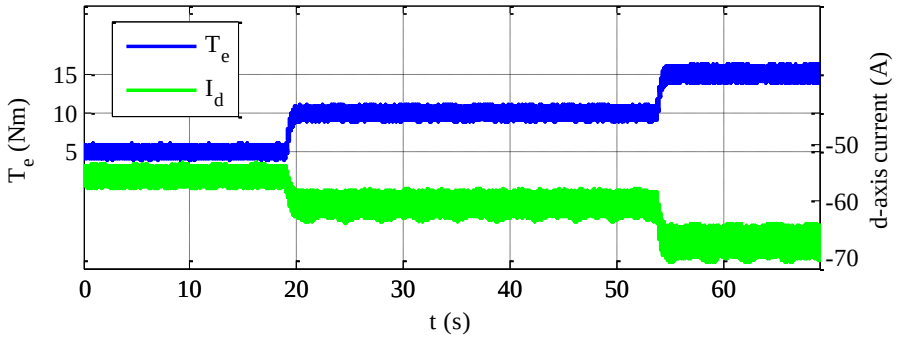

(b) Torque and *d*- axis current responses

Fig. 3.17 Drive responses at twice the base speed; 2700 r/min

3.6. SUMMARY

A new observer structure for DTC based IPM-BLAC drives has been described in this chapter. The observer accounts for real-world nonlinear machine behaviour by employing high fidelity modelling. By doing so, the flux and the torque is observed more accurately over a wide operating range. Unlike the conventional observer structures, it has been verified that the proposed structure is independent from nonlinear inverter characteristics, dead-time and variation of the stator resistance with temperature as these nonlinearities are compensated quickly by the measured phase currents.

Cross-coupling effects of flux linkages, magnetic saturations and spatial harmonics are taken into account in the high-fidelity machine modelling. In addition, the proposed structure does not contain filters for well-known integrator drift elimination. Therefore, the time delays and oscillatory responses due to filters are avoided in the proposed approach. The proposed drive is also robust against the low speed performance deterioration pertinent to the conventional observer structures where the performance may significantly deteriorate because of the cross-interference problems discussed in previous chapter.

It has been discussed that the proposed technique is sensitive to modelling error. These errors are dominated by the variation of the operating temperature. The influence of the modelling error is addressed in the constant power operation by utilizing the voltage saturations. The modelling errors and their resultant effect on the proposed DTC based drive system has been studied by realistic simulations. It has been verified that the error in the estimated torque is relatively small. The superiority of the proposed drive has been validated by simulations and experiments over a wide operating range.

CHAPTER 4 – ANALYSIS OF STATOR FLUX VECTOR CONTROLLED (SFVC) DRIVES

4.1. INTRODUCTION AND LITERATURE REVIEW

In order to have fast dynamic response and reduced torque ripples, direct torque control has become an attractive alternative to FOC drives since late 90s. However, despite the fact that torque seems to be regulated directly, in fact, direct torque control is an indirect realization of the stator flux vector which will be analysed thoroughly in this chapter. Thus, the DTC drives, hereafter, will also be referred to as indirect stator flux vector controlled (SFVC) BLAC drives.

The SFVC is commonly realized in the stator flux reference frame ($f\tau$), where f stands for *"flux"* and τ stands for *"torque"*. The angular displacement between the dq and the $f\tau$ frames is defined as torque angle (δ – Fig. 4.1). δ is constant in steady-states and hence the $f\tau$ frame rotates at synchronous speed in steady-states whereas the rotation might be faster or slower than the synchronous speed in transient-states.

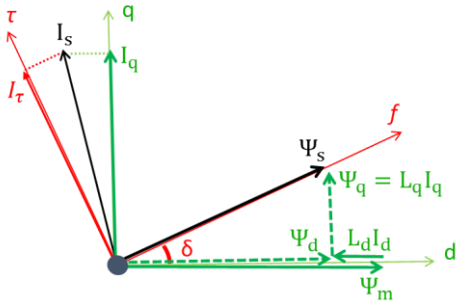

Fig. 4.1 Stator flux frame and the regulated state variables

Whilst dq- axis currents are the regulated state variables to generate command voltages in FOC drives [91-96], the case is different in the SFVC drives. To date, a great number of SFVC drives in the literature have realized the phase of the stator flux vector indirectly via either torque regulation [24, 26-32, 67, 68, 82, 97-103] or τ- axis current regulation [12, 54, 59, 65, 66, 86-88, 104-106]. Theoretical analysis of the machine behaviour, however, suggests that the controlled state variable should be δ rather than T_e or I_τ regardless of the switching technique either hysteresis based [30-32, 97, 98] or PWM based [12, 14, 15]. Despite the fact that T_e or I_τ are dependent on δ, indirect control of δ introduces several problems to a drive system such as strongly coupling and high nonlinearity in the control loop. These problems may reduce the robustness, vary the control bandwidth and pose a challenge for controller tuning.

Another fundamental problem associated with the indirect control is that there are two pairs of *dq*- axis currents for a given (T_e, Ψ_s) or for a given (I_τ, Ψ_s) commands. Indeed, only one of the pairs is on the accurate trajectory whereas the other pair reduces the drive efficiency drastically. This issue will be theoretically verified in details.

Apart from the problems discussed above, MTPV control is a great challenge in conventional indirect SFVC drives. It will be shown that the MTPV control is realized by limiting δ. Since δ is not a regulated state variable in conventional drives, the MTPV operation has not been adopted until recent years. Its implementation for conventional I_τ regulated drives has been discussed in [59] where δ is limited indirectly by employing an additional PI controller. However, although the MTPV was a particular attention of Gianmario Pellegrino *et al.,* in [54, 59, 65, 66], its implementation is not theoretically accurate since δ is confined by a constant value which is much higher than the theoretical maximum δ. In theory, there is an optimum δ_{max} per stator flux magnitude which implies that the limitation needs to be imposed online as a function of Ψ_s. Thus, the constant value would be valid only for a certain speed if the value were lower than the theoretical maximum torque angle. Besides, the additional PI controller to adopt the MTPV control increases the complexity and reduces the control bandwidth. Thus, the direct SFVC simplifies the MTPV adoption to a great extent as the δ can be limited online simply and directly.

The SFVC is realized in the stationary frame ($\Psi_\alpha - \Psi_\beta$ control) by Yukinori Inoue *et al.,* in [57, 58, 71] by employing an additional PI controller that generates the reference stator flux phase angle from the torque error. However, cascaded controllers in these drives not only reduce the response time, but increase the observer dependency significantly as the additional controller relies on a different estimated variable and hence reduced accuracy. Also, there is still nonlinearity in the control loop which leads to bandwidth variation with the operating points unless the linearization is addressed [71]. In addition, these drives perform only above certain speeds due to estimator limitation. It is well-known that voltage based estimation deteriorates at low speeds and, hence, is not accurate. Further, deviations in the phase and the magnitude of the estimated stator flux vector due to employed low-pass filters are not compensated for these drives. Hence, these drives would not have high performance over a wide speed range.

Recently, direct SFVC has been reported in [20, 21] in the $f\tau$ frame. These drives are based on dead-beat control technique. Namely, PI controllers are replaced by predictive algorithms which rely on machine parameters as well as flux observer. Accordingly, these drives would suffer from two significant problems. First, the magnetic flux linkage is assumed to be a constant. However, in a practical IPM machine, it is significantly dependent on both the temperature (Fig. 3.5) and the *dq*- axis currents (Fig. 2.8). Hence, the drive performance degrades when loading and the operating temperature change. Secondly, the drives would suffer from the cross-interference problems associated with the conventional hybrid closed-loop observers [56]. How seriously it may deteriorate the drive performance has been validated by simulations and experiments in Chapter 2. Although the direct SFVC has been proposed, the aforesaid problems have not been addressed, the potential of direct SFVC drives have not been realised, nor have the comparative studies between the conventional and the proposed drives been made. Thus, the followings are the novel contributions to knowledge in this chapter.

- The relationship between the torque and the stator flux vector is analysed thoroughly considering operating trajectories and practical nonlinearities.
- The theoretical realisation of the MTPV control in the SFVC drives is analysed and introduced.
- Issues pertinent to indirect SFVC (*i.e.*, DTC) drives are analysed and addressed.
- A novel direct SFVC drive for IPM machines is proposed and compared to the conventional indirect SFVC drives.

The proposed direct SFVC drive improves the dynamic response and facilitates simple control tuning with the desired bandwidth. Simply adopted linearization techniques avoid bandwidth variation with the operating points. The coupled control issues are eliminated by the proposed decoupling. Cascaded controllers which may limit the control bandwidth and increases observer dependency can be avoided. The machine nonlinearities are considered in the proposed approach and hence, the problems associated with the parameter variations are reasonably alleviated. The proposed drive does not suffer from the cross-interference problems associated with the conventional observers. Furthermore, MTPV control can be achieved simply by online limiting the torque angle directly. Whilst conventional drives operate in a coupled manner in all

MTPA, FW and MTPV regions, it will be shown that the proposed drive achieves decoupled control in any operating region.

The content of this chapter has been published by the author in [C2] detailed in List of Publications and [J7] is under preparation.

4.2. TORQUE VS STATOR FLUX VECTOR

The motivation for the analysis of the relationship between the electromagnetic torque and the stator flux vector arises from the need to clarify the alleged features associated with the conventional DTC drives in which the torque seems to be controlled directly. Hence, the torque and the stator flux vector relationship will be analysed thoroughly in this section.

Clearly, (1.10) suggests that the voltage commands should be generated from the stator flux magnitude and the torque angle regulations, *i.e.* (Ψ_s, δ). It is evident in (1.11) that torque is a function of the stator flux vector (Ψ_s, δ). Thus, based on the two equations, the torque is realized by the stator flux vector control regardless of its phase δ being controlled directly or indirectly through torque regulation. However, as can be seen from (1.11), there is high nonlinearity between the torque and the torque angle. Thus the relationship is investigated as follows.

Rearranging (1.11), one obtains the following expression for the electromagnetic torque.

$$T_e = \frac{3p\Psi_{ratio}{\Psi_m}^2}{2L_d}\left(sin\,\delta - \frac{(\rho-1)\Psi_{ratio}\,sin\,2\delta}{2\rho}\right) \tag{4.1}$$

where ρ is the saliency ratio $(= L_q/L_d)$ and Ψ_{ratio} is the ratio of the stator flux magnitude to the permanent magnet flux linkage $(= \Psi_s/\Psi_m)$. It is clear that the electromagnetic torque is proportional to the expression in (4.2).

$$T_e \propto sin\,\delta - \frac{(\rho-1)\Psi_{ratio}\,sin\,2\delta}{2\rho} \tag{4.2}$$

As can be seen, the torque expression in (4.2) is dependent on the saliency ratio and flux linkage ratio and hence the relationship between the torque and the stator flux vector can be generalized and analysed thoroughly for any type of BLAC machines.

It can be deduced from (4.2) that for a given torque angle δ the torque is dependent on the ρ and Ψ_{ratio}. The saliency ratio ρ is typically between one and five where one is for non-salient SPM-BLAC machines, and five is for highly salient IPM-BLAC machines. Ψ_{ratio} varies during operating conditions and its minimum value is zero in which the machines operate at the theoretical deepest field weakening. As can be deduced from Fig. 4.1, when δ = 0, Ψ_{ratio} = 1. Therefore, T_e vs δ can be plotted for typical values of ρ and Ψ_{ratio} representing all BLAC machines.

Fig. 4.2 (a) illustrates T_e - δ relationship in (4.2) for different BLAC machines when Ψ_{ratio} is 1.5 and, similarly, Fig. 4.2 (b) illustrates the relationship for ρ = 5 machines when Ψ_{ratio} varies between zero and 1.5, respectively. It is seen that T_e - δ curves have negative slope around zero-crossing of δ when ρ is 5 and above in Fig. 4.2 (a) and when Ψ_{ratio} is 1.3 and above in Fig. 4.2 (b). Because the torque is very low and it decreases with δ, the increase of δ results in torque reversal around the zero-crossing. In addition to low δ, the negative slope might exist again when $\delta \geq 90°$ depending on the values of ρ and Ψ_{ratio}. In this condition torque reversal does not occur, but nevertheless the achievable torque reduces. Therefore, the negative slope between T_e and δ needs to be avoided in either cases. This can be achieved by linearization of the torque with respect to torque angle.

4.2.1. LINEARIZATION OF TORQUE WITH RESPECT TO TORQUE ANGLE

In theory, the slope of the torque and the torque angle can be evaluated by the derivative of the torque with respect to torque angle. From (4.2), one obtains the partial derivative given by (4.3).

$$\frac{\partial T_e}{\partial \delta} \propto \cos\delta - \frac{(\rho - 1)\Psi_{ratio}\, cos\, 2\delta}{\rho} \tag{4.3}$$

Fig. 4.3 illustrates the derivative in (4.3), for the same conditions as Fig. 4.2.

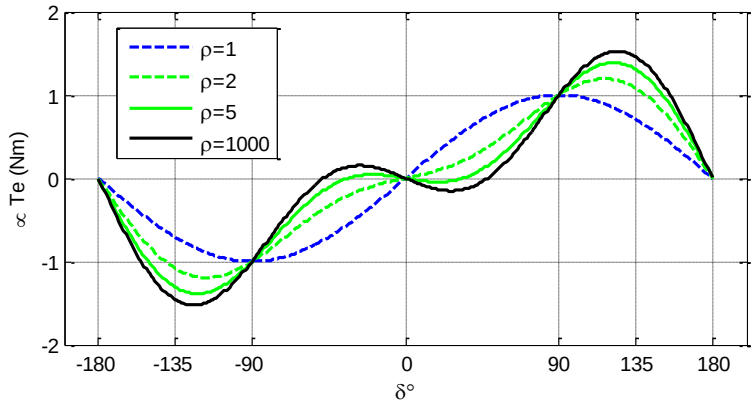

(a) Plot of (4.2) when Ψ_{ratio}=1.5

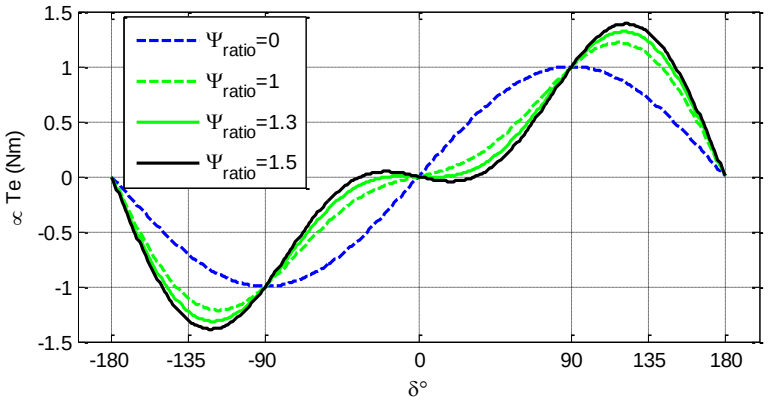

(b) Plot of (4.2) for ρ=5 machines

Fig. 4.2 $\propto T_e$ versus δ representing any type of BLAC machines

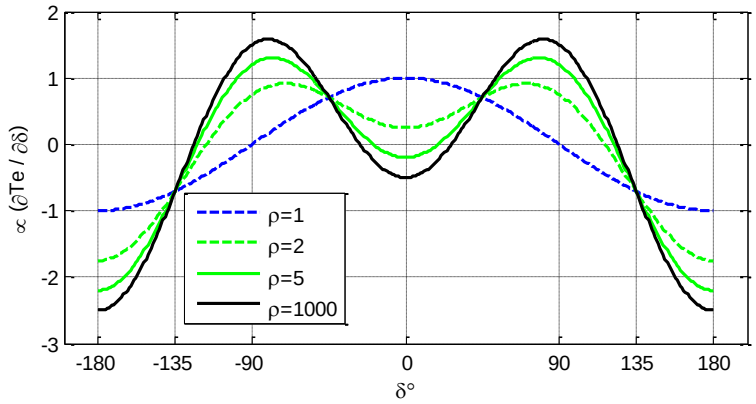

(a) Plot of (4.3) when Ψ_{ratio}=1.5

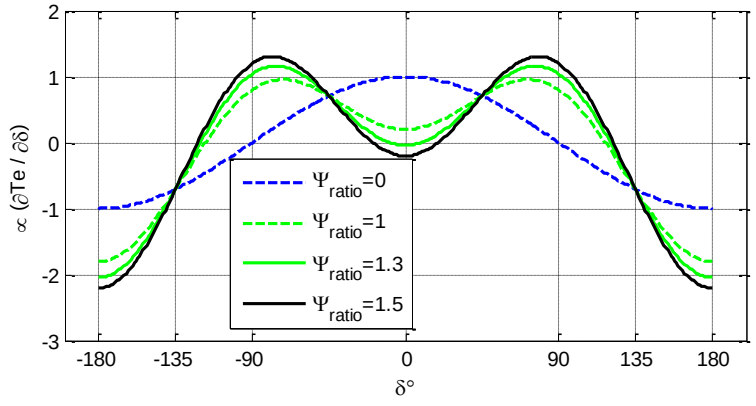

(b) Plot of (4.3) for ρ=5 machines

Fig. 4.3 $\propto \partial T_e/\partial\delta$ versus δ for the same conditions as Fig. 4.2

It is evident in Fig. 4.3 that (4.3) might become negative at low δ for IPM machines and always negative when $\delta_{max} \geq 135°$. In these conditions, the torque reduces with the increase in the torque angle. This can be avoided by limiting either Ψ_s or δ since (4.3) is dependent on Ψ_s and δ for a certain machine. The Ψ_s limit criterion is obtained by posing (4.3) to zero.

$$\Psi_{ratio} \leq \frac{\rho \cos \delta}{(\rho - 1) \cos 2\delta} \tag{4.4}$$

Substituting $\cos 2\delta = 2\cos^2 \delta - 1$ in (4.4) and solving for the quadratic equation, the torque angle limit criterion is obtained.

$$\delta \leq \cos^{-1}\left[\frac{\rho}{4(\rho - 1)\Psi_{ratio}} - \sqrt{\left(\frac{\rho}{4(\rho - 1)\Psi_{ratio}}\right)^2 + \frac{1}{2}}\right] \tag{4.5}$$

It is noteworthy that if one of the criteria is satisfied, the torque does not reduce with the increase in the torque angle. The two conditions and the potential nonlinearity between the torque and the torque angle needs to be analysed considering the operating trajectories. It will be shown that the nonlinearity at low δ might occur in MTPA or FW operations and the prevention of the negative slope at high δ is the condition for MTPV control. Thus, the negative slope of the torque - torque angle curve will be further analysed with particular attention to MTPA, FW and MTPV operations of IPM machines which are shown in Fig. 4.4-(a). Why the nonlinearity at low δ does not occur in an MTPV operation and why the prevention of the negative slope at high δ is the condition for MTPV control are extrapolated as follows.

Considering steady-states and neglecting the resistance, one can obtain the following expression from (1.1) and (1.2).

$$\left(\frac{V}{\omega}\right)^2 = \Psi_s^2 = L_d^2\left(\frac{\Psi_m}{L_d} + I_d\right)^2 + L_q^2 I_q^2 \tag{4.6}$$

Rearranging (4.6) one obtains;

$$1 = \frac{\left(\frac{\Psi_m}{L_d} + I_d\right)^2}{\left(\frac{\Psi_s}{L_d}\right)^2} + \frac{I_q^2}{\left(\frac{\Psi_s}{L_q}\right)^2} \tag{4.7}$$

Clearly, (4.7) is the equation of an ellipse in $I_d - I_q$ plane. It is evident from (4.6) that any point on an ellipse in Fig. 4.4 represents a constant stator flux magnitude and a constant voltage magnitude operation. This implies that there is a unique torque angle at any point on an ellipse as the stator flux magnitude at these points are the same.

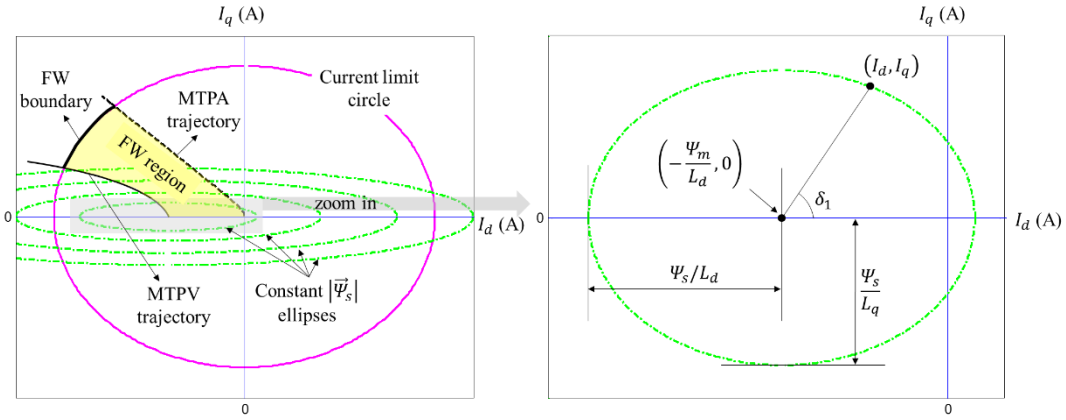

(a) MTPA, FW and MTPV trajectories (b) zoom in a constant stator flux magnitude ellipse

Fig. 4.4 Operating trajectories of IPM machines

The torque angle is obtained from (1.2) and Fig. 4.1.

$$\delta = \tan^{-1}\left(\frac{\Psi_q}{\Psi_d}\right) = \tan^{-1}\left(\frac{L_q I_q}{L_d I_d + \Psi_m}\right) \tag{4.8}$$

The torque angle can also be expressed as a function of δ_1 shown in Fig. 4.4-(b) as follows.

$$\delta_1 = \tan^{-1}\left(\frac{I_q}{\frac{\Psi_m}{L_d} + I_d}\right) = \tan^{-1}\left(\frac{L_q I_q \frac{L_d}{L_q}}{\Psi_m + L_d I_d}\right) \tag{4.9}$$

Substituting (4.8) into (4.9) yields;

$$\delta_1 = \tan^{-1}\left(\frac{\tan\delta}{\rho}\right) \tag{4.10}$$

Hence, the torque angle can be obtained from inverse solution of (4.10);

$$\delta = \tan^{-1}(\rho \tan\delta_1) \tag{4.11}$$

It is evident from (4.11) that the torque angle is dependent on the δ_1 and the saliency ratio. One can deduce from (4.11) that $\delta = \delta_1$ for SPM machines. Fig. 4.5, illustrates the torque angle as a function of δ_1 for given saliency ratios.

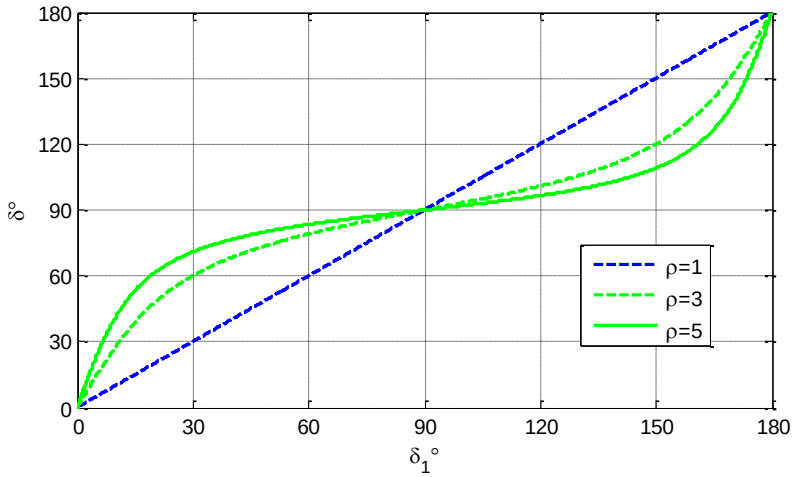

Fig. 4.5 δ vs δ_1 for different types of BLAC machines

It is seen from Fig. 4.5 that the torque angle is higher than 90° when $\delta_1 > 90°$. As can be verified from Fig. 4.4, δ_1 is always higher than 90° when the machine operates on the MTPV trajectory. This implies that the torque reversal due to the nonlinearity at low δ shown in Fig. 4.2 does not exist in an MTPV operation as the torque angle is already high in this region. In contrast, the nonlinearity at high torque angle in Fig. 4.2 is the condition to achieve the MTPV control. Accordingly, the linearization of the torque is discussed separately considering the operating trajectories as follows.

4.4.2.1. NONLINEARITY AT LOW δ (MTPA/FW)

Fig. 4.6 shows the criteria given by (4.4) and (4.5) when δ is low. It is noteworthy that the plot of (4.4) and (4.5) are the same.

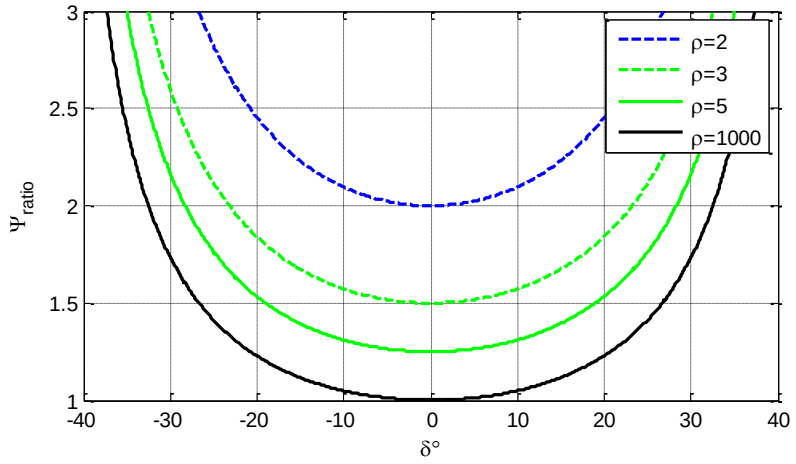

Fig. 4.6 Linearization of torque at low torque angles

Based on Fig. 4.6, for machines with ρ = 5, the nonlinearity at low δ occurs if the Ψ_{ratio} > 1.25 when δ = 0° or if -20° < δ < 20° when Ψ_{ratio} = 1.5. This implies that either Ψ_s or δ needs to satisfy (4.4) or (4.5), respectively.

The nonlinearity at light loads (low δ) may exist if the stator flux magnitude is higher than the boundary shown in Fig. 4.6. Since the stator flux magnitude in a FW operation is weaker than in an MTPA operation at the same torque, the worst case is in the MTPA operation. It is seen from Fig. 4.3 and Fig. 4.6 that the Ψ_{ratio} limit criterion becomes more critical when δ approaches to zero. Hence, the worst case at δ = 0° would be sufficient to represent any operating point. It can be deduced from Fig. 4.1 that when δ = 0°, $I_d = I_q$ = 0, $\Psi_s = \Psi_m$, and hence Ψ_{ratio} = 1 for any BLAC drives. As can be seen from Fig. 4.6, at δ = 0° the nonlinearity occurs when the Ψ_{ratio} is much higher than 1. However, one can deduce from Fig. 4.1 that this is only possible when a large quantity of positive *d*- axis current flows (δ = 0°, I_q = 0). It is well know that the positive *d*- axis current is not theoretically accurate [11] in BLAC drives.

The torque reversal analysis is further investigated for the machine under study with particular attention to the corresponding *dq*- axis currents. In fact, the torque reversal is only dependent on the reluctance torque. In IPM machines, the reluctance torque component is negative if there is positive *d*- axis current flow in the drive. Fig. 4.7 illustrates the reluctance and the permanent magnet based torque components and the total torque of the IPM machine in Table 1.1 when the current magnitude is 120A. It is seen that the reluctance torque is negative when *d*- axis current is positive and the total torque reduces with the positive *d*- axis current. Fig. 4.8 (a), (b) and (c) show the *d*- axis

current versus Ψ_{ratio}, the torque versus Ψ_{ratio} and the torque versus *d*- axis current, respectively, for the same machine when the *q*- axis current is constant at the specified values as shown in the figures. As can be seen from Fig. 4.8 (a), the Ψ_{ratio} is around 1 when the *d*- axis current is very low and increases with the *d*- axis current for constant *q*- axis current. This is due to the increased *d*- axis flux linkage. It is seen in Fig. 4.8 (b) that torque reversal occurs when $\Psi_{ratio} \approx 1.57$. This matches with Fig. 4.6 as the saliency ratio of the machine under study is $\rho \approx 2.88$. Clearly, the torque reversal occurs around $I_d \approx$110A and the corresponding *d*- axis current variation where the torque becomes negative is relatively less for different *q*- axis currents as shown in Fig. 4.8 (c). This implies that the torque nonlinearity at low δ would occur when extremely large positive *d*- axis current ($I_d \approx$110A) flows in the drive train. Even though the practical issues in a drive system are taken into account, it is very unlikely that this extreme condition occurs.

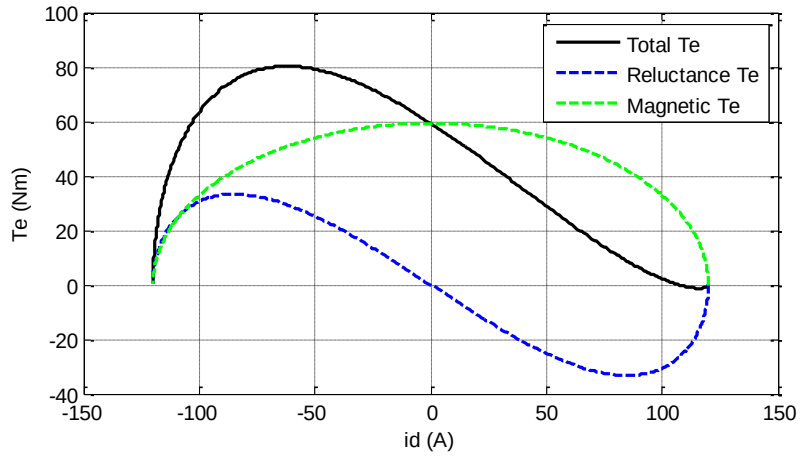

Fig. 4.7 Influence of reluctance torque in IPM machines

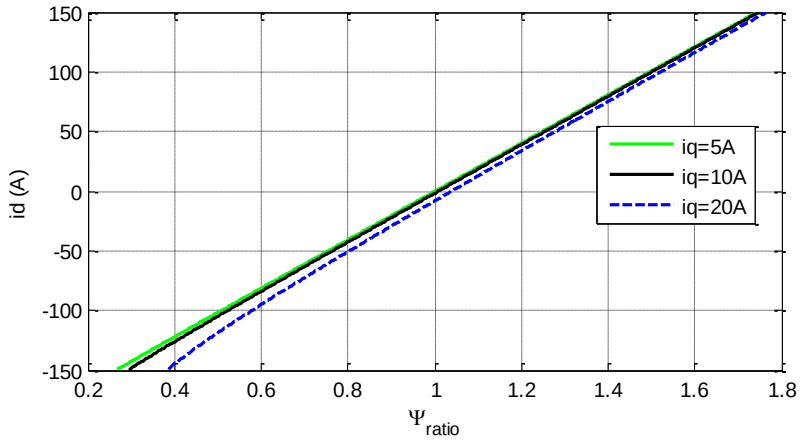

(a) *d*- axis current versus Ψ_{ratio}

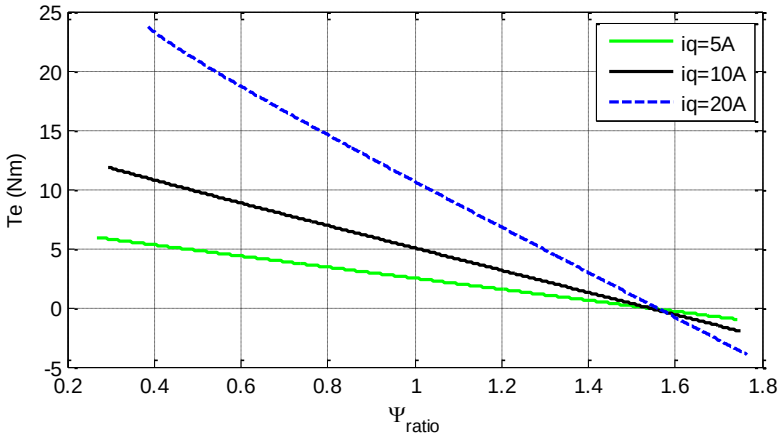

(b) Torque versus Ψ_{ratio}

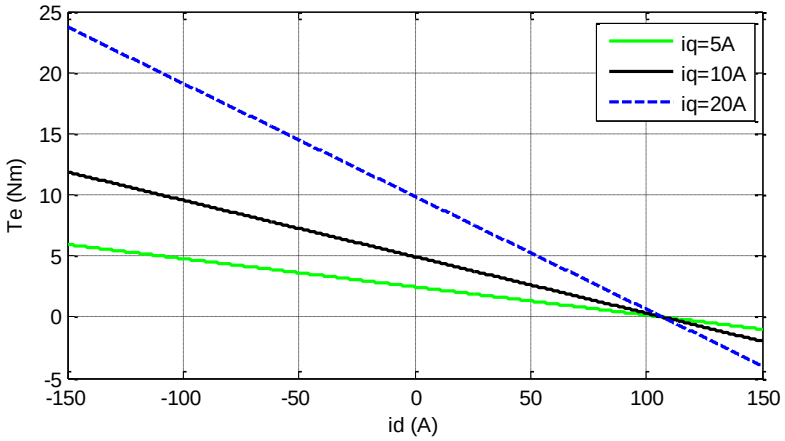

(c) Torque versus *d*- axis current

Fig. 4.8 Torque reversal analysis in *dq*- plane

All things considered, none of the BLAC drives suffer from the torque nonlinearity at low δ unless there is an extreme positive *d*- axis current flow in a drive system.

4.4.2.1. NONLINEARITY AT HIGH δ: MTPV CONTROL

The maximum torque per voltage (MTPV) operation is a specific control in a deep FW region. It maximizes the torque production per voltage (= per stator flux magnitude) and facilitates more extended speed range, and hence it is quite attractive for EV applications. The MTPV control has been discussed in great details for FOC drives in [37]. Recently, simplicity of the MTPV adoption in direct SFVC drives has been pointed out superficially [20]. However, deep analysis of the MTPV control in SFVC drives and the theory behind δ limitation strategy have not been discussed to date.

The MTPV control is a continuation of the torque reversal analysis since both are associated with the slope of the torque and the torque angle evaluated by $(\partial T_e/\partial\delta)$.

MTPV control might be required for certain machines whose critical current point is inside the current limit circle (type II – Fig. 1.6). Hence, the need for the MTPV operation depends on the machine design.

It is evident in Fig. 4.2-(a) that the maximum torque for a given stator flux magnitude is obtained when δ is 90° in SPM machines, whereas it is achieved between 90° and 135° in IPM machines. Thus, δ_{max} = 90° and 90° ≤ δ_{max} ≤ 135° for SPM and IPM machines, respectively. As can be seen, the low saliency ($\rho \approx 1$) tends to $\delta_{max} \approx$ 90° and high saliency tends to $\delta_{max} \approx$ 135° for IPM machines. Further, as can be verified from Fig. 4.3, the maximum torque is achieved when$(\partial T_e/\partial\delta)$ = 0 except for the zero-crossing. Therefore, MTPV control which maximizes the achievable torque per stator flux magnitude is obtained by posing $(\partial T_e/\partial\delta)$ to zero for a given stator flux magnitude. This is achieved by (4.5).

It is seen from Fig. 4.2-(b) that the maximum torque is achieved at a lower δ once Ψ_s reduces and, as will be seen, δ_{max} reduces down to 90° at the theoretical deepest FW where Ψ_s = 0. This implies that there is an optimum δ_{max} per stator flux magnitude. Hence, δ should be confined online as a function of Ψ_s, via the constraint given by (4.5). Hereby, MTPV control can be adopted by online limitation of δ.

Fig. 4.9 illustrates the torque angle constraint in (4.5) to maximize the achievable torque production per stator flux magnitude. As can be seen, δ_{max} is theoretically between 90° and 135° for salient machines. One can deduce from Fig. 4.9 that constant δ_{max} corresponds to a unique Ψ_s and hence valid for a certain speed. Thus, it is important to vary the δ_{max} online via (4.5).

MTPV control is further investigated by simulation studies. The prototype motor in Table 1.1 does not operate in an MTPV region. Since the MTPV control in SFVC drives is in particular attention of [59], simulations are carried out with the analogous MTPV implementation employing the same motor ratings as in [59]. By doing so, the results can be compared and how inaccurate MTPV implementation (not only in [59] but also in [20, 54, 59, 65, 66]) deteriorates the drive performance can be distinguished.

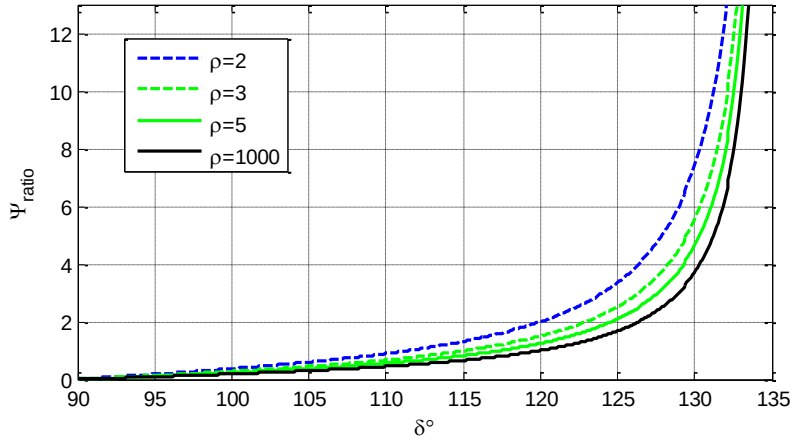

(a) δ_{max} constraint to achieve MTPV

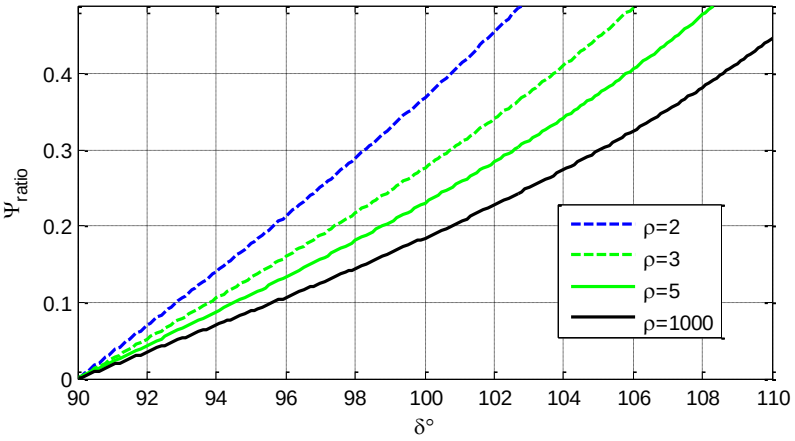

(b) zoom of (a)

Fig. 4.9 Maximum torque angle per stator flux magnitude for MTPV operation

The motor and the inverter specifications are listed in Table 4.1 and Table 1.2, respectively. The drive schematic of the conventional drive can be found in section 4.3 (Fig. 4.12-b) where the conventional drives are discussed in details.

Table 4.1 Specifications of type II IPM machine

Number of pole-pairs	2
Rated torque	1.4 Nm
Phase resistance	8 Ω
Maximum current	5A
DC link voltage	380V
Nominal *d*- axis inductance (L_d)	25 mH
Saliency ratio $(\rho = L_q/L_d)$	5
Permanent magnet flux linkage (Ψ_m)	0.05 Wb

The simulated results with and without adopting MTPV control are compared in Fig. 4.10. Unlike [20, 54, 59, 65, 66], where δ_{max} is set to a constant value manually ranging from 110° – 170° , it is seen that the maximum theoretical δ reduces online with the stator flux magnitude via (4.5). As can be seen, the achievable torque at 12000 r/min increases about 0.4 Nm once the MTPV operation is adopted. Thus, further extended speed range can be obtained. On the contrary, when the torque angle is limited to 160°, which is the case in [59], the achievable torque will reduce dramatically (≈ 29 % of the rated torque). The consequences are deteriorated acceleration performance, reduced torque capability, inability to achieve higher extended speed range and lower efficiency in the MTPV region. Considering the consequences, it is highly important to adopt the MTPV control online on a theoretical basis rather than selecting a random δ_{max} which is unique for a certain speed. It is noteworthy that if the δ_{max} is limited higher than 135° it is not unique even for a certain speed and hence results in low efficiency.

Fig. 4.11 shows the electromagnetic torque of the same machine as a function of δ for a given Ψ_s. It is seen that Ψ_s = 0.09 Wb corresponds to $\delta_{max} \approx 122°$ that matches well with Fig. 4.10 (a). At this point, the maximum achievable torque both in Fig. 4.10 (a) and Fig. 4.11 is $T_e \approx 0.8$ Nm. As can be seen from Fig. 4.11, the electromagnetic torque reduces to ≈ 0.4 Nm when δ approaches 160° which is 38° higher than the theoretical optimum δ_{max}. This is indeed the case in Fig. 4.10 (b) where MTPV control is not adopted. Therefore, the torque angle needs to be confined online by the trajectory shown in Fig. 4.10 and Fig. 4.11 via (4.5).

It should be noted that the drives do not necessarily need to operate at δ_{max} in an MTPV region. This implies that $\delta \leq \delta_{max}$. In other words, the operating torque might be lower than the maximum achievable torque.

As has been discussed greatly, the MTPV control is adopted by limiting the δ directly. However, in conventional drives δ is not a regulated state variable and realized indirectly by either torque or τ- axis current regulations. Accordingly, MTPV control cannot be adopted directly. Further discussions will be made in the following section.

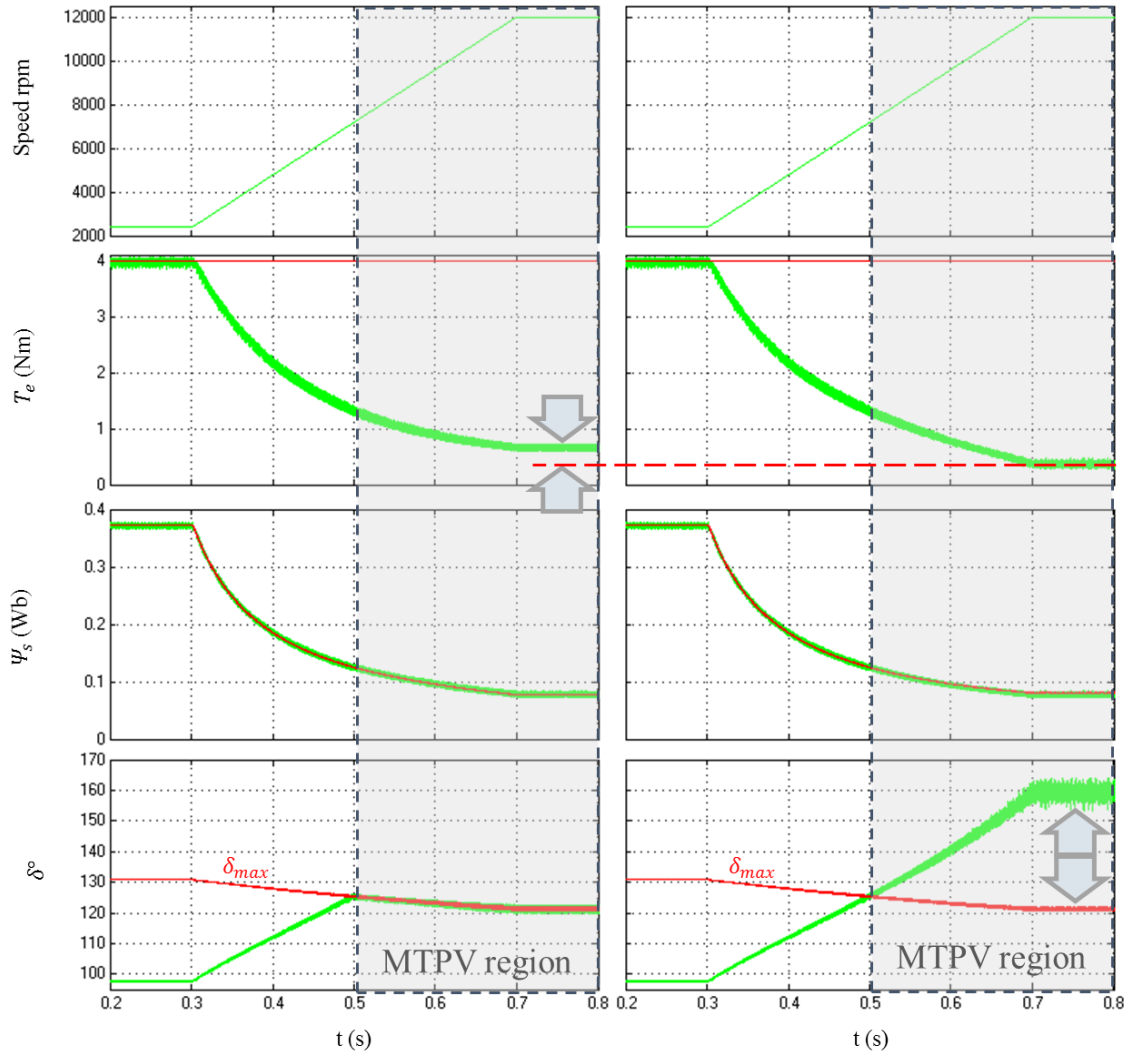

(a) by adopting MTPV control (b) without adopting MTPV control

Fig. 4.10 Simulation results with/without MTPV control

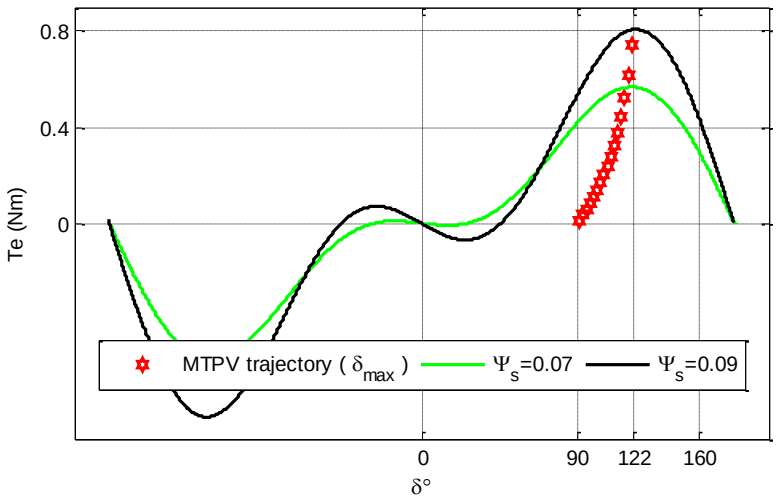

Fig. 4.11 T_e of the machine given in Table 4.1 as a function of δ for given Ψ_s

4.3. CONVENTIONAL INDIRECT, COUPLED AND NONLINEAR SFVC

Fig. 4.12 illustrates the schematic of the conventional indirect SFVC based IPM-BLAC drives where superscript '*' and '^' denote reference (red) and estimated (blue) variables, respectively.

Conventionally, the quadrature axis voltage V_τ is generated from either torque or τ-axis current regulations. The voltage commands from the PI controller outputs are confined by the over-modulation (OM) block and the confined voltage commands are denoted by '**'. Once the voltage vectors saturate, the differences between saturated and non-saturated voltage commands are fed back to the PI controllers to avoid integrator wind-up.

As can be seen, the stator flux magnitude reference, Ψ_s^*, for MTPA operation is generated by a predefined LUT with the torque reference as its input, and is further conditioned by (1.13) for field weakening operation. Since the current limit cannot be imposed directly in SFVC drives, the electromagnetic torque demand is confined by (2.5) to limit the current indirectly.

The reference voltages generated in the $f\tau$ frame are transformed into the stationary frame $(\alpha\beta)$ by the inverse Park transformation before being fed to the SVPWM block in which the switching commands are generated for power electronics to drive the motor.

It is noteworthy that the rotor position and the measured DC-link voltage are readily available in the controllers because of the reasons discussed in sections 1.2 and 2.2.

As can be seen from Fig. 4.12 (b), since the torque angle is not controlled directly, the MTPV control can only be achieved by indirect limitation of the torque angle by employing an additional PI controller [59].

The problems associated with the conventional drives are discussed as follows.

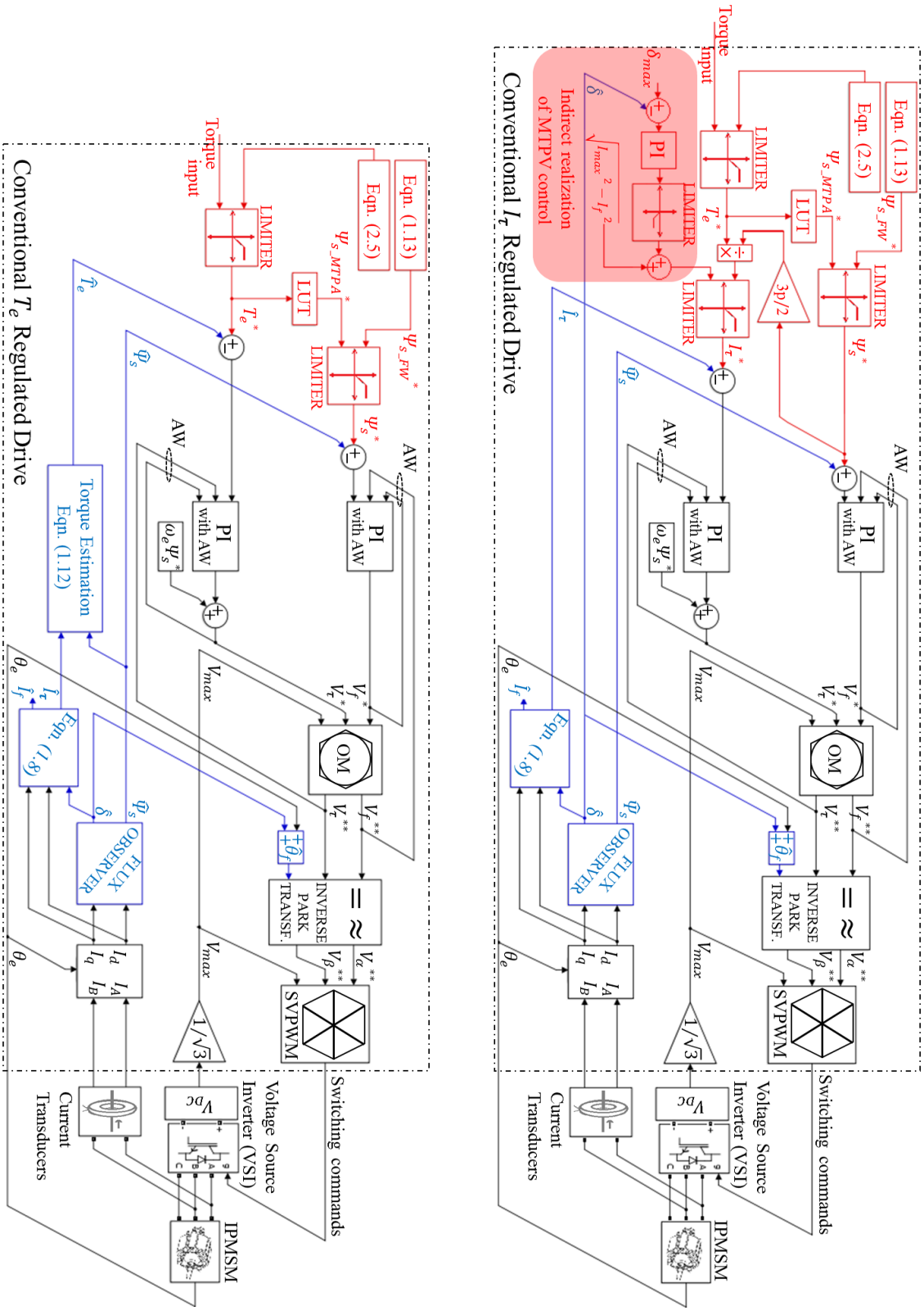

(a) Conventional T_e regulated drive

(b) Conventional I_τ regulated drive

Fig. 4.12 Schematic of the conventional indirect, coupled and nonlinear SFVC drives

4.3.1. ISSUES PERTINENT TO INDIRECT CONTROL OF TORQUE ANGLE

Although the conventional drives are quite common in the literature, (1.10) clearly implies that the stator flux magnitude can be effectively controlled by the *f*- axis voltage and the torque angle can be controlled by the *τ*- axis voltage. This implies that genuine direct torque control can only be obtained by controlling the stator flux vector (Ψ_s, δ) rather than the torque.

The above observation can be further verified by analysing the conventional schemes in which the torque, or the *τ*- axis current is controlled by the *τ*- axis voltage. Dividing (1.11) by (1.12) gives *τ*- axis current.

$$I_\tau = \frac{\Psi_m \sin\delta}{L_d} - \frac{(L_q - L_d)\Psi_s \sin 2\delta}{2L_d L_q} \tag{4.12}$$

From (1.11) and (4.12), both T_e and I_τ are functions of (Ψ_s, δ). Hence their time-derivatives can be expressed as:

$$\frac{dT_e}{dt} = \left(\frac{\partial T_e}{\partial \Psi_s}\right)\frac{d\Psi_s}{dt} + \frac{1}{\Psi_s}\left(\frac{\partial T_e}{\partial \delta}\right)\Psi_s \frac{d\delta}{dt} \tag{4.13}$$

$$\frac{dI_\tau}{dt} = \left(\frac{\partial I_\tau}{\partial \Psi_s}\right)\frac{d\Psi_s}{dt} + \frac{1}{\Psi_s}\left(\frac{\partial I_\tau}{\partial \delta}\right)\Psi_s \frac{d\delta}{dt} \tag{4.14}$$

where $\frac{d\Psi_s}{dt}$ and $\Psi_s \frac{d\delta}{dt}$ are obtained from (1.10) as follows:

$$\frac{d\Psi_s}{dt} = (V_f - R\, I_f) \tag{4.15}$$

$$\Psi_s \frac{d\delta}{dt} = (V_\tau - \omega_e \Psi_s - R\, I_\tau) \tag{4.16}$$

The other partial derivatives can be obtained from (1.11) and (4.12), and they are expressed in (4.17) – (4.20).

$$f_1 = \left(\frac{\partial T_e}{\partial \Psi_s}\right) = \frac{3p}{2}\left[\frac{\Psi_m \sin\delta}{L_d} - \frac{\Psi_s\left(L_q - L_d\right)\sin 2\delta}{L_d L_q}\right] \tag{4.17}$$

$$f_2 = \frac{1}{\Psi_s}\left(\frac{\partial T_e}{\partial \delta}\right) = \frac{3p}{2}\left[\frac{\Psi_m \cos\delta}{L_d} - \frac{\Psi_s\left(L_q - L_d\right)\cos 2\delta}{L_d L_q}\right] \tag{4.18}$$

$$f_3 = \left(\frac{\partial I_\tau}{\partial \Psi_s}\right) = \frac{\left(L_d - L_q\right)\sin 2\delta}{2L_d L_q} \tag{4.19}$$

$$f_4 = \frac{1}{\Psi_s}\left(\frac{\partial I_\tau}{\partial \delta}\right) = \frac{\Psi_m \cos\delta}{\Psi_s L_d} - \frac{\left(L_q - L_d\right)\cos 2\delta}{L_d L_q} \tag{4.20}$$

Neglecting the resistance terms in (4.15) and (4.16) and substituting, (4.15) – (4.20), into (4.13) and (4.14), one obtains the time derivative of the torque and the τ- axis current as given by (4.21) and (4.22), respectively. Similarly, time-derivatives of the torque angle and the stator flux magnitude is written as (4.23) and (4.24), respectively.

$$\frac{dT_e}{dt} = f_1(\Psi_s, \delta)V_f + f_2(\Psi_s, \delta)(V_\tau - \omega\Psi_s) \tag{4.21}$$

$$\frac{dI_\tau}{dt} = f_3(\delta)V_f + f_4(\Psi_s, \delta)(V_\tau - \omega\Psi_s) \tag{4.22}$$

$$\frac{d\delta}{dt} = f_5(\Psi_s)(V_\tau - \omega\Psi_s) \tag{4.23}$$

$$\frac{d\Psi_s}{dt} = V_f \tag{4.24}$$

where $f_1 - f_4$ are defined in (4.17) – (4.20), respectively. $f_5 = {\Psi_s}^{-1}$.

Eqn. (4.24) implies that the stator flux magnitude can be effectively controlled by the *f*- axis voltage vector. This is, indeed, the case in both conventional and the proposed drives. However, the phase of the stator flux vector can be controlled indirectly by (4.21), (4.22) or directly by (4.23).

The conventionally regulated state variables, T_e or I_τ, are dependent on $f_1 - f_4$ and hence on the operating conditions (Ψ_s, δ). Therefore, linear controller design based on a fixed operating point will lead to variable control bandwidth when operating conditions change, and deterioration of performance.

The FW operation in *dq*- axis current controlled drives is realized in a coupled manner as the stator flux magnitude is weakened by regulating both the *d*- and the *q*- axis currents. Likewise, the MTPV operation is also coupled due to the same reason. In SFVC drives, however, the flux is weakened in a decoupled manner by limiting the stator flux magnitude reference directly. In addition, it is evident from (4.5) that MTPV control in direct SFVC drives is also realized in a decoupled manner by limiting the torque angle directly. Realization of the torque control in a decoupled manner in all MTPA, FW and MTPV operating regions render the SFVC drives quite attractive, whilst FOC drives achieves decoupled control only in MTPA region. However, it is evident in (4.21) and (4.22) that the conventionally regulated state variables are influenced by both V_f and V_τ and hence the flux and the torque control loops or the flux and the τ- axis current control loops are strongly coupled in any of the MTPA, FW and MTPV regions. Therefore, the attractive feature of SFVC drives (decoupled control) might be compromised in conventional indirect SFVC drives due to the strong coupling between the control loops.

The nonlinear and the coupling term in (4.23), on the other hand, can be compensated by reference flux in the feed-forward path. Hence, linearization and decoupled control of the stator flux vector can be achieved by controlling Ψ_s and δ based on (4.23) and (4.24).

In addition to nonlinear and coupled control issues, accurate operating trajectory may not be guaranteed if the torque angle is realized indirectly. In theory, the constant stator flux magnitude ellipse and the constant torque loci intersect each other at two points. Each point represents a unique set of *dq*- axis currents. Whilst one pair is on the theoretically accurate operating trajectory, the other pair is off the trajectory where the drive efficiency would reduce much. This issue is further investigated on different IPM motors as follows.

Fig. 4.13 illustrates MTPA trajectories, voltage ellipses, constant torque loci and current limit circles of two IPM machine types in $I_d - I_q$ plane. The prototype machine under study (Table 1.1) is type I as the critical current point, the centre of the ellipses in

(1.7), is outside the current limit circle. The example type II motor ratings have been taken from [59] and the specifications are listed in Table 4.1.

As can be seen, the constant torque loci and the constant stator flux magnitude ellipses intersect each other at points A, A', B, B', whereas, they intersect the MTPA trajectory only at points A and B. The details of the operations at these points are listed in Table 4.2 and Table 4.3 for the type I and type II machines, respectively.

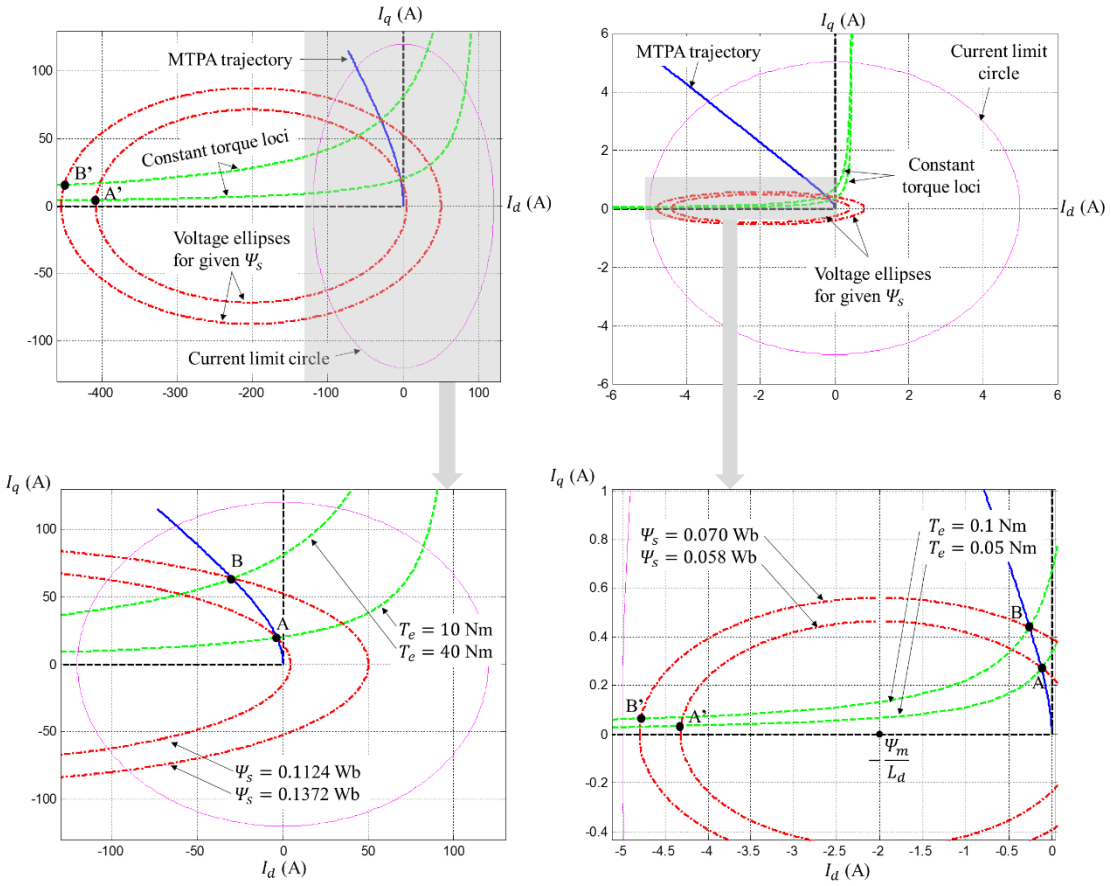

(a) Type I motor – Table 1.1 (b): Type II motor – Table 4.1

Fig. 4.13 Current limit circle, constant stator flux magnitude ellipses, constant torque loci and MTPA trajectories of two types of IPM-BLAC machines in $I_d - I_q$ plane

Table 4.2 The operating points of type I motor given in Fig. 4.13 – (a)

Point	T_e (Nm)	I_τ (A)	Ψ_s (Wb)	δ (*deg*)	I_d (A)	I_q (A)	$< I_{max}$?
A	10	19.77	0.1124	015.9	-003.46	19.57	Yes
A'				176.6	-407.72	04.21	No
B	40	64.79	0.1372	046.7	-029.13	63.54	Yes
B'				169.7	-449.55	15.56	No

Table 4.3 The operating points of type II motor given in Fig. 4.13 – (b)

Point	T_e (Nm)	I_τ (A)	Ψ_s (Wb)	δ (deg)	I_d (A)	I_q (A)	$< I_{max}$?
A	0.05	0.29	0.058	035.7	-0.12	0.27	Yes
A’				175.7	-4.31	0.04	Yes
B	0.1	4.76	0.070	051.6	-0.26	0.44	Yes
B’				173.5	-4.78	0.06	Yes

It is evident in the figures and the tables that for a certain torque and stator flux magnitude, there are two pairs of *dq*- axis currents in theory. One can obtain the τ- axis currents from (1.12). As will be seen, the τ- axis currents at points A and A’ are the same. Likewise, they are the same at points B and B’. Whilst the *dq*- axis currents at points A’ and B’ are at the outside the current limit circle for type I machines, they are still inside the current limit circle for type II machines. Therefore, in conventional drives with type II machines, for certain set-points of (T_e, Ψ_s) or (I_τ, Ψ_s), there are two pairs of *dq*- axis currents inside the current constraint and the drive system is not commanded to operate on the accurate pair.

It is important to note that Fig. 4.13, Table 4.2 and Table 4.3 represent the MTPA operation. As seen in the figure, the voltage ellipse shrinks when the stator flux magnitude reduces. Accordingly, the voltage ellipse for a given torque will be shrunk in a FW region. Hence, the issue is still there in a FW region, too. Thus, the problem arises at a large operating speed and torque envelope for type II machines. On the other hand, as seen in Table 4.2 and Table 4.3, there is a unique torque angle at any operating point on a voltage ellipse. Therefore, operations at A or B are guaranteed with the proposed direct SFVC.

When the voltage ellipses in Fig. 4.13 are replaced by voltage circles in order to represent the SPM-BLAC machines, one can deduce that there will be still two pairs of *dq*- axis currents for certain torque and stator flux magnitude commands.

It follows that, theoretically, decoupled or direct torque in BLAC machine drives is difficult to realise and the conventional DTC schemes are indeed indirect SFVC. Accordingly, direct SFVC control of BLAC machines is proposed and discussed in the next section as follows.

4.4. PROPOSED DIRECT, DECOUPLED AND LINEARIZED SFVC

To circumvent the problems associated with the conventional indirect SFVC drives, the magnitude and the phase of the stator flux vector (Ψ_s, δ) are controlled directly. Fig. 4.14 illustrates the schematic of the proposed direct SFVC based IPM-BLAC drive.

The notations, reference flux generation, torque limitation, coordinate transformations, AW and OM phenomena have been discussed in section 4.3 and hence will not be repeated.

As has been discussed, the electromagnetic torque is a function of the stator flux vector, *i.e.*, T_e (Ψ_s, δ). Thus, the torque angle is a function of the torque and the stator flux magnitude, *i.e.*, δ (Ψ_s, T_e). However, online generation of the reference torque angle is a great challenge for IPM machine drives due to the implicit equation given by (1.11). Hence, the torque angle for a given torque and stator flux magnitude can be computed offline and stored in a table. In the proposed drive, thereby, the reference torque angle is obtained from a second LUT with the reference torque and stator flux magnitude as inputs. The reference flux magnitude and the reference torque angle, then, are tracked by two independent PI control loops which can be tuned based on desired bandwidth.

As can be seen from the schematic of the proposed drive, the torque observer is not needed as the stator flux vector is directly controlled. The stator flux vector can be observed by employing the observer structures proposed in Chapter 2 or the one in Chapter 3. Indeed, simulations and experiments have been carried out employing various observer structures discussed previously including the voltage based and the current model based estimators as well as the conventional Gopinath style closed-loop flux observers [60]. It has been validated that they are all applicable to the proposed drive. However, the drive will, of course, suffer from the limitations of the observer structure. These observer limitations have already been discussed extensively in previous chapters. Since the observer structure proposed in Chapter 3 is more accurate throughout wide operating range and it is superior to others, this state-of-art observer is employed in the proposed drive. The schematic of the observer is illustrated in Fig. 3.4 and its details will not be repeated in this chapter.

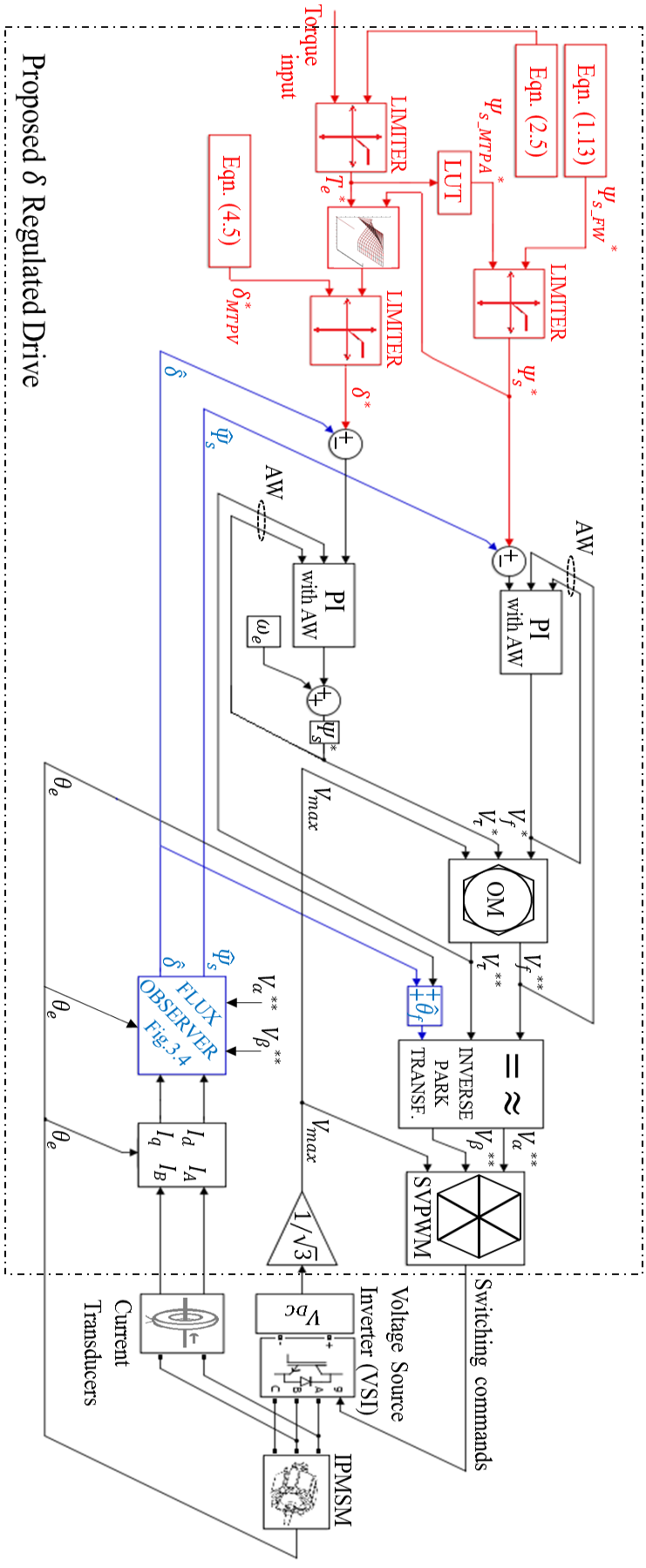

Fig. 4.14 Schematic of the proposed direct, decoupled and linearized SFVC drives

4.4.2. REFERENCE TORQUE ANGLE GENERATION

One can obtain the torque angle from (1.11) for SPM machines as follows;

$$\delta = \sin^{-1}\left(\frac{2LT_e}{3p\Psi_s\Psi_m}\right) \tag{4.25}$$

This implies that the torque angle can be generated online for SPM machines. As for IPM machines, however, it is a challenge to generate it online due to the implicit equation (1.11). Thus, the torque angle is calculated beforehand as a function of torque and stator flux magnitude and stored in the controller as a two dimensional look-up table. It is noteworthy that if a drive system requires only MTPA operation, then the torque angle is modelled simply as a function of torque and hence it is stored in one dimensional table. However, the FW operation is required for traction applications and hence the torque angle is predefined in two dimensions.

Based on (1.11), the machine parameters; *dq*- axis inductances and the permanent magnet flux linkage need to be employed to compute the torque angle offline. To account for parameter variations with currents due to magnetic saturation, the *dq*- axis inductances and the magnetic flux linkage employed in the table generation are modelled as functions of *dq*- axis currents as shown in Fig. 2.8. Then, the Newton-Raphson method described in [36] may be utilized for ease of computing. The *dq*- axis flux linkages are approximated in this technique with a few iterations and the torque angle can be computed offline via (4.8). However, it has been discovered that the MTPA points based on approximation with this technique in [36, 49, 95] are not correct even though the parameters employed in the technique are accurate. This issue will be discussed in great details in the next chapter. Although the Newton-Raphson iteration method provides ease of computing for torque angle, an alternative technique is suggested for more accurate torque angle calculation.

The alternative approach can be described as follows. Simulations are carried out by employing a nonlinear machine model. By doing so, the parameter variations are taken into account. The nonlinear parameter based machine model (shown in the appendix – Fig. A.20) or nonlinear *dq*- axis flux linkage based high fidelity machine model (shown in the appendix – Fig. A.21) can be employed in the simulations. As has been discussed in the previous chapter, the high fidelity machine model is more accurate than the other.

The machine is controlled by a DTC technique in which the torque and the stator flux magnitude errors are regulated. By way of example, Fig. 2.2 illustrates a DTC scheme which can be employed. The drive is simulated for given torque and stator flux magnitude commands and the corresponding torque angle at the steady-state are saved as shown in Table 4.4. This step is repeated for other torque and stator flux magnitude commands and the torque angle map is obtained. m and n in Table 4.4 are the number of simulation points for torque and stator flux magnitude, respectively. It is important to note that the observer and the inverter should be ideal in the simulations. This implies that the actual flux and the torque of the simulated motor are employed in the feedback and the command voltages are directly applied to the motor without power electronics. Otherwise, observer inaccuracy will result in inaccurate torque angle for given commands. The accuracy of the generated torque angle is directly dependent on how accurately the nonlinear machine model represents the real-world motor. The good accuracy of the high fidelity machine model has already been verified in the previous chapter and in [79]. It is noteworthy that the drive speed may be kept constant at the rated value during simulations. The resultant torque angle will be accurate for the particular torque and the stator flux magnitude.

Table 4.4 Torque angle map as a function of torque and stator flux magnitude

	T_e^1	T_e^2	…	T_e^m
Ψ_s^1	δ^{11}	δ^{21}	…	δ^{m1}
Ψ_s^2	δ^{12}	δ^{22}	…	δ^{m2}
…	…	…	…	…
Ψ_s^n	δ^{1n}	δ^{2n}	…	δ^{mn}

Fig. 4.15 illustrates the torque angle as a function of torque and stator flux magnitude for the prototype motor whose specifications have been listed in Table 1.1. It is seen from Fig. 4.2 that the torque angle is negative when torque is negative. Therefore, for negative torque references, the reference torque angle will also be negative as shown in Fig. 4.15. It should be noted that the inaccuracies in the torque angle will cause torque error at steady-states. This is indeed not a serious problem for EV traction applications as accurate torque control is not necessary. More importantly, motor efficiency can be optimized even though the reference torque angle is not accurate. It is evident that high efficiency is achieved by optimal stator flux magnitude for a given torque in SFVC drives [12, 55, 70]. Therefore, the high efficiency can be achieved by online optimization of the stator flux magnitude such as described in [12, 55].

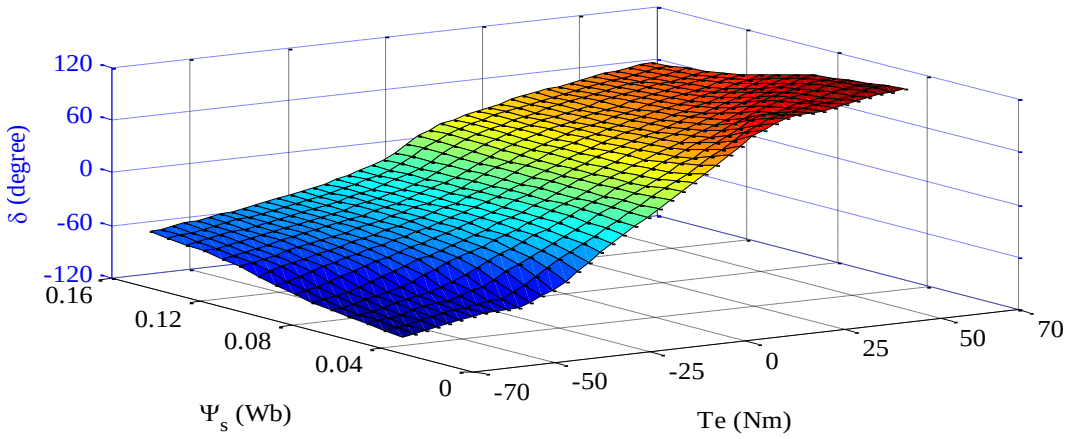

Fig. 4.15 Torque angle as a function of stator flux magnitude and electromagnetic torque

4.4.3. CONTROLLER GAIN TUNING

The simplified transfer function block diagrams of the direct SFVC based on (4.23) and (4.24) are shown in Fig. 4.16 (a) and (b). Inverter and observer dynamics can be assumed ideal for control tuning as reported in [59]. f_5 in (4.23) is compensated in the feed-forward path, and as a result, the torque angle control loop is linearized. It is noteworthy that the reference flux, Ψ_s^*, and the actual flux, Ψ_s, in Fig. 4.16-(b) are not the same and the compensation will not be perfect. However, the imperfect compensation will be minimised by the feedback loop.

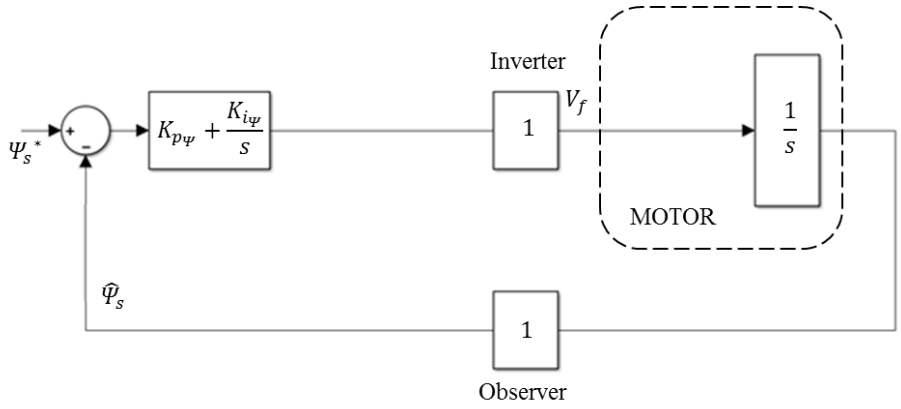

(a) Ψ_s loop

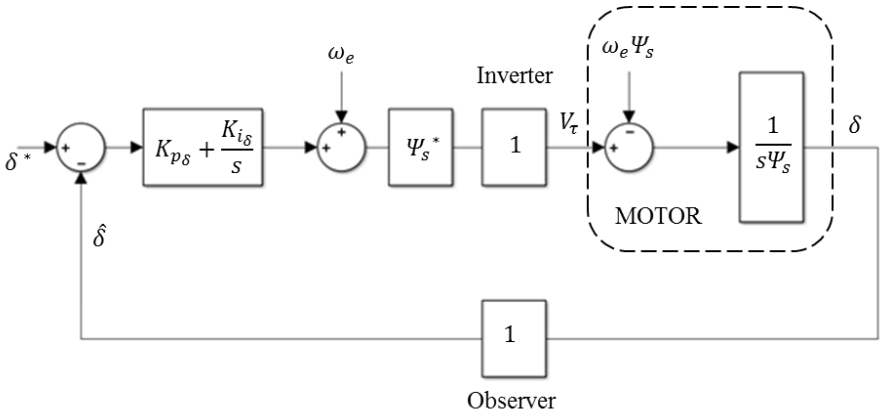

(b) δ loop with the proposed linearization

Fig. 4.16 Simplified scheme representing the dynamics of the $\Psi_s - \delta$ regulators

The tuning of the controllers for a desired bandwidth can be obtained from the closed loop transfer functions (CLTF) of Fig. 4.16 (a) and (b) as follows:

$$CLTF = \frac{(sK_p + K_i)}{(s^2 + sK_p + K_i)} \tag{4.26}$$

where K_p and K_i are the proportional and integral gains of the flux and delta control loops. The controllers then are tuned from the characteristic equation of the standard second order system as follows:

$$s^2 + sK_p + K_i = s^2 + s2\xi\omega_n + {\omega_n}^2 \tag{4.27}$$

where ξ is the damping ratio and ω_n is the natural frequency selected by a designer. Hence, the proposed decoupled control is achieved with a simple control tuning.

4.5. VALIDATION OF PROPOSED DRIVE AND COMPARATIVE STUDIES

The theoretical analysis of the conventional and the proposed drives have been performed in details in the previous sections. In this section, comparative studies with simulation and experimental results of the conventional and the proposed drives will be presented to validate the superiority and efficacy of the proposed drive. Conventional torque regulated drive, τ- axis current regulated drive and the proposed torque angle regulated drives are implemented as shown in Fig. 4.12-(a), Fig. 4.12-(b) and Fig. 4.14, respectively.

4.5.4. SIMULATION STUDIES

How coupled control problems associated with the conventional drives may deteriorate the drive performance is studied through simulations. The inverter and the motor based harmonics are deliberately not represented in the simulations in order to separate them from those due to coupled control. The reference voltages generated from the controller are directly fed to the motor model whose ratings are listed in Table 1.1. It is important to note that fundamental sampling time, flux observer, controller tuning, motor models and machine parameters are identical in each drive and the only difference between the simulated drives is the regulated state variable. Hence, the differences between the results are only caused by the indirect regulation of the torque angle. The proportional and integral gains of the controllers are tuned based on (4.27) in which the damping ratio and the natural frequency are 0.707 and 100 Hz, respectively.

A step torque demand from 20 to 30 Nm is applied to the simulated drives at t=0.25 second when the motor operates at 1000 r/min. The results with the conventional torque regulated, τ- axis current regulated and the proposed torque angle regulated drives are presented in Fig. 4.17 – Fig. 4.19, respectively. Torque, stator flux magnitude, torque angle δ, phase currents and the $f\tau$- axis motor voltages are shown in the figures. Clearly, indirect control in the conventional drives may cause two significant problems which are explained as follows.

First, as can be seen, for the same nominal control bandwidth (gains), the conventional drives exhibit high frequency ripples on the current waveforms and on the resultant torque although the inverter is ideal and PWM operation is not represented in the simulations. It is likely that due to the strong coupling and the influence of the V_f voltage in (4.21) and (4.22), the conventional drives are much vulnerable to instability in the form of limited circle oscillation when the controller gain is high. However, it is evident in (4.23) that the proposed drive is decoupled and the results are exempt from such oscillation associated with the coupling between the control loops.

Secondly, the stator flux magnitude error is not driven to zero in steady states in the conventional drives. As will be seen from Fig. 4.17 and Fig. 4.18, the resultant flux magnitude to a step demand initially reduces and then increases. This is also caused by the strong coupling as V_f voltage not only regulates the stator flux magnitude but also influences the torque. Although the flux controller gain tuning of each drive are the same,

the problem does not exist in the proposed drive as V_f voltage is only dedicated to regulate the stator flux magnitude.

It is evident that the accurate MTPA operation can be achieved by optimal stator flux magnitude for a given torque [12]. Thus, when there is a stator flux magnitude error in steady-states, the drive deviates from the accurate trajectory and hence efficiency reduces.

As a result, the conventional drives may suffer from increased harmonics and reduced efficiency due to strong coupling between the control loops.

It is noteworthy that low control gains, on the other hand, leads to slow response and poor performance in conventional drives. This will be verified experimentally in next section.

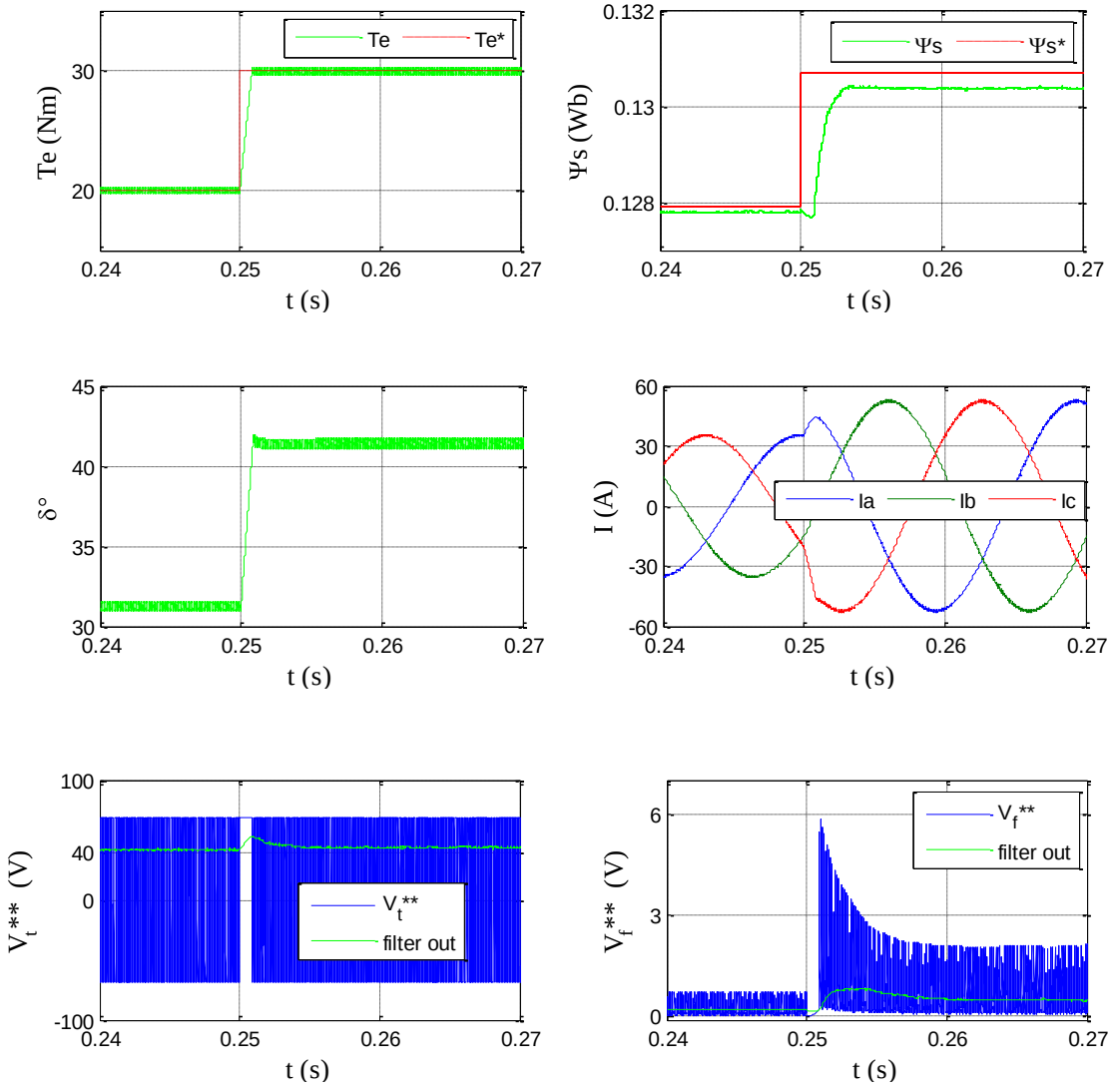

Fig. 4.17 Simulation results of conventional indirect SFVC; (Ψ_s, T_e) regulation

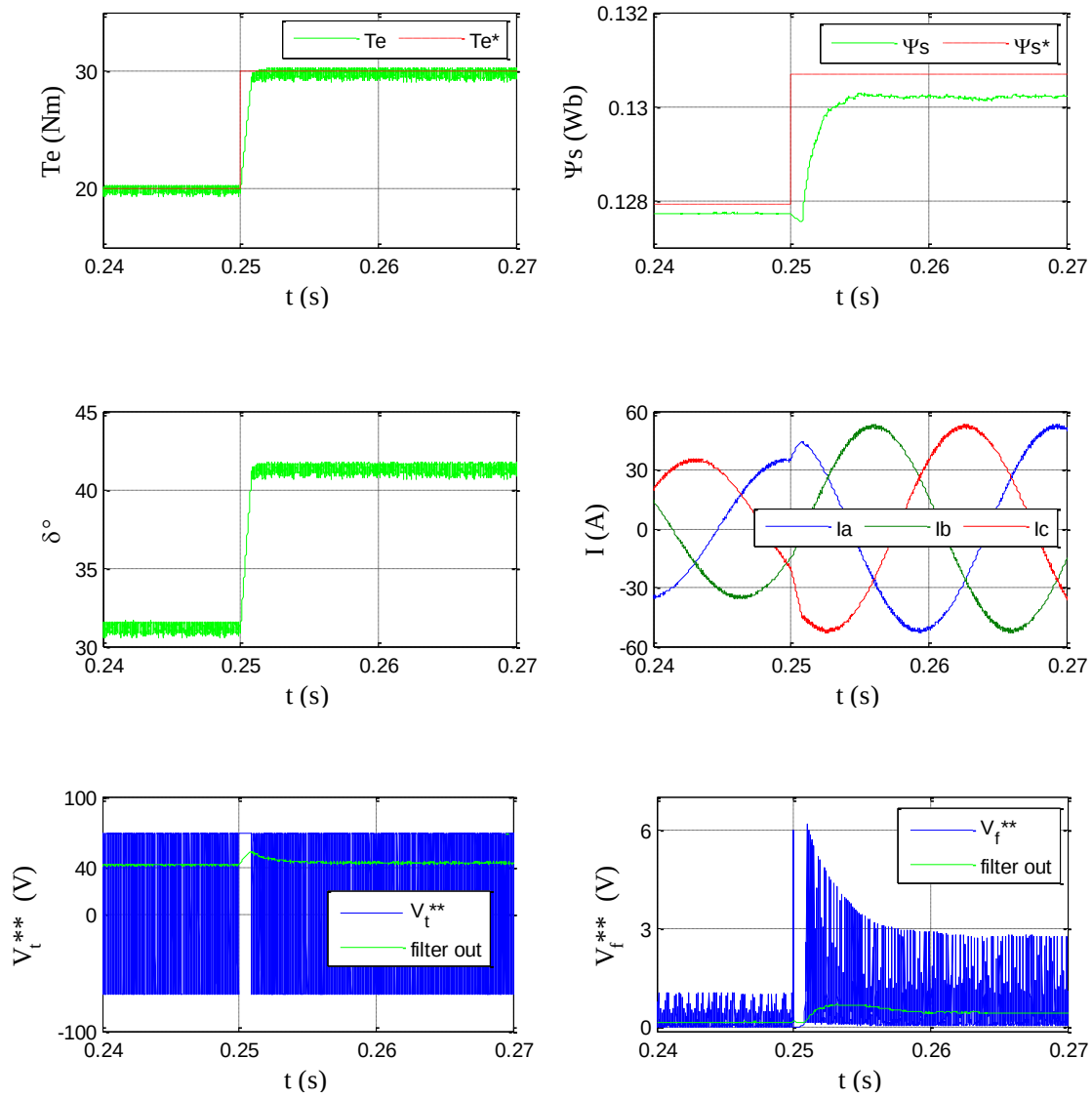

Fig. 4.18 Simulation results of conventional indirect SFVC; (Ψ_s, I_τ) regulation

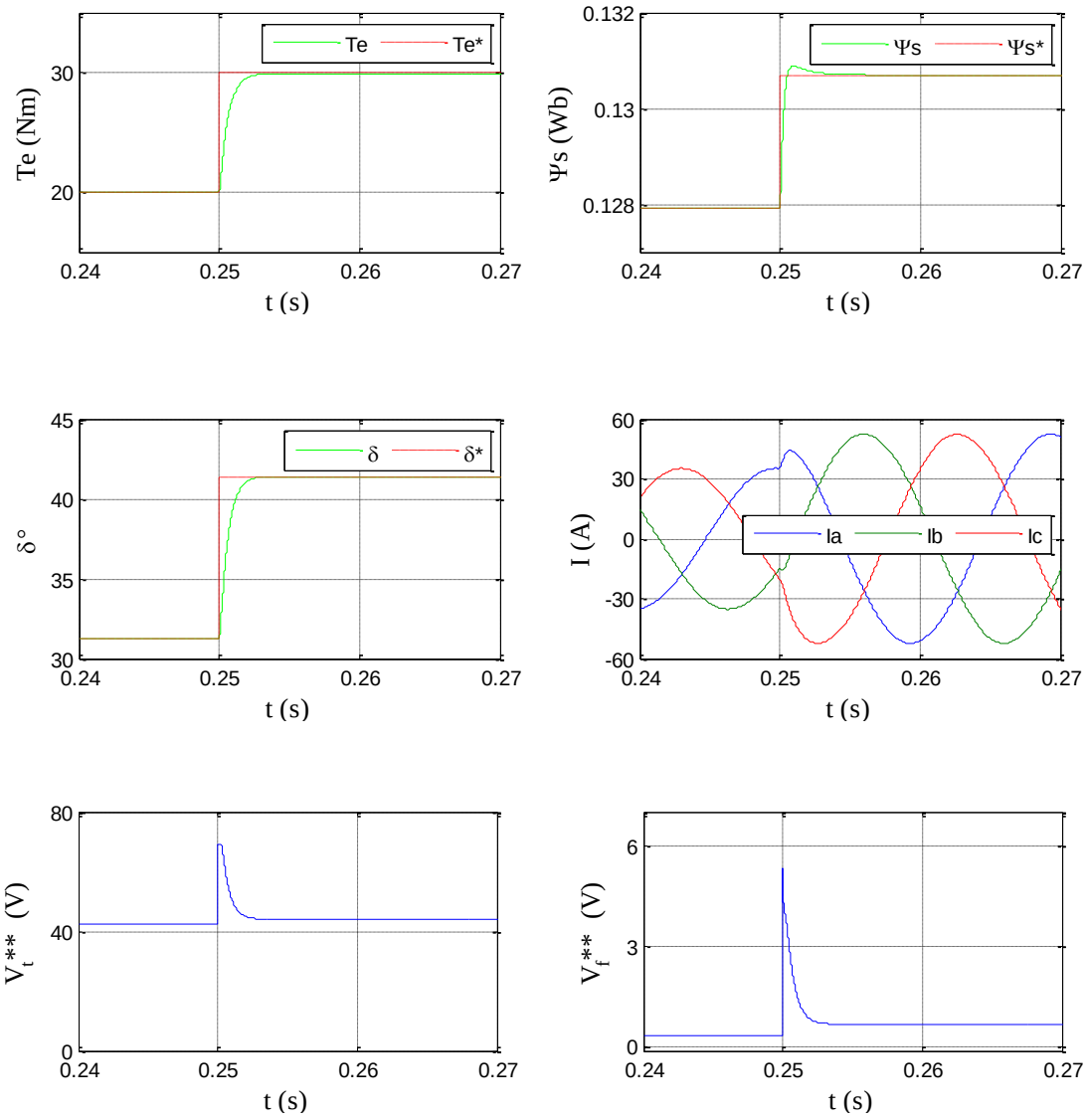

Fig. 4.19 Simulation results of proposed direct SFVC; (Ψ_s, δ) regulation

4.5.5. EXPERIMENTAL RESULTS

Experiments have been carried out on the test rig shown in Fig. 1.3 to verify the high performance of the proposed drive in constant torque and constant power operating regions. For the purpose of comparisons, conventional indirect SFVC drives are also implemented and tested.

Fig. 4.20 compares the torque responses to step changes in torque demand, which result with the conventional and the proposed control schemes when the speed is 1000 r/min. As will be seen, not only better dynamic torque response is achieved but steady state performance of the proposed drive also improves due to the realization of the torque in a decoupled manner.

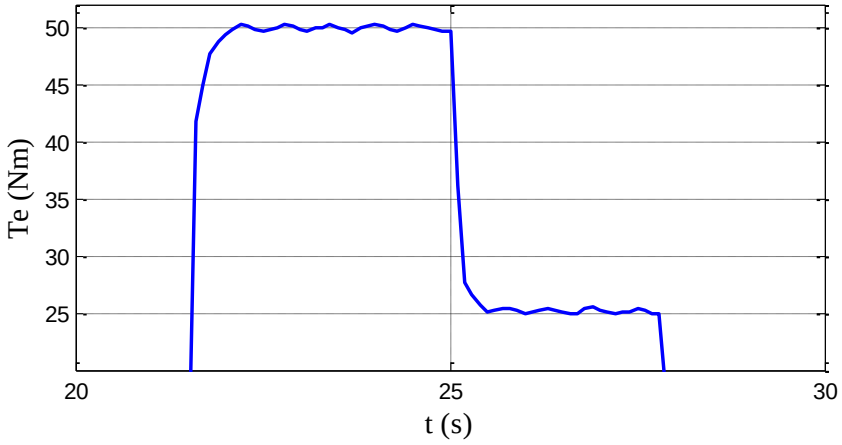

(a) Conventional indirect SFVC: (Ψ_s, T_e) regulation

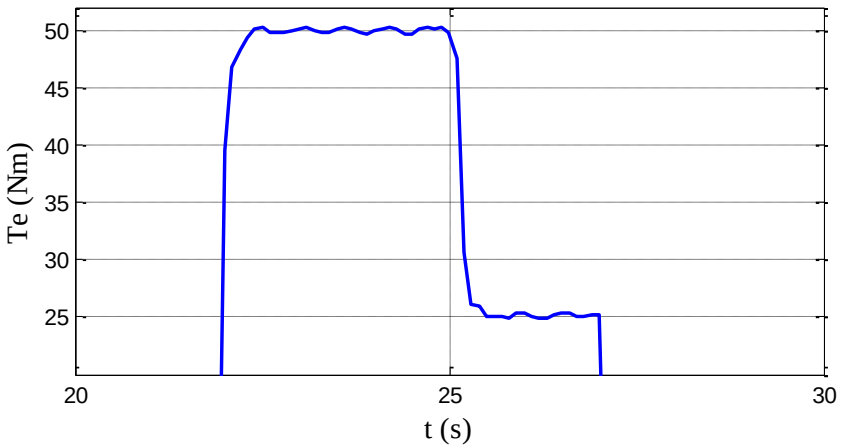

(b) Conventional indirect SFVC: (Ψ_s, I_τ) regulation

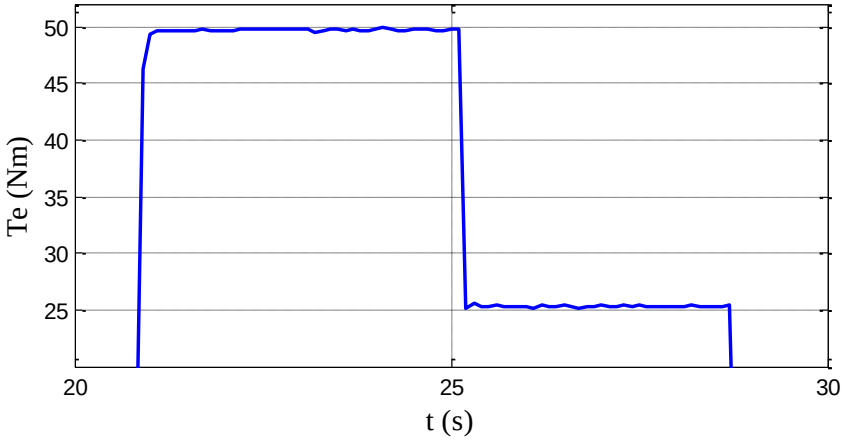

(c) Proposed direct SFVC: (Ψ_s, δ) regulation

Fig. 4.20 Torque response comparisons at 1000 r/min

Fig. 4.21 illustrates the torque and the torque angle responses of the proposed drive in response to step changes in torque demand when the drive operates in MTPA region at 1000 r/min. Similar responses are shown in Fig. 4.22 when the drive operates in the constant power operating region at 2700 r/min, twice the base speed. In both cases, the drive exhibits fast dynamic torque response with good steady-state torque control performance. It is seen in Fig. 4.21 that there are small steady-state torque errors at certain operating points since the torque is not the directly regulated state variable. This is indeed caused by the inaccuracies in the reference torque angle for a given torque as well as by the observer errors. It is also evident from Fig. 4.21 and Fig. 4.22 that the torque angle regulation is quite good in both MTPA and FW operations. It is noteworthy that whilst the reference torque angle is exempt from harmonics in MTPA region, high frequency ripple appears on the reference torque angle in the FW region. This is because the reference torque angle generator is influenced by the current harmonics in FW region where the harmonics are injected to the LUT shown in Fig. 4.15 via (1.13) which adopts the field weakening. The phase currents contain more significant high frequency ripple due to high order space and tooth ripple harmonics in the FW region. These harmonics can be effectively supressed in the MTPA region when the voltage saturation is not reached but nevertheless the reference torque angle is not influenced by the current harmonics in the MTPA region since (1.13) is only effective in FW region.

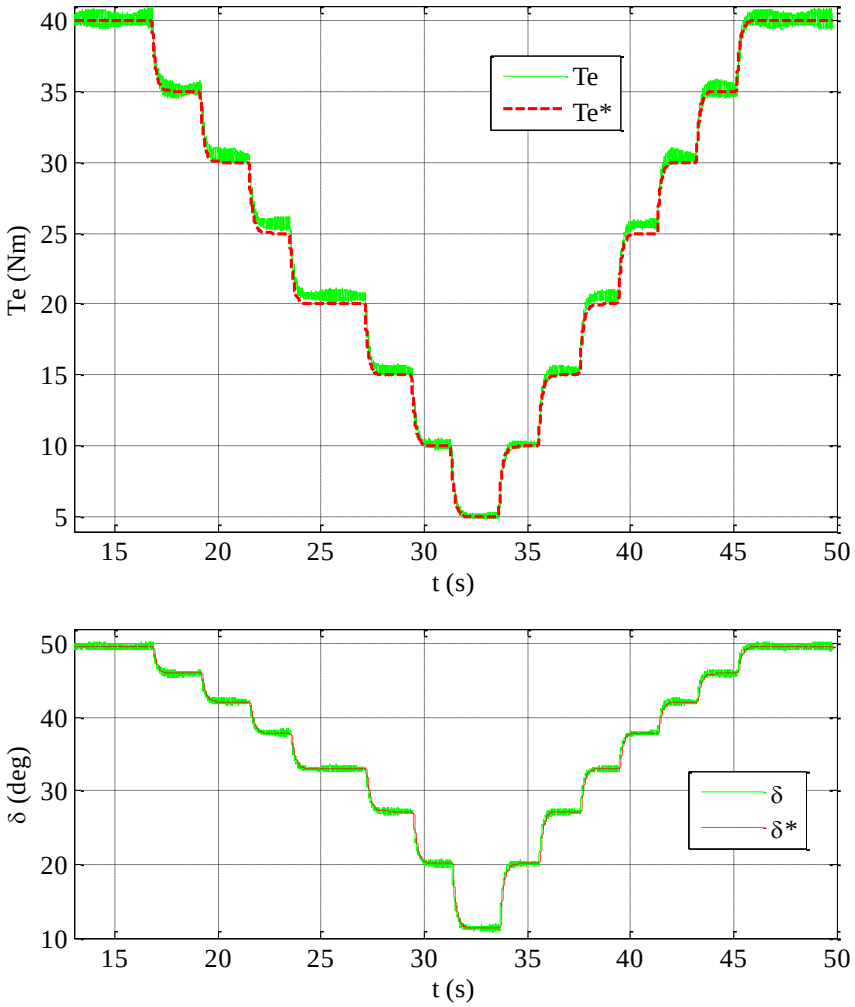

Fig. 4.21 Torque and torque angle responses at 1000 r/min in MTPA operation

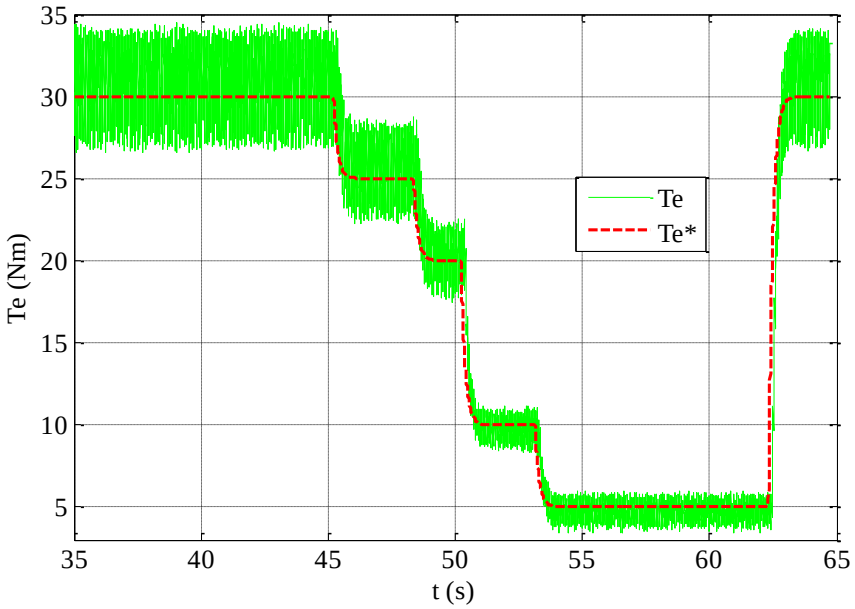

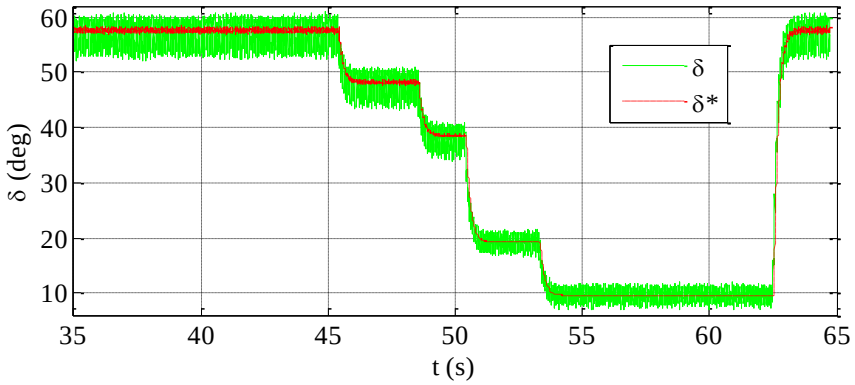

Fig. 4.22 Torque and torque angle responses at 2700 r/min in FW operation

Precise control of the transition from MTPA to FW regions and vice versa is a challenge for IPM-BLAC drives. Performance of the transitions between the two regions are tested with the proposed direct SFVC drive. Fig. 4.23 validates the smooth transitions from MTPA to FW region and vice versa when the speed varies between 1000 and 2700 r/min. The flux is automatically weakened in a decoupled manner directly via (1.13). As has been discussed, the harmonics increases significantly in the FW operation.

4.6. SUMMARY

In this chapter, the relationship between the torque and the stator flux vector has been analysed in great details representing all BLAC machines and considering practical nonlinearities such as machine parameter variations.

Besides, theoretical analysis of the MTPV control in the SFVC drives has been made thoroughly. It has been introduced in this chapter that the MTPV control is realized by online limitation of the torque angle as a function of the stator flux magnitude.

Moreover, the significant problems associated with the indirect SFVC drives have been studied widely. It has been shown that the nonlinearity in the control loop caused by the indirect regulation of the torque angle not only results in bandwidth variation with operating points, but introduces strong coupling between the control loops. Consequently, indirect regulation deteriorates the drive performance both in transient states and in steady states. The coupling between the control loops does exist not only in MTPA region but also in FW and MTPV regions. It has been shown that the consequences of the strong coupling may be remarkably distorted current waveform and reduced drive efficiency. It has also been shown that the MTPV control implementation is a challenge if the torque angle is controlled indirectly.

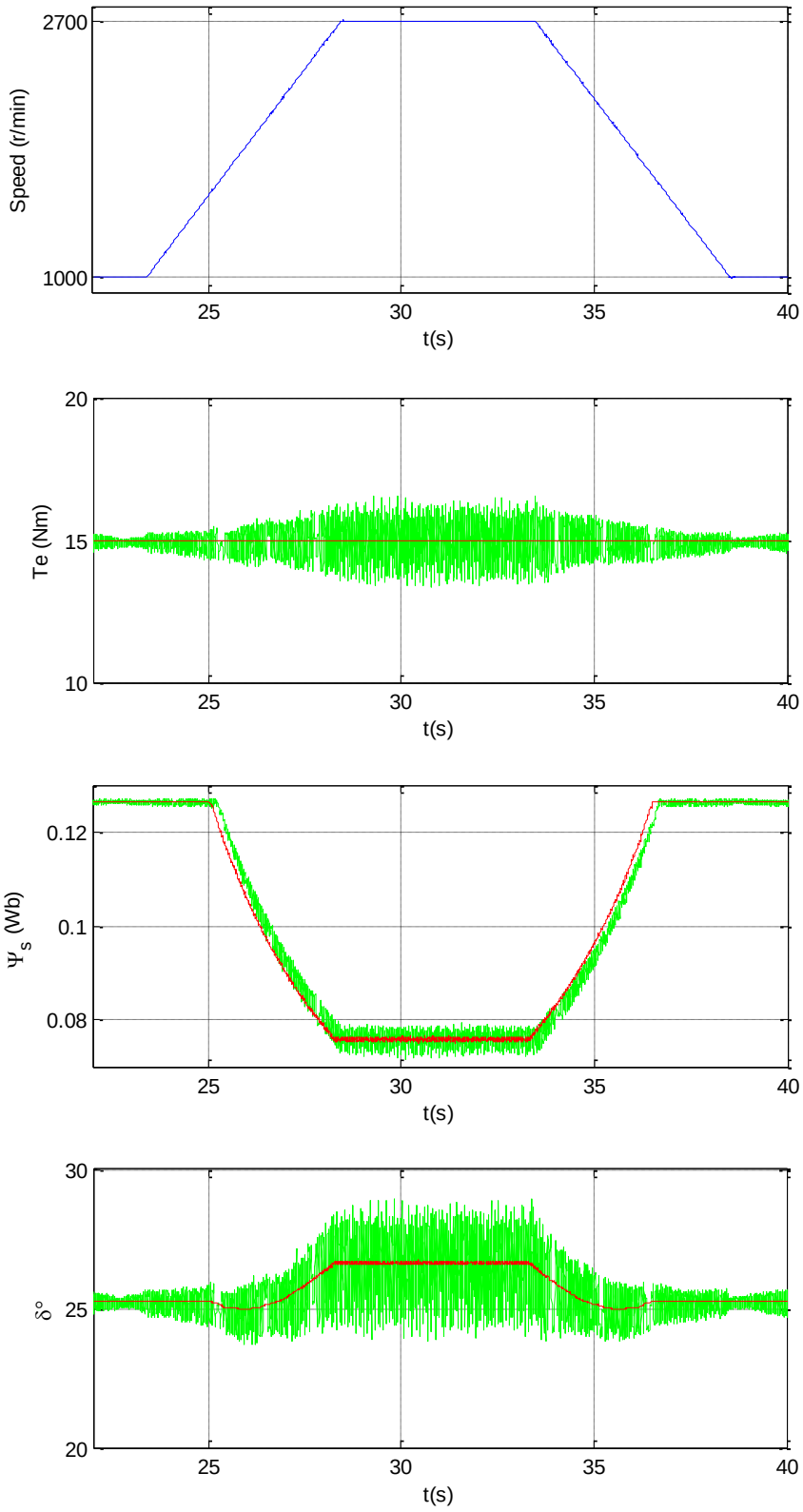

Fig. 4.23 Validation of smooth transitions from MTPA to FW regions and vice-versa

It follows that the direct control of the stator flux vector becomes prominent and the theoretical analysis of the machine behaviour reveals that it is difficult to achieve direct torque control in BLAC machine drives with the conventional schemes. It has been shown that direct SFVC achieves decoupled control in any of the MTPA, FW and MTPV regions. Also, adoptions of the FW and MTPV control techniques are much simple and straightforward compared to the FOC drives where FW and MTPV is achieved in a coupled manner [37]. Therefore, the theoretical analysis suggests that, from the motor's point of view, what needs to be controlled is the stator flux vector rather than the currents as in FOC drives or the torque as in DTC drives.

The proposed direct SFVC control technique has been implemented and its performance has been validated. It has been shown that the proposed drive improves the torque response in transient and steady states and facilitates simple control tuning with desired bandwidth. Simply adopted linearization techniques avoid bandwidth variation with the operating points. Employing nonlinear machine model to generate the reference torque angle alleviates the problems associated with the parameter variations. MTPV control can be achieved simply by direct and online limitation of the torque angle in the proposed drive.

CHAPTER 5 – ONLINE EFFICIENCY OPTIMIZATION FOR FOC-IPM DRIVES BASED ON VIRTUAL SIGNAL INJECTION

5.1. INTRODUCTION AND LITERATURE REVIEW

The field oriented control (FOC) has been researched extensively in the literature. The implementation of the FOC drives is more universal comparing to the direct torque controlled drives since their application has started much earlier than the DTC based drives.

Because one of the significant challenges associated with the IPM motors is to achieve high efficiency operation, there are a large number of studies have been reported in the literature to improve the efficiency in these drives.

It is well-known that the iron loss in the constant torque region has negligible influence on the optimum operating point [18]. Hence, MTPA operation ensures high efficiency by minimizing the copper losses for a given torque demand. The MTPA in the constant torque region is defined as the operation at the optimum current angle at any operating conditions. Thus, the challenge is to obtain the optimum current angle online, *i.e.* β in Fig. 5. 1

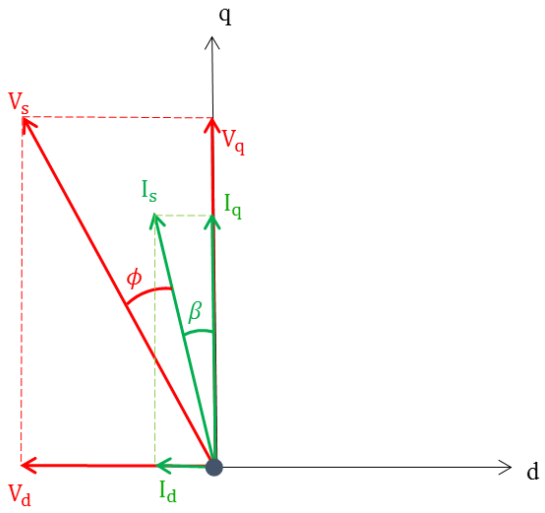

Fig. 5. 1 Current and voltage vectors in *dq*- plane

The optimum current angle has been obtained from nominal machine parameters in early applications of IPM drives [34, 37, 45, 107-111]. However, highly nonlinear characteristics of the real-world IPM machines in particular *q*- axis inductance results in reduced efficiency as the current angle deviates from the optimal. The machine parameters of a real-world IPM machine vary depending on a number of factors such as

the current and hence the load, temperature, material properties, manufacturing tolerances and so on. Accordingly, the operation based on nominal parameters is very poor.

To alleviate the problems raised by the nonlinear machine characteristics, the parameters can be modelled as functions of phase currents. Look-up tables (LUTs) are therefore employed in [36, 49, 50, 52, 53, 57, 58, 95, 112-114] to adopt the MTPA control. These drives are certainly improved comparing to the drives which employ nominal machine parameters. However, it will be shown that the accurate MTPA operation in these drives cannot be achieved even though the machine parameters are perfectly modelled and stored in the LUTs. The deviation from the optimal increases with the load. It will be shown that the deviation is significant and hence not negligible. This problem, indeed, is the main concern of this chapter and it will be clarified in great detail.

In [115-119], the MTPA points are detected by employing search algorithms without the need to know the machine parameters. Under the constant torque condition, the minimum current magnitude is searched by altering the current vector and hence the optimum current angle is obtained. However, the search algorithm based MTPA operations have several problems. Poor dynamic performance due to the slow convergence rate and the reduced accuracy under the disturbances as well as current harmonics are the problems that can only be tolerated to some extent [18, 118]. Moreover, the stability of the search algorithms cannot be guaranteed under rapid variations of load torque conditions [120]. Therefore, the search algorithm based drives and their performance are limited by speed and torque variations as well as other conditions [121].

In recent years, signal injection based MTPA operation has been researched widely. These can be classified as real signal injection based drives [120, 122-127] and virtual signal injection based drives [11, 12, 16-18]. Whilst the former injects the real signal into machine phase currents/voltages to seek the optimum current angle online, the latter does not. Instead, the signal is mathematically injected into the current angle β and the *d*- axis reference current is obtained in the controller without injecting a real signal into the machine.

The common problems pertinent to the injection of a real signal into the machine are deteriorated control performance due to the additional speed and torque ripples and the increased copper and iron losses due to the injected current/voltage into the machine phases. The variable torque component associated with the injected signal is obtained from the measured torque in [122]. Since the torque measurement is not preferred in industrial applications, the drives in [124-126] obtain the variable component from the

measured speed. However, the performance of these drives are limited by the resolution of the speed sensor since the small variation with the small signal requires high resolution to be realized [124]. It is evident in [120] that the frequency and the amplitude of the injected signal needs to be carefully selected in real signal injection based drives due to the resonant problems and the presence of voltage/current harmonics.

Virtual signal injection, on the other hand, obtains the extremum point mathematically without injecting any real signal into the motor. Therefore, additional power losses, increased current/voltage harmonics and the resonant problems associated with the real signal injection are inherently avoided. The resolution of the speed sensor does not limit the performance and the torque measurement is not required. All these advantages render virtual signal injection based MTPA control more attractive than their real signal injection based counterparts. However, this technique has been adopted to only one motor to date [11, 12, 16-18]. It has been discovered that the conventional approach relies on machine characteristics and it may not be suitable for other IPM machines which will be validated in this chapter. In addition, virtual signal injection control adopted in FOC [17, 18] and DTC [12] drives suffer from considerably slow converging time *i.e.* several seconds to reach the extremum. Self-learning control schemes have been reported in [11, 16] in order to improve the response time. However, online training of the self-learning control not only increases the complexity but is a burden on the microprocessor.

In this chapter, a new virtual signal injection based extremum seeking control is proposed. The response time in the novel approach is significantly improved by optimization of the signal processing unit and hence the adoption of the self-learning control schemes are not necessarily needed. More importantly, the proposed scheme is universal and can be adopted to any machine whilst the virtual signal injection based control schemes reported to date may not be suitable for other IPM machines. The variation of the magnetic flux linkage is addressed online whereas the *dq*- axis inductances are modelled as functions of *dq*- axis currents and stored in look-up tables. It will be shown that the influence of *q*- axis inductance variation on MTPA operation is partially accounted. Since the *d*- axis inductance is modelled as a function of *dq*- axis currents and it has less influence on the drive performance comparing to the other parameter variations, the proposed drive is remarkably robust to the parameter variations. Although the implementation of the conventional virtual signal injection based drives do not employ machine parameters, it will be shown that they are still parameter dependent due to the omitted error terms and much sensitive to parameter variations. These errors

are analysed and compensated in the proposed drive and hence the sensitivity to parameter variations is lessened. It will be supported by realistic simulation studies that the accuracy of the resultant operating point is much improved with the proposed approach. It is noteworthy that the experimental validation of the proposed drive lacks in this chapter.

The main content of this chapter is under preparation by the author for publication in [J8] detailed in List of Publications.

5.2. EFFICIENCY VERSUS CURRENT ANGLE

It is well-known that the influence of the iron loss in the constant torque region is negligible and the maximum efficiency is obtained around the MTPA point by minimizing the copper losses [33]. The influence of the iron loss on the prototype machine in Table 1.1 is shown in Fig. 5.2 when the speed, current magnitude and the electromagnetic torque are 1350 r/min, 100 A and 60 Nm, respectively. The iron-loss model presented in [79, 128, 129] is employed in the simulations as it is simple and more accurate. The drive has been simulated twice employing and ignoring the iron loss model whose details are given in the appendix. Clearly, the iron loss reduces the active power. However, as can be seen from the figure, the influence of the iron loss on the motor efficiency is nearly 0.02 %. This is because in constant torque region where speed is relatively low, the copper loss is dominant. The optimum current angles when the iron loss is considered and ignored are also much close to each other and, hence, the deviation is negligible. Therefore, it is evident that the iron loss has negligible influence on both the efficiency and the optimum current angle. This implies that the efficiency can be optimized by minimising the copper losses in the constant torque region, *i.e.* MTPA.

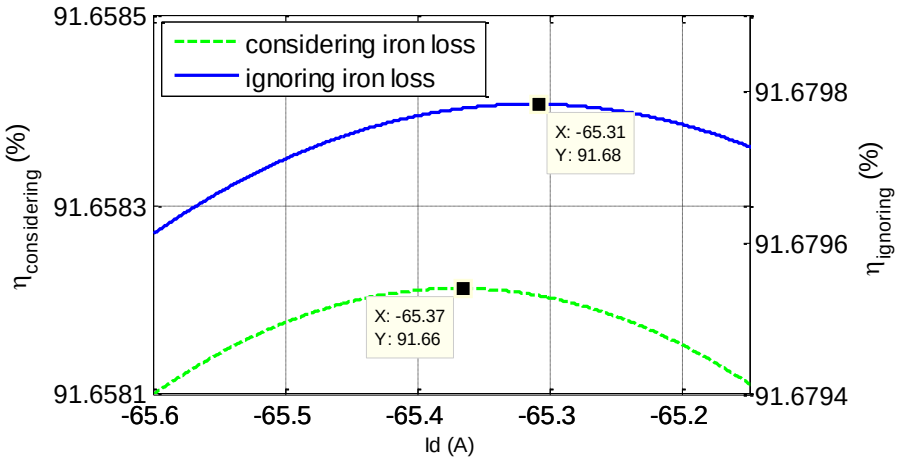

Fig. 5.2 Iron loss effect in constant torque region

Theoretically, the relationship between the input power, output power, electromagnetic torque and the optimum current angle can be expressed as follows. Ignoring the iron loss, the governing voltage equations of an IPM machine at steady-states, are obtained from substituting (1.2) into (1.1) and they are given as follows:

$$\begin{aligned} V_d &= RI_d - \omega L_q I_q \\ V_q &= RI_q + \omega L_d I_d + \omega \Psi_m \end{aligned} \tag{5.1}$$

The input power of an AC machine is given by [18, 120]:

$$P_{in} = \frac{3}{2}\left(V_d I_d + V_q I_q\right) \tag{5.2}$$

Substituting (5.1) into (5.2),

$$\begin{aligned} P_{in} &= \frac{3}{2}\left(RI_d^2 - \omega L_q I_d I_q + RI_q^2 + \omega L_d I_d I_q + \omega \Psi_m I_q\right) \\ &= \frac{3R}{2} I_a^2 + \frac{3\omega}{2} T \end{aligned} \tag{5.3}$$

where the model dependent function T is expressed as follows,

$$T = \left(-L_q I_d + L_d I_d + \Psi_m\right) I_q \tag{5.4}$$

The electromagnetic torque can also be expressed as a function of T.

$$T_e = \frac{3p}{2} T \tag{5.5}$$

The output power is given by:

$$P_{out} = \omega_m T_e \tag{5.6}$$

where ω_m is the mechanical speed in rad/s. Substituting (5.5) into (5.6) gives the alternate expression of the output power;

$$P_{out} = \frac{3\omega}{2} T \tag{5.7}$$

From (5.3), (5.5) and (5.7), one obtains the partial derivatives of the input power, output power and the electromagnetic torque with respect to current angle as follows.

$$\frac{\partial P_{in}}{\partial \beta} = \frac{3\omega}{2}\left(\frac{\partial T}{\partial \beta}\right) \tag{5.8}$$

$$\frac{\partial P_{out}}{\partial \beta} = \frac{3\omega}{2}\left(\frac{\partial T}{\partial \beta}\right) \tag{5.9}$$

$$\frac{\partial T_e}{\partial \beta} = \frac{3p}{2}\left(\frac{\partial T}{\partial \beta}\right) \tag{5.10}$$

By comparisons of (5.8), (5.9) and (5.10), one can deduce that the gradients of the input power, output power and the electromagnetic torque are proportional to each other at steady-states which can be expressed as:

$$\frac{\partial P_{in}}{\partial \beta} \propto \frac{\partial P_{out}}{\partial \beta} \propto \frac{\partial T_e}{\partial \beta} \propto \frac{\partial T}{\partial \beta} \tag{5.11}$$

Therefore, it is evident that the accurate current angle optimization with the T function will be theoretically accurate for the maximization of torque production for a given current magnitude.

5.3. THE PROBLEM OF CONVENTIONAL CURRENT ANGLE OPTIMIZATION

It has been shown in the previous section that the optimum current angle is obtained by posing $\partial T/\partial \beta$ to zero. In this section, problems associated with a large number of drives in the literature will be discussed. Substituting (1.2) into (1.3) gives the model dependent expression for the electromagnetic torque.

$$T_e = \frac{3p}{2}\left(\Psi_m I_q - I_d I_q\left(L_q - L_d\right)\right) \tag{5.12}$$

The *dq*- axis currents are given by:

$$\begin{aligned} I_d &= -I_s \sin\beta \\ I_q &= I_s \cos\beta \end{aligned} \tag{5.13}$$

where β is the current angle as shown in Fig. 5. 1.

Substituting (5.13) into (5.12) and dividing by (5.5) yields T as a function of current angle.

$$T = \Psi_m I_s \cos\beta + \left(L_q - L_d\right) {I_s}^2 \sin\beta \cos\beta \tag{5.14}$$

As has been discussed, the optimum current angle is obtained by posing $(\partial T/\partial\beta)$ to zero. One can obtain the derivative from (5.14) as follows:

$$\frac{\partial T}{\partial \beta} = f(I_s, \beta) + e(I_s, \beta) \tag{5.15}$$

where f and e are given by (5.16) and (5.17), respectively.

$$f(I_s, \beta) = -\Psi_m I_s \sin\beta + \left(L_q - L_d\right) {I_s}^2 (\cos^2\beta - \sin^2\beta) \tag{5.16}$$

$$e(I_s, \beta) = \frac{\partial \Psi_m}{\partial \beta} I_s \cos\beta + \frac{\partial L_q}{\partial \beta} {I_s}^2 \sin\beta \cos\beta - \frac{\partial L_d}{\partial \beta} {I_s}^2 \sin\beta \cos\beta \tag{5.17}$$

To date, a great number of publications in the literature have obtained the optimum current angle by posing $f(I_s, \beta)$ to zero and the influence of the error function in (5.17) has been omitted [6, 36, 49, 50, 52, 53, 57, 58, 95, 112-114] by assuming that the inductances and PM flux linkage are constant or each of $[\partial\Psi_m/\partial\beta]$, $[\partial L_q/\partial\beta]$ and $[\partial L_d/\partial\beta]$ is zero. Under this assumption, substituting $(\cos^2\beta = 1 - \sin^2\beta)$ into (5.16) and posing to zero, one obtains the optimum current angle in which the f function becomes zero.

$$\beta = \sin^{-1}\left(\frac{-\Psi_m + \sqrt{{\Psi_m}^2 + 8\left(L_q - L_d\right)^2 {I_s}^2}}{4\left(L_q - L_d\right) I_s}\right) \tag{5.18}$$

Substituting (5.18) into (5.13) and solving for the *d*- axis current, one obtains:

$$I_d = \frac{\Psi_m}{2\left(L_q - L_d\right)} - \sqrt{\frac{{\Psi_m}^2}{4\left(L_q - L_d\right)^2} + {I_q}^2} \tag{5.19}$$

Conventionally, in IPM machine drives, the optimum current angle and the *d*- axis current commands are generated from (5.18) and (5.19), respectively. Although these

equations are employed in IPM drives extensively, the resultant operating point derived from these equations deviates from the actual MTPA point due to the omitted error function. It is highly important to note that even though the machine parameters employed in (5.18) and (5.19) are accurately modelled and employed in IPM drives, the accurate MTPA operation still cannot be achieved. This is because (5.18) and (5.19) yields (5.16) to zero but the error function in (5.17) is not. The deviation from the optimal is not negligible and increases with the load which will be verified in the following sections.

Fig. 5.3-(a) and (b) illustrate the torque characteristic of the IPM machine whose specifications are listed in Table 1.1. Fig. 5.3-(a) shows the magnetic and reluctance torque components together with total torque when the nominal machine parameters are employed in (5.12) at a 100 A current amplitude, whereas Fig. 5.3-(b) shows the variation in the reluctance and total torques when machine parameters are altered as specified in the figure, but are kept constant. It is seen that the MTPA point varies when the machine parameters change which demonstrates the importance of the online optimization of the current angle. It should be noted that although the machine parameters are changed in Fig. 5.3-(b), the magnetic and the reluctance torque components are maximum when $\beta = 0°$ and $\beta = 45°$, respectively. This can be verified from (5.12) in which the left and right-hand sides of the equation (magnetic and reluctance torque components, respectively) are maximized when *q*- axis current is maximum, *i.e.* $\beta = 0°$ and when *d*- and *q*- axis currents are equal to each other, *i.e.* $\beta = 45°$ respectively. This implies that the optimum current angle cannot be higher than 45°. However, this assumption is only valid when the error function in (5.17) is zero.

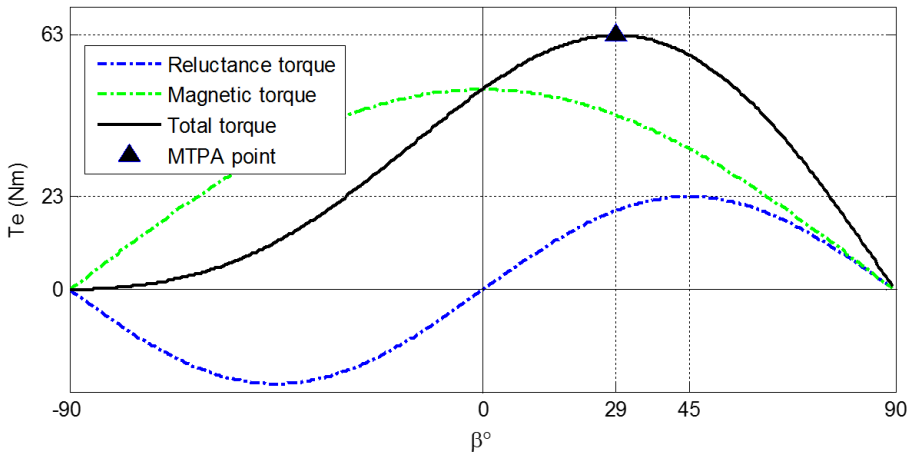

(a) Magnet alignment, reluctance and total torques of an IPM machine

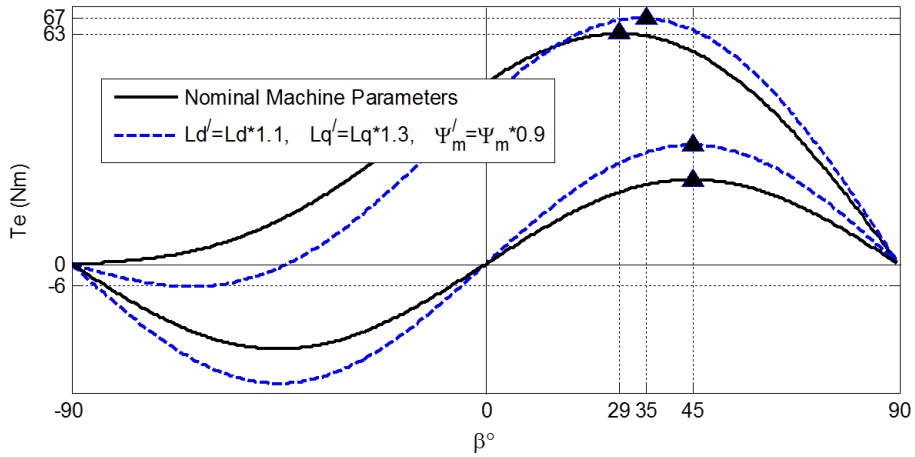

(b) Reluctance and total torque of the same machine when parameters change

Fig. 5.3 Torque characteristic of an IPM machine based on (5.16)

In a real IPM machine, since the machine parameters are functions of *dq*- axis currents, the reluctance torque may be at the maximum when current angle β is other than 45°. Reluctance and magnetic torque components in (5.12) can be expressed as follows:

$$T_e^{magnet} = \frac{3p}{2}\Psi_m(I_d, I_q)I_q \tag{5.20}$$

$$T_e^{reluctance} = \frac{3p}{2}\left[L_d(I_d, I_q)I_dI_q - L_q(I_d, I_q)I_dI_q\right] \tag{5.21}$$

Fig. 5.4 illustrates the torque characteristic of the same motor when high fidelity machine models are employed. This implies that the torque components are illustrated based on (5.20) and (5.21). As can be seen from the figure, the influence of the error function given by (5.17) shifts the maximum reluctance torque being obtained at 57° when the current amplitude is 100A. Therefore, the MTPA might be obtained when the current angle is higher than 45° and it is very important to obtain it online considering the error function in (5.17). The error function can be taken into account and posed to zero online by adopting virtual signal injection control scheme.

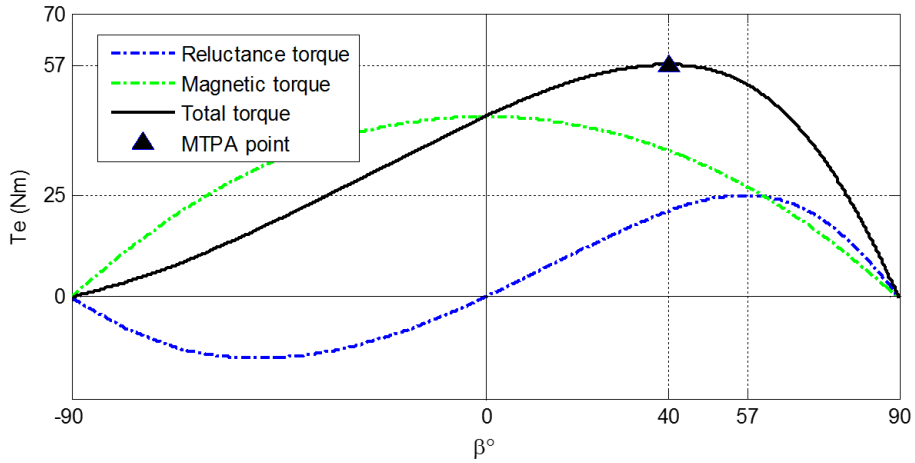

Fig. 5.4 Torque characteristic of an IPM machine based on (5.15)

5.4. VIRTUAL SIGNAL INJECTION FOR ONLINE CURRENT ANGLE OPTIMIZATION

To date, virtual signal injection based drives have been proposed for online optimization of the current angle without prior knowledge of the machine parameters. The current angle is optimized by signal process through T function in (5.4). Although this expression is model dependent, it will be shown that they are obtained from command voltages.

Based on (5.11), it is noteworthy that the optimization can be obtained by employing input or output power expressions in (5.3) and (5.7), respectively. However, the response time of the signal process will vary with the speed since the power is a function of speed. The torque and the T function in (5.4) is not a function of speed and hence the response time is speed invariant.

The theoretical analysis of the virtual signal injection based control is made in the following section.

5.4.1. MATHEMATICAL EXPRESSIONS FOR THE SIGNAL PROCESS

A high frequency small sinusoidal signal can be expressed as:

$$\Delta\beta = Asin(\omega_h t) \tag{5.22}$$

where A is the amplitude of the signal whose frequency is ω_h rad/s. When the signal is injected into the current angle, the *dq*- axis currents become:

$$\begin{aligned} I_d^h &= -I_a sin(\beta + \Delta\beta) \\ I_q^h &= I_a cos(\beta + \Delta\beta) \end{aligned} \tag{5.23}$$

Substituting (5.23) into (5.4) gives the high frequency signal injected T function.

$$T^h = \left(-L_q I_d^h + L_d I_d^h + \Psi_m\right) I_q^h \tag{5.24}$$

As can be seen from (5.24), prior knowledge of machine parameters, *viz. dq*- axis inductances and the permanent magnet flux linkage are required to implement the signal process with T^h function. To circumvent this problem, the machine parameters can be obtained from *dq*- axis inverter reference voltages. Hence, Ψ_m and L_q are obtained from (5.1), and they are given in (5.25) and (5.26), respectively.

$$\Psi_m = \frac{V_q - RI_q}{\omega} - L_d I_d \tag{5.25}$$

$$L_q = -\frac{V_d - RI_d}{\omega I_q} \tag{5.26}$$

Substituting (5.25) and (5.26) into (5.24), one obtains;

$$T^h = \left[\left(\frac{V_d - RI_d}{\omega I_q}\right) I_d^h + L_d I_d^h + \left(\frac{V_q - RI_q}{\omega}\right) - L_d I_d\right] I_q^h \tag{5.27}$$

It is seen that (5.27) is dependent on L_d whose variation and influence is much less than the influence of L_q and Ψ_m variations in a real-world IPM machine. L_d is modelled as a function of *dq*- axis currents, stored in a LUT as shown in Fig. 2.8-(a) and employed in the proposed scheme.

The T^h function contains variable components which can be expressed from Taylor's series expansion as follows:

$$T\big(\beta + Asin(\omega_h t)\big) = T(\beta) + \frac{\partial T(\beta)}{\partial \beta} A \sin(\omega_h t) + \frac{\partial}{\partial \beta}\left(\frac{\partial T(\beta)}{\partial \beta}\right) A^2 sin^2(\omega_h t) + \cdots \quad (5.28)$$

Since the amplitude of the injected signal is very small, the influence of the second and higher order terms are relatively small on the variation of T function. However, this is not of concern in the virtual signal injection based drives since only the first order term in (5.28) associated with $(\partial T/\partial \beta)$ is of interest. $(\partial T/\partial \beta)$ can be extracted from the first order term in (5.28) as shown in Fig. 5.5. For this purpose, a band-pass filter (BPF) with a centre frequency being equal to the injected signal frequency is utilized to extract the first-order component in (5.28). The output of the BPF can be expressed as $KA\frac{\partial T}{\partial \beta} sin(\omega_h t)$ where K is the gain of the BPF. BPF output is, then, multiplied by $sin(\omega_h t)$ which can be expressed as follows:

$$KA\frac{\partial T}{\partial \beta} sin^2(\omega_h t) = KA\frac{\partial T}{\partial \beta}\left(\frac{1 - cos(2\omega_h t)}{2}\right) = \frac{1}{2} KA\frac{\partial T}{\partial \beta} - \frac{1}{2} KA\frac{\partial T}{\partial \beta} cos(2\omega_h t) \quad (5.29)$$

As can be seen from (5.29), the $(\partial T/\partial \beta)$ can be extracted by eliminating the high frequency component. Therefore, a LPF with a cut-off frequency being much lower than twice the injected signal frequency is employed to filter out the right-hand side of (5.29). Finally, the output of the LPF proportional to $(\partial T/\partial \beta)$ is regulated by an integral regulator to generate the *d*- axis current command. The integral action will stop if and only if $(\partial T/\partial \beta) = 0$, *i.e.*, the MTPA operating conditions. The details of the drive system configuration will be discussed in the following sections.

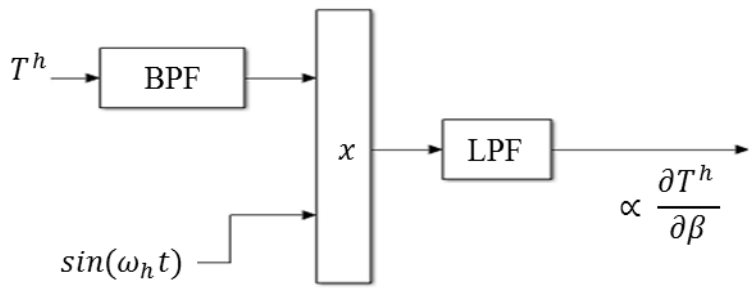

Fig. 5.5 Schematic illustration for extraction of $\partial T/\partial \beta$

5.4.2. EXISTING VIRTUAL SIGNAL INJECTION BASED CONTROL

It has been shown in recent publications [11, 12, 16-18] that the MTPA operation can be achieved online without prior knowledge of the machine parameters; L_d, L_q and Ψ_m. In these schemes, the virtual signal process is realized by the equation given in (5.30).

$$T^{h\_conv} = \left[\left(\frac{V_d - RI_d}{\omega I_q}\right) I_d^h + \left(\frac{V_q - RI_q}{\omega}\right)\right] I_q^h \tag{5.30}$$

As can be seen, the signal process with T^{h_conv} can be implemented without the *dq*-axis inductances and the permanent magnet flux linkage. Indeed, *d*- axis inductance terms in (5.27) are omitted in the existing schemes. However, although the resultant operating points in the existing schemes are very close to the MTPA operation, it will be shown that these drives suffer from error terms causing deviation from the optimal point. The error terms are dependent on machine characteristics and hence the existing technique may not be suitable for other IPM machines. The error analysis is made in the following section.

5.5. ERROR ANALYSIS OF VIRTUAL SIGNAL INJECTION BASED DRIVES

The *dq*- axis currents and their derivatives with respect to current angle are given by (5.31) and (5.32), respectively.

$$\begin{aligned} I_d &= -I_s sin(\beta) \\ I_q &= I_s cos(\beta) \end{aligned} \tag{5.31}$$

$$\begin{aligned} \frac{\partial I_d}{\partial \beta} &= -I_s cos(\beta) = -I_q \\ \frac{\partial I_q}{\partial \beta} &= -I_s sin(\beta) = I_d \end{aligned} \tag{5.32}$$

The derivative of T function with respect to current angle β is obtained from (5.4) and (5.32);

$$\frac{\partial T}{\partial \beta} = f(I_d, I_q) + e(I_d, I_q) \tag{5.33}$$

where f and e are given by (5.34) and (5.35), respectively.

$$f(I_d, I_q) = L_q I_q^2 - L_q I_d^2 - L_d I_q^2 + L_d I_d^2 + \Psi_m I_d \tag{5.34}$$

$$e(I_d, I_q) = \left[-\frac{\partial L_q}{\partial \beta} I_d + \frac{\partial L_d}{\partial \beta} I_d + \frac{\partial \Psi_m}{\partial \beta} \right] I_q \tag{5.35}$$

Indeed, (5.15) and (5.33) are the same. Whilst the former is in polar coordinates, the latter is in Cartesian (*dq*) frame. The maximum torque is obtained when (5.33) is equal to zero. However, although the parameter variations in virtual signal injection based drives are addressed online, these drives also suffer from neglecting the error function.

As can be seen from (5.24) the machine parameters; L_d, L_q and Ψ_m are considered as constant during the signal process. This implies that the influence of $[\partial L_d/\partial \beta]$, $[\partial L_q/\partial \beta]$ and $[\partial \Psi_m/\partial \beta]$ are not accounted in the virtual signal process regardless of the parameters being obtained from phase voltages or perfectly modelled. This can be explained simply as follows. The *dq*- axis inductances and the magnetic flux linkage are functions of *dq*- axis currents; $L_d(I_d, I_q)$, $L_q(I_d, I_q)$ and $\Psi_m(I_d, I_q)$, respectively. In order to extract the $[\partial L_d/\partial \beta]$, $[\partial L_q/\partial \beta]$ and $[\partial \Psi_m/\partial \beta]$ from the signal processing unit, the resultant $L_d(I_d^h, I_q^h)$, $L_q(I_d^h, I_q^h)$ and $\Psi_m(I_d^h, I_q^h)$ must be employed in the signal processing unit. Otherwise, the output of the signal processing unit based on (5.24) or (5.27) assuming constant machine parameters may expressed in relation to true $(\partial T/\partial \beta)$ as follows;

$$\frac{\partial T^h}{\partial \beta} = \frac{\partial T}{\partial \beta} - e(I_d, I_q) = f(I_d, I_q) \tag{5.36}$$

One can deduce from (5.36) that even though the machine parameters are obtained from (5.25) and (5.26) or perfectly modelled in the virtual signal injection based drives, their variations can only be accounted in f function since the error still remains at the output of the signal processing unit.

Above analysis has been made for drives which employ (5.24) and (5.27). As for the method based on (5.30), the error analysis can be made as follows. The *d*- axis flux linkage can be obtained from (5.1) and it is given in (5.37).

$$\Psi_d = \left(\frac{V_q - RI_q}{\omega}\right) \tag{5.37}$$

Substituting (5.26) and (5.37) into (5.30) gives;

$$T^{h\_conv} = \left(-L_q I_d^h + \Psi_d\right) I_q^h \tag{5.38}$$

As can be seen from (5.38), in conventional drives, $[\partial L_q/\partial\beta]$ and $[\partial\Psi_d/\partial\beta]$ cannot be extracted from the signal process even though L_q and Ψ_d are obtained from the command voltages. Therefore, the error function of the signal process is obtained as follows.

$$\begin{aligned} e_{conv}(I_d, I_q) &= \left[-\frac{\partial L_q}{\partial\beta} I_d + \frac{\partial\Psi_d}{\partial\beta}\right] I_q \\ &= \left[-\frac{\partial L_q}{\partial\beta} I_d + \frac{\partial L_d}{\partial\beta} I_d - L_d I_q + \frac{\partial\Psi_m}{\partial\beta}\right] I_q \end{aligned} \tag{5.39}$$

Subtracting (5.39) from (5.33), one obtains

$$f_{conv}(I_d, I_q) = L_q I_q^2 - L_q I_d^2 + L_d I_d^2 + \Psi_m I_d \tag{5.40}$$

Thus, the conventional signal process can be expressed as follows.

$$\frac{\partial T^{h\_conv}}{\partial\beta} = \frac{\partial T}{\partial\beta} - e_{conv}(I_d, I_q) = f_{conv}(I_d, I_q) \tag{5.41}$$

Therefore, virtual signal injection based MTPA tracking adopting (5.27) or (5.30) poses f and f_{conv} functions in (5.36) and (5.41), respectively, to zero and the optimal operating point cannot be achieved in either cases due to the error functions given in (5.35) and (5.39), respectively.

The influence of each error term in (5.35) and (5.39) will be analysed on two different IPM motors and the error functions are modified as follows:

$$e(I_d, I_q) = e1 + e2 + e3 \tag{5.42}$$

$$e_{conv}(I_d, I_q) = e1 + e2 + e3 + e4 \tag{5.43}$$

where;

$$e1 = -\frac{\partial L_q}{\partial \beta} I_d I_q \tag{5.44}$$

$$e2 = \frac{\partial L_d}{\partial \beta} I_d I_q \tag{5.45}$$

$$e3 = \frac{\partial \Psi_m}{\partial \beta} I_q \tag{5.46}$$

$$e4 = -L_d I_q^2 \tag{5.47}$$

It is evident that whilst the error function in (5.42) suffers from three error terms, the existing method has one more error term given by (5.47) due to the omitted L_d terms in (5.27). It is noteworthy that the influence of these errors increases with the current amplitude and hence the load. This is due to multiplication with the current in (5.44)-(5.47).

5.5.1. ERROR ANALYSIS WITH P-MOB MOTOR

The theoretical analysis of the errors associated with the virtual signal injection based MTPA control has been made in the previous section. In this section, the influence of these errors including the exiting schemes will be illustrated by simulation studies employing the high fidelity machine model which accounts for the magnetic saturations and the cross-coupling effects of *dq*- axis flux linkages. Therefore, the nonlinearity of the machine parameters are represented in the simulations. However, the maps of the nonlinear machine models need to be represented by polynomials in order to obtain the partial derivatives of the variables with respect to current angle. Hence, the machine flux-linkage maps shown in Fig. 3.2 are converted to polynomials utilizing Matlab curve-fitting tool. The polynomial representation of the high fidelity machine models for the IPM motor in Table 1.1 is given in the appendix.

Fig. 5.6 illustrates $[\partial T/\partial \beta]$ as well as the influence of the each error term in (5.44)-(5.47) when the current magnitude is 100 A. It is seen that $[\partial T/\partial \beta]$ is zero when the current angle is 40°. This implies that the maximum torque is obtained at $\beta = 40°$ when the current magnitude is 100 A. It is also seen that the current angle significantly deviates from the optimal when the error terms are neglected.

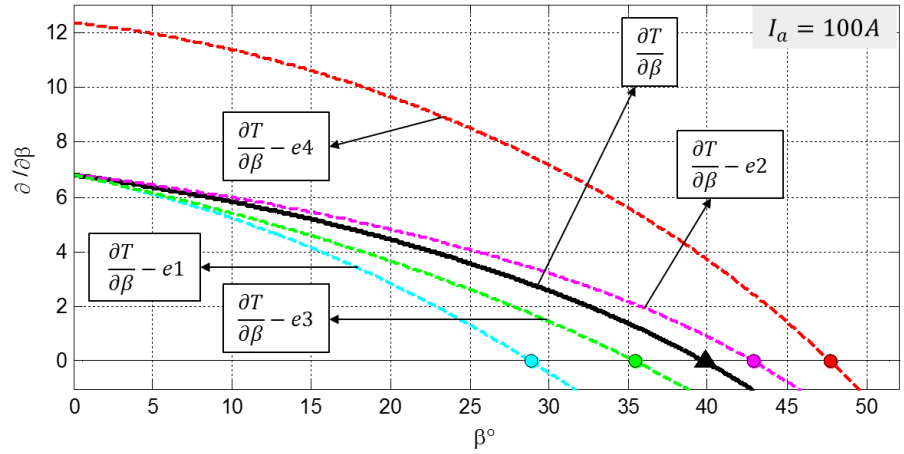

Fig. 5.6 $[\partial T/\partial \beta]$ at 100 A current magnitude considering error terms

Fig. 5.6 represents the machine behaviour only at 100 A. Simulations are carried out to represent the whole current range of the motor under study and the operating trajectories are obtained in which the partial derivatives become zero. Fig. 5.7 shows the optimum trajectory of the highly nonlinear machine as well as the operating trajectories when there is the specified error terms in the figure. It is evident that none of the error terms given by (5.44)-(5.47) has negligible influence on tracking the MTPA trajectory. It is also seen that the deviation from the optimal increases with the current magnitude. Therefore, it is highly important to consider the error terms which have been omitted in a great number of drive control schemes reported in the literature to date.

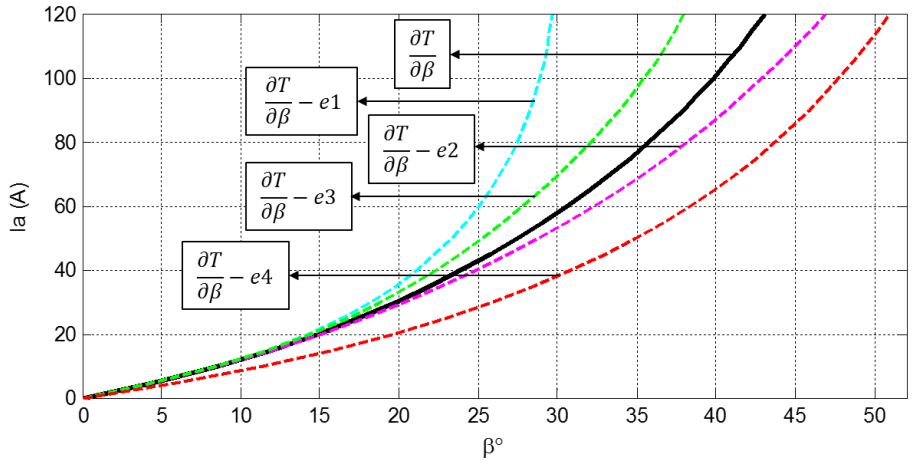

Fig. 5.7 MTPA trajectory and the trajectories considering error terms

To better illustrate the deviations from the optimal trajectory associated with these errors, $\Delta\beta$ versus operating current magnitude associated with each error term are plotted in Fig. 5.8. It is seen that $e1 - e3$ shows similar behaviour such that they have very low errors at light loads (low current) and the deviation increases proportionally to the current magnitude. On the other hand, $e4$ causes large deviation even at low current magnitude and settles above certain load.

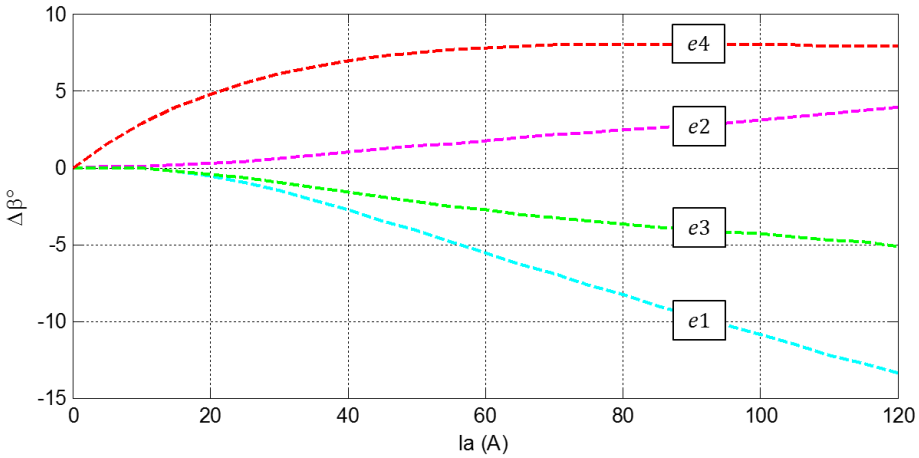

Fig. 5.8 Deviations from the optimal associated with each error term

Whilst the virtual signal injection based drives based on (5.27) suffer from each of $e1 - e3$, the existing approach based on (5.30) suffers from each of $e1 - e4$. The deviation from the optimal is, therefore, illustrated in Fig. 5.9 for these drives. It is evident in the figure that $e2$ and $e3$ reasonably cancel each other and their overall contribution on the deviation is negligible throughout wide operating range. Accordingly, $e1$ dominates the total error. This implies that compensation for the error term $e1$ associated with $[\partial L_q/\partial\beta]$ improves the resultant trajectory as illustrated by $(e2 + e3)$ in the figure. In the existing schemes, on the other hand, $e1$ and $e4$ cancels each other to some extend and the resultant deviation is illustrated in the figure. As can be seen, there is positive deviation at light loads (low current) and the deviation becomes negative above certain load. Although the deviation when $60A < I_s < 100A$ is within $\mp 2°$, it is within $\mp 5°$ during whole operating range whereas it is $-2° < \Delta\beta \leq 0°$ if $e1$ is compensated.

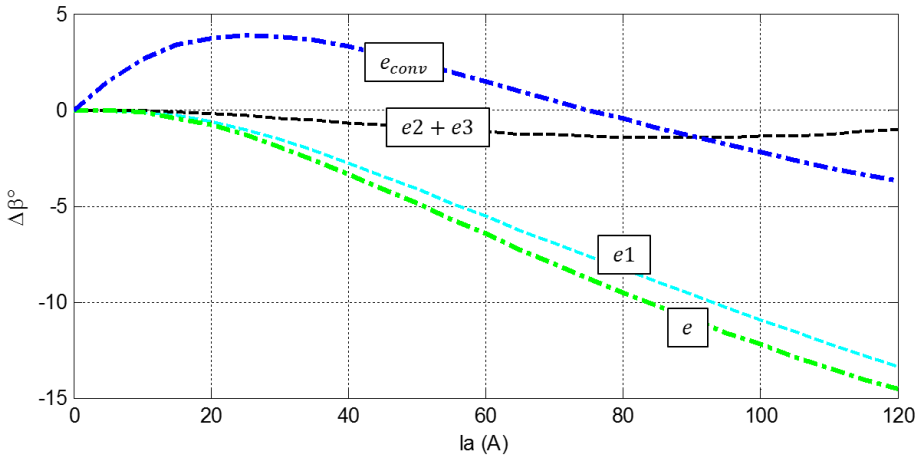

Fig. 5.9 Deviations from the optimal associated with the virtual signal injection based drives

In Fig. 5.10, the optimum MTPA trajectory considering machine nonlinearities and the trajectories associated with the virtual signal injection drives based on (5.27) and

(5.30) are illustrated. Clearly, the drives based on (5.27) is closer to the optimum when $0A < I_s < 40A$ and the existing approach provides better accuracy above $40A$.

It is noteworthy that MTPA operation and the trajectories shown in the figure are independent of machine speed. Thus, the trajectories represent any speed in the constant torque region.

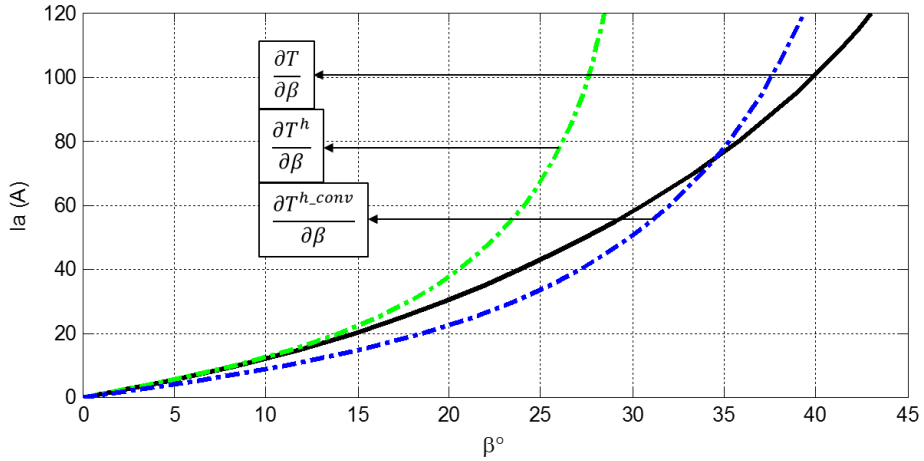

Fig. 5.10 MTPA trajectory and the trajectories obtained from virtual signal injection based drives

5.5.2. ERROR ANALYSIS WITH NISSAN-LEAF MOTOR

Although the theoretical background of the error analysis is the same, the resultant influence of these errors is dependent on machine characteristics. Therefore, their influence on the operating trajectories might differ in other IPM motors. To consolidate how it might differ in other motors, the same error analysis through simulation studies are carried out by employing another IPM motor (Nissan-Leaf) designed for electric vehicle traction applications. The machine specifications are listed in Table 5.1, the high fidelity machine models and the polynomial representation of the machine is given in the Appendix.

Table 5.1 Specifications of the IPM machine (Nissan - Leaf)

Number of pole-pairs	4
Nominal phase resistance	0.01327 Ω
Continuous torque	109 Nm
Peak torque / current	280 Nm / 450 A
Base speed	2728 r/min
Rated speed	7000 r/min
Peak power below base speed	80 kW
Peak power at rated speed	80 kW

Fig. 5.11 illustrates the trajectories for the Nissan-Leaf machine from no load to peak torque at which the current magnitude is 450 A. The errors deviate the trajectory from the MTPA in a similar way as shown in Fig. 5.7 for the previous motor.

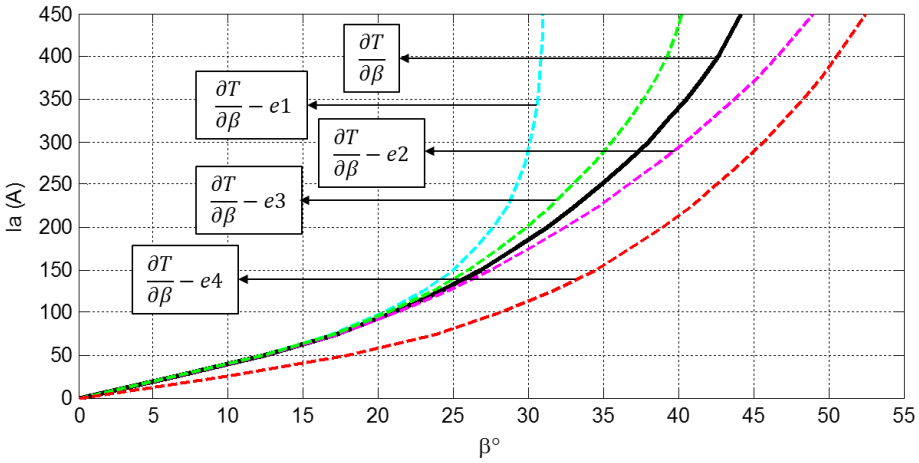

Fig. 5.11 MTPA trajectory and the trajectories considering error terms

In Fig. 5.12, $\Delta\beta$ versus I_s are illustrated for each error term. As can be compared from Fig. 5.8, the errors result in similar deviations from the optimal. The errors associated with $[\partial L_d/\partial\beta]$, $[\partial L_q/\partial\beta]$ and $[\partial \Psi_m/\partial\beta]$ have low influence at light loads ($I_s < 100A$) and increases proportionally to the current magnitude. On the other hand, the $e4$ term associated with the existing virtual signal injection based drives, has large error even at light loads. By way of example, the deviation at 50 A is above 5°.

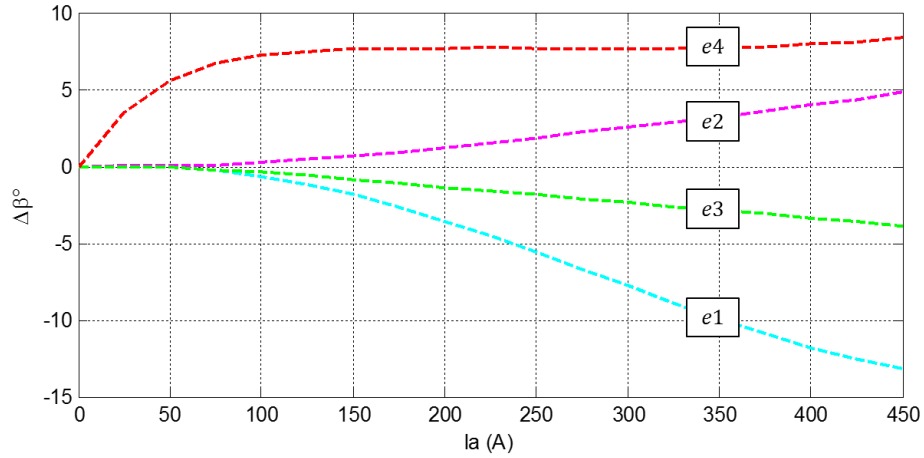

Fig. 5.12 Deviations from the optimal associated with each error term

In Fig. 5.13, the optimum MTPA trajectory and the trajectories associated with the virtual signal injection drives based on (5.27) and (5.30) are illustrated. Although the errors result in similar deviations from the optimal in both motors, one can deduce that the accuracy of the existing schemes is much lower for the Nissan-Leaf motor. It is seen

that the existing approach is highly inaccurate at light loads. Evidently, the drives based on (5.27) is much close to the optimum below $150A$ and the existing approach provides better accuracy above $200A$. It is clear that both of the trajectory are not suitable to achieve efficient operation.

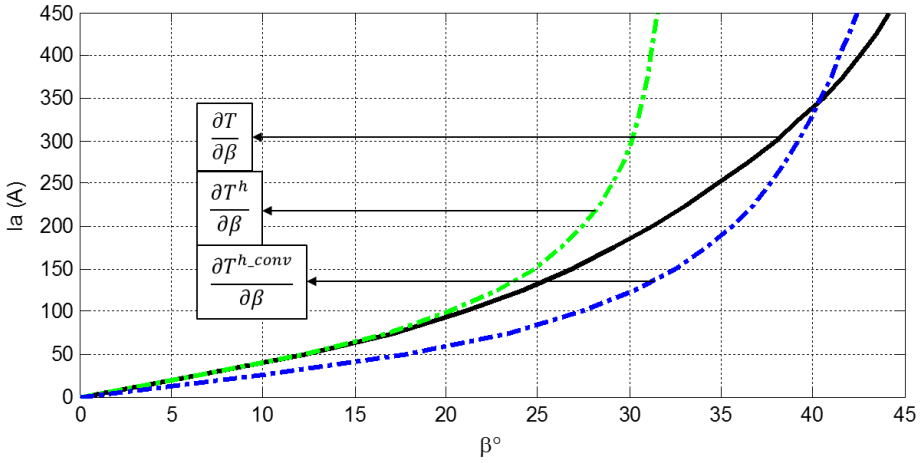

Fig. 5.13 MTPA trajectory and the trajectories obtained from virtual signal injection based drives

It should be noted that the trajectories for $[\partial T^h/\partial \beta]$ in Fig. 5.10 and Fig. 5.13 not only represent the virtual signal injection based drives but also represent the drives in which the optimum current angle is obtained from (5.18) and (5.19) with perfect machine models assuming constant parameters. As has been discussed, this is because of the omitted error functions in (5.17) and (5.42).

5.6. PROPOSED VIRTUAL SIGNAL INJECTION BASED CONTROL

It is evident in Fig. 5.8 and Fig. 5.12 that the errors associated with $[\partial L_d/\partial \beta]$ and $[\partial \Psi_m/\partial \beta]$ cancels each other reasonably on both motors throughout wide operating range and the deviation is dominated by the error term associated with $[\partial L_q/\partial \beta]$. This is indeed because of the highly saturated characteristic of the q- axis inductance in IPM machines. In conventional virtual signal injection based drives which employ (5.30), the influence of the error associated with $[\partial L_q/\partial \beta]$ is alleviated by another error term in (5.47) as they have opposite signs. Although the resultant trajectory is improved in P-MOB motor in conventional approach, it has been validated that the accuracy depends on the machine characteristics. It is clear from (5.47) that the influence of $e4$ depends on the value of the d- axis inductance which differs in other IPM machines. Thus, the cancellation of $e1$ and

$e4$ cannot be guaranteed. Consequently, it is proposed that the error term $e1$ associated with the q- axis inductance saturation is compensated. When this error is compensated, the resultant operating trajectory for both motors are much improved as shown in Fig. 5.14 and Fig. 5.15.

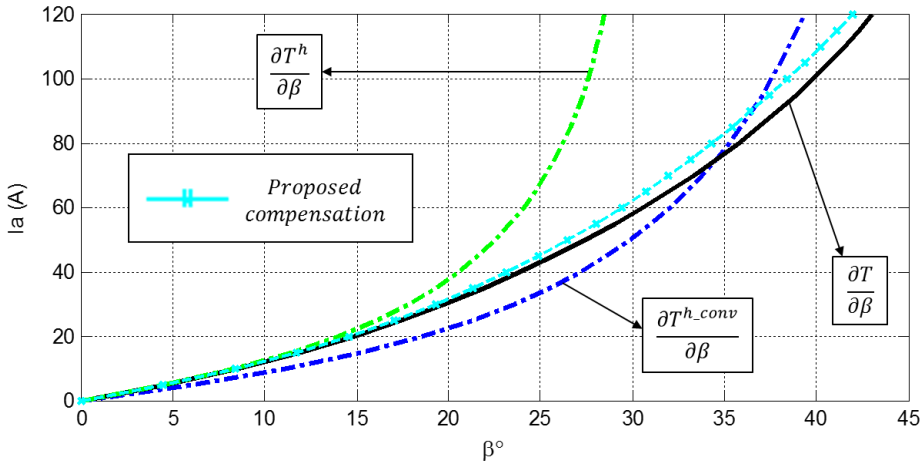

Fig. 5.14 The trajectory of the P-Mob machine with the proposed compensation

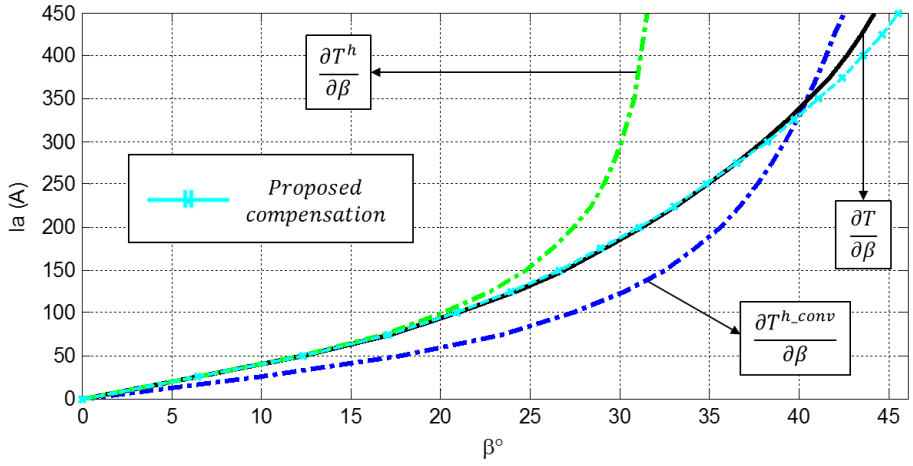

Fig. 5.15 The trajectory of the Nissan-Leaf machine with the proposed compensation

To compensate the error term associated with $[\partial L_q/\partial \beta]$, the q- axis inductance is modelled as dq- axis currents. T^h is implemented as usual based on (5.27). In order to extract the $[\partial L_q/\partial \beta]$ from the signal process, a high frequency signal injected q- axis inductance function (or map) is needed which can be expressed as follows:

$$L_q^h = L_q(I_d^h, I_q^h) \tag{5.48}$$

The high frequency signal injected q- axis inductance in (5.48) contains variable components which can be expressed from Taylor's series expansion as follows:

$$L_q\big(\beta + Asin(\omega_h t)\big) = L_q + \frac{\partial L_q}{\partial \beta} A \sin(\omega_h t) + \frac{\partial}{\partial \beta}\left(\frac{\partial L_q}{\partial \beta}\right) A^2 sin^2(\omega_h t) + \cdots \tag{5.49}$$

It is evident in (5.49) that the error term associated with $[\partial L_q/\partial\beta]$ can be extracted if the q- axis inductance variation as a result of the signal injection is processed in the same manner as shown in Fig. 5.5. The schematic of the proposed compensation is illustrated in Fig. 5.16. Since the extraction steps are the same, the methodology will not be repeated. However, it should be noted that the $e1$ error in (5.44) has dq- axis current factors. Hence, the resultant q- axis inductance must be multiplied by dq- axis currents in order to extract $e1$ error from the signal process. As has been shown in Fig. 5.16, the output of the signal process does not include the $e1$ error term so that the proposed trajectory shown in Fig. 5.14 and Fig. 5.15 can be achieved.

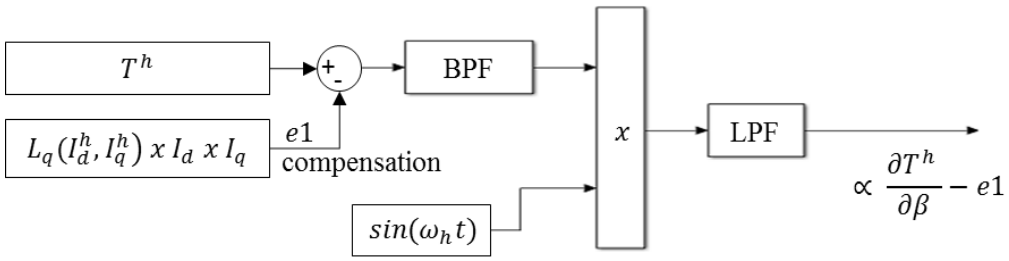

Fig. 5.16 Schematic of the proposed signal processing unit

It is important to note that the error terms associated with $[\partial L_d/\partial\beta]$ and $[\partial \Psi_m/\partial\beta]$ can also be compensated similar to the $[\partial L_q/\partial\beta]$ compensation. However, it is evident in Fig. 5.14 and Fig. 5.15 that these errors has negligible influence over wide operating range as they cancel each other to a great extent. If these errors are to be compensated, $L_d(I_d, I_q)$ and $\Psi_m(I_d, I_q)$ need to be modelled and stored in look-up tables. It has been validated through simulations that the perfect MTPA trajectory can be achieved by full compensation in the virtual signal injection scheme when the machine parameters employed in the controller matches perfectly to those in the motor model. In a practical implementation, however, perfect modelling is almost impossible as the parameters are also dependent on the temperature, and hence the modelling errors associated with these compensations will most likely cause deviation of the MTPA

trajectory. This implies that the compensation of these errors may not lead to better MTPA trajectory due to the inevitable modelling errors. Accordingly, the most dominant error term associated with $[\partial L_q/\partial\beta]$, is compensated in the proposed drive.

5.6.1. CONTROL SYSTEM CONFIGURATION

The schematic of the proposed FOC drive is shown in Fig. 5.17. As will be seen from the figure, the *d*- axis reference current is generated by the proposed signal processing unit in order to obtain optimum *d*- axis reference current for a given command torque. Since the input is generally command torque in traction applications, the corresponding *q*- axis current is obtained from the following equation. Solving (5.12) for the *q*- axis current, one obtains (5.50):

$$I_q = \left(\frac{3p}{2}\right)^{-1} \frac{T_e}{\Psi_m - I_d\left(L_q - L_d\right)} \tag{5.50}$$

It is evident in (5.50) that the machine parameters L_d, L_q and Ψ_m are necessary to generate the *q*- axis current command. Therefore, the deviation of the machine parameters from those employed in (5.50) will result in generating inaccurate *q*- axis current command for a given torque demand. Accordingly, there will be torque error at steady state. However, the proposed virtual signal injection method seeks the extremum point based on the resultant torque. This implies that any inaccuracy in the *q*- axis current command does not lead the machine to deviate from the MTPA trajectory. Therefore, the machine parameters in (5.50) can be obtained from predefined look-up tables or they can be employed even with their nominal values. In either cases the motor operates at the MTPA trajectory.

It should be noted that the steady-state torque error associated with (5.50) can be eliminated by a speed control loop. If the motor speed is controlled, then the accurate *q*-axis current command can be generated for a given speed command. However, if the torque control is necessary, such as for traction applications, then predefined look-up tables for these parameters are often adequate since the perfect torque control accuracy is not essential, rather the efficiency is much of concern which is ensured by the proposed signal injection method in either cases.

The generated *dq*- axis current commands are then tracked by two independent PI controllers in order to generate *dq*- axis reference voltages which need to be applied to the machine. Since the machine has coupling terms associated with *dq*- axis flux linkages, these terms are decoupled at the output of the PI current controllers as shown in Fig. 5.17. The coupling terms and *dq*- axis flux linkages associated with these coupling are given by (1.1) and (1.2), respectively.

The decoupled reference voltages are then fed into the over-modulation block in order to prevent voltage saturation. It is noteworthy that the DC-link voltage is not fully utilized in a constant torque region and hence the voltage does not saturate at steady-state. This implies that the over-modulation block does not alter the command voltages at steady-state, however, in a transient operation, the command voltage might saturate due to large current tracking errors. In such conditions, the over-modulation block confines the command voltage to prevent demanding a voltage higher than the available DC-link.

If the voltage saturates, the integrating action in the PI controllers needs to be avoided in order to prevent winding-up phenomenon as has been discussed in previous chapters. Therefore, once the input and output of the over-modulation block differs, the integrators are stopped by the anti-windup (AW) so that they do not integrate further.

The inverter command voltages that are generated in *dq*- rotating reference frame are transformed to the $\alpha\beta$ stationary reference frame for being fed to the SVPWM block. The modulation technique has been discussed in details in previous chapters.

The schematic of the proposed virtual signal processing unit is shown in Fig. 5.18. As will be seen from the figure, a high-frequency small sinusoidal signal $(A\sin(\omega_h t))$ is mathematically injected into the current angle. The signal injected T function which is proportional to electromagnetic torque and the compensation term are then processed by the filters whose details have been discussed greatly. The output of the LPF is proportional to the derivative of T function with respect to current angle β. The integral regulator is utilized to generate the *d*- axis current command. Hence, the extremum point, MTPA, can be achieved.

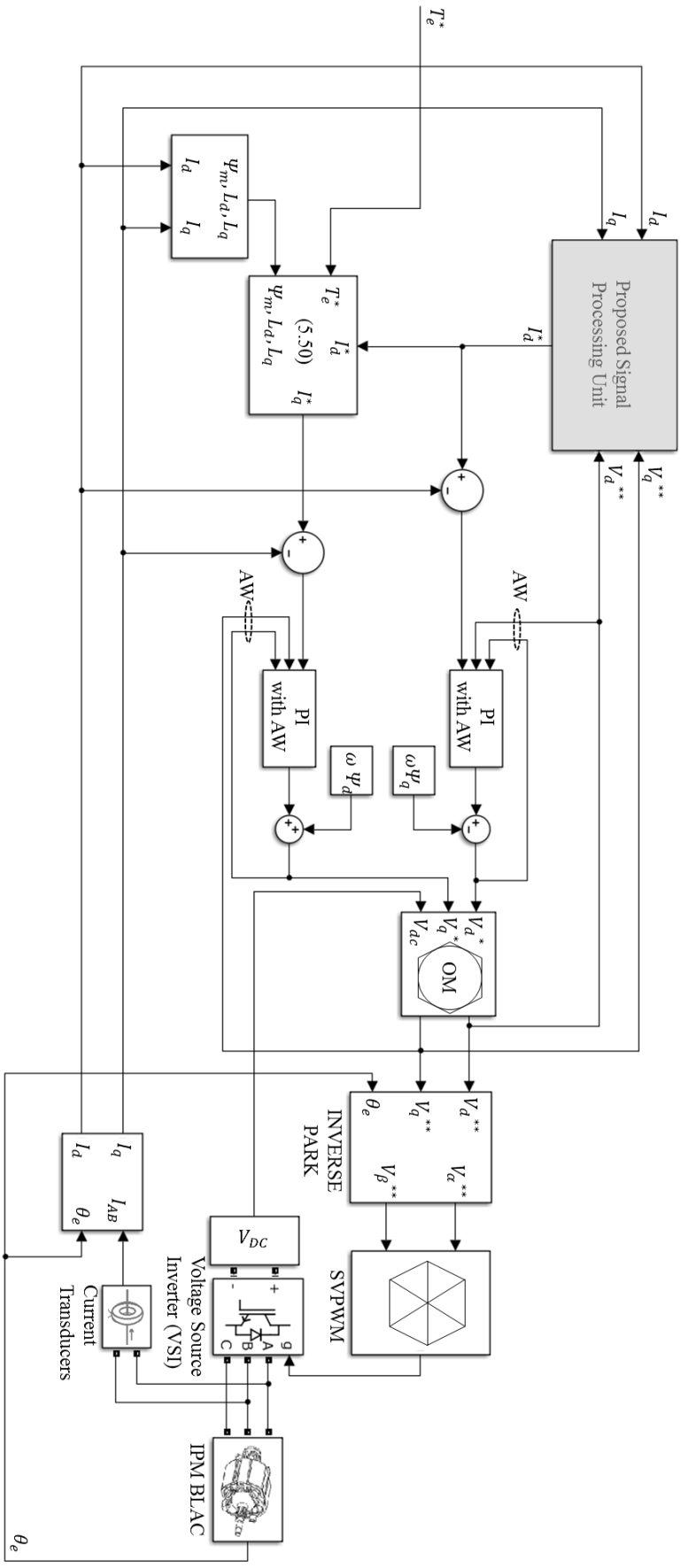

Fig. 5.17 Schematic of the proposed drive

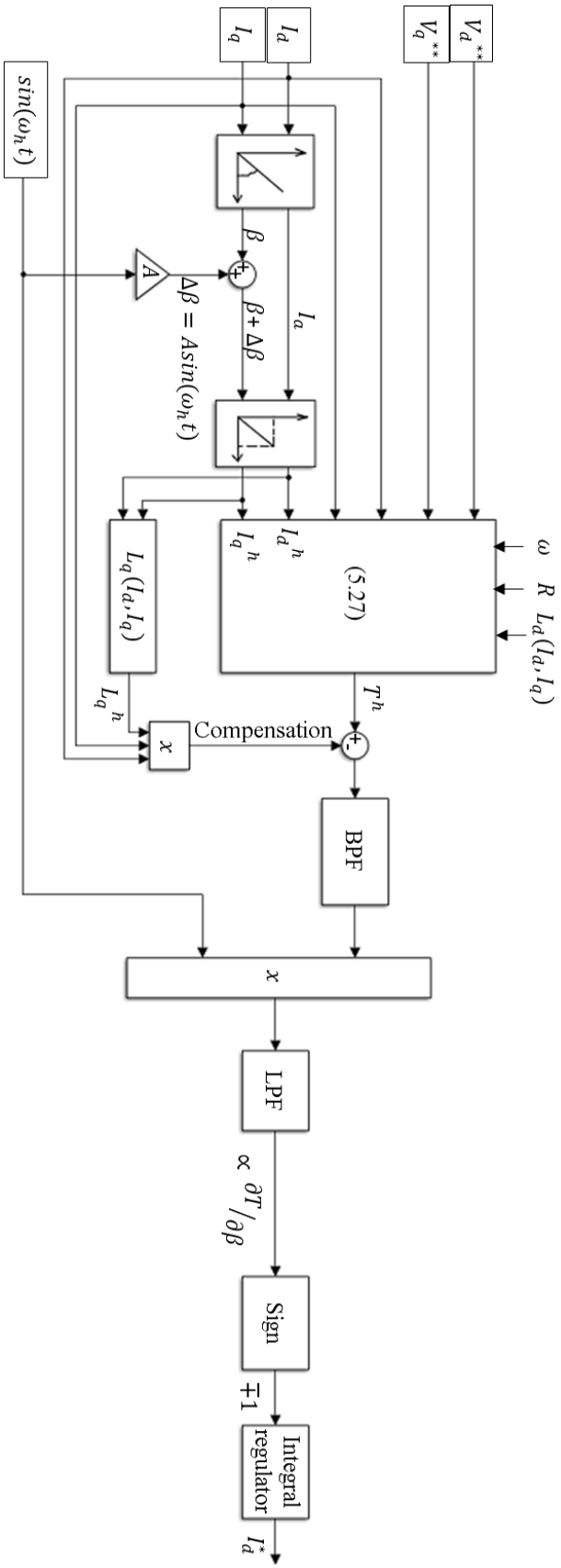

Fig. 5.18 Schematic of the proposed signal processing unit

5.6.2. MEASURES TO IMPROVE RESPONSE TIME

In real signal injection based methods, the frequency and the amplitude of the signal are constrained by resolution of sensors and the resonant problems. By way of example, the variable component when the amplitude is low may not be realized due to the resolution limitation in a real signal injection method whereas high magnitude increases the power losses. Similarly, it is evident that the frequency of the signal needs to be adjusted online to avoid resonant problems [120].

Since the signal is not injected into the real machine phase currents or voltages, rather it is injected mathematically, the amplitude and the frequency selection is more flexible than the real signal injection based methods. The frequency should be as high as possible for fast response. The frequency selection strategy is given by (5.51).

$$\omega_h = \frac{f_{inv}}{n_{min}} \; x \; 2\pi \tag{5.51}$$

where f_{inv} is the inverter switching frequency and n_{min} is the number of sample per period to represent a sinusoidal signal.

The frequency of the injected sinusoidal signal is 4 kHz (=8/2) when 2 samples are taken per period in a system in which the inverter switching frequency is 8 kHz. As has been discussed, the centre frequency of the BPF must be equal to the frequency of the sinusoidal signal. This implies that, if two samples are taken per period, the frequency of the injected sinusoidal signal and the centre frequency of the BPF will be 4 kHz. However, the centre frequency of the BPF must be lower than half of the inverter switching frequency in theory. Consequently, the sinusoidal signal cannot be represented by 2 samples. The minimum number of sample for a sinusoidal signal is three. If three samples are taken, then the frequency of the sinusoidal signal and the centre frequency of the BPF will be 2.667 kHz as shown in Fig. 5.19. The BPF in this study has been designed as a second order filter utilizing Matlab filter design and analysis tool (fdatool). As can be seen from the figure, only the components with 2.667 kHz (second terms of (5.28) and (5.49)) passes from the filter and the rest is filtered out with a strong attenuation. This implies that the additional low-pass filters to eliminate the noise are not necessary. In the existing virtual signal injection based control schemes each of *dq*- axis currents and voltages have been filtered by employing 4 low-pass filters to attenuate the noise.

However, this inevitably causes response delay as well as oscillatory response [18] and they are removed in the proposed approach.

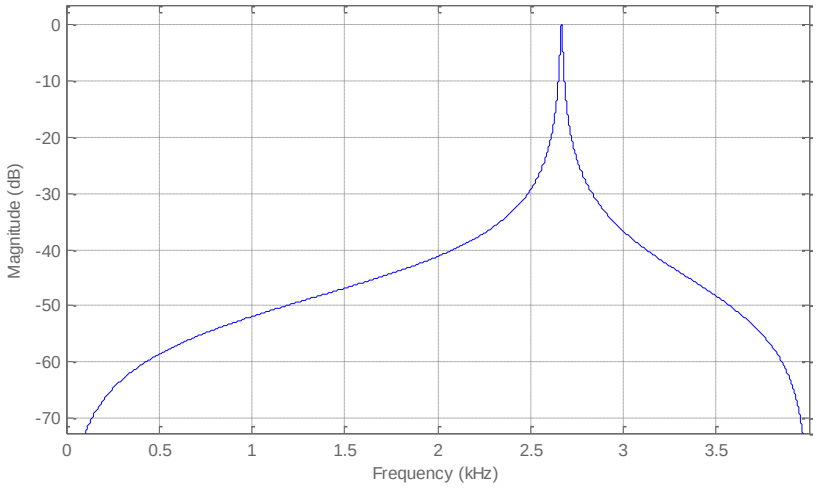

(a) Magnitude (dB) plot of the filter

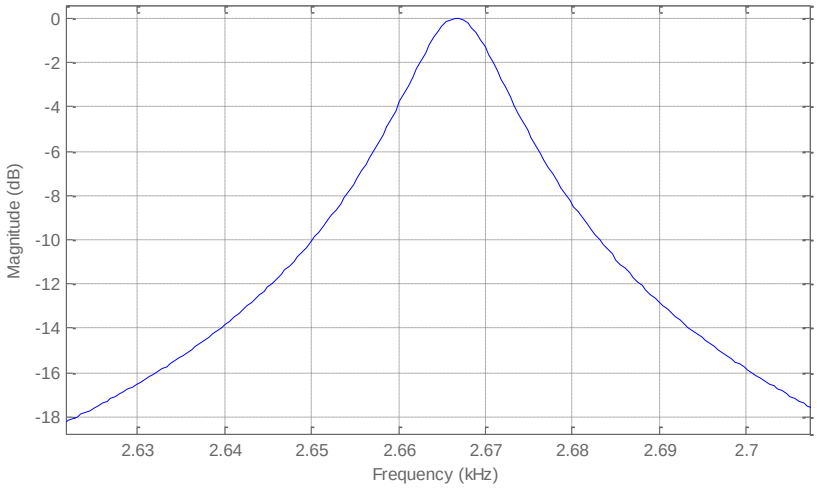

(b) Zoom at the centre frequency

Fig. 5.19 Band-pass filter

Typically, 4 samples (2 for positive half – 2 for negative half) is preferred to represent a sinusoidal signal. Experiments have been carried out by injecting 2.667 kHz (=3 samples) and 2 kHz (=4 samples) signals and it has been validated that both works well.

The LPF in Fig. 5.18 must have a cut-off frequency which is much lower than twice the injected signal frequency. This is to eliminate the right-hand side of (5.29) so that the term which is proportional to $(\partial T/\partial \beta)$ can be extracted. Experiments have been carried out employing LPFs with cut-off frequency ranging between a few Hz and a few

kHz and it has been validated that it is much flexible to design the LPF. The LPF output, then, is checked if it is positive or negative. Afterwards, the integral regulator is employed to generate the *d*- axis current command. It should be noted that the input of the integral regulator is either +1 or -1. This is due to facilitate the integral gain tuning based on desired response time of reference *d*- axis current generation for MTPA operation as per the following criteria. Since the signal processing unit is already fast enough to obtain $(\partial T/\partial \beta)$ for any operating condition, the integral gain defined in (5.52) may be used to tune the control response.

$$K_{i\_SPU} = \frac{\Delta I_d^*}{\Delta t} \tag{5.52}$$

where K_{i_SPU} is the gain of the integral regulator in the signal processing unit. ΔI_d^* is the desired *d*- axis reference current variation within Δt time interval. For example, to obtain 100 A current variation in 1 second, the K_{i_SPU} should be 100.

Fig. 5.20 experimentally validates that the fast response can be achieved with the virtual signal injection based drives. Whilst the response time is significantly slow ~10 seconds to a torque command from 40 to 45 Nm in conventional virtual signal injection based drive in Fig. 5.20-(a), it is evident that the response time is significantly improved in Fig. 5.20-(b) with the design measures discussed above. Due to the LPFs to eliminate measurement noise in the existing scheme, the response is also oscillatory.

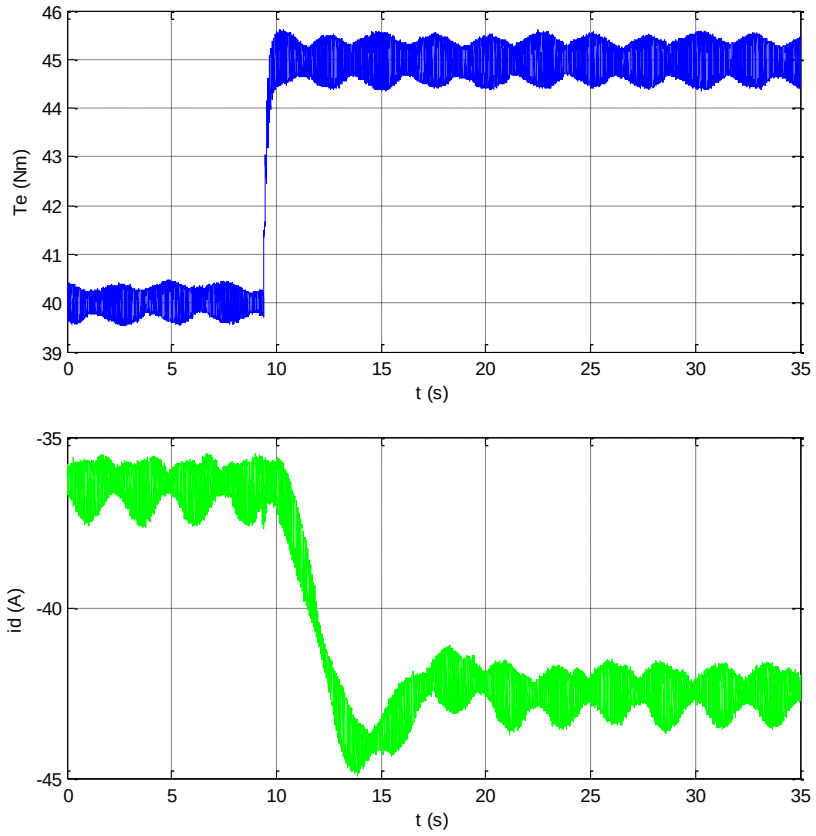

(a) Conventional drive [18]

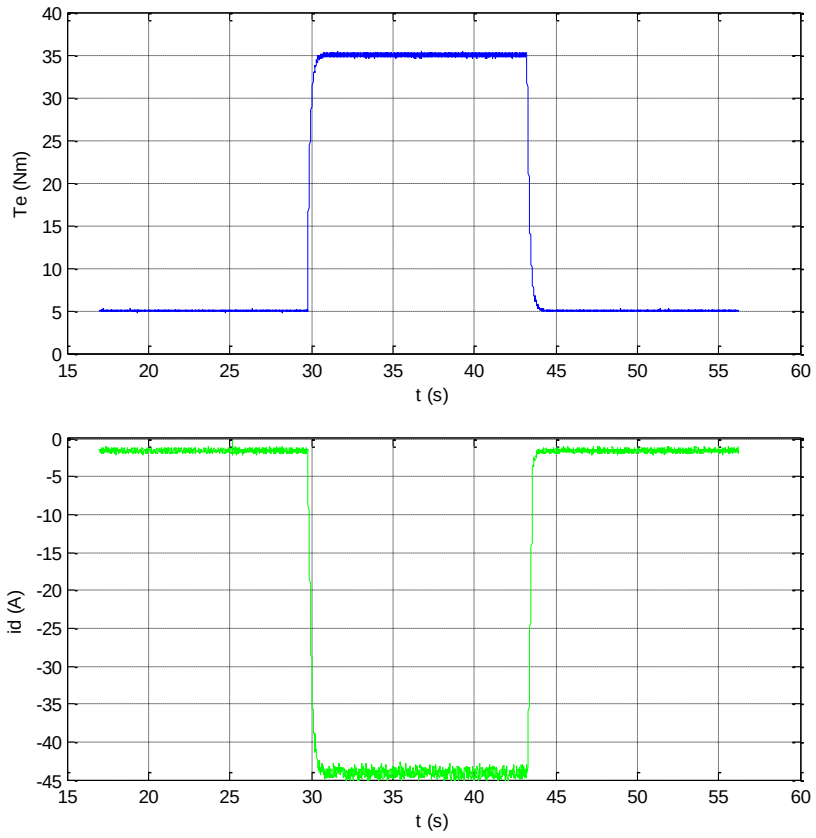

(b) Improved response time with design measures

Fig. 5.20 Experimental validation of the improved response time

5.7. COMPARATIVE STUDIES

The drive system whose schematic is shown in Fig. 5.17 and Fig. 5.18 has been implemented employing (5.27), (5.30) and the proposed compensation discussed in section 5.6. The polynomial representation of the high fidelity machine model for the IPM motor in Table 1.1 has been employed in the simulated drives.

The peak current of the machine is 120 A. Thus, constant current loci are obtained for every 10 A from 20 A to 120 A as shown in Fig. 5.21. By way of example, the current magnitude is kept at 120 A and the current angle of the simulated drive is increased from 0° to 90° in order to obtain the 120 A current locus. As can be seen, the maximum torque is obtained at a certain current angle (MTPA point) and the torque reduces down to 0 Nm when the current angle is 90°. It is seen that the torque that can be produced at $I_s = 120$ A and $\beta = 10°$ is almost same as the torque that can be produced at $I_s = 100$ A and $\beta = 40°$. This implies that 20 A current magnitude can be reduced with 30° current angle variation. Therefore, obtaining optimum current angle is highly important as it minimizes the current magnitude per torque.

It is noteworthy that the MTPA trajectory does not vary with the speed since the torque is not a function of speed. Hence, the simulations in this section are obtained when the machines operate at 1000 r/min. The drives have been simulated at other speeds and the results are the same, as long as the voltage saturation is not reached.

In Fig. 5.21, the drive is simulated employing (5.27) and the trajectory is illustrated by yellow squares. It is evident that the $[\partial T^h/\partial\beta]$ trajectory that is obtained from the simulated virtual signal injection based drive exactly matches the trajectory shown in Fig. 5.10. The simulated drive includes the errors $e1 - e3$ associated with $[\partial L_d/\partial\beta]$, $[\partial L_q/\partial\beta]$ and $[\partial \Psi_m/\partial\beta]$. As will be seen, the deviation from the optimal increases with the current amplitude.

The drive has also been simulated without signal injection. Instead, the reference current angle and the *d*- axis currents for given current magnitude have been obtained by (5.18) and (5.19), respectively. Although the perfect machine parameters have been employed to obtain the current angle, the same trajectory as $[\partial T^h/\partial\beta]$ in Fig. 5.21 have been obtained. This is because both of the virtual signal injection based drive and the drive which employ most common (5.18) and (5.19) suffer from the same error terms

associated with $[\partial L_d/\partial\beta]$, $[\partial L_q/\partial\beta]$ and $[\partial\Psi_m/\partial\beta]$ even though the accurate parameters are employed. As a result, these drives cannot achieve high efficiency operation. In addition, the peak torque production at 120 A is $T_e \approx 66$ Nm whereas the achievable torque is $T_e \approx 68.5$ Nm. Consequently the acceleration performance also reduces.

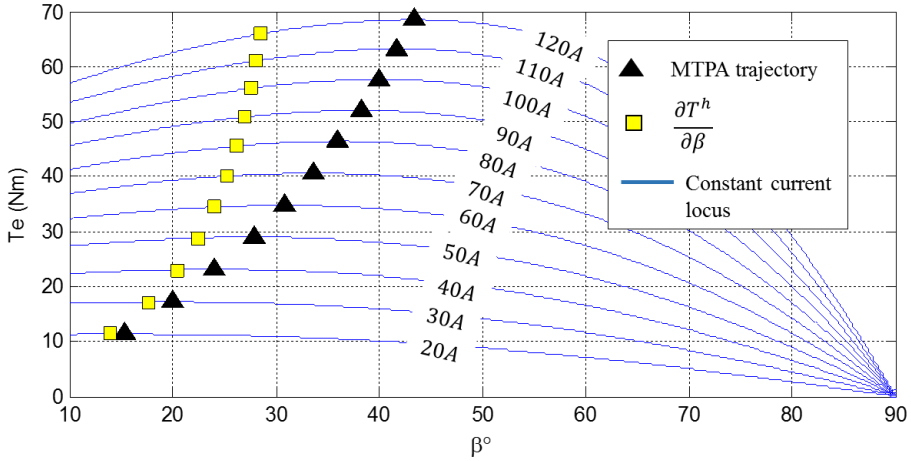

Fig. 5.21 Torque versus current angle for constant current magnitude employing (5.27)

In Fig. 5.22, the drive is simulated employing the existing virtual signal injection based drive. As can be seen, the trajectory is much improved comparing to the techniques in Fig. 5.21. One can compare that the trajectory in Fig. 5.22, matches well with the $[\partial T^{h\_conv}/\partial\beta]$ in Fig. 5.10. Although the trajectory is much improved for this particular IPM machine, the resultant operating point depends on the machine characteristics. In other words, good accuracy of the trajectory is not guaranteed and might be highly inaccurate for other IPM machines as has been evident in Fig. 5.13.

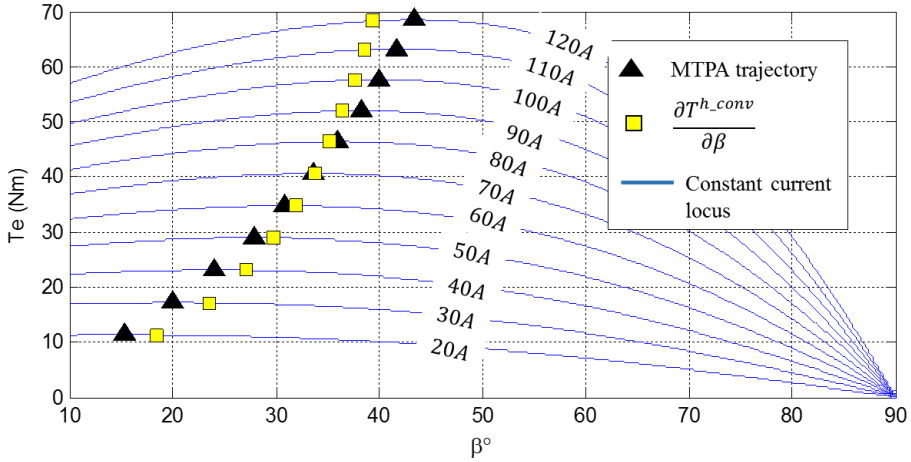

Fig. 5.22 Torque versus current angle for constant current magnitude employing (5.30)

The proposed virtual signal injection based drive with the error compensation associated with $[\partial L_q/\partial\beta]$ is simulated and the resultant operating points are shown in

Fig. 5.23. It is evident that the simulated drive and the theoretical trajectory are matching quite well as shown in Fig. 5.14. Comparing to the Fig. 5.22, the proposed compensation further improves the accuracy. Unlike the existing virtual signal injection based drives, theoretically addressed error compensation renders the proposed technique universal and the operating points very close to the actual MTPA can be achieved.

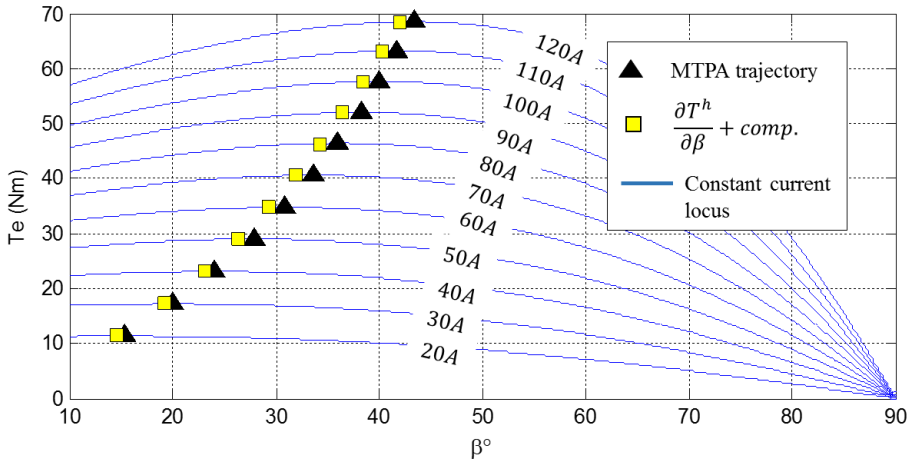

Fig. 5.23 Torque versus current angle for constant current magnitude employing proposed scheme

Fig. 5.24 illustrates the torque versus *d*- axis current for constant current magnitude employing (5.27) in the signal processing unit. The deviation from the optimal *d*- axis current increases with the current magnitude and reaches up to ~24 A at the peak current operation.

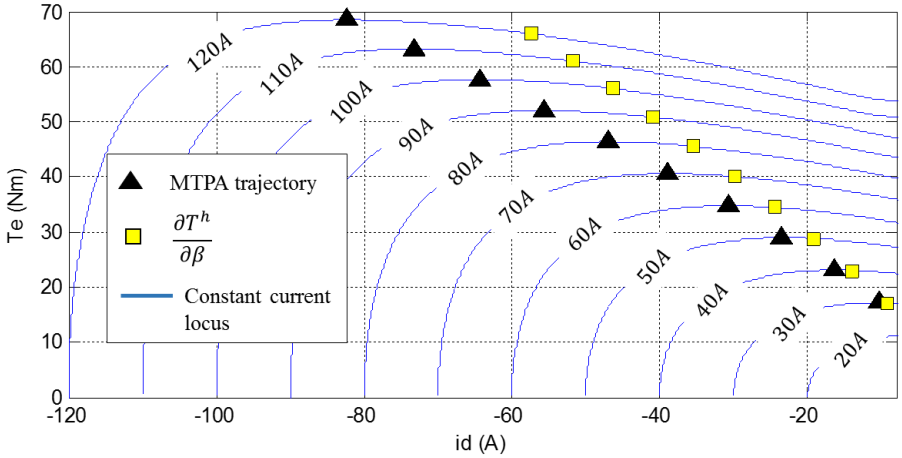

Fig. 5.24 Torque versus *d*- axis current for constant current magnitude employing (5.27)

Fig. 5.25 illustrates the torque versus *d*- axis current for constant current magnitude when the existing virtual signal injection based drive is employed. It is seen in Fig. 5.25-(a) that the operating *d*- axis current magnitude is higher than the optimum

when the torque is below 40 Nm and it is lower than the optimum when the torque is above 40 Nm. Indeed, this is also the case in experimental results in Fig. 5.25-(b) [18]. One can see that the deviation from the optimal *d*- axis current is ~5 A at the peak current operation in Fig. 5.25-(a).

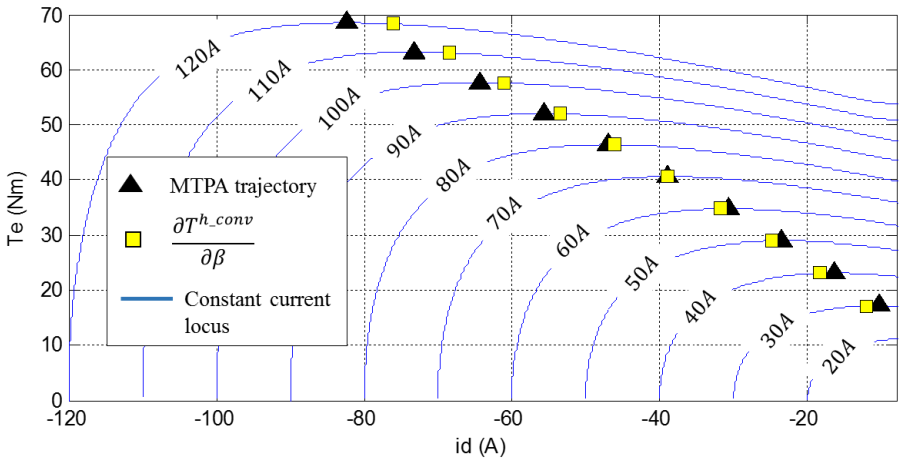

(a) Simulation results

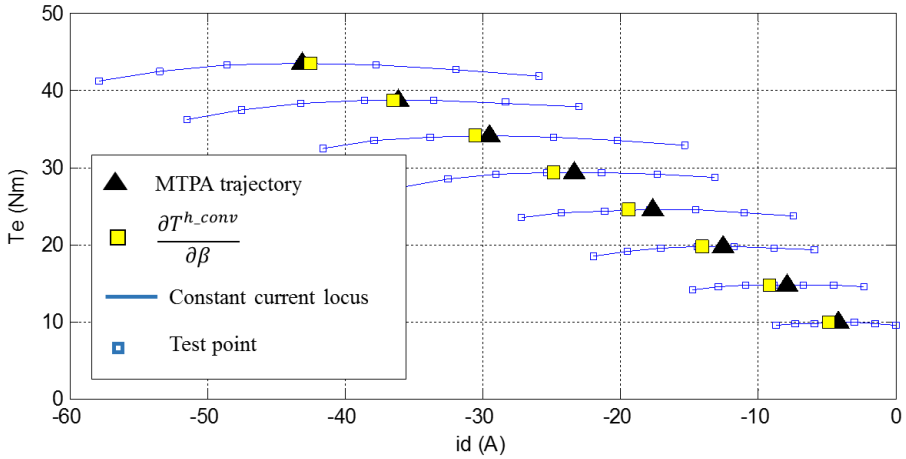

(b) Experimental results [18]

Fig. 5.25 Torque versus *d*- axis current for constant current magnitude employing (5.30)

Fig. 5.26 illustrates the torque versus *d*- axis current for constant current magnitude when the proposed virtual signal injection based drive is employed in the drive. As can be seen, the *d*- axis current deviation from the optimal at 120 A operation is less than 2 A whilst it is around 5 A in the existing virtual signal injection based drives.

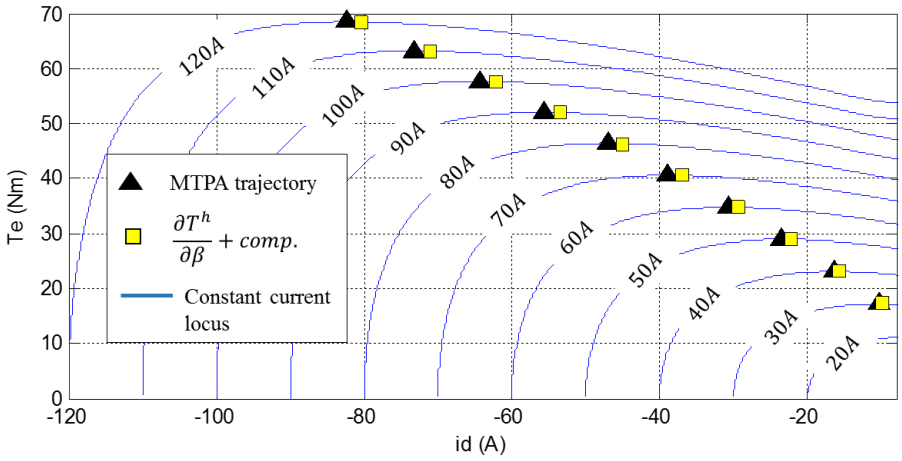

Fig. 5.26 Torque versus *d*- axis current for constant current magnitude employing proposed scheme

The input power versus current angle is shown in Fig. 5.27 when the simulated drive is run with the proposed signal injection method. Since the power is a function of speed, the figure represents the input powers at 1000 r/min. Likewise, Fig. 5.28 shows the output power versus current angle when the simulated drive is run with the proposed scheme. As has been discussed, the virtual signal injection method can be adopted employing input or output power equations and $[\partial P_{in}/\partial\beta]$ or $[\partial P_{out}/\partial\beta]$ can be posed to zero online so that the extremum point can be sought. However, since the power proportionally varies with the speed, the response time also varies at different operating speeds.

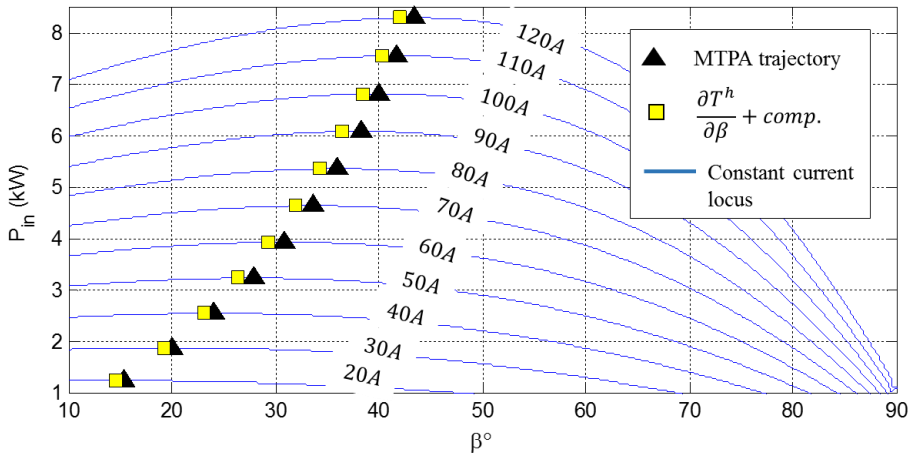

Fig. 5.27 Input power versus *d*- axis current for constant current magnitude with proposed scheme

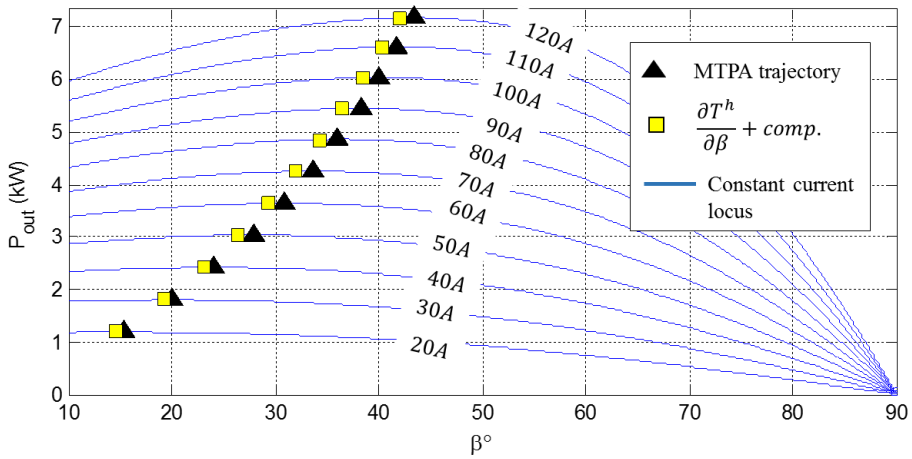

Fig. 5.28 Output power versus *d*- axis current for constant current magnitude with proposed scheme

Fig. 5.29 illustrates the motor efficiency versus current angle for constant current magnitude operation when the proposed scheme is adopted in the drive system. It is evident that the efficiency of the machine reduces when the current amplitude increases. This is because of the copper losses. It is noteworthy that the iron loss is not represented due to its negligible influence in the constant torque region. When the current magnitude increases, the copper losses increases proportional to the square of the current magnitude ($= I^2R$).

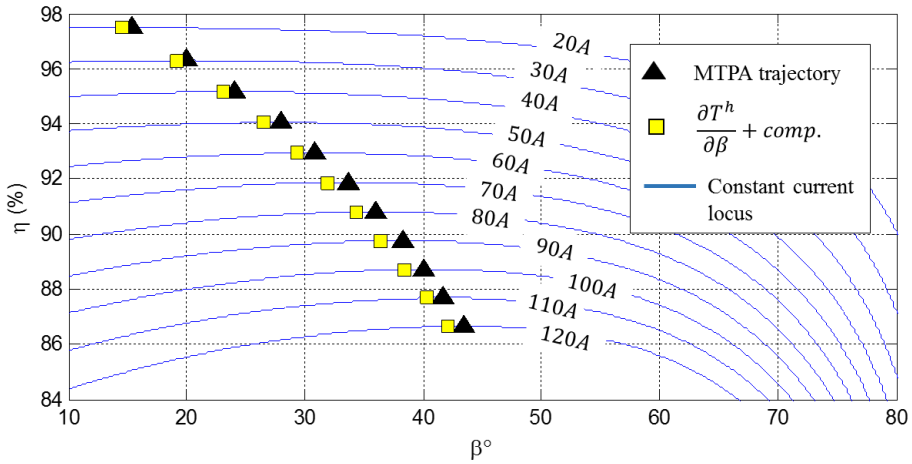

Fig. 5.29 Efficiency versus *d*- axis current for constant current magnitude with proposed scheme

It is evident in Fig. 5.21 that the torque production at $I_s = 120$ A, $\beta = 10°$ and $I_s = 100$ A, $\beta = 40°$ are ~58 Nm. Accordingly, the output powers at these operating points are similar and ~6kW. However, the input powers at these particular operating points are different and they are ~7.05 kW and ~6.8 kW, respectively. This implies that the same torque production can be generated by 250 W lower input power by the current

angle optimization at this particular condition. One can see from Fig. 5.29 that the motor efficiency at these two particular operating points are 84.5% and 88.8%.

5.7.1. INFLUENCE OF PARAMETER VARIATIONS

It has been validated in section 5.5 that the virtual signal injection based drives are model dependent even though they are implemented without employing machine parameters; (L_d, L_q, Ψ_m) such as in the existing virtual signal injection based drives which employ (5.30). Indeed, the existing technique is more vulnerable to parameter variations as they inevitably suffer from each of the errors $e1 - e4$. None of the error terms is compensated whereas the proposed technique accounts the parameter variations by employing *dq*- axis inductances as functions of *dq*- axis currents. In addition, the proposed technique does not include the error term $e4$ and it has been validated that the errors $e2$ and $e3$ reasonably cancels each other. Thus, the proposed technique provides a very good accuracy throughout a wide operating range.

The sensitivity to parameter variations in both the existing and the proposed schemes can be investigated deeply through realistic simulations. In the simulated drives, the parameters L_d, L_q and Ψ_m in the motor model are deliberately altered $\mp 10\%$ whilst the parameters employed in the controller remains same. By doing so, the influence of a real-world motor parameter variations can be studied by the simulated drives. In the following sections, the variations of the permanent magnet flux linkage and the *dq*- axis inductances are studied separately in order to see how the proposed and the existing drives robust/sensitive to their variations.

It is noteworthy that the parameter variations can be studied through simulated drive in two ways. First, the parameters employed in the controller might be altered whereas they remain same in the motor model and the second is vice-versa. Whilst the former does not represent the real-world drive system, the latter does. This is because in a real drive system, the machine parameters deviate from those employed in the controller. Thus, the other way around is not realistic. The difference between the former and the latter is that the optimum trajectory does not vary in the former whereas the optimum trajectory varies in the latter. For these reasons, the motor model has been altered in the simulated drives to represent the real-world machine nonlinearity.

5.7.1.1. VARIATION OF PERMANENT MAGNET FLUX LINKAGE

Fig. 5.30 illustrates the influence of the permanent magnet flux variation for the proposed drive. There are three torque loci which are obtained when Ψ_m in the motor model is altered $\mp 10\%$ as specified in the figure. The current magnitude is constant at 100 A in each locus. The drive is simulated when the current angle varies and the current magnitude is constant and the resultant torque is plotted for varying current angle. As can be seen, the reluctance torque becomes dominant once magnet alignment torque reduces and hence the optimal current angle is increased and vice versa. The resultant operating points with the proposed drive for each condition are also shown in the figure. Since Ψ_m is not employed in the signal injection based control system, the drive system is expected to be robust to its variations. Indeed, this is the case in Fig. 5.30 where the resultant operating point with the proposed technique varies when magnetic flux linkage varies. However, the deviation from the optimal point might be expected to be the same on each locus to represent its adoption. However, this is not the case which can be understood as follows. Although its variation is accounted online, the $e3$ error term associated with $[\partial\Psi_m/\partial\beta]$ differs at each operation and hence the deviation from the optimal point is not the same on each locus.

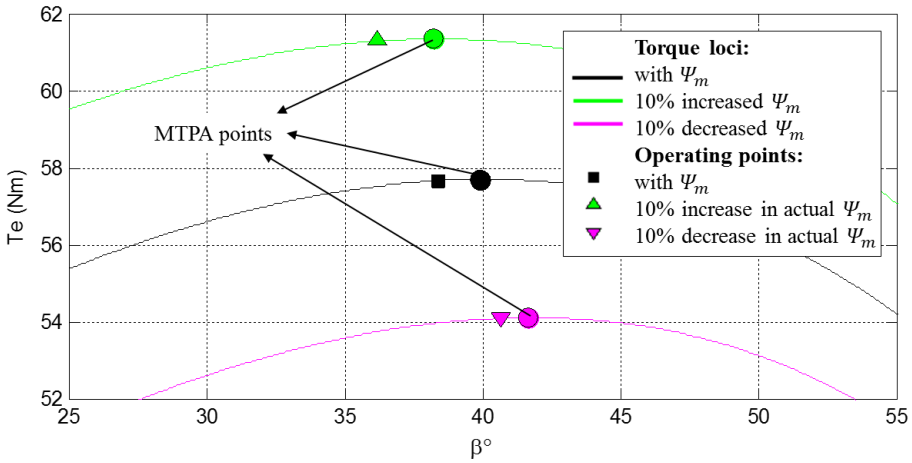

Fig. 5.30 Torque versus current angle when Ψ_m varies (I_s=100 A, proposed drive)

Fig. 5.30 represents a certain operating point at a unique current magnitude and hence it is not comprehensive. Therefore, Fig. 5.31 illustrates the MTPA trajectories of the machine under study throughout whole current range when the permanent magnet flux linkage varies $\mp 10\%$. One can see that Fig. 5.30 and Fig. 5.31 exactly matches at I_s=100 A. The proposed drive is simulated at I_s=60, I_s=80, I_s=100 and I_s=120 A and the resultant operating points are shown in the figures. It is seen that the proposed drive is

robust to permanent magnet flux linkage variation at a wide operating range and the deviation from the MTPA is very low.

The same simulation as in Fig. 5.31 has been done employing the existing virtual signal injection based drive and the results are illustrated in Fig. 5.32. At 120 A operation, the deviation from the optimum is $\Delta\beta \approx 3°$ when the Ψ_m increases 10%. On the other hand, the deviation is $\Delta\beta > 4°$ when Ψ_m reduces 10%. Thus, it is evident that the existing scheme is also model dependent in spite of the fact that the implementation is model-free. By comparisons of Fig. 5.31 and Fig. 5.32, it could be concluded that the proposed drive is more robust to permanent magnet flux variation as it provides better accuracy at a wide operating range.

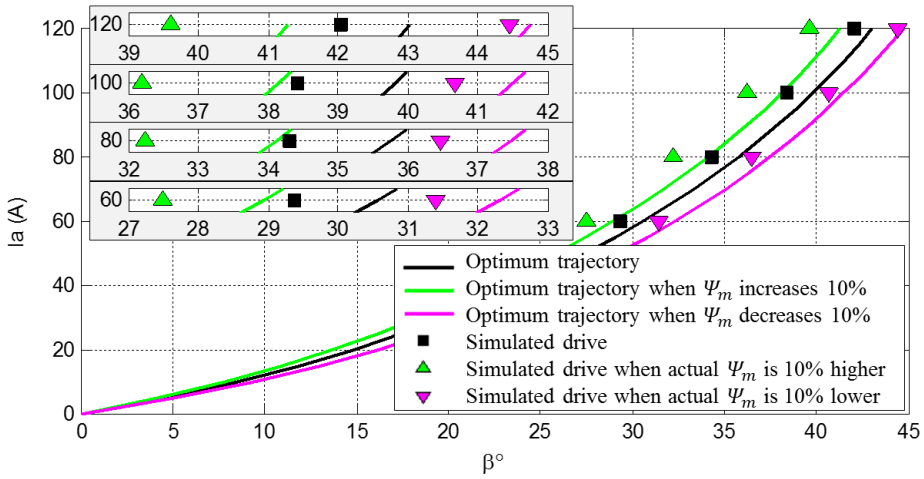

Fig. 5.31 Influence of $\Delta\Psi_m$ on MTPA and the operating points of proposed drive

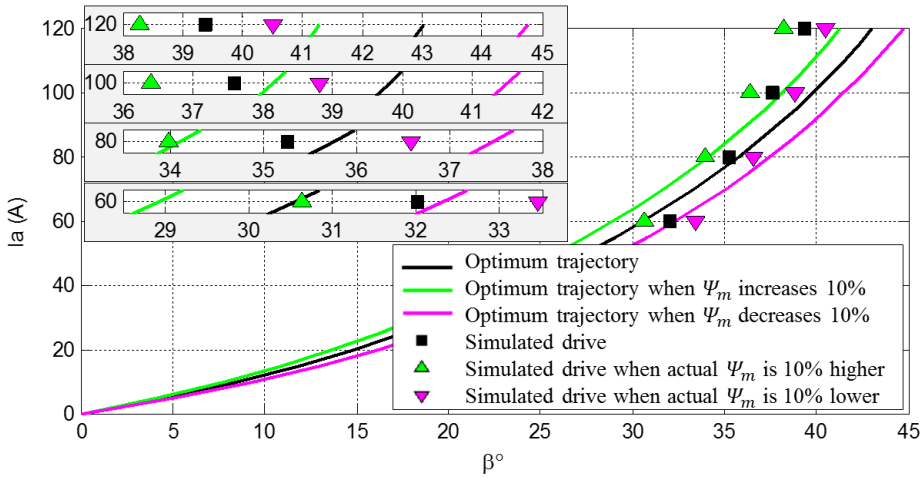

Fig. 5.32 Influence of $\Delta\Psi_m$ on MTPA and the operating points of existing drive

5.7.1.2. VARIATION OF D- AXIS INDUCTANCE

Fig. 5.33 and Fig. 5.34 illustrate the influence of the $\mp 10\%$ *d*- axis inductance variation on the resultant operating points when the proposed and the existing virtual signal injection based drives are employed, respectively. Similar to the permanent magnet flux linkage variation, when the *d*- axis inductance reduces, the MTPA angle increases as shown in the figures and vice-versa. This is due to the fact that the increased reluctance torque and vice-versa. By comparisons of Fig. 5.31 and Fig. 5.33, one can realize that the 10% *d*- axis inductance variation has less influence on the MTPA trajectory than 10% permanent magnet flux linkage variation. It is evident from Fig. 5.33 and Fig. 5.34 that the proposed drive achieves more efficient operation over a wide operating range despite the 10% *d*- axis inductance inaccuracy.

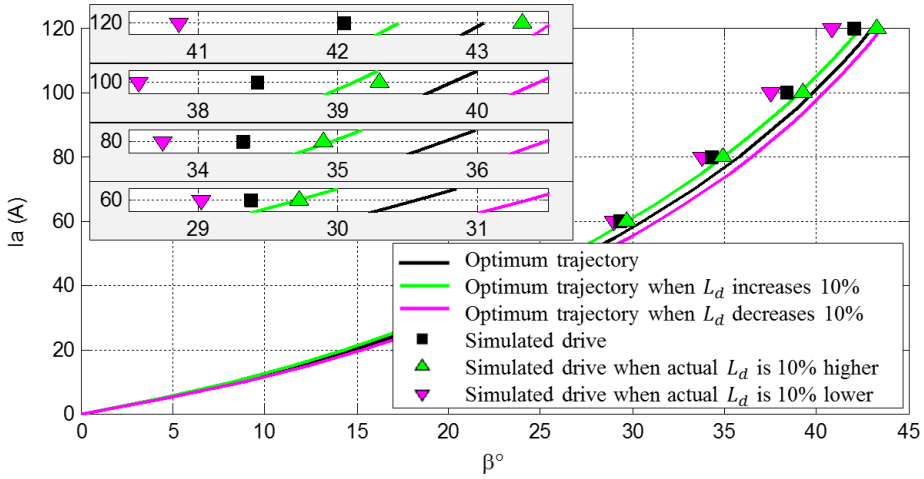

Fig. 5.33 Influence of ΔL_d on MTPA and the operating points of proposed drive

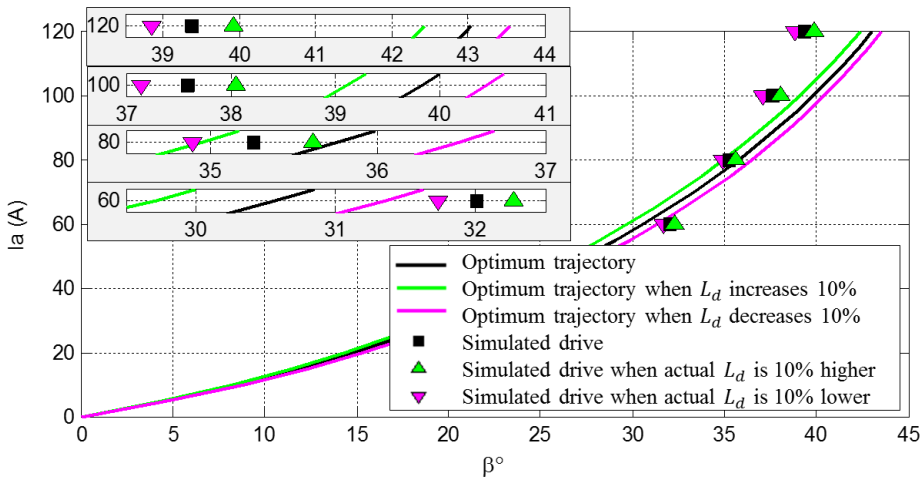

Fig. 5.34 Influence of ΔL_d on MTPA and the operating points of existing drive

5.7.1.3. VARIATION OF Q- AXIS INDUCTANCE

Fig. 5.35 and Fig. 5.36 illustrate the influence of the $\mp 10\%$ *q*- axis inductance variation on the resultant operating points when the proposed and the existing drives are employed, respectively. Unlike the *d*- axis inductance and the permanent magnet flux linkage variations, the reduction in the *q*- axis inductance decreases the MTPA angle and vice-versa as the reluctance torque reduces and the magnet alignment torque becomes more dominant and vice-versa. As can be seen, the proposed drive provides better accuracy over a wide operating range.

It is important to note that the parameter variations in IPM machines pose a significant challenge to achieve high efficiency operation. In particular, the *q*- axis inductance varies more comparing to the other parameters. The *q*- axis inductance of a real-world IPM machine might vary up to several hundred percent [130] as a result of magnetic saturation. However, since the *dq*- axis inductances are modelled as *dq*- axis currents in the proposed drive, 10% error would be the worst scenario. In the existing virtual signal injection based drives, however, the machine parameters are not employed in the controller. This implies for the existing drives that 10% parameter variation would not represent the worst scenario. In other words, 100% *q*- axis inductance variation, which might be the case, will certainly reduce the efficiency further in the existing drives.

5.8. SUMMARY

A great number of field oriented controlled IPM drives suffer from the error terms associated with $[\partial L_d/\partial\beta]$, $[\partial L_q/\partial\beta]$ and $[\partial \Psi_m/\partial\beta]$ for MTPA operation, including the existing virtual signal injection based drives. Indeed, the existing virtual signal injection based drives suffer from an additional error term. It has been validated through detailed theoretical analysis and realistic simulations with high-fidelity machine models that neglecting these errors significantly deviates the operating trajectory from the MTPA. Accordingly, the conventional drives cannot achieve optimal efficiency operation. Moreover, conventional drives may not produce the maximum achievable torque. This would reduce the acceleration performance of the drive train. Furthermore, it has been shown that although the existing virtual signal injection based drive is implemented without employing the machine parameters (L_d, L_q, Ψ_m) they are still model dependent

as the deviation from the MTPA is sensitive to the parameter variations. Evidentially, each of the omitted error terms are sensitive to parameter variations.

In this chapter, a new virtual signal injection based extremum seeking control has been proposed. The response time is much improved by design measures for the signal processing unit. In addition, it has been validated that the proposed drive is much robust to parameter variations. The *dq*- axis inductances are modelled and employed as functions of *dq*- axis currents in the proposed drive and hence the drive operations are very close to the accurate MTPA trajectory.

The superiority of the proposed drive system has been validated by realistic simulation studies and the feasibility of the virtual signal injected drives with improved response time has been confirmed experimentally.

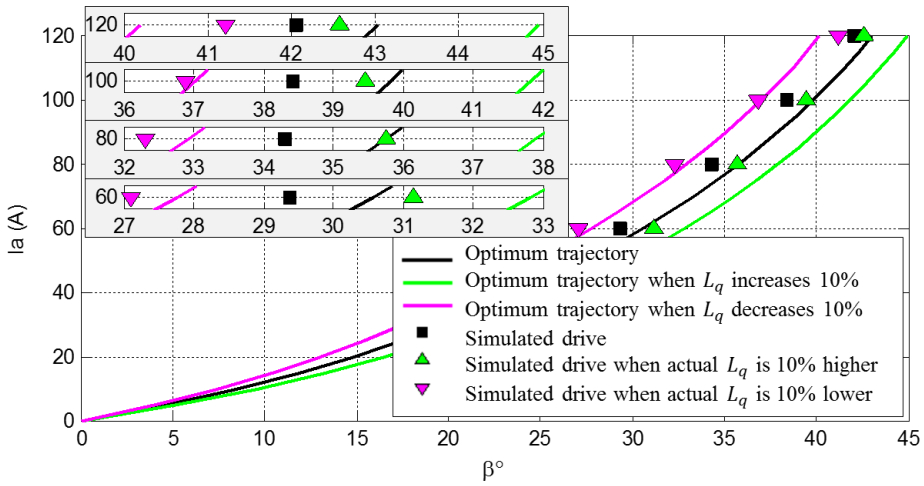

Fig. 5.35 Influence of ΔL_q on MTPA and the operating points of proposed drive

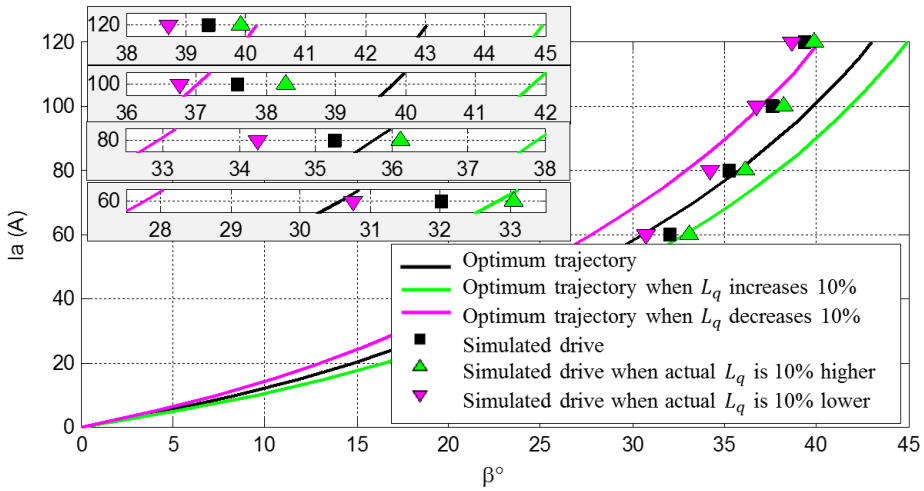

Fig. 5.36 Influence of ΔL_q on MTPA and the operating points of existing drive

CHAPTER 6 – CONCLUSIONS AND FUTURE WORK

6.1. CONCLUSIONS

This thesis investigates the state-of-art control strategies for both FOC and DTC based IPM-BLAC drives for EV and HEV traction applications. As has been discussed widely in the thesis, the ultimate objectives in these drives are to achieve high efficiency operation over wide operating range, smooth output torque production with reasonably fast response and reduced burden on the microprocessor owing to simplified control schemes. To achieve these objectives, it has been shown that a number of challenges as a result of highly nonlinear real-world machine characteristics, distorted inverter output voltage and variation on the DC-link voltage need to be addressed online by employing advanced control strategies and parameter adaptation laws. This thesis, therefore, has proposed and employed novel control schemes for IPM drives to improve the torque control quality with high efficiency operation.

To date, a great number of DTC drives employed Gopinath style closed loop flux observers. However, it has been shown that the torque production with these drives may significantly deteriorate at low speeds. This problem has been addressed by a novel approach in which the current and the voltage based flux estimators are combined with a linear transition trajectory. The distorted torque production has been addressed by a much simpler technique. Thus, low speed performance of these drives has been much improved.

The aforementioned drives, including the one which improves the low speed performance, employ flux observers which combine two different techniques for low and high speed operations. It has been shown that the combined observer structure in these drives results in torque variation when speed varies, although the command torque remains the same. Indeed, in EV applications this may cause a gap in the accelerator pedal if the variation is much. A unified observer structure has been proposed and validated to address the problem. Since the proposed structure consists of high fidelity machine models, the accuracy of the observed variables for feedback control are much improved. This, of course improves the efficiency of the drive train.

It has been discovered that the direct regulation of the electromagnetic torque, such as in DTC drives, results in significant nonlinearity and coupling problems in the control loop. In addition, linear controller design based on a fixed operating point leads to variable control bandwidth for different operating points. MTPV control in DTC drives

is also a challenge since it cannot be adopted directly. These problems have been addressed by the proposed direct stator flux vector control. The proposed approach facilitates simple control tuning and achieves decoupled control in any operating region. Consequently, the proposed drive improves the torque control quality and simplifies the control system.

A large number of FOC based IPM drives, on the other hand, suffer from inaccurate implementation of MTPA control. It has been discovered that even though the machines are accurately modelled and employed in the drives, the operating trajectory still much deviates from the accurate MTPA points because of the implementation inaccuracy. Accordingly, the drive efficiency reduces greatly. A mathematically injected high-frequency small sinusoidal signal has been utilized to realize the accurate MTPA control. The realistic simulation studies with high-fidelity machine models for traction applications show much improvement on the system efficiency owing to online extremum seeking control, *i.e.* MTPA. In addition, the response time of the existing techniques has been much improved by the design measures in the proposed approach.

6.2. FUTURE WORK

As the thesis deals with both the FOC and the SFVC BLAC drives, the future work can also be discussed in two groups. However, it is noteworthy that the power conversion techniques are common in both schemes and hence its development is applicable to both drive systems.

Space vector PWM has been adopted as a power conversion technique in this thesis as it is the most common technique in modern drives. The inverter output voltage, however, can be enhanced by ~10% by adopting six-step operation. Further utilization of the DC-link voltage is attractive for EV traction applications as it facilitates more extended speed range. There are several techniques to implement six-step operation. The current waveforms, harmonic distortion and the efficiencies in FW region should be compared thoroughly with different six-step strategies and the classical circle-limit (SVPWM) operations in order to assess how the voltage distortion in the nonlinear region of the hexagon degrades the current quality. In other words, the comparative study between the extended speed range and the distorted torque production with six-step operation may be further investigated to close a knowledge gap in the literature.

6.2.1. FUTURE WORK FOR FOC DRIVES

High efficiency operation has been achieved in the constant torque region with the proposed virtual signal injection based control scheme. The efficiency optimization may also be extended for constant power operation by utilization of the voltage saturation.

In addition, the concept of the virtual signal injection control may be utilized for other machine types such as induction machines. Hence, the online optimal efficiency control may be studied for various drives.

Moreover, various applications which employ real signal injection techniques such as sensorless control may also be enhanced by virtual signal injection concept.

The coupling terms of the machine model in rotor reference frame is decoupled in the feed-forward path employing either machine parameters or estimated *dq*- axis flux linkages. The decoupling compensation is important when speed changes rapidly in a drive system. Thus, the decoupling may be improved by high fidelity machine models such as discussed in Chapter 3.

6.2.2. FUTURE WORK FOR SFVC DRIVES

The MTPA operation in stator flux oriented drives is realized by optimum stator flux magnitude for a given torque. The reference stator flux magnitude is commonly generated from a LUT with the command torque being input. However, the modelling errors in the LUT will deviate the trajectory from MTPA points. Therefore, online compensation for the modelling errors or a different approach to generate reference stator flux magnitude may significantly improve the drive efficiency in the constant torque region. By way of example, the proposed virtual signal injection concept in Chapter 5 may be utilized for the optimal efficiency operation (reference stator flux magnitude compensation) in SFVC drives.

In addition, the SFVC drives are more sensitive to inverter nonlinearities when voltage based flux estimation is employed in the feedback. Clearly, it is due to the voltage distortion at the output of the inverter. To date, a large number of publications reported in the literature have studied the inverter nonlinearity compensation in the feed-forward path. In other words, the inverter reference voltages or the on-time commands for the switches have been altered/compensated in a large number of studies. However, since the

drive system is closed-loop, the compensation study in the feedback has significant potential to further improve observer accuracy and hence the drive efficiency. Therefore, online estimation of the voltage drop at the output of the inverter considering the dead-time and the threshold voltages of the power electronic devices may be utilized for compensations to improve the observer quality in the feedback path.

In conventional SFVC drives where the torque or the τ- axis current is regulated, the phase angle of the stator flux vector is realized indirectly in a coupled way. Therefore, the conventional schemes are more vulnerable to instability if the control gain (bandwidth) is high. The study on instability conditions of conventional drives may be quite useful since these schemes are extensively adopted in the literature.

A computationally efficient approaches to generate the reference torque angle for given torque command may be studied in future since creating 2D LUTs through time domain simulation is time consuming and not scalable.

The proposed observer in Chapter 3 is vulnerable to machine temperature variations. Although the resultant influence is relatively small compared to the other observer schemes, the proposed observer can be further improved by taking temperature variation into account. Thus, the compensation for temperature variation can be addressed if the winding temperature is measured in a drive system. The winding and magnet temperatures may be different in a practical drive, however, small difference between the two will have negligible influence as has been shown in Chapter 3.

REFERENCES

[1] W. Sweet, "Greenhouse Gas Trends," *IEEE Spectrum*, vol. 45, pp. 88-88, 2008.

[2] S. Walker, K. W. Hipel, and I. Takehiro, "Strategic analysis of the Kyoto Protocol," in *Systems, Man and Cybernetics, 2007. ISIC. IEEE International Conference on*, 2007, pp. 1806-1811.

[3] B. M. Wilamowski and J. D. Irwin, *The Industrial Electronics Handbook Power electronics and motor drives* 2nd ed.: CRCPress, 2011.

[4] D. G. Holmes and T. Lipo, *Pulse Width Modulation for Power Converters: Principles and Practice*: IEEE Press, 2003.

[5] R. Ottersten and J. Svensson, "Vector current controlled voltage source converter-deadbeat control and saturation strategies," *IEEE Transactions on Power Electronics*, vol. 17, pp. 279-285, 2002.

[6] K. Yong-Cheol, K. Sungmin, and S. Seung-Ki, "Six-Step Operation of PMSM With Instantaneous Current Control," *IEEE Transactions on Industry Applications*, vol. 50, pp. 2614-2625, 2014.

[7] N. Bianchi and T. M. Jahns, *Design, analysis, and control of interior PM synchronous machines*. IAS Annu. Meeting: Proc. IEEE IAS Tutorial Course Notes, 2004

[8] S. Jul-Ki, K. Joohn-Sheok, and S. Seung-Ki, "Overmodulation strategy for high-performance torque control," *IEEE Transactions on Power Electronics*, vol. 13, pp. 786-792, 1998.

[9] L. Dong-Choon and G. M. Lee, "A novel overmodulation technique for space-vector PWM inverters," *IEEE Transactions on Power Electronics*, vol. 13, pp. 1144-1151, 1998.

[10] K. SeHwan and S. Jul-Ki, "Maximum Voltage Utilization of IPMSMs Using Modulating Voltage Scalability for Automotive Applications," *IEEE Transactions on Power Electronics*, vol. 28, pp. 5639-5646, 2013.

[11] T. Sun, J. Wang, M. Koc, and X. Chen, "Self-Learning MTPA Control of Interior Permanent Magnet Synchronous Machine Drives Based on Virtual Signal Injection," *IEEE Transactions on Industry Applications*, vol. 52, pp. 3062-3070, 2016.

[12] T. Sun, J. Wang, and M. Koc, "Virtual Signal Injection Based Direct Flux Vector Control of IPMSM Drives," *IEEE Transactions on Industrial Electronics*, vol. 63, pp. 4773-4782, 2016.

[13] M. Koc, J. Wang, and T. Sun, "Stator flux oriented control for high performance interior permanent magnet synchronous machine drives," in *Power Electronics, Machines and Drives (PEMD 2016), 8th IET International Conference on*, 2016, pp. 1-6.

[14] M. Koc, J. Wang, and T. Sun, "An Inverter Nonlinearity Independent Flux Observer for Direct Torque Controlled High Performance Interior Permanent Magnet Brushless AC Drives," *IEEE Transactions on Power Electronics*, vol. 32, pp. 490-502, 2017.

[15] M. Koc, T. Sun, and J. Wang, "A linear combination of current and voltage based flux observers for direct torque controlled IPM drives," in *Power Electronics, Machines and Drives (PEMD 2016), 8th IET International Conference on*, 2016, pp. 1-6.

[16] T. Sun, J. Wang, M. Koc, and X. Chen, "Self-learning MTPA control of interior permanent magnet synchronous machine drives based on virtual signal injection," in *Electric Machines & Drives Conference (IEMDC), 2015 IEEE International*, 2015, pp. 1056-1062.

[17] T. F. Sun and J. B. Wang, "Extension of Virtual-Signal-Injection-Based MTPA Control for Interior Permanent-Magnet Synchronous Machine Drives Into the Field-Weakening Region," *IEEE Transactions on Industrial Electronics*, vol. 62, pp. 6809-6817, Nov 2015.

[18] T. Sun, J. Wang, and X. Chen, "Maximum Torque Per Ampere (MTPA) Control for Interior Permanent Magnet Synchronous Machine Drives Based on Virtual Signal Injection," *IEEE Transactions on Power Electronics*, vol. 30, pp. 5036-5045, 2015.

[19] X. Wei and R. D. Lorenz, "Reduced Parameter Sensitivity Stator Flux Linkage Observer in Deadbeat-Direct Torque and Flux Control for IPMSMs," *IEEE Transactions on Industry Applications*, vol. 50, pp. 2626-2636, 2014.

[20] B. Boazzo and G. Pellegrino, "Model Based, Direct Flux Vector Control of Permanent Magnet Synchronous Motor Drives," *IEEE Transactions on Industry Applications*, vol. 51, pp. 3126-3136, 2015.

[21] G. Pellegrino, B. Boazzo, and T. Jahns, "Plug-in, Direct Flux Vector Control of PM Synchronous Machine Drives," *IEEE Transactions on Industry Applications*, vol. 51, pp. 3848-3857, 2015.

[22] G. Pellegrino, B. Boazzo, and T. M. Jahns, "Direct Flux Control of PM synchronous motor drives for traction applications," in *Transportation Electrification Conference and Expo (ITEC), 2014 IEEE*, 2014, pp. 1-6.

[23] G. Pellegrino, B. Boazzo, and T. M. Jahns, "Plug-in, direct flux vector control of PM synchronous machine drives," in *Energy Conversion Congress and Exposition (ECCE), 2014 IEEE*, 2014, pp. 4835-4842.

[24] T. Lixin, Z. Limin, M. F. Rahman, and H. Yuwen, "A novel direct torque controlled interior permanent magnet synchronous machine drive with low ripple in flux and torque and fixed switching frequency," *IEEE Transactions on Power Electronics*, vol. 19, pp. 346-354, 2004.

[25] I. Takahashi and T. Noguchi, "A New Quick-Response and High-Efficiency Control Strategy of an Induction Motor," *IEEE Transactions on Industry Applications*, vol. IA-22, pp. 820-827, 1986.

[26] M. E. Haque and M. F. Rahman, "Incorporating control trajectories with the direct torque control scheme of interior permanent magnet synchronous motor drive," *Electric Power Applications, IET*, vol. 3, pp. 93-101, 2009.

[27] L. Zhong, M. F. Rahman, W. Y. Hu, K. W. Lim, and M. A. Rahman, "A direct torque controller for permanent magnet synchronous motor drives," *IEEE Transactions on Energy Conversion*, vol. 14, pp. 637-642, 1999.

[28] M. F. Rahman, L. Zhong, and L. Khiang Wee, "A direct torque-controlled interior permanent magnet synchronous motor drive incorporating field weakening," *IEEE Transactions on Industry Applications*, vol. 34, pp. 1246-1253, 1998.

[29] L. Zhong, M. F. Rahman, W. Y. Hu, and K. W. Lim, "Analysis of direct torque control in permanent magnet synchronous motor drives," *IEEE Transactions on Power Electronics*, vol. 12, pp. 528-536, 1997.

[30] H. Khoa Dang, Z. Zi-Qiang, and M. Foster, "Direct torque control of permanent magnet brushless AC drive with single-phase open-circuit fault accounting for influence of inverter voltage drop," *Electric Power Applications, IET*, vol. 7, pp. 369-380, 2013.

[31] K. D. Hoang, Z. Q. Zhu, and M. Foster, "Optimum look-up table for reduction of current harmonics in direct torque controlled dual three-phase permanent magnet brushless AC machine drives," in *Power Electronics, Machines and Drives (PEMD 2012), 6th IET International Conference on*, 2012, pp. 1-6.

[32] H. Khoa Dang, R. Yuan, Z. Zi-Qiang, and M. Foster, "Modified switching-table strategy for reduction of current harmonics in direct torque controlled dual-three-phase permanent magnet synchronous machine drives," *Electric Power Applications, IET*, vol. 9, pp. 10-19, 2015.

[33] H. Aorith, J. Wang, and P. Lazari, "A new Loss Minimization Algorithm for Interior Permanent Magnet Synchronous Machine drives," in *Electric Machines & Drives Conference (IEMDC), 2013 IEEE International*, 2013, pp. 526-533.

[34] S. Morimoto, M. Sanada, and Y. Takeda, "Wide-speed operation of interior permanent magnet synchronous motors with high-performance current regulator," *IEEE Transactions on Industry Applications*, vol. 30, pp. 920-926, 1994.

[35] S. Morimoto, M. Sanada, and Y. Takeda, "Performance of PM/reluctance hybrid motor with multiple flux-barrier," in *Power Conversion Conference - Nagaoka 1997., Proceedings of the*, 1997, pp. 649-654 vol.2.

[36] K. D. Hoang, J. Wang, M. Cyriacks, A. Melkonyan, and K. Kriegel, "Feed-forward torque control of interior permanent magnet brushless AC drive for traction applications," in *Electric Machines & Drives Conference (IEMDC), 2013 IEEE International*, 2013, pp. 152-159.

[37] S. Morimoto, Y. Takeda, T. Hirasa, and K. Taniguchi, "Expansion of operating limits for permanent magnet motor by current vector control considering inverter capacity," *IEEE Transactions on Industry Applications*, vol. 26, pp. 866-871, 1990.

[38] S. R. Macminn and T. M. Jahns, "Control techniques for improved high-speed performance of interior PM synchronous motor drives," *IEEE Transactions on Industry Applications*, vol. 27, pp. 997-1004, 1991.

[39] R. Krishnan, "Control and operation of PM synchronous motor drives in the field-weakening region," in *Industrial Electronics, Control, and Instrumentation, 1993. Proceedings of the IECON '93., International Conference on*, 1993, pp. 745-750 vol.2.

[40] M. N. Uddin and M. Azizur Rahman, "High-Speed Control of IPMSM Drives Using Improved Fuzzy Logic Algorithms," *IEEE Transactions on Industrial Electronics*, vol. 54, pp. 190-199, 2007.

[41] M. M. Bech, T. S. Frederiksen, and P. Sandholdt, "Accurate torque control of saturated interior permanent magnet synchronous motors in the field-weakening region," in *Industry Applications Conference, 2005. Fourtieth IAS Annual Meeting. Conference Record of the 2005*, 2005, pp. 2526-2532 Vol. 4.

[42] H. W. de Kock, A. J. Rix, and M. J. Kamper, "Optimal Torque Control of Synchronous Machines Based on Finite-Element Analysis," *IEEE Transactions on Industrial Electronics*, vol. 57, pp. 413-419, 2010.

[43] S. Shinn-Ming and P. Ching-Tsai, "Voltage-Constraint-Tracking-Based Field-Weakening Control of IPM Synchronous Motor Drives," *IEEE Transactions on Industrial Electronics*, vol. 55, pp. 340-347, 2008.

[44] N. Bianchi, S. Bolognani, and M. Zigliotto, "High-performance PM synchronous motor drive for an electrical scooter," *IEEE Transactions on Industry Applications*, vol. 37, pp. 1348-1355, 2001.

[45] K. Jang-Mok and S. Seung-Ki, "Speed control of interior permanent magnet synchronous motor drive for the flux weakening operation," *IEEE Transactions on Industry Applications*, vol. 33, pp. 43-48, 1997.

[46] J. Wai and T. M. Jahns, "A new control technique for achieving wide constant power speed operation with an interior PM alternator machine," in *Industry Applications Conference, 2001. Thirty-Sixth IAS Annual Meeting. Conference Record of the 2001 IEEE*, 2001, pp. 807-814 vol.2.

[47] T. M. Jahns, "Flux-Weakening Regime Operation of an Interior Permanent-Magnet Synchronous Motor Drive," *IEEE Transactions on Industry Applications*, vol. IA-23, pp. 681-689, 1987.

[48] K. Tae-Suk and S. Seung-Ki, "Novel Antiwindup of a Current Regulator of a Surface-Mounted Permanent-Magnet Motor for Flux-Weakening Control," *IEEE Transactions on Industry Applications*, vol. 42, pp. 1293-1300, 2006.

[49] K. D. Hoang, J. Wang, and H. Aorith, "Online feedback-based field weakening control of interior permanent magnet brushless AC drives for traction applications accounting for nonlinear inverter characteristics," in *Power Electronics, Machines and Drives (PEMD 2014), 7th IET International Conference on*, 2014, pp. 1-6.

[50] K. Tae-Suk, C. Gi-Young, K. Mu-Shin, and S. Seung-Ki, "Novel Flux-Weakening Control of an IPMSM for Quasi-Six-Step Operation," *IEEE Transactions on Industry Applications*, vol. 44, pp. 1722-1731, 2008.

[51] B. Bon-Ho, N. Patel, S. Schulz, and S. Seung-Ki, "New field weakening technique for high saliency interior permanent magnet motor," in *Industry Applications Conference, 2003. 38th IAS Annual Meeting. Conference Record of the*, 2003, pp. 898-905 vol.2.

[52] Y. Jung-Sik, S. Seung-Ki, B. Bon-Ho, N. R. Patel, and S. Hiti, "Modified Current Control Schemes for High-Performance Permanent-Magnet AC Drives With Low Sampling to Operating Frequency Ratio," *IEEE Transactions on Industry Applications*, vol. 45, pp. 763-771, 2009.

[53] R. U. Lenke, R. W. De Doncker, K. Mu-Shin, K. Tae-Suk, and S. Seung-Ki, "Field Weakening Control of Interior Permanent Magnet Machine using Improved Current Interpolation Technique," in *Power Electronics Specialists Conference, 2006. PESC '06. 37th IEEE*, 2006, pp. 1-5.

[54] G. Pellegrino, R. I. Bojoi, and P. Guglielmi, "Unified Direct-Flux Vector Control for AC Motor Drives," *IEEE Transactions on Industry Applications*, vol. 47, pp. 2093-2102, 2011.

[55] T. Sun, J. Wang, and M. Koc, "Self-learning Direct Flux Vector Control of Interior Permanent Magnet Machine Drives," *IEEE Transactions on Power Electronics*, 2016.

[56] M. Koc, T. Sun, and J. Wang, "Performance improvement of direct torque controlled interior mounted permanent magnet drives by employing a linear combination of current and voltage based flux observers," *IET Power Electronics*, vol. 9, pp. 2052-2059, 2016.

[57] Y. Inoue, S. Morimoto, and M. Sanada, "Control Method Suitable for Direct-Torque-Control-Based Motor Drive System Satisfying Voltage and Current Limitations," *IEEE Transactions on Industry Applications*, vol. 48, pp. 970-976, 2012.

[58] Y. Inoue, S. Morimoto, and M. Sanada, "Comparative Study of PMSM Drive Systems Based on Current Control and Direct Torque Control in Flux-Weakening Control Region," *IEEE Transactions on Industry Applications*, vol. 48, pp. 2382-2389, 2012.

[59] G. Pellegrino, E. Armando, and P. Guglielmi, "Direct-Flux Vector Control of IPM Motor Drives in the Maximum Torque Per Voltage Speed Range," *IEEE Transactions on Industrial Electronics*, vol. 59, pp. 3780-3788, 2012.

[60] Y. Anno and S. Seung-Ki, "Design of Flux Observer Robust to Interior Permanent-Magnet Synchronous Motor Flux Variation," *IEEE Transactions on Industry Applications*, vol. 45, pp. 1670-1677, 2009.

[61] P. L. Jansen and R. D. Lorenz, "A physically insightful approach to the design and accuracy assessment of flux observers for field oriented induction machine drives," *IEEE Transactions on Industry Applications*, vol. 30, pp. 101-110, 1994.

[62] L. Jae Suk, C. Chan-Hee, S. Jul-Ki, and R. D. Lorenz, "Deadbeat-Direct Torque and Flux Control of Interior Permanent Magnet Synchronous Machines With Discrete Time Stator Current and Stator Flux Linkage Observer," *IEEE Transactions on Industry Applications*, vol. 47, pp. 1749-1758, 2011.

[63] K. Jang-Hwan, C. Jong-Woo, and S. Seung-Ki, "Novel rotor-flux observer using observer characteristic function in complex vector space for field-oriented induction motor drives," *IEEE Transactions on Industry Applications*, vol. 38, pp. 1334-1343, 2002.

[64] Y. Jeong and S. Sul, "Adaptive Flux Observer with On-line Inductance Estimation of an IPMSM Considering Magnetic Saturation," in *Power Electronics Specialists Conference, 2005. PESC '05. IEEE 36th*, 2005, pp. 2467-2473.

[65] G. Pellegrino, E. Armando, and P. Guglielmi, "Direct Flux Field-Oriented Control of IPM Drives With Variable DC Link in the Field-Weakening Region," *IEEE Transactions on Industry Applications*, vol. 45, pp. 1619-1627, 2009.

[66] G. Pellegrino, E. Armando, and P. Guglielmi, "Direct-flux field-oriented control of IPM motor drives with robust exploitation of the maximum torque per voltage speed range," in *Industrial Electronics (ISIE), 2010 IEEE International Symposium on*, 2010, pp. 1271-1277.

[67] M. F. Rahman and L. Zhong, "Comparison of torque responses of the interior permanent magnet motor under PWM current and direct torque controls," in *Industrial Electronics Society, 1999. IECON '99 Proceedings. The 25th Annual Conference of the IEEE*, 1999, pp. 1464-1470 vol.3.

[68] M. F. Rahman, M. E. Haque, T. Lixin, and Z. Limin, "Problems associated with the direct torque control of an interior permanent-magnet synchronous motor drive and their remedies," *IEEE Transactions on Industrial Electronics*, vol. 51, pp. 799-809, 2004.

[69] T. Seki, Y. Inoue, S. Morimoto, and M. Sanada, "Estimated flux compensation for direct torque control in M-T frame synchronized with stator flux-linkage vector," in *ECCE Asia Downunder (ECCE Asia), 2013 IEEE*, 2013, pp. 759-764.

[70] T. Inoue, Y. Inoue, S. Morimoto, and M. Sanada, "Mathematical Model for MTPA Control of Permanent-Magnet Synchronous Motor in Stator Flux Linkage Synchronous Frame," *IEEE Transactions on Industry Applications*, vol. 51, pp. 3620-3628, 2015.

[71] Y. Inoue, S. Morimoto, and M. Sanada, "Examination and Linearization of Torque Control System for Direct Torque Controlled IPMSM," *IEEE Transactions on Industry Applications*, vol. 46, pp. 159-166, 2010.

[72] C. Chan-Hee, S. Jul-Ki, and R. D. Lorenz, "Wide-Speed Direct Torque and Flux Control for Interior PM Synchronous Motors Operating at Voltage and Current Limits," *IEEE Transactions on Industry Applications*, vol. 49, pp. 109-117, 2013.

[73] X. Wei and R. D. Lorenz, "High frequency injection-based stator flux linkage and torque estimation for DB-DTFC implementation on IPMSMs considering cross-saturation effects," in *Energy Conversion Congress and Exposition (ECCE), 2013 IEEE*, 2013, pp. 844-851.

[74] W. Yukai, S. Tobayashi, and R. D. Lorenz, "Deadbeat-direct torque and flux control on low switching frequency induction machine drives using the enhanced flux observer and torque model," in *Energy Conversion Congress and Exposition (ECCE), 2013 IEEE*, 2013, pp. 1786-1793.

[75] B. Boazzo and G. Pellegrino, "Predictive direct flux vector control of Permanent Magnet Synchronous Motor drives," in *Energy Conversion Congress and Exposition (ECCE), 2013 IEEE*, 2013, pp. 2086-2093.

[76] Y. Anno, S. Seung-Ki, L. Dong-Cheol, and J. Cha-Seung, "Novel Speed and Rotor Position Estimation Strategy Using a Dual Observer for Low-Resolution Position Sensors," *IEEE Transactions on Power Electronics*, vol. 24, pp. 2897-2906, 2009.

[77] A. Visioli, "Modified anti-windup scheme for PID controllers," *Control Theory and Applications, IEE Proceedings* -, vol. 150, pp. 49-54, 2003.

[78] A. S. Hodel and C. E. Hall, "Variable-structure PID control to prevent integrator windup," *IEEE Transactions on Industrial Electronics*, vol. 48, pp. 442-451, 2001.

[79] X. Chen, J. Wang, B. Sen, P. Lazari, and T. Sun, "A High-Fidelity and Computationally Efficient Model for Interior Permanent-Magnet Machines Considering the Magnetic Saturation, Spatial Harmonics, and Iron Loss Effect," *IEEE Transactions on Industrial Electronics*, vol. 62, pp. 4044-4055, 2015.

[80] X. Chen, J. Wang, and A. Griffo, "A High-Fidelity and Computationally Efficient Electro-thermally Coupled Model for Interior Permanent-Magnet Machines in Electric Vehicle Traction Applications," *IEEE Transactions on Transportation Electrification*, vol. 1, pp. 336-347, 2015.

[81] B. Singh, S. Jain, and S. Dwivedi, "Torque ripple reduction technique with improved flux response for a direct torque control induction motor drive," *Power Electronics, IET*, vol. 6, pp. 326-342, 2013.

[82] N. Q. Dai, R. Dutta, and M. F. Rahman, "Comparative performance analysis of field-oriented control and direct torque control for a fractional-slot concentrated winding

interior permanent magnet synchronous machine," in *Electrical Machines (ICEM), 2012 XXth International Conference on*, 2012, pp. 879-885.

[83] Y. Choi, H. Choi, and J. Jung, "Feedback Linearization Direct Torque Control with Reduced Torque and Flux Ripples for IPMSM Drives," *IEEE Transactions on Power Electronics*, vol. 31, pp. 3728-3737, 2015.

[84] L. Jae Suk, C. Chan-Hee, S. Jul-Ki, and R. D. Lorenz, "Deadbeat direct torque and flux control of interior permanent magnet machines with discrete time stator current and stator flux linkage observer," in *Energy Conversion Congress and Exposition, 2009. ECCE 2009. IEEE*, 2009, pp. 2504-2511.

[85] S.-K. Sul, *Control of Electric Machine Drive System*: IEEE Press 2011.

[86] R. Bojoi, G. Pellegrino, A. Cavagnino, and P. Guglielmi, "Direct Flux Vector Control of Axial Flux IPM Motors for in-wheel traction solutions," in *IECON 2010 - 36th Annual Conference on IEEE Industrial Electronics Society*, 2010, pp. 2224-2229.

[87] G. Pellegrino, R. Bojoi, and P. Guglielmi, "Unified Direct-Flux Vector Control for AC motor drives," in *Energy Conversion Congress and Exposition (ECCE), 2010 IEEE*, 2010, pp. 1150-1157.

[88] G. Pellegrino, R. Bojoi, and P. Guglielmi, "Impact of the motor magnetic model on direct flux vector control of interior PM motors," in *IECON 2011 - 37th Annual Conference on IEEE Industrial Electronics Society*, 2011, pp. 1879-1884.

[89] H. Khoa Dang and H. K. A. Aorith, "Online Control of IPMSM Drives for Traction Applications Considering Machine Parameter and Inverter Nonlinearities," *IEEE Transactions on Transportation Electrification*, vol. 1, pp. 312-325, 2015.

[90] T. Sun, J. Wang, and M. Koc, "Hybrid Control of Interior Permanent Magnet Synchronous Machine Drives," *IEEE Transactions on Power Electronics*, 2016.

[91] A. Sarikhani and O. A. Mohammed, "Demagnetization Control for Reliable Flux Weakening Control in PM Synchronous Machine," *IEEE Transactions on Energy Conversion*, vol. 27, pp. 1046-1055, 2012.

[92] L. Seungho, J. Yu-Seok, K. Yong-Jae, and J. Sang-Yong, "Novel Analysis and Design Methodology of Interior Permanent-Magnet Synchronous Motor Using Newly Adopted Synthetic Flux Linkage," *IEEE Transactions on Industrial Electronics*, vol. 58, pp. 3806-3814, 2011.

[93] H. Seon-Hwan and K. Jang-Mok, "Dead Time Compensation Method for Voltage-Fed PWM Inverter," *IEEE Transactions on Energy Conversion*, vol. 25, pp. 1-10, 2010.

[94] K. Sam-Young, L. Wootaik, R. Min-Sik, and P. Seung-Yub, "Effective Dead-Time Compensation Using a Simple Vectorial Disturbance Estimator in PMSM Drives," *IEEE Transactions on Industrial Electronics*, vol. 57, pp. 1609-1614, 2010.

[95] K. D. Hoang, Z. Q. Zhu, and M. Foster, "Online optimized stator flux reference approximation for maximum torque per ampere operation of interior permanent magnet machine drive under direct torque control," in *Power Electronics, Machines and Drives (PEMD 2012), 6th IET International Conference on*, 2012, pp. 1-6.

[96] K. D. Hoang, Z. Q. Zhu, M. P. Foster, and D. A. Stone, "Comparative study of current vector control performance of alternate fault tolerant inverter topologies for three-phase PM brushless ac machine with one phase open - circuit fault," in *Power Electronics,*

Machines and Drives (PEMD 2010), 5th IET International Conference on, 2010, pp. 1-6.

[97] K. D. Hoang, Z. Q. Zhu, and M. P. Foster, "Influence and Compensation of Inverter Voltage Drop in Direct Torque-Controlled Four-Switch Three-Phase PM Brushless AC Drives," *IEEE Transactions on Power Electronics*, vol. 26, pp. 2343-2357, 2011.

[98] Z. Q. Zhu, K. Utaikaifa, K. Hoang, Y. Liu, and D. Howe, "Direct torque control of three-phase PM brushless AC motor with one phase open-circuit fault," in *Electric Machines and Drives Conference, 2009. IEMDC '09. IEEE International*, 2009, pp. 1180-1187.

[99] D. Xiao and M. F. Rahman, "Sensorless direct torque and flux control for matrix converter-fed interior permanent magnet synchronous motor using adaptive sliding mode observer," in *Power and Energy Society General Meeting, 2010 IEEE*, 2010, pp. 1-5.

[100] X. Zhuang and M. F. Rahman, "Comparison of a Sliding Observer and a Kalman Filter for Direct-Torque-Controlled IPM Synchronous Motor Drives," *IEEE Transactions on Industrial Electronics*, vol. 59, pp. 4179-4188, 2012.

[101] G. H. B. Foo and M. F. Rahman, "Direct Torque Control of an IPM-Synchronous Motor Drive at Very Low Speed Using a Sliding-Mode Stator Flux Observer," *IEEE Transactions on Power Electronics*, vol. 25, pp. 933-942, 2010.

[102] M. E. Haque and M. F. Rahman, "Control Trajectories for Interior Permanent Magnet Synchronous Motor Drives," in *Electric Machines & Drives Conference, 2007. IEMDC '07. IEEE International*, 2007, pp. 306-311.

[103] M. F. Rahman, L. Zhong, K. W. Lim, and M. A. Rahman, "A direct torque controlled permanent magnet synchronous motor drive without a speed sensor," in *Electric Machines and Drives, 1999. International Conference IEMD '99*, 1999, pp. 123-125.

[104] G. Pellegrino, E. Armando, and P. Guglielmi, "Optimal exploitation of the Constant Power Region of IPM Drives Based on Field Oriented Control," in *Industry Applications Conference, 2007. 42nd IAS Annual Meeting. Conference Record of the 2007 IEEE*, 2007, pp. 1335-1340.

[105] G. Pellegrino, E. Armando, and P. Guglielmi, "Field oriented control of IPM drives for optimal constant power operation," in *Power Electronics and Applications, 2007 European Conference on*, 2007, pp. 1-10.

[106] E. Armando, R. I. Bojoi, P. Guglielmi, G. Pellegrino, and M. Pastorelli, "Experimental Identification of the Magnetic Model of Synchronous Machines," *IEEE Transactions on Industry Applications*, vol. 49, pp. 2116-2125, 2013.

[107] S. Morimoto, K. Hatanaka, Y. Tong, Y. Takeda, and T. Hirasa, "Servo drive system and control characteristics of salient pole permanent magnet synchronous motor," *IEEE Transactions on Industry Applications*, vol. 29, pp. 338-343, 1993.

[108] T. M. Jahns, G. B. Kliman, and T. W. Neumann, "Interior Permanent-Magnet Synchronous Motors for Adjustable-Speed Drives," *IEEE Transactions on Industry Applications*, vol. IA-22, pp. 738-747, 1986.

[109] M. N. Uddin, T. S. Radwan, and M. A. Rahman, "Performance of interior permanent magnet motor drive over wide speed range," *IEEE Transactions on Energy Conversion*, vol. 17, pp. 79-84, 2002.

[110] P. Ching-Tsai and S. M. Sue, "A linear maximum torque per ampere control for IPMSM drives over full-speed range," *IEEE Transactions on Energy Conversion*, vol. 20, pp. 359-366, 2005.

[111] A. Consoli, G. Scelba, G. Scarcella, and M. Cacciato, "An Effective Energy-Saving Scalar Control for Industrial IPMSM Drives," *IEEE Transactions on Industrial Electronics*, vol. 60, pp. 3658-3669, 2013.

[112] S. Morimoto, M. Sanada, and Y. Takeda, "Effects and Compensation of Magnetic Saturation in Flux-Weakening Controlled Permanent Magnet Synchronous Motor Drives," *IEEE Transactions on Industry Applications*, vol. 30, pp. 1632, 1994.

[113] K. Tae-Suk and S. Seung-Ki, "Analysis of the effect of the parameter variation on the flux weakening controller for improving torque capability," in *Applied Power Electronics Conference and Exposition, 2008. APEC 2008. Twenty-Third Annual IEEE*, 2008, pp. 91-97.

[114] R. Gubae, L. Jaesang, N. Kwanghee, I. Hyung-Bin, and K. Ho-Gi, "A MTPA control scheme for an IPM synchronous motor considering magnet flux variation caused by temperature," in *Applied Power Electronics Conference and Exposition, 2004. APEC '04. Nineteenth Annual IEEE*, 2004, pp. 1617-1621 Vol.3.

[115] R. S. Colby and D. W. Novotny, "An efficiency-optimizing permanent-magnet synchronous motor drive," *IEEE Transactions on Industry Applications*, vol. 24, pp. 462-469, 1988.

[116] A. Dianov, Y.-K. Kim, S.-J. Lee, and S.-T. Lee, "Robust self-tuning MTPA algorithm for IPMSM drives," in *Industrial Electronics, 2008. IECON 2008. 34th Annual Conference of IEEE*, 2008, pp. 1355-1360.

[117] K. W. Lee and S. B. Lee, "MTPA operating point tracking control scheme for vector controlled PMSM drives," in *SPEEDAM 2010*, 2010, pp. 24-28.

[118] A. Ahmed, Y. Sozer, and M. Hamdan, "Maximum torque per ampere control for interior permanent magnet motors using DC link power measurement," in *2014 IEEE Applied Power Electronics Conference and Exposition - APEC 2014*, 2014, pp. 826-832.

[119] Z. Q. Zhu, Y. S. Chen, and D. Howe, "Online optimal flux-weakening control of permanent-magnet brushless AC drives," *IEEE Transactions on Industry Applications*, vol. 36, pp. 1661-1668, 2000.

[120] K. Sungmin, Y. Young-Doo, S. Seung-Ki, and K. Ide, "Maximum Torque per Ampere (MTPA) Control of an IPM Machine Based on Signal Injection Considering Inductance Saturation," *IEEE Transactions on Power Electronics*, vol. 28, pp. 488-497, 2013.

[121] K. Sungmin, Y. Young-Doo, S. Seung-Ki, K. Ide, and K. Tomita, "Parameter independent maximum torque per ampere (MTPA) control of IPM machine based on signal injection," in *Applied Power Electronics Conference and Exposition (APEC), 2010 Twenty-Fifth Annual IEEE*, 2010, pp. 103-108.

[122] Y. Tan, W. H. Moase, C. Manzie, D. Ne, x, x, *et al.*, "Extremum seeking from 1922 to 2010," in *Proceedings of the 29th Chinese Control Conference*, 2010, pp. 14-26.

[123] S. Bolognani, L. Peretti, and M. Zigliotto, "Online MTPA Control Strategy for DTC Synchronous-Reluctance-Motor Drives," *IEEE Transactions on Power Electronics*, vol. 26, pp. 20-28, 2011.

[124] S. Bolognani, R. Petrella, A. Prearo, and L. Sgarbossa, "Automatic Tracking of MTPA Trajectory in IPM Motor Drives Based on AC Current Injection," *IEEE Transactions on Industry Applications*, vol. 47, pp. 105-114, 2011.

[125] R. Antonello, M. Carraro, and M. Zigliotto, "Towards the automatic tuning of MTPA algorithms for IPM motor drives," in *Electrical Machines (ICEM), 2012 XXth International Conference on*, 2012, pp. 1121-1127.

[126] R. Antonello, M. Carraro, and M. Zigliotto, "Theory and implementation of a MTPA tracking controller for anisotropic PM motor drives," in *IECON 2012 - 38th Annual Conference on IEEE Industrial Electronics Society*, 2012, pp. 2061-2066.

[127] R. Antonello, M. Carraro, and M. Zigliotto, "Maximum-Torque-Per-Ampere Operation of Anisotropic Synchronous Permanent-Magnet Motors Based on Extremum Seeking Control," *IEEE Transactions on Industrial Electronics*, vol. 61, pp. 5086-5093, 2014.

[128] P. H. Mellor, R. Wrobel, and D. Holliday, "A computationally efficient iron loss model for brushless AC machines that caters for rated flux and field weakened operation," in *Electric Machines and Drives Conference, 2009. IEMDC '09. IEEE International*, 2009, pp. 490-494.

[129] J. Goss, P. H. Mellor, R. Wrobel, D. A. Staton, and M. Popescu, "The design of AC permanent magnet motors for electric vehicles: A computationally efficient model of the operational envelope," in *Power Electronics, Machines and Drives (PEMD 2012), 6th IET International Conference on*, 2012, pp. 1-6.

[130] S. K. Sul. (15.12.2012, 03.08.2016). *Control of Electric Machine Drive System*. Available: https://vimeo.com/55668658

APPENDICES

Appendix A. INVERTER CONFIGURATION AND PROGRAMMING PROCEDURES

The prototype inverter has been specifically designed for P-Mob motor in Table 1.1 by Siemens manufacturer. Its block diagram is shown in Fig. A.1. It has been designed to operate at 120 V nominal DC link voltage. Rotor position angle and winding temperatures are obtained by a magnetic encoder and temperature sensors, respectively, and are transmitted to the inverter and hence they are readily available in the drive system. The communication between PC and the inverter is facilitated by Ethernet.

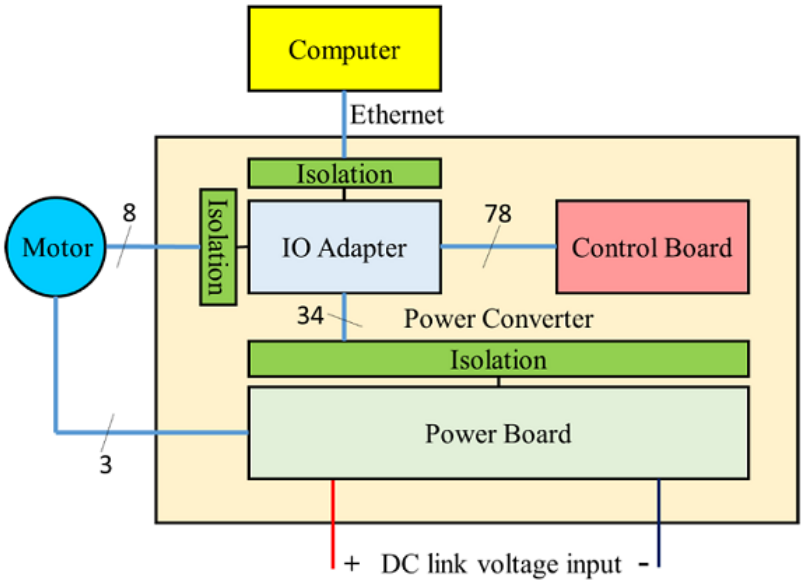

Fig. A.1 Block diagram of 3-phase voltage source inverter

Fig. A.2 illustrates the block diagram of controller board. The inverter is controlled by Tigersharc ADSP-TS201S (Analog Devices). The code for the controller is built by Visual DSP++ and transmitted to the flash memory via NIOS embedded CPU in FPGA. NIOS embedded CPU facilitates the use of Matlab Graphical User Interface (GUI). The control and the monitoring of the drive system operation is achieved via GUI on a supervisory PC which is connected to the inverter with an Ethernet cable. The command values during the tests are inputted to the system from PC via Matlab GUI where the real-time state variables can also be saved to the PC.

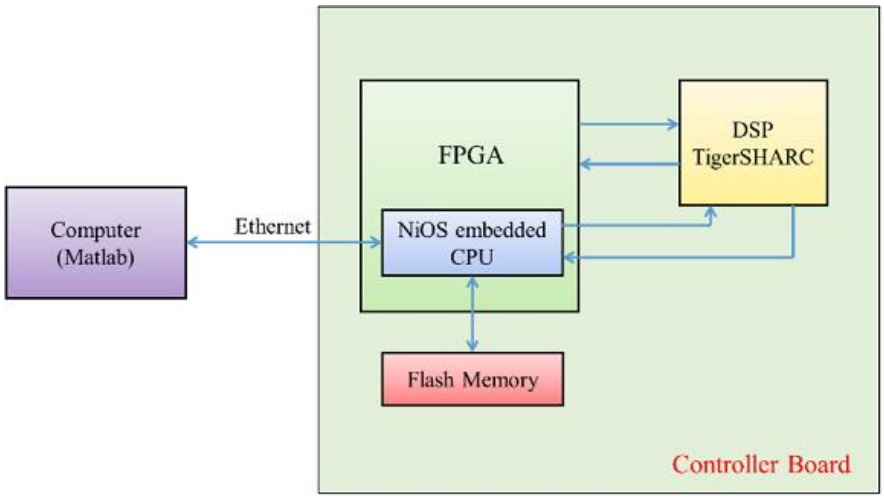

Fig. A.2 Block diagram of controller board

The controller code generation and flashing the code via Ethernet is done as per the following procedures:

1. The simulation file that is ready for code generation is saved into the Simulation folder provided by the Siemens and the folder is added with subfolders as path of the Matlab with the first and second steps shown in Fig. A.3

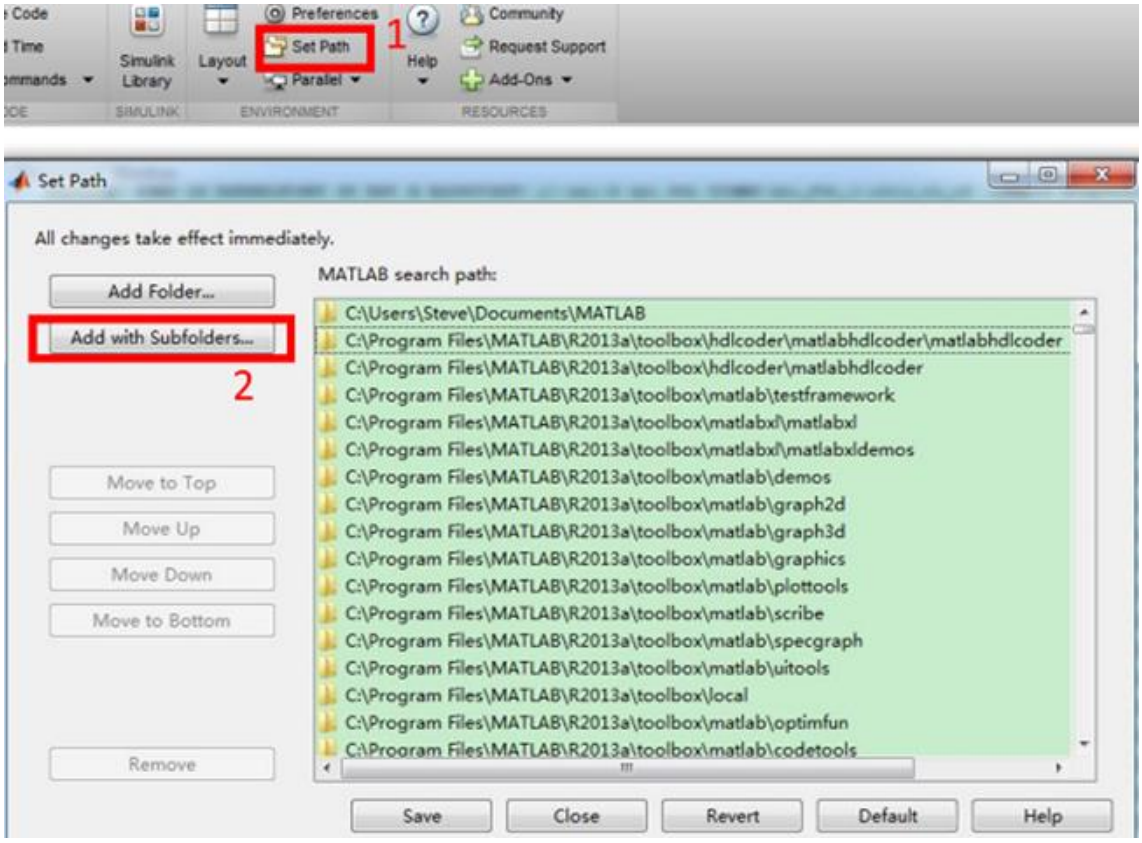

Fig. A.3 Setting for Matlab path

2. The proposed control scheme which is under the 'ControlUnit' subsystem as shown in Fig. A.4 is simulated to make sure that the drive system runs properly in the simulation.

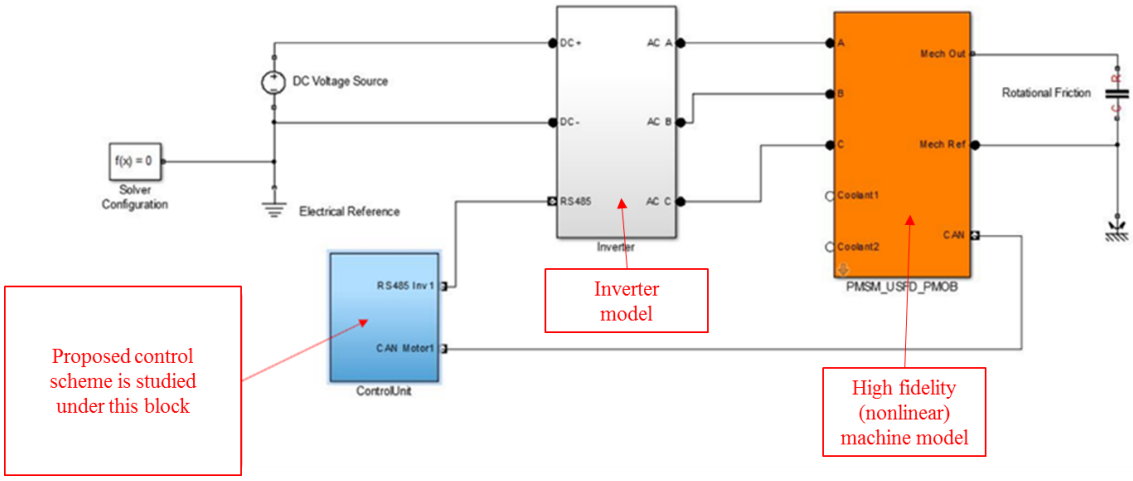

Fig. A.4 Simulink model of Siemens Code Generator

3. Right click 'InverterCtrl_IPM' and select 'Build This Subsystem' under the 'C/C++ Code' to generate the code as shown in Fig. A.5.

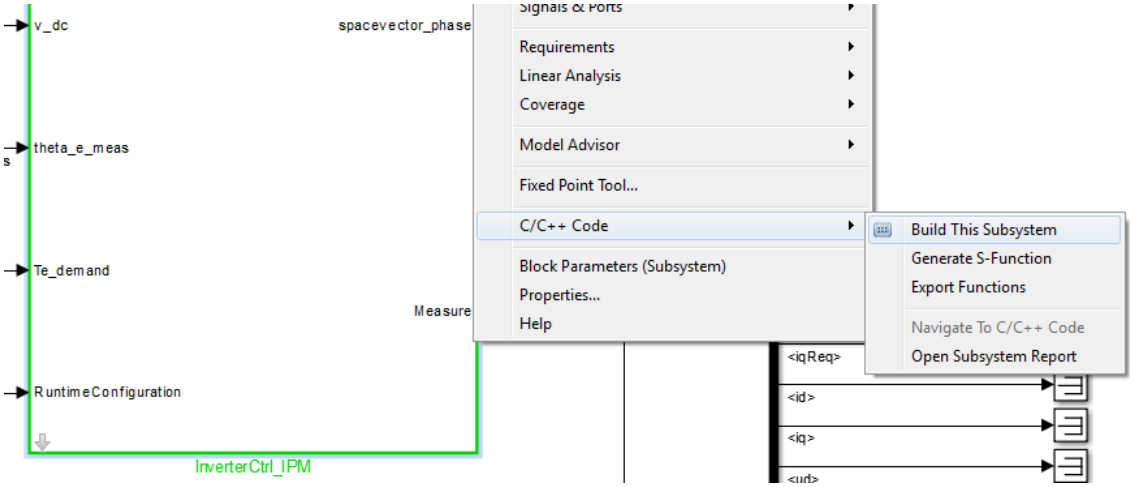

Fig. A.5 Code generation procedure in the Simulink

4. The generated code is transferred to the Tigersharc folder (Tigersharc → RealtimeCode → UpdateCode)
5. 'PMOB_Inverter' file is run which is in the Tigersharc folder
6. After the code is recompiled (F7) it is ready for transmitting.
7. The interface ports of the inverter shown in Fig. A.6 are connected properly and 12 V power supply is switched on.

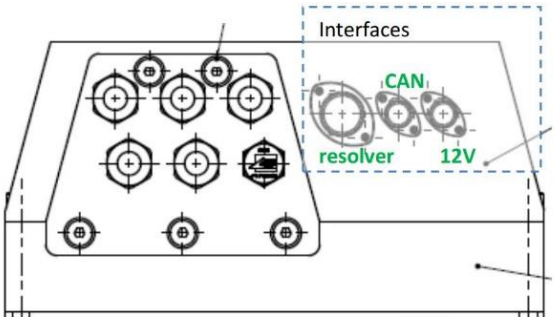

Fig. A.6 Inverter interface ports

8. The inverter and the PC is connected via LAN port.
9. The IP address of the computer is set as follows: Control Panel\Network and Internet\Network and Sharing Center, and then click on Local Area Connection and Properties, respectively. Afterwards, double click on Internet Protocol Version 4 (TCP/IPv4). Use the following IP address: 192.168.32.1 and use the following DNS server address: 225.255.255.0.
10. The code is transmitted as per the following steps: Open the following folder: Tigersharc\RealtimeCode\Release and then double click on the following file: FlashTigersharcCodeViaEthernet.
11. The 12 V power supply is switched off and then on again for the new code to be active.

Appendix B. EXPERIMENTAL PROCEDURES FOR THE PROPOSED OBSERVER WITH LINEAR TRAJECTORY

The Simulink model for the code generation of the drive system with the proposed observer in Chapter 2 is shown in Fig. A.7. The blocks and elements shown in the figure are under the InverterCtrl_IPM subsystem in Fig. A.5.

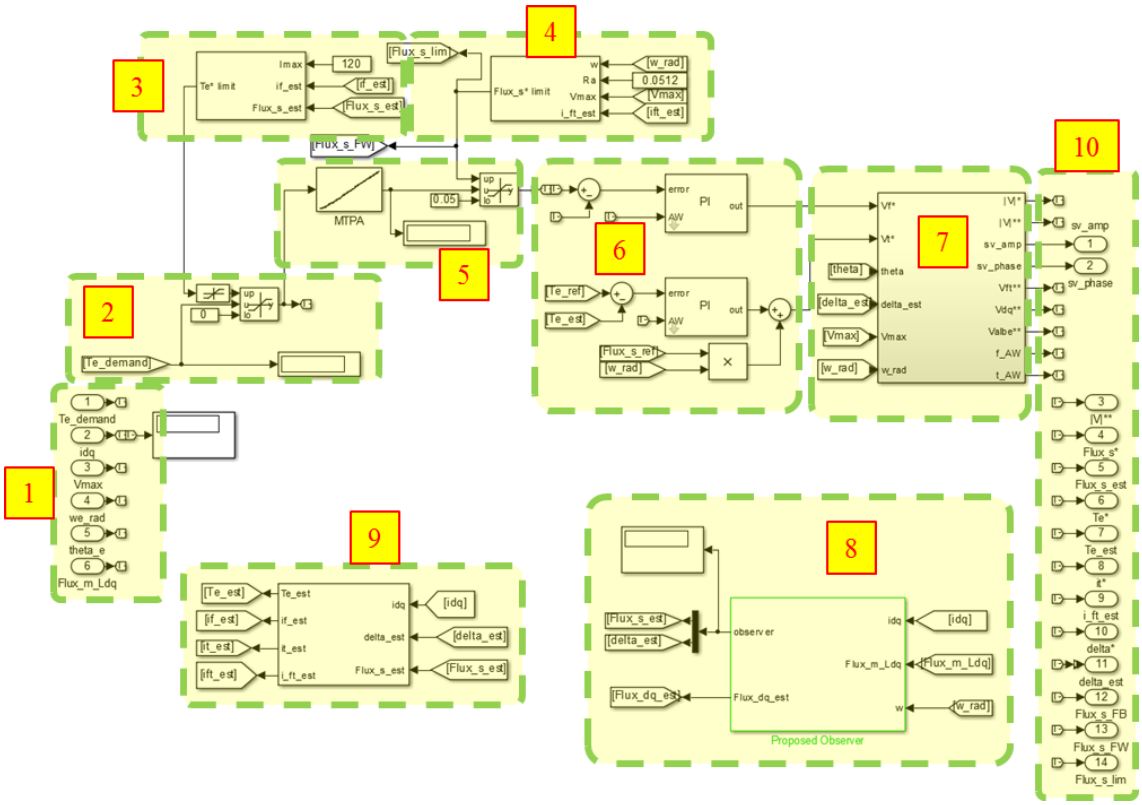

Fig. A.7 Simulink model for code generation of the proposed drive system in Chapter 2

The numbered subsystems/blocks are explained as follows:

1- Inputs of the system such as measured currents, torque command, measured DC-link voltage, speed etc.
2- The demanded torque with its constraint.
3- Torque limitation via (2.5).
4- Stator flux limitation for FW operation via (1.13).
5- Stator flux magnitude reference for MTPA operation.
6- PI controllers to regulate flux and torque.
7- Coordinate transformation of the reference voltages.
8- Proposed observer with linear trajectory
9- Coordinate transformation and the torque estimation via (1.8) and (1.12).
10- The outputs that can be monitored and saved to the PC.

The script of a PI controller in 6th subsystem of Fig. A.7 is given as follows:

```
%------------------------------------------------------------------------
function [result, Integral_out, Pval] = PiController(err, Integral,
Kp, Kpold, Ti, Tt, Ts, maxOutput, minOutput, maxI, minI, AW)
% This block supports the Embedded MATLAB subset.

% Bumpless transfer
Integral_out = (Kpold-Kp) * err + Integral;

% Update output
Pval = Kp*err;
resultNoSat = Pval + Integral_out;

result = resultNoSat;

% Limit output
if result > maxOutput
    result = maxOutput;
elseif result < minOutput
    result = minOutput;
end;

% compute antiwindup
localAntiWindup = result - resultNoSat;

%compute the integral part
Integral_out = Integral_out + Kp*Ts/Ti*err+Ts/Tt*(AW+localAntiWindup);

% limit the integral part
if Integral_out > maxI
    Integral_out = maxI;
elseif Integral_out < minI
    Integral_out = minI;
end;
%------------------------------------------------------------------------
```

The Simulink model of the proposed observer is shown in Fig. A.8.

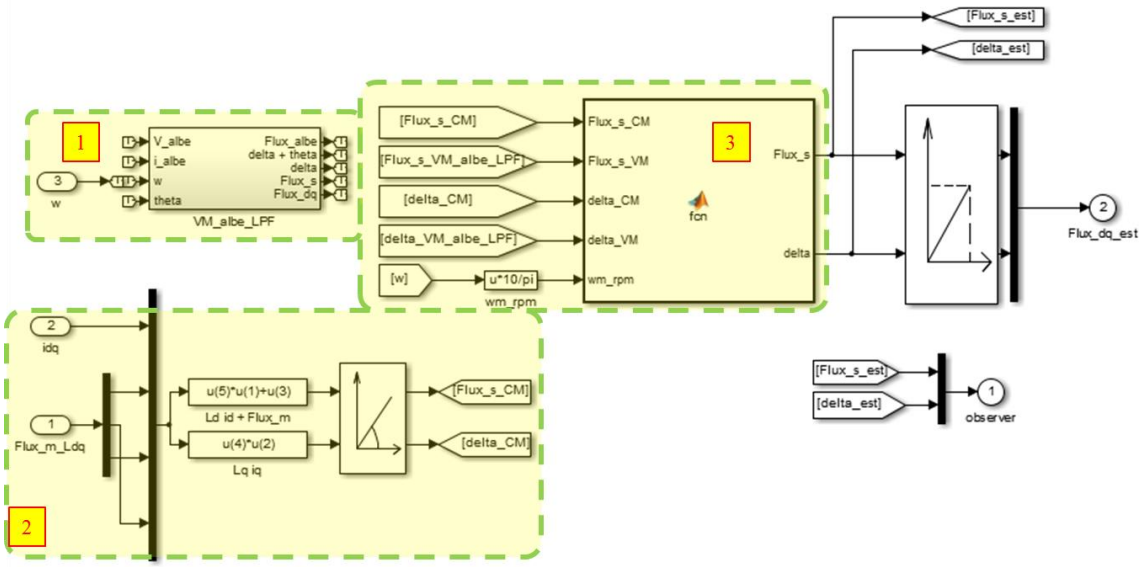

Fig. A.8 Simulink model of the proposed observer

1- The voltage based flux estimator via (2.12) and Fig. 2.9.

2- The current based flux estimator by substituting (1.2) into (1.8) and (1.9).

3- The proposed linear combination of the two estimators via (2.11).

The script of 3 is given below and the subsystem of 1 is shown in Fig. A.9.

```
%-----------------The script of the proposed combination--------------
function [Flux_s,delta] =
fcn(Flux_s_CM,Flux_s_VM,delta_CM,delta_VM,wm_rpm)

wm_CM=single(450);
wm_VM=single(550);
L=wm_VM-wm_CM;

    Flux_s=Flux_s_CM*(wm_VM-wm_rpm)/L+Flux_s_VM*(wm_rpm-wm_CM)/L;
    delta=delta_CM*(wm_VM-wm_rpm)/L+delta_VM*(wm_rpm-wm_CM)/L;

if wm_rpm<=wm_CM;
    Flux_s=Flux_s_CM;
    delta=delta_CM;
end


if wm_rpm>=wm_VM;
    Flux_s=Flux_s_VM;
    delta=delta_VM;
end
%-------------------------------------------------------------------------
```

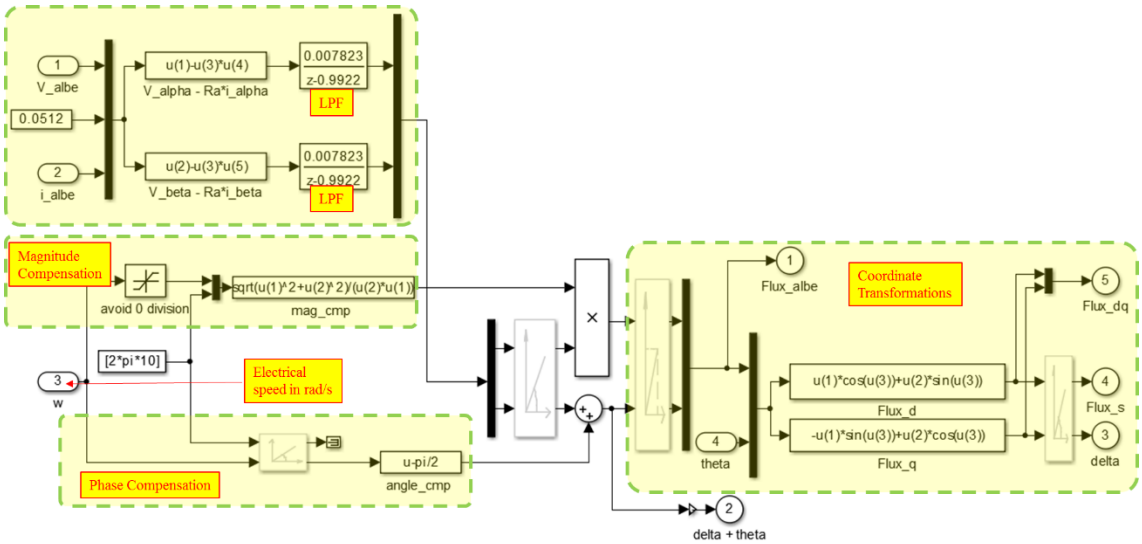

Fig. A.9 The subsystem of the voltage based estimation in the proposed approach (1 in Fig. A.8)

Appendix C. EXPERIMENTAL PROCEDURES FOR THE PROPOSED OBSERVER WITH HIGH FIDELITY MODELLING

The Simulink model for the code generation of the drive system with the proposed observer in Chapter 3 is shown in Fig. A.10. The blocks and elements shown in the figure are under the InverterCtrl_IPM subsystem in Fig. A.5.

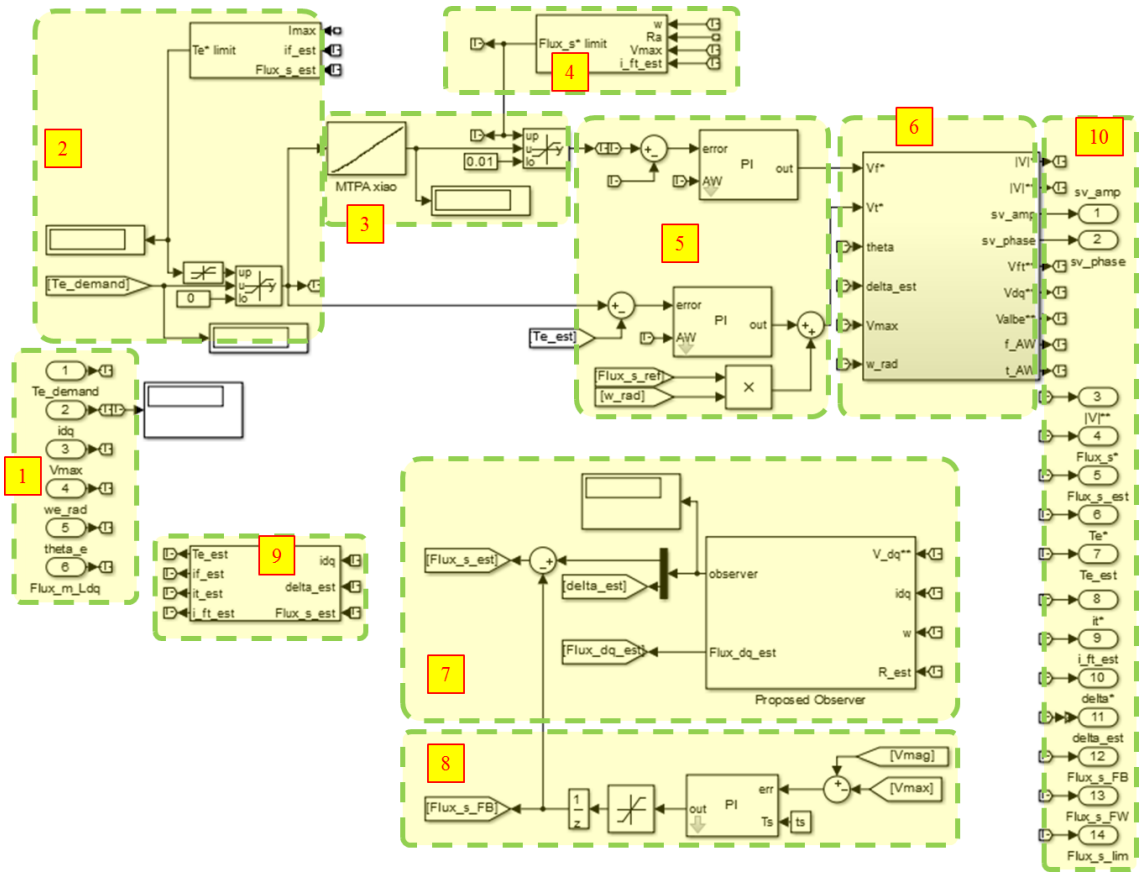

Fig. A.10 Simulink model for code generation of the proposed drive system in Chapter 3

The numbered subsystems/blocks are explained as follows:

1- Inputs of the system such as measured currents, torque command, measured DC-link voltage, speed etc.
2- The demanded torque with its constraint via (2.5).
3- Stator flux magnitude reference for MTPA operation.
4- Stator flux limitation for FW operation via (1.13).
5- PI controllers to regulate flux and torque.
6- Coordinate transformation of the reference voltages.
7- Proposed observer with high fidelity machine models.
8- Proposed FW compensation as has been discussed in section 3.3.2.

9- Coordinate transformation and the torque estimation via (1.8) and (1.12).

10- The outputs that can be monitored and saved to the PC.

The script of a PI controller in 5th subsystem of Fig. A.10 is same as the one given in the previous appendix. The Simulink model of the proposed observer is shown in Fig. A.11. The high-fidelity models for the P-MOB motor (Table 1.1) are shown in Fig. 3.3.

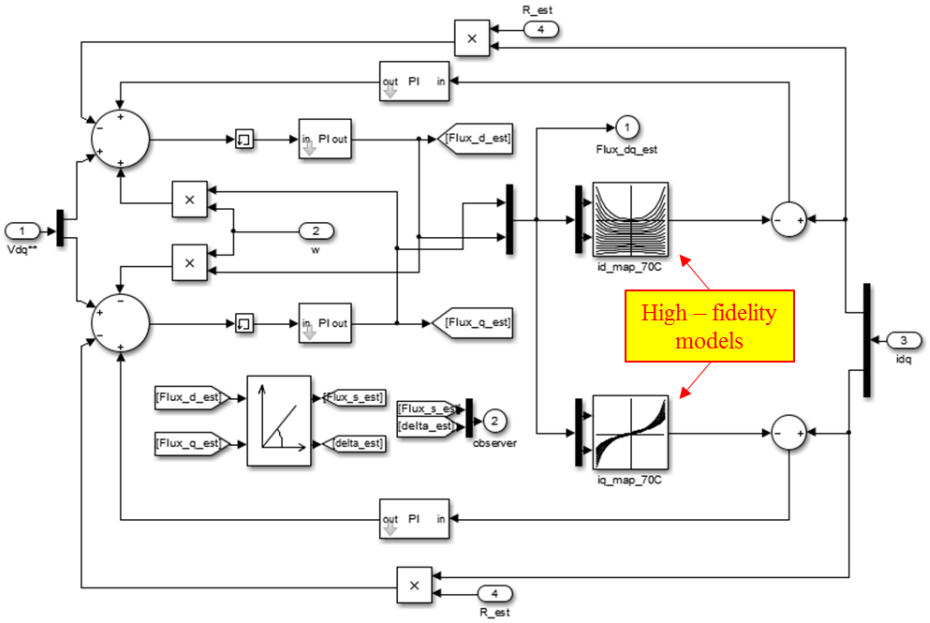

Fig. A.11 Simulink model of the proposed observer with high fidelity machine models

Appendix D. EXPERIMENTAL PROCEDURES FOR THE PROPOSED DIRECT, DECOUPLED AND LINEARIZED SFVC DRIVE

The Simulink model for the code generation of the proposed direct, decoupled and linearized SFVC based drive system with the proposed observer in Chapter 3 is shown in Fig. A.12. The blocks and elements shown in the figure are under the InverterCtrl_IPM subsystem in Fig. A.5.

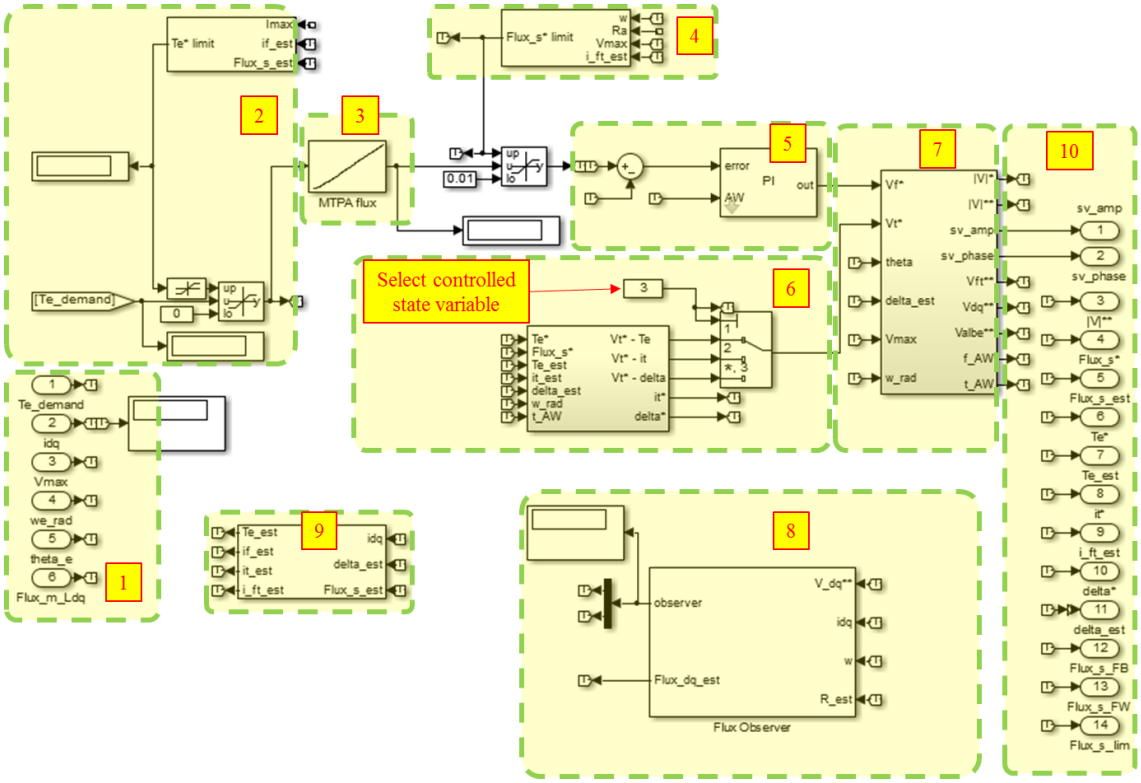

Fig. A.12 Simulink model for code generation of the direct, decoupled and linearized SFVC drive

The numbered subsystems/blocks are explained as follows:

1- Inputs of the system such as measured currents, torque command, measured DC-link voltage, speed etc.
2- The demanded torque with its constraint via (2.5).
3- Stator flux magnitude reference for MTPA operation.
4- Stator flux limitation for FW operation via (1.13).
5- PI controller to regulate stator flux magnitude.
6- The controllable state variables in SFVC drives.
7- Coordinate transformation of the reference voltages.
8- Flux observer for feedback control.

9- Coordinate transformation and the torque estimation via (1.8) and (1.12).

10- The outputs that can be monitored and saved to the PC.

The Simulink model of the proposed and the conventional SFVC based drives are combined in 6th subsystem in Fig. A.12 and the state variable to regulate the phase angle of the stator flux vector is selected based on Fig. A.13.

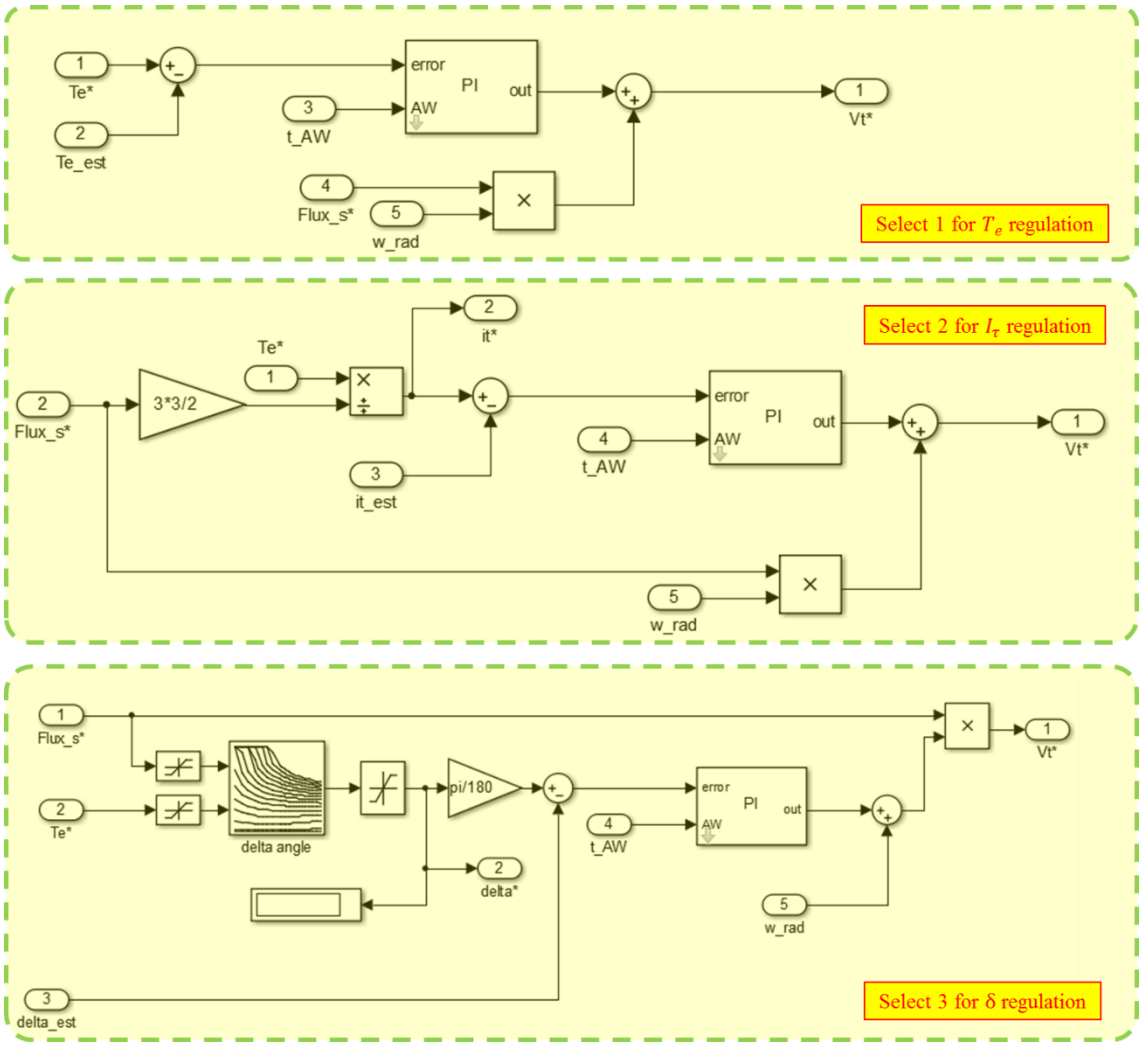

Fig. A.13 Simulink model of the controllable state variables in SFVC drives

Appendix E. EXPERIMENTAL PROCEDURES FOR THE PROPOSED ONLINE EFFICIENCY OPTIMIZED FOC DRIVE

The Simulink model for the code generation of the proposed virtual signal injection based online efficiency optimized drive system in Chapter 5 is shown in Fig. A.14. The blocks and elements shown in the figure are under the InverterCtrl_IPM subsystem in Fig. A.5.

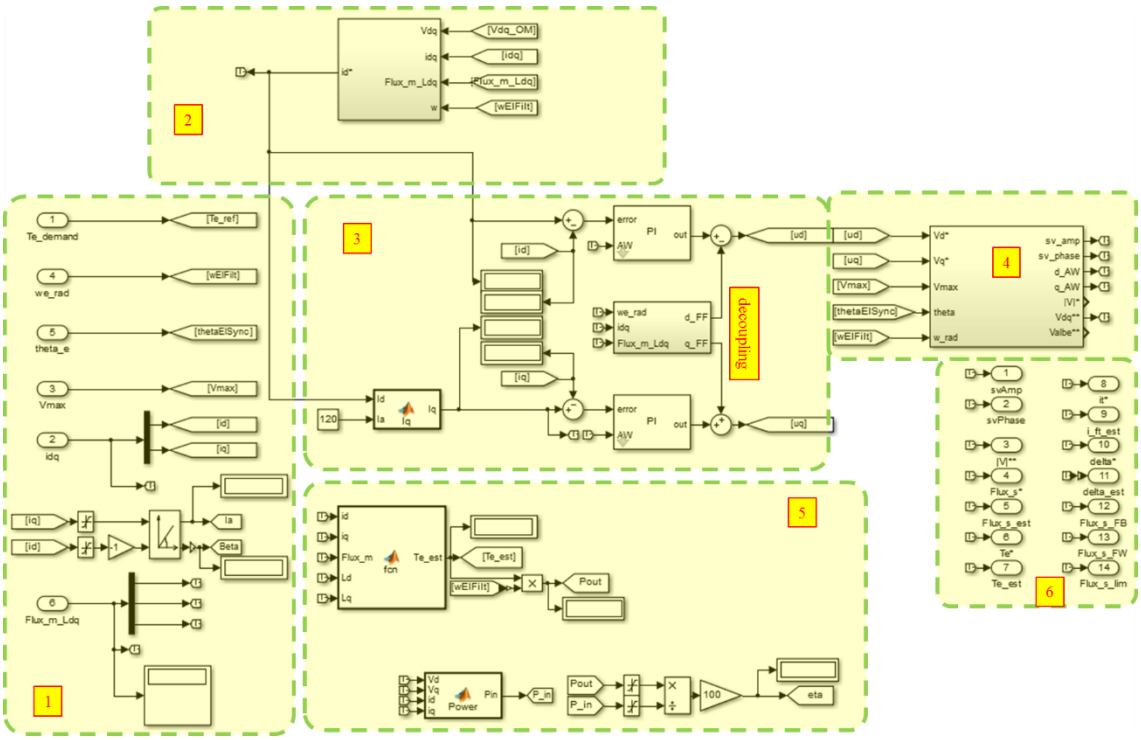

Fig. A.14 Simulink model for code generation of the virtual signal injection based FOC drive

The numbered subsystems/blocks are explained as follows:

1- Inputs of the system such as measured currents, torque command, measured DC-link voltage, speed etc.
2- The virtual signal injection based online *d*- axis reference current generator.
3- *dq*- axis current controllers and the decoupling terms in (1.1).
4- Coordinate transformation of the reference voltages.
5- Online calculations for torque, input/output powers and the efficiency.
6- The outputs that can be monitored and saved to the PC.

The virtual signal injection subsystem with number 2 is shown in Fig. A.15.

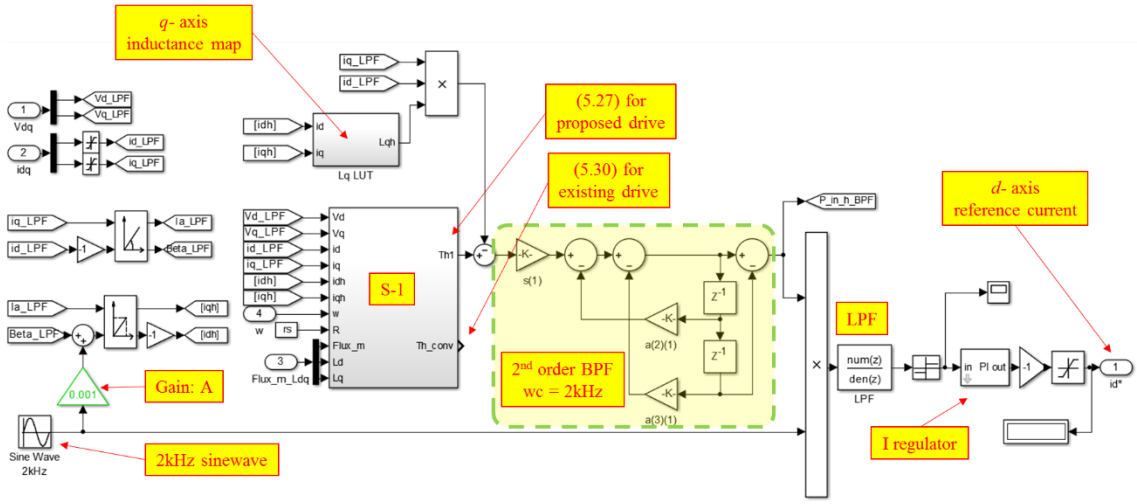

Fig. A.15 Virtual signal injection strategy (2nd subsystem in Fig. A.14)

The script under the S-1 subsystem in Fig. A.15 is given as follows:

```
%-----------------------------S-1-------------------------------------

function [Th1,Th_conv] = fcn(Vd,Vq,id,iq,idh,iqh,w,R,Ld)

Th1 = (((Vd-R*id)/(w*iq))*idh+Ld*idh+((Vq-R*iq)/w)-Ld*id)*iqh;
% Th1 is for the proposed approach

Th_conv=(((Vd-R*id)/(w*iq))*idh+((Vq-R*iq)/w))*iqh;
% Th_conv is for the existing approach.
% It is noteworthy that the compensation term in the proposed approach
% is disconnected once the existing approach is connected.

%-----------------------------------------------------------------------
```

Appendix F. SVPWM - SIMULINK IMPLEMENTATION

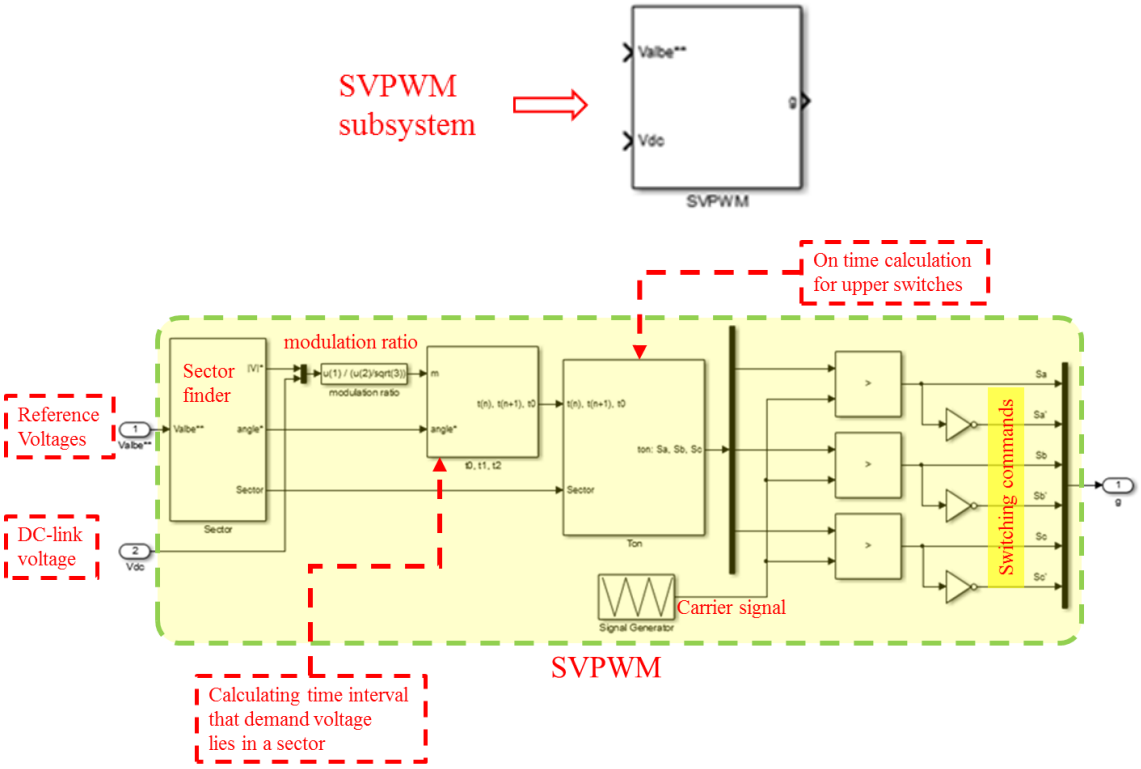

Fig. A.16 SVPWM modulation technique MATLAB implementation

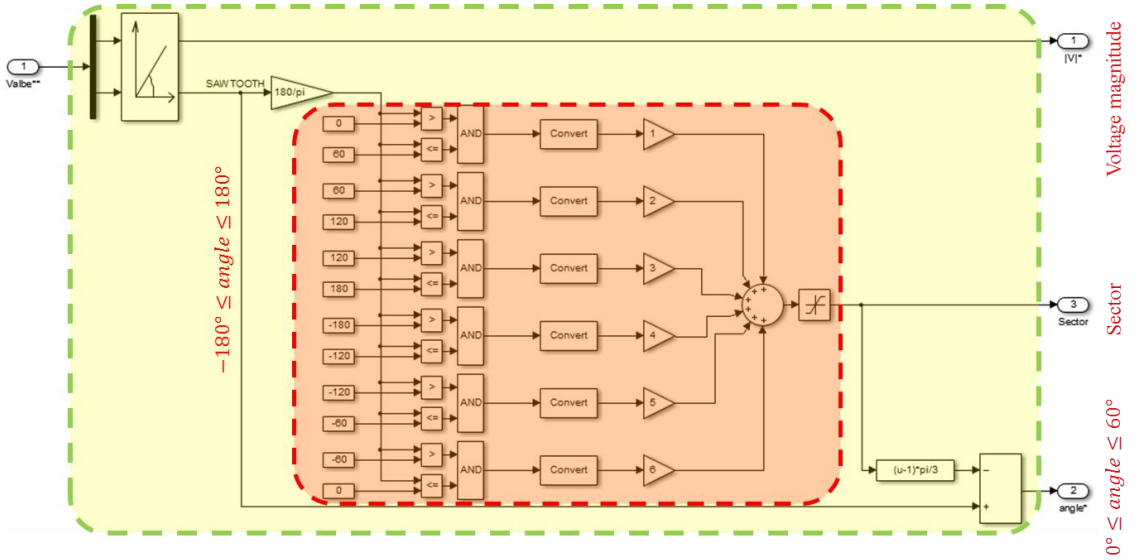

Fig. A.17 Sector finder where demand voltage lies in

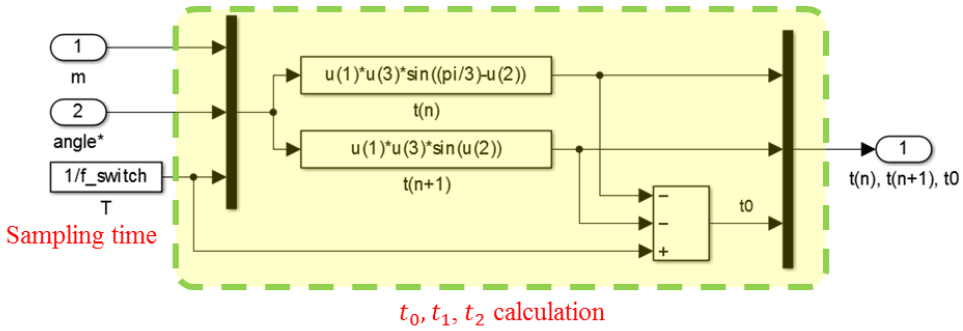

Fig. A.18 Calculating time interval that demand voltage lies in a sector

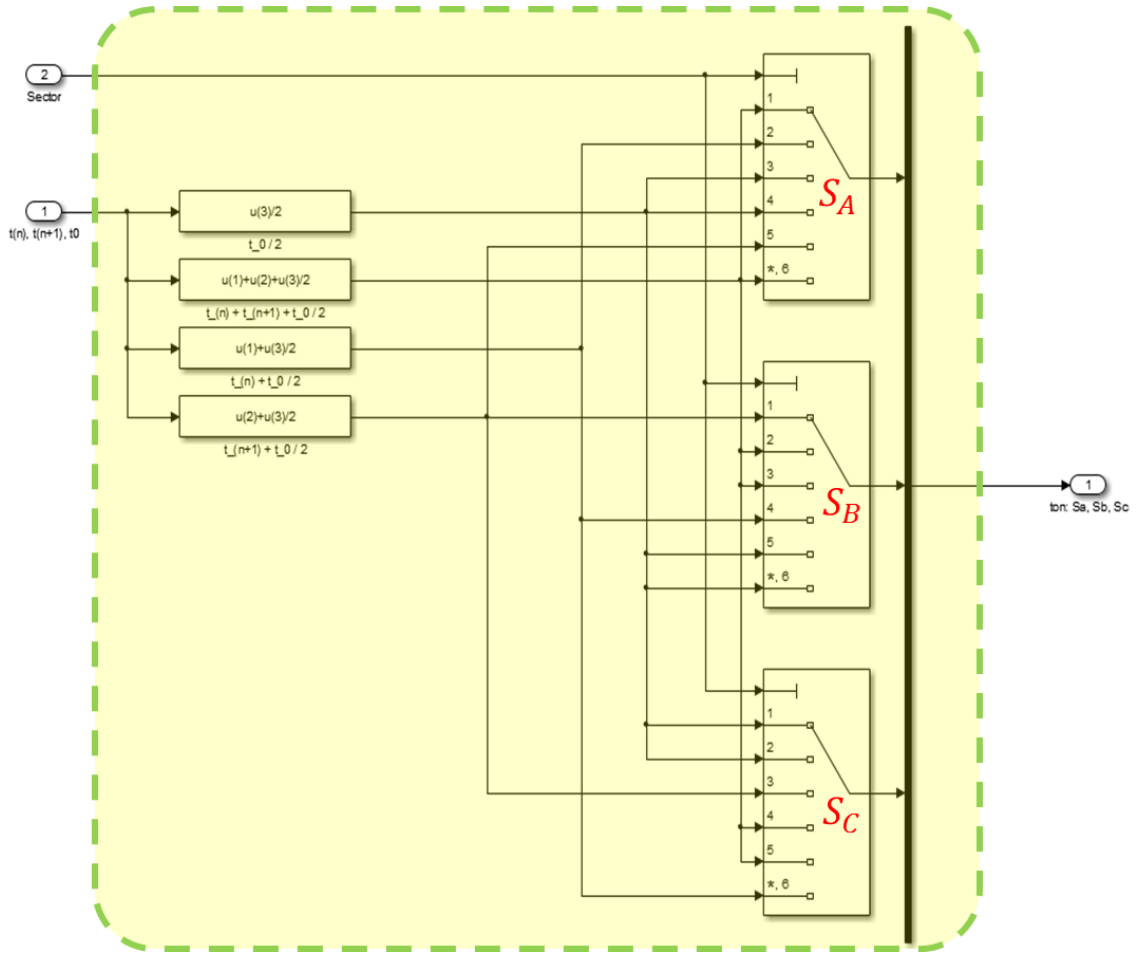

Fig. A.19 On-time calculation for upper switches

Appendix G. NONLINEAR MACHINE MODELS

The schematic of nonlinear parameter based machine model is illustrated in Fig. A.20. The look-up tables for nonlinear machine parameters of P-MOB motor are shown in Fig. 2.8.

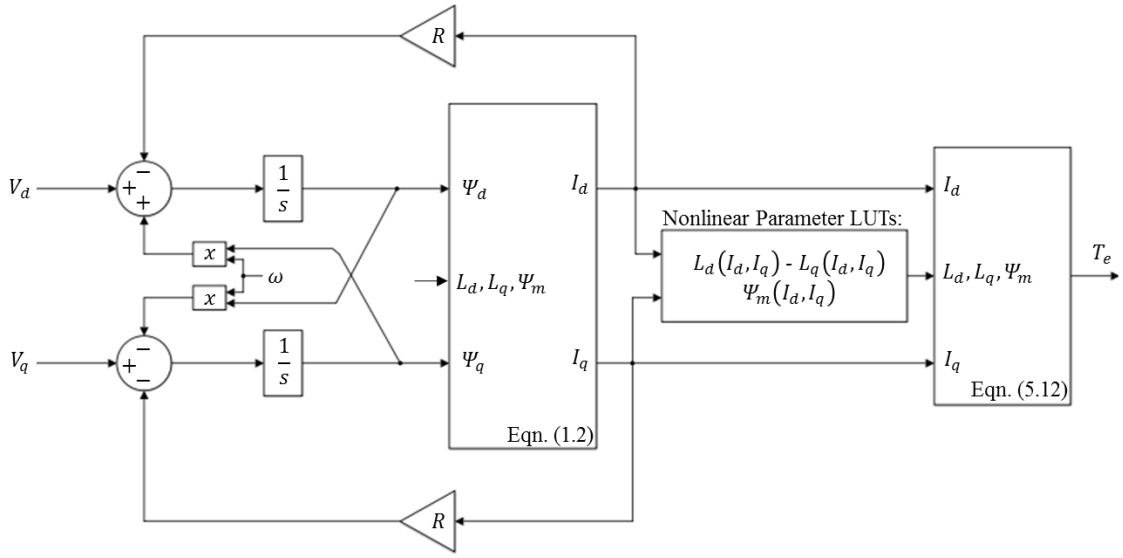

Fig. A.20 Schematic of nonlinear parameter based machine model

The schematic of high fidelity machine model is illustrated in Fig. A.21. The high-fidelity maps for P-MOB motor when the mean value of the rotor position angle is taken are shown in Fig. 3.3.

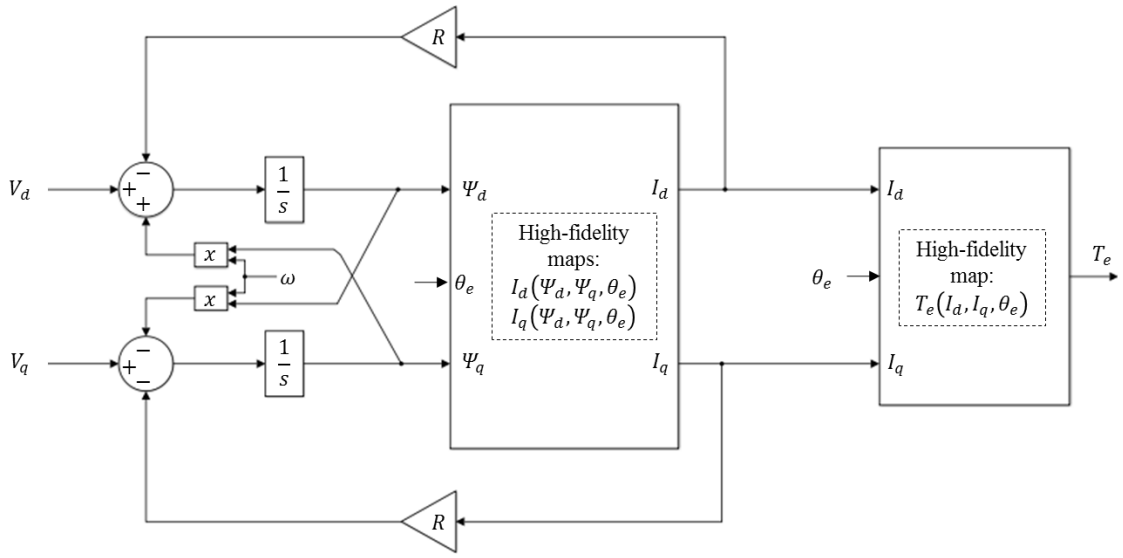

Fig. A.21 Schematic of high-fidelity machine model

Appendix H. IRON LOSS MODEL (P-MOB MOTOR)

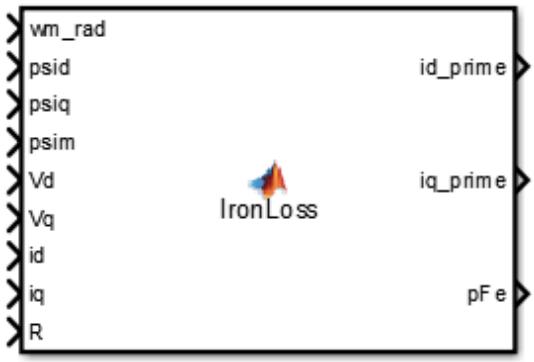

Fig. A.22 Simulink model for the iron loss

```
function [id_prime,iq_prime,pFe] =
IronLoss(wm_rad,psid,psiq,psim,Vd,Vq,id,iq,R)


% Considering build factor 1.5
ah=0.460253418;
ae=0.001931859;
ax=0.010292989;
bh=0.314854657;
be=0.004514867;
bx=0.020854884;

m=3; %number of phases

Vm=wm_rad*sqrt(psid^2+psiq^2);
Vda=-wm_rad*(psid-psim);

if psim~=0
    pFe_hy_oc=ah*(abs(Vm/(2*pi*psim)));
    pFe_ed_oc=ae*(abs(Vm/(2*pi*psim)))^2;
    pFe_ex_oc=ax*(abs(Vm/(2*pi*psim)))^1.5;

    pFe_hy_sc=bh*(abs(Vda/(2*pi*psim)));
    pFe_ed_sc=be*(abs(Vda/(2*pi*psim)))^2;
    pFe_ex_sc=bx*(abs(Vda/(2*pi*psim)))^1.5;

    pFe_hy=pFe_hy_oc+pFe_hy_sc;
    pFe_ed=pFe_ed_oc+pFe_ed_sc;
    pFe_ex=pFe_ex_oc+pFe_ex_sc;

    pFe_oc=pFe_hy_oc+pFe_ed_oc+pFe_ex_oc;
    pFe_sc=pFe_hy_sc+pFe_ed_sc+pFe_ex_sc;
    pFe=pFe_hy+pFe_ed+pFe_ex;

    if sqrt(psid^2+psiq^2)~=0
        pFe_md=abs(psiq/sqrt(psid^2+psiq^2))*pFe_oc+pFe_sc;
        pFe_mq=abs(psid/sqrt(psid^2+psiq^2))*pFe_oc;
    else
        pFe_md=0.5*pFe_oc+pFe_sc;
        pFe_mq=0.5*pFe_oc;
    end
```

```
    Vd1=Vd-id*R;
    if abs(Vd1)>=0.1
        if (psid*iq-psiq*id)*wm_rad>=0                  %motor
            if id<=0
                id_prime=id+2/m*abs(pFe_md/Vd1);
            else
                id_prime=id-2/m*abs(pFe_md/Vd1);
            end
        else                                             %generator
            if id<=0
                id_prime=id-2/m*abs(pFe_md/Vd1);
            else
                id_prime=id+2/m*abs(pFe_md/Vd1);
            end
        end
    else
        id_prime=id;
    end

    Vq1=Vq-iq*R;
    if abs(Vq1)>=0.1
        if (psid*iq-psiq*id)*wm_rad>=0                  %motor
            if iq>=0
                iq_prime=iq-2/m*abs(pFe_mq/Vq1);
            else
                iq_prime=iq+2/m*abs(pFe_mq/Vq1);
            end
        else                                             %generator
            if iq>=0
                iq_prime=iq+2/m*abs(pFe_mq/Vq1);
            else
                iq_prime=iq-2/m*abs(pFe_mq/Vq1);
            end
        end
    else
        iq_prime=iq;
    end


else
    id_prime=id;
    iq_prime=iq;
    pFe_hy=0;
    pFe_ed=0;
    pFe_ex=0;
    pFe=0;
end
```

Appendix I. P-MOB POLYNOMIAL BASED MACHINE MODEL

Matlab curve-fitting tool (cftool) has been utilized to generate the polynomial based nonlinear machine model from the high fidelity models.

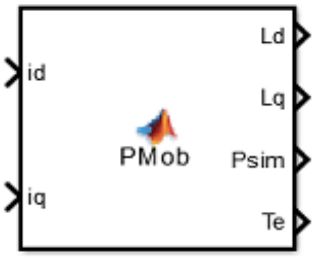

Fig. A.23 Schematic of the polynomial based high fidelity machine model for P-Mob motor

```
function [Ld, Lq, Psim, Te] = PMob(id,iq)

% Ld is the d- axis inductance,
% Lq is the q- axis inductance,
% Psim is the permanent magnet flux linkage,
% Te is the electromagnetic torque,
% id is the d- axis current,
% iq is the q- axis current,

x_mean=-60;
x_std=40.41; % where x is normalized by -60 and std 40.41,
x1=(id-x_mean)/x_std;
x2=(0-x_mean)/x_std;

y_mean=60;
y_std=40.41; % where y is normalized by 60 and std 40.41,
y=(iq-y_mean)/y_std;

% d- axis flux linkage:

Psid = (0.0694) + (0.03026)*x1 + (-0.006249)*y + (-.001085)*x1^2 + (-
.005634)*x1*y + (-.001437)*y^2 + (-.00038)*x1^3 + (.0001184)*x1^2*y +
(.001055)*x1*y^2 + (.00134)*y^3 + (-.0001349)*x1^4 + (.0003124)*x1^3*y
+ (.0003729)*x1^2*y^2 + (.0004452)*x1*y^3 + (4.322e-7)*y^4 + (-1.863e-
5)*x1^5 + (.0001649)*x1^4*y + (-2.715e-5)*x1^3*y^2 + (-
.0002926)*x1^2*y^3 + (-.000347)*x1*y^4 + (-.0001622)*y^5;

% q- axis flux linkage:

Psiq = (0.109) + (-.006133)*x1 + (0.03699)*y + (-0.002902)*x1^2 + (-
.003217)*x1*y + (-.01521)*y^2 + (-.0001093)*x1^3 + (.0011)*x1^2*y +
(.004276)*x1*y^2 + (.005523)*y^3 + (6.132e-5)*x1^4 + (.0001653)*x1^3*y
+ (.0008807)*x1^2*y^2 + (.0004635)*x1*y^3 + (-.0006843)*y^4 + (4.138e-
5)*x1^5 + (-4.548e-6)*x1^4*y + (-5.815e-5)*x1^3*y^2 + (-
.000717)*x1^2*y^3 + (-.001185)*x1*y^4 + (-.0001304)*y^5;

% permanent magnet flux linkage:

Psim = (0.0694) + (0.03026)*x2 + (-0.006249)*y + (-.001085)*x2^2 + (-
.005634)*x2*y + (-.001437)*y^2 + (-.00038)*x2^3 + (.0001184)*x2^2*y +
(.001055)*x2*y^2 + (.00134)*y^3 + (-.0001349)*x2^4 + (.0003124)*x2^3*y
```

```
+ (.0003729)*x2^2*y^2 + (.0004452)*x2*y^3 + (4.322e-7)*y^4 + (-1.863e-
5)*x2^5 + (.0001649)*x2^4*y + (-2.715e-5)*x2^3*y^2 + (-
.0002926)*x2^2*y^3 + (-.000347)*x2*y^4 + (-.0001622)*y^5;

Ld = (Psid-Psim)/id;

Lq = Psiq/iq;

Te = 3*3/2*(Psim*iq+id*iq*(Ld-Lq)); % 3 is the number of pole-pair.
```

Appendix J. NISSAN-LEAF POLYNOMIAL BASED MACHINE MODEL

Matlab curve-fitting tool (cftool) has been utilized to generate the polynomial based nonlinear machine model from the high fidelity models.

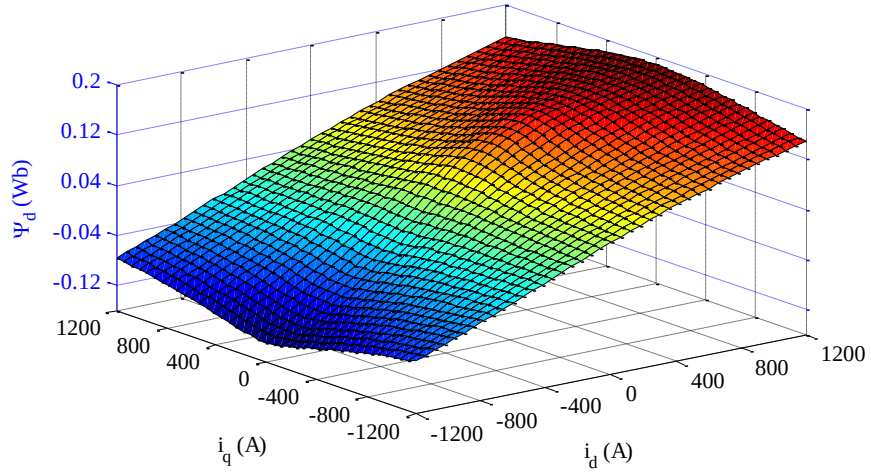

Fig. A.24 The *d*- axis flux linkage as a function of *dq*- axis currents

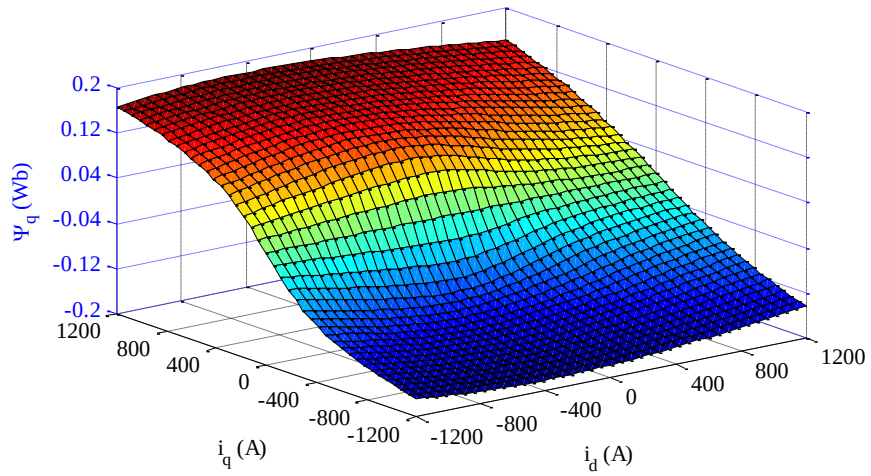

Fig. A.25 The *q*- axis flux linkage as a function of *dq*- axis currents

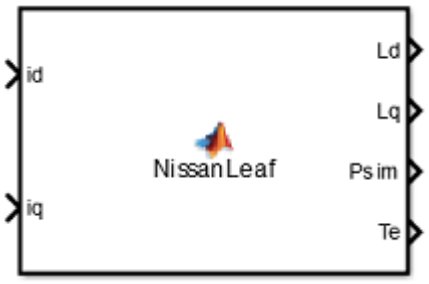

Fig. A.26 Schematic of the polynomial based high fidelity machine model for Nissan-Leaf motor

```
function [Ld, Lq, Psim, Te] = NissanLeaf(id,iq)

% Ld is the d- axis inductance,
% Lq is the q- axis inductance,
% Psim is the permanent magnet flux linkage,
% Te is the electromagnetic torque,
% id is the d- axis current,
% iq is the q- axis current,

x_mean=-200;
x_std=143.8; % where x is normalized by -200 and std 143.8,
x1=(id-x_mean)/x_std;
x2=(0-x_mean)/x_std;

y_mean=250;
y_std=173.7; % where y is normalized by 250 and std 173.7,
y=(iq-y_mean)/y_std;

% d- axis flux linkage:

Psid = (0.04131) + (0.02698)*x1 + (-0.001326)*y + (-0.0006792)*x1^2 +
(-0.004689)*x1*y + (-0.001749)*y^2 + (-0.0002877)*x1^3 + (-
0.0005168)*x1^2*y + (0.0005322)*x1*y^2 + (0.0007557)*y^3 + (-2.406e-
5)*x1^4 + (2.27e-6)*x1^3*y + (0.0003487)*x1^2*y^2 + (0.000661)*x1*y^3
+ (0.0002342)*y^4 + (4.638e-5)*x1^4*y + (0.0001079)*x1^3*y^2 + (-
1.153e-6)*x1^2*y^3 + (-0.0003724)*x1*y^4 + (-0.0002289)*y^5;

% q- axis flux linkage:

Psiq = (0.11) + (-0.001057)*x1 + (0.03413)*y + (-0.00183)*x1^2 + (-
0.00303)*x1*y + (-0.0219)*y^2 + (-0.000175)*x1^3 + (0.0001506)*x1^2*y
+ (0.00176)*x1*y^2 + (0.0131)*y^3 + (-2.543e-5)*x1^4 +
(0.0001058)*x1^3*y + (0.0006789)*x1^2*y^2 + (0.0009967)*x1*y^3 +
(0.001259)*y^4 + (3.923e-5)*x1^4*y + (7.943e-5)*x1^3*y^2 + (-
0.0002942)*x1^2*y^3 + (-0.0008617)*x1*y^4 + (-0.002917)*y^5;

% permanent magnet flux linkage:

Psim = (0.04131) + (0.02698)*x2 + (-0.001326)*y + (-0.0006792)*x2^2 +
(-0.004689)*x2*y + (-0.001749)*y^2 + (-0.0002877)*x2^3 + (-
0.0005168)*x2^2*y + (0.0005322)*x2*y^2 + (0.0007557)*y^3 + (-2.406e-
5)*x2^4 + (2.27e-6)*x2^3*y + (0.0003487)*x2^2*y^2 + (0.000661)*x2*y^3
+ (0.0002342)*y^4 + (4.638e-5)*x2^4*y + (0.0001079)*x2^3*y^2 + (-
1.153e-6)*x2^2*y^3 + (-0.0003724)*x2*y^4 + (-0.0002289)*y^5;

Ld = (Psid-Psim)/id;

Lq = Psiq/iq;

Te = 3*4/2*(Psim*iq+id*iq*(Ld-Lq)); % 4 is the number of pole-pair.
```

Appendix K. PROCEDURE TO OBTAIN OPERATING TRAJECTORIES

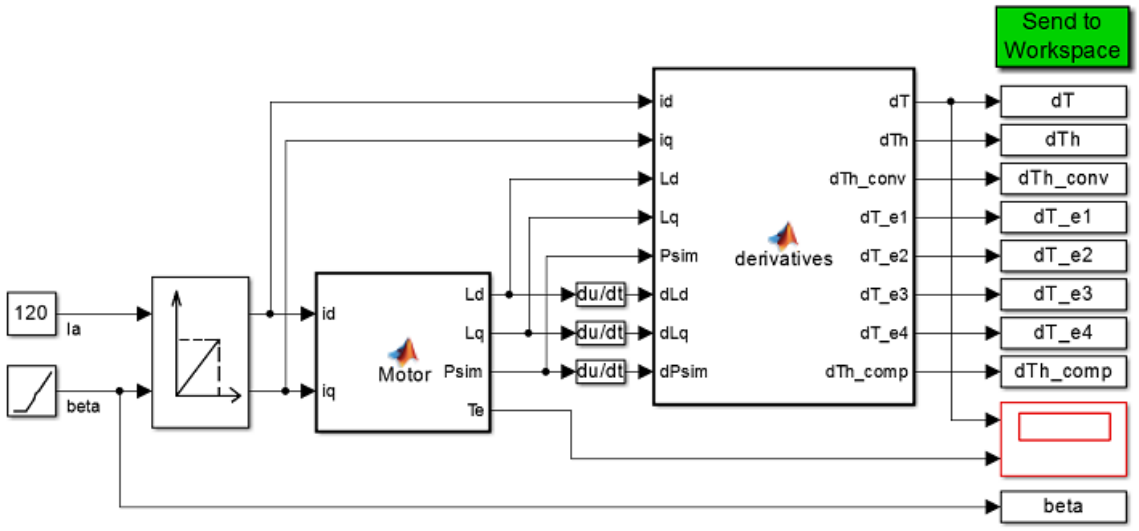

Fig. A.27 Schematic of the procedure to obtain operating trajectories

```
%Δt=Δβ

function [dT,dTh,dTh_conv,dT_e1,dT_e2,dT_e3,dT_e4,dTh_comp] =
derivatives(id,iq,Ld,Lq,Psim,dLd,dLq,dPsim)

%dT is the derivative of torque with respect to current angle
dT = Lq*iq^2-Lq*id^2-Ld*iq^2+Ld*id^2+Psim*id+(-
dLq*id+dLd*id+dPsim)*iq;

%dTh is (36)
dTh = Lq*iq^2-Lq*id^2-Ld*iq^2+Ld*id^2+Psim*id;

%dTh_conv is (41)
dTh_conv = Lq*iq^2-Lq*id^2+Ld*id^2+Psim*id;

%dT_e1 is utilized to obtain the trajectory with e1 error
dT_e1 = dT+dLq*id*iq;

%dT_e2 is utilized to obtain the trajectory with e2 error
dT_e2 = dT-dLd*id*iq;

%dT_e3 is utilized to obtain the trajectory with e3 error
dT_e3 = dT-dPsim*iq;

%dT_e4 is utilized to obtain the trajectory with e4 error
dT_e4 = dT+Ld*iq^2;

%dTh_comp represents the trajectory with the proposed approach
dTh_comp = dT-(dLd*id+dPsim)*iq;
```

The simulation is performed as per the following procedure:

1) Make sure that the initial value of β is $\pi/2$ with a slope of 1.
2) Run the simulation at a constant current magnitude for $\pi/2$ seconds so that $\pi/2 \leq \beta \leq \pi$. (Note that the unit of the angle is in radian!).
3) Save the results in the workspace.
4) Specify the current angles in which the equations are zero.
5) Repeat the steps from 1 to 4 for other current magnitudes.
6) Plot the current magnitudes versus current angles obtained for each equations.

Appendix L. MODELLING ERROR ANALYSIS OF THE OBSERVER WITH HIGH FIDELITY MACHINE MODELS

The elements of the M^{-1} (s) matrix, and the transfer functions associated with $\Delta\Psi_I(s)$, $\Delta\Psi_R(s)$ and $\Delta\Psi_M(s)$ are given by:

$$M^{-1} = \begin{bmatrix} \dfrac{s^3 + s^2(K_pJ_{22}) + s(K_iJ_{22})}{\sigma_1} & \dfrac{s^2(\omega - K_pJ_{12}) - s(K_iJ_{12})}{\sigma_1} \\ -\dfrac{s^2(\omega + K_pJ_{21}) + s(K_iJ_{21})}{\sigma_1} & \dfrac{s^3 + s^2(K_pJ_{11}) + s(K_iJ_{11})}{\sigma_1} \end{bmatrix}$$

where; $\boldsymbol{\sigma_1} = \boldsymbol{s^4} + \boldsymbol{s^3}\left(K_p(J_{11} + J_{22})\right) + \boldsymbol{s^2}\left(\omega^2 + K_i(J_{11} + J_{22}) - \omega K_p(J_{12} - J_{21}) + K_p{}^2(J_{11}J_{22} - J_{12}J_{21})\right) + \boldsymbol{s}\left(\omega K_i(J_{21} - J_{12}) + 2K_pK_i(J_{11}J_{22} - J_{12}J_{21})\right) + K_i{}^2(J_{11}J_{22} - J_{12}J_{21})$

$$\Delta\Psi_I(s) = \begin{bmatrix} \dfrac{\left(\boldsymbol{s^3}\left(\Delta V_d(s)\right) + \boldsymbol{s^2}\left(\Delta V_d(s)K_pJ_{22} + \Delta V_q(s)(\omega - K_pJ_{12})\right)\right)}{+\boldsymbol{s}\left(\Delta V_d(s)K_iJ_{22} - \Delta V_q(s)K_iJ_{12}\right)} \\ \sigma_1 \\ \dfrac{\left(\boldsymbol{s^3}\left(\Delta V_q(s)\right) + \boldsymbol{s^2}\left(\Delta V_q(s)K_pJ_{11} - \Delta V_d(s)(\omega + K_pJ_{21})\right)\right)}{+\boldsymbol{s}\left(\Delta V_q(s)K_iJ_{11} - \Delta V_d(s)K_iJ_{21}\right)} \\ \sigma_1 \end{bmatrix}$$

$$\Delta\Psi_R(s) = \begin{bmatrix} \dfrac{\left(\boldsymbol{s^3}\left(\Delta RI_d(s)\right) + \boldsymbol{s^2}\left(\Delta RI_d(s)K_pJ_{22} + \Delta RI_q(s)(\omega - K_pJ_{12})\right)\right)}{+\boldsymbol{s}\left(\Delta RI_dK_iJ_{22} - \Delta RI_q(s)K_iJ_{12}\right)} \\ \sigma_1 \\ \dfrac{\left(\boldsymbol{s^3}\left(\Delta RI_q(s)\right) + \boldsymbol{s^2}\left(\Delta RI_q(s)K_pJ_{11} - \Delta RI_d(s)(\omega + K_pJ_{21})\right)\right)}{+\boldsymbol{s}\left(\Delta RI_q(s)K_iJ_{11} - \Delta RI_d(s)K_iJ_{21}\right)} \\ \sigma_1 \end{bmatrix}$$

$$\Delta\Psi_M(s) = \begin{bmatrix} \dfrac{\left(\boldsymbol{s^3}\left(K_p\Delta f_1\right) + \boldsymbol{s^2}\left(\Delta f_1\left(K_i + K_p{}^2J_{22}\right) + \Delta g_1K_p(\omega - K_pJ_{12})\right)\right.}{\left.+\boldsymbol{s}\left(2\Delta f_1K_pK_iJ_{22} + \Delta g_1K_i(\omega - 2K_pJ_{12})\right) + K_i{}^2(\Delta f_1J_{22} - \Delta g_1J_{12})\right)} \\ \sigma_1 \\ \dfrac{\left(\boldsymbol{s^3}\left(K_p\Delta g_1\right) + \boldsymbol{s^2}\left(\Delta g_1\left(K_i + K_p{}^2J_{11}\right) - \Delta f_1K_p(\omega + K_pJ_{21})\right)\right.}{\left.+\boldsymbol{s}\left(2\Delta g_1K_pK_iJ_{11} - \Delta f_1K_i(\omega + 2K_pJ_{21})\right) + K_i{}^2(\Delta g_1J_{11} - \Delta f_1J_{21})\right)} \\ \sigma_1 \end{bmatrix}$$

It can be shown based on the final value theorem that:

$$\lim_{s\to 0}\Delta\Psi_I(s) = \lim_{s\to 0}\Delta\Psi_R(s) = \begin{bmatrix} 0 \\ \hline K_i{}^2(J_{11}J_{22} - J_{12}J_{21}) \\ 0 \\ \hline K_i{}^2(J_{11}J_{22} - J_{12}J_{21}) \end{bmatrix} = \begin{bmatrix} 0 \\ 0 \end{bmatrix}$$

$$\lim_{s\to 0}\Delta\Psi_M(s) = \begin{bmatrix} \dfrac{K_i{}^2(\Delta f_1 J_{22} - \Delta g_1 J_{12})}{K_i{}^2(J_{11}J_{22} - J_{12}J_{21})} \\ \dfrac{K_i{}^2(\Delta g_1 J_{11} - \Delta f_1 J_{21})}{K_i{}^2(J_{11}J_{22} - J_{12}J_{21})} \end{bmatrix} = \begin{bmatrix} \dfrac{\Delta f_1 J_{22} - \Delta g_1 J_{12}}{J_{11}J_{22} - J_{12}J_{21}} \\ \dfrac{\Delta g_1 J_{11} - \Delta f_1 J_{21}}{J_{11}J_{22} - J_{12}J_{21}} \end{bmatrix} = \begin{bmatrix} c_1 \\ c_2 \end{bmatrix}$$